

**Mechanisms and Mechanics of  
Bonding in 3D Printed Moulds and  
Critical Roles of Specific  
Constituents**

**Solaman Bobby Selvaraj**

A thesis submitted to

Auckland University of Technology in partial fulfilment of

the requirement for the degree of

**Doctor of Philosophy (PhD)**

**September 2015**

# Table of Contents

List of Figures.....	vii
List of Tables.....	xii
List of Publications .....	xiii
List of Abbreviations .....	xiv
Attestation of Authorship.....	xvi
Acknowledgement.....	xvii
Abstract.....	xx
<b>Chapter 1. Introduction.....</b>	<b>1</b>
1.1    Metal Casting.....	1
1.2    Rapid Prototyping and Tooling.....	4
1.3    Rapid Casting.....	6
1.4    3D Printing.....	7
1.5    Objectives, Methodologies and the Structure of the Thesis..	10
<b>Chapter 2. Literature Review.....</b>	<b>14</b>
2.1    Traditional Casting and Time Constraints.....	14
2.2    Rapid Prototyping Solutions for Casting.....	15
2.3    Direct Laser Sintering of Moulding Sand.....	24
2.4    3D Printing of a Mould for Sand Casting.....	27
2.5    Research Gaps, Hypothesis and Questions.....	36
2.6    Objectives of the Current Research.....	42

2.7	Methodologies.....	43
2.7.1	Development of Experimental Material Systems.....	44
2.7.2	3D Printing.....	46
2.7.3	Mould Material Characterisation.....	47
2.7.3.1	Metallographic Evaluation.....	47
2.7.3.2	Compression Test.....	48
2.7.3.3	Printed Moulds.....	50
2.7.4	Casting Trials and Characterisation.....	52
2.7.5	Tensile Testing.....	53
2.7.6	Surface Roughness Measurements.....	54
2.8	Nomenclature of material systems used.....	54

**Chapter 3. Plaster Based Material System.....55**

3.1	Printing Sand Moulds.....	55
3.2	Basic Ingredients and the bonding Mechanism.....	57
3.3	The Plaster Hydration, Dehydration, and accelerated Crystallisation.....	59
3.4	The Material System.....	65
3.5	Mechanism of Gypsum Bonding with varying Levels of Pre- Moisture.....	71
3.6	Mechanics of Bonding.....	77
3.6.1	Percent Volume Error.....	79
3.6.2	Compressive Strength.....	84
3.7	Summary of Pre-Moisturised Plaster System used for 3D	

Printing.....	89
<b>Chapter 4. Sodium Silicate Treated Plaster-Clay Material System.....</b>	<b>91</b>
4.1 Clay and Sodium Silicate Treatment in Sand Casting.....	91
4.2 Clay Hydration and Dehydration Mechanism.....	93
4.3 Sodium Silicate as a Foundry Sand Binder.....	96
4.4 Mechanisms of Clay Bonding in 3D Printing.....	100
4.4.1 Initial Trails with Bentonite Clay.....	100
4.4.2 The Clay Plaster Combination and the Mechanism of Bonding in the green State.....	102
4.4.3 Post Backing Concerns and the Sodium Silicate Treatment.....	106
4.5 Mechanism of Bonding 3D Printed Plaster-Clay-Sand Composites together with the Sodium Silicate Treatment...	112
4.5.1 Volume Error.....	114
4.5.2 Flexural Strength.....	119
4.5.3 Compressive Strength.....	122
4.6 Summary of Clay and Sodium Silicate Treatment.....	129
<b>Chapter 5. Resin Coated Sand Material System.....</b>	<b>130</b>
5.1 Clays and Resins Coated Sands; the Ingredients for High Refractories.....	130
5.2 Refractory Clays.....	132
5.3 Resin Bonding.....	133

5.4	Clay and Resin Based Material Combinations for 3DPrinting.....	136
5.5	The Clay Bonding Mechanism in the Green State.....	140
5.6	Resin Bonding in Baked Samples.....	143
5.7	Experimental Evaluation of the Influence of varying Compositions.....	148
5.7.1	Mechanisms of Green and Dry Bonding.....	148
5.7.2	Volume Error.....	152
5.7.3	Compressive Strength.....	154
5.7.4	Flexural Strength.....	156
5.8	Chapter Summary.....	157

**Chapter 6. Casting Quality Evaluation.....159**

6.1	Casting Trials.....	159
6.2	Moulds Printed using Plaster based material System for Non-Ferrous Casting.....	160
6.2.1	Volume Error.....	160
6.2.2	Surface Roughness.....	164
6.2.3	Tensile Strength.....	168
6.2.4	Mould-Metal Interactions.....	170
6.3	Sodium Silicate Treated Plaster – Clay System Moulds for Aluminium Casting.....	175
6.3.1	Percent Volume Error.....	175
6.3.2	Surface Roughness.....	178

6.3.3	Ultimate Tensile Strength.....	179
6.3.4	Mould-Metal Interactions in the case of the Sodium Silicate Treated Plaster-Clay-Sand Composites.....	180
6.4	Ferrous Casting on Moulds Printed using Resin Coated Sand Material System.....	181
6.4.1	Percent Volume Error.....	183
6.4.2	Surface Roughness.....	185
6.4.3	Tensile Strength.....	185
6.5	Case Studies.....	186
6.5.1	A Single Cylinder Engine Block based on the Sodium Silicate Treated Plaster Material System.....	187
6.5.2	Stainless Steel Step-Cone Cylinder Cast in Printed Moulds on the Resin Coated Material System.....	192
6.6	Summary of Casting Trials and Results.....	197

**Chapter 7. Conclusions and Recommendations.....198**

7.1	The experimental research done and the overarching results.....	198
7.2	General observations with different material systems.....	200
7.2.1	Pre-moisturised $\alpha$ -hemihydrate-sand composite.....	200
7.2.2	Clay-silica-sand composites with sodium silicate treatment.....	202
7.2.3	Resin coated sand system .....	203
7.3	Significant conclusions based on experimental results.....	204

7.3.1	Pre-moisturised plaster-sand composites.....	205
7.3.2	Clay-plaster-sand composites with sodium silicate treatment.....	206
7.3.3	Clay-silica flour-resin coated sand composites.....	208
7.4	Casting trials.....	210
7.4.1	Moulds by plaster based material system for casting Aluminium Alloy.....	210
7.4.2	Sodium Silicate Treated Plaster-Clay Material System Moulds for Aluminium Casting.....	211
7.4.3	Moulds for Ferrous casting based on Resin Coated Sand Material System.....	212
7.5	Future work.....	213
	<b>References.....</b>	<b>215</b>
	<b>Appendices.....</b>	<b>230</b>
	<b>Appendix 1: Plaster based Material System: Additional experimental data and results.....</b>	<b>230</b>
	<b>Appendix 2: Plaster-clay Material System with Sodium Silicate Treated: Additional experimental data and results.....</b>	<b>236</b>
	<b>Appendix 3: Resin Coated Sand Material System: Additional experimental data and results.....</b>	<b>257</b>

## List of Figures

Fig. 2.1: The Z-Printer® 310 plus.....	46
Fig. 2.2: HITACHI E-1045 magnetron sputter ion.....	47
Fig. 2.3: The Hitachi SU-70 Schottky field emission SEM.....	48
Fig. 2.4: CAD drawings and printed samples of compression and 3-point bending test pieces.....	49
Fig. 2.5: Test specimens printed for compression tests as per the ASTM standards and preserved in the desiccator.....	49
Fig. 2.6: The compression test in progress and a test specimen fractured on 45° shear planes.....	50
Fig. 2.7: CAD model of the mould.....	51
Fig. 2.8: Printed moulds and pouring cups waiting to be cast.....	51
Fig. 2.9: A finished casting.....	52
Fig. 2.10: Tensile test specimens prepared as per the ASTM E8 standard.....	53
Fig. 2.11: The hounsfield tensile tester and the specimens before and after brake.....	53
Fig. 2.12: The taylor hobson talysurf surface roughness tester.....	54
Fig. 3.1: Initial trials printed manually in ice-trays.....	68
Fig. 3.2: Fig. 3.2 Printed and baked rectangular samples.....	69
Fig. 3.3: (a) Spherical silica sand particles, (b) $\beta$ -hemihydrate, mould material mixtures with 33% plaster and 67% silica sand and varying pre- moisture levels; (c&d) 2% and (e&f) 4%.....	73
Fig. 3.4: Di-hydrate nucleation and growth in green printed samples with 33% Plaster and pre-moisture levels at 2% (a&b), 3% (c&d), and 4% (e&f). .....	74
Fig. 3.5: Crystallographic changes due to baking: samples with 33% plaster, and pre-moisture levels at 2% baked at 300°C (a & b), 3% baked at 200°C (c & d), and 4% baked at 200°C (e & f).....	76
Fig. 3.6: Percent green volume error vs percent pre-moisture at different levels of $\beta$ -hemihydrate.....	81

Fig. 3.7 Percent volume error after baking vs percent pre-moisture at different levels of $\beta$ – hemihydrate.....	83
Fig. 3.8: Green compressive strength vs (a) percent $\beta$ -Hemihydrate and (b) percent pre-moisture.....	86
Fig. 3.9: Variation in compressive strengths of baked samples with varying (a-c) $\beta$ -hemihydrate, (d-f) percent pre-moisture, and (g-i) baking temperature.....	88
Fig. 4.1: SEM photomicrographs of green samples 3D printed with varying compositions.....	104
Fig. 4.2: SEM photomicrographs 3D printed and sodium silicate soaked samples after baking.....	109
Fig. 4.3: Variations in sodium silicate infiltration in the green state (terra alba 12.5%, $\alpha$ -Hemihydrate 50% and bentonite 6.25%).....	110
Fig. 4.4: Mechanism of bonding at various states green (a), after impregnation and baked and at the mould centre (b), and at the surface (c) with varying bentonite, but terra alba and $\alpha$ -hemihydrate fixed at 12.5 % and 50% respectively.....	111
Fig. 4.5: Variation of volume error in the green state.....	116
Fig. 4.6: Variation in the percent volume error further to sodium silicate soaking and baking with varying % $\alpha$ -hemihydrate.....	118
Fig. 4.7: Flexural strength measurement.....	120
Fig. 4.8: Flexural strength in the green state with varying $\alpha$ -hemihydrate.....	120
Fig. 4.9: Flexural strength further to sodium silicate treatment and baking with varying $\alpha$ -hemihydrate percentage.....	122
Fig. 4.10: Variation in the green compressive strength with varying $\alpha$ -hemihydrate.....	124
Fig. 4.11: The role of plaster on the extent of gypsum crystallisation at 18.75% bentonite.....	125
Fig. 4.12: Gypsum crystal growth increases with increasing $\alpha$ -hemihydrate, at 37.5% bentonite.....	125

Fig. 4.13: Crystal structures post soaking and baking show increasing sodium silicate bonding with increasing $\alpha$ -hemihydrate at terra alba 37.5% and bentonite 12.5%.....	126
Fig. 4.14: Variation in the compressive strength further to sodium silicate soaking and baking with varying $\alpha$ -Hemihydrate.....	127
Fig. 4.15: Comparative compressive strengths; green, directly baked, and sodium silicate impregnated and baked states.....	128
Fig. 5.1: SEM photomicrograph and the EDS spectra of the printed samples in the green state.....	142
Fig. 5.2: SEM photomicrograph and the EDS spectral analysis of printed Samples after baking.....	145
Fig. 5.3: Schematic representation of the possible bonding mechanisms in clay-resin based moulding sands.....	147
Fig. 5.4: SEM photomicrographs of green samples printed with varying compositions.....	149
Fig. 5.5: SEM photomicrographs of baked samples printed with varying compositions.....	151
Fig. 5.6: The inter-particle neck regions.....	152
Fig. 5.7: Volume errors in printed green and baked samples.....	153
Fig. 5.8: Comparative evaluation of the compressive strengths in green and baked states with varying compositions.....	155
Fig. 5.9: Comparative evaluation of the flexural strengths in green and baked states with varying compositions.....	157
Fig. 6.1: Percent volume error of aluminium casting with varying gypsum percent in plaster based material System.....	163
Fig. 6.2: Surface roughness (Ra) values of aluminium A356 casting with varying gypsum percent in mould material system.....	166
Fig. 6.3: Ultimate tensile strength values of aluminium (A356) casting with varying compositions.....	169
Fig. 6.4: Photomicrographs of the mould material further to casting; (a) to (c): mould wall and (d) to (f) interior.....	172

Fig. 6.5: EDS Analysis of mould metal interaction on the surface of the aluminium casting.....	172
Fig. 6.6: EDS Analysis of the surface of the aluminium casting based on the photomicrograph in Fig. 6.5 (d).....	173
Fig. 6.7: EDS Analysis of the surface of the aluminium casting based on the photomicrograph in Fig. 6.5 (e).....	174
Fig. 6.8: Percent Volume error of aluminium castings made using moulds printed by the plaster-clay system and treated with sodium silicate and baked .....	178
Fig. 6.9: Average surface roughness (Ra) of aluminium (A356) castings with varying $\alpha$ -hemihydrate.....	179
Fig. 6.10: Variation in the ultimate tensile strength of aluminium (A356) castings with varying $\alpha$ -hemihydrate.....	180
Fig. 6.11: Percent volume error of the stainless steel casting by varying clay percent in the mould material system.....	184
Fig. 6.12: Average surface roughness (Ra) values of the stainless steel casting by varying clay percent in the mould material system.....	184
Fig. 6.13: Ultimate tensile strength of the stainless steel casting by varying clay percent in the mould material system.....	186
Fig. 6.14: The CAD file of the single cylinder engine block with vertical water jackets.....	188
Fig. 6.15: The CAD model of the mould designed for the single cylinder engine block.....	188
Fig. 6.16: The casting process and outcomes (a) assembled mould, (b) A 356 filled in the mould backed-up by foundry sand, (c) the solidified shape, and (d) final casting.....	189
Fig. 6.17: Aluminium casting machined for dimensional quality assessment....	190
Fig. 6.18: Percent errors in dimensions plotted against locations.....	192
Fig. 6.19: The CAD model of the mould for the step-cone casting.....	193
Fig. 6.20: The baked mould (a) and stainless steel solidifying in the step-cone mould.....	194
Fig. 6.21: The stainless steel step-cone casting.....	195

Fig. 6.22: The percent dimensional error around the periphery of the step cone casting.....	196
Fig. 6.23: The percent dimensional error along the axis of the step cone casting.....	196

## List of Tables

Table 1.1: A sector-wise application of the casting technologies.....	03
Table 3.1: Process parameters and their levels.....	79
Table 3.2: Box-Behnken experimental design and key responses with the plaster based material system.....	80
Table 4.1: The mould material system.....	103
Table 4.2: Factors and their levels.....	112
Table 4.3: Experimental factors and critical responses with sodium silicate treated plaster-clay material system ....	113
Table 5.1: Experimental factors and critical responses based on the resin coated sand system .....	141
Table 6.1: Mechanical properties of the Aluminium (A356) casting.....	161
Table 6.2: Mechanical properties of the Aluminium (A356) casting.....	176
Table 6.3: Mechanical properties of the Stainless Steel casting.....	182
Table 6.4: Percentage errors in the dimensions of the cast cylinder block.....	191

## List of Publications

1. Bobby. S. S, Singamneni. S. (2013), "Conformal cooling through thin shell moulds produced by 3D printing", Australian Journal of Multi-Disciplinary Engineering, 9, (2): 155-163
2. Bobby. S. S, Singamneni. S. (2014), "Influence of moisture in the gypsum moulds made by 3D printing", Procedia Engineering, 97: 1618-1625.
3. Solaman B. Selvaraj, Sarat Singamneni. (2015), "Pre-Moisturised  $\beta$ -hemihydrate for 3D Printed Moulds", Journal of Materials and Manufacturing Processes, 1-11.
4. Solaman B. Selvaraj, Sarat Singamneni, "Mechanism and Mechanics of bonding in 3D printed materials systems based on traditional mould materials", Journal of Advanced Ceramic Technology (under review).
5. Solaman B. Selvaraj, Sarat Singamneni, "Mechanisms of bonding in 3D printed moulds through foundry clays and resin coated sands", Journal of Materials and Manufacturing Processes (under review).

## Abbreviations

3DP	–	Three Dimensional Printing
AFS	–	American Foundry Society
AM	–	Additive Manufacturing
ANOVA	–	Analysis of Variances
ASTM	–	American Society for Testing and Material
AUT	–	Auckland University Technology
BC	–	Before Christ
CAD	–	Computer Aided Design
CNC	–	Computer Numerical Control
DLVO	–	Derjguin, Landau, Verwey and Overbeel
DMA	–	Dynamic Mechanical Analysis
DMLS	–	Direct Metal Laser Sintering
DSPC	–	Direct Shell Production Casting
EBSD	–	Electron Backscatter Diffraction
EDS	–	Energy Dispersion X-ray Spectroscopy
FDM	–	Fused Deposition Modelling
FTIR	–	Fourier Transform Infrared Spectroscopy
IT	–	International Tolerance
LM	–	Layered Manufacturing
LOM	–	Laminated Object Manufacturing
MIT	–	Massachusetts Institute of Technology
PF	–	Phenol Formaldehyde
PUCB	–	Phenolic Urethane Cold Box
Ra	–	Average Surface Roughness

RC	–	Rapid Casting
RM	–	Rapid Manufacturing
RP	–	Rapid Prototyping
RT	–	Rapid Tooling
SEM	–	Scanning Electron Microscope
SLA	–	Stereolithography
SLS	–	Selective Laser Sintering
TGA	–	Thermo Gravimetric Analysis
UV	–	Ultra Violet
XRD	–	X-ray Powder Diffraction
Z-Corp	–	Z –Corporation
mP	–	Pfefferkorn number

## **Attestation of Authorship**

“I hereby declare that this thesis submission is my own work and that, to the best of my knowledge and belief, it contains no material previously published or written by another person (Except where explicitly defined in the acknowledgements), nor material which to a substantial extent has been submitted for the award of any other degree or diploma of a University or other institutions of higher learning”.

**(Solaman Bobby Selvaraj)**

**Date:**

## **Acknowledgement**

First off all I would like to thank my lord and saviour “Jesus Christ” for his mercy and faithfulness shown on me. Though, I am not faithful to him. However, He gave me the opportunity to do this PhD from New Zealand which I never thought of going abroad for my higher studies. His thoughts and ways are beyond the knowledge and wisdom of humans.

I would like to express my deepest gratitude to my ever loving and prayerful wife Dr. Patricia. S for her prayers, patience, dedication, support, kindness, and compromise throughout my research and my children Timothy P. Solomon and Daniel P. Solomon, who compromised with four years of their childhood without me, for the sake of my studies. The words from my elder son “Eat well”, “Pray well”, “Study well”, and “Come back soon with flying colours” and my younger son who always used to ask me, “Are you in the flight to come back home”? or “still in the New Zealand”? made me survive the rigours, failures and numerous disappointments during times when experiments used to go wrong.

I would like to thank my supervisor Assoc. Prof. Sarat Singamneni for his patience, thirst for science, knowledge, and support all these years. Ever since the meeting at a conference in Thailand in 2010, he had been a constant source of encouragement and motivation and helped me become a researcher pursuing science in every aspect investigated. Without his support, dedication and kindness

I would not have completed this research. I would also like to extend my sincere thanks to my second supervisor Prof Thomas Neitzert.

I would like to thank Chancellor Dr. G. Viswanathan of VIT University, Vellore, India, who allowed me sabbatical leave with 50% salary support to carry out my research work at AUT University for all these years. Vice Chancellor Prof. Raju, and Pro-vice chancellor Prof. S. Narayanan also need to be mentioned here for their help and encouragement. It was Prof Narayanan who encouraged me to write a paper for the GCMM 2010 conference where I met the primary supervisor and got into this research. Prof. Anand A. Samuel encouraged me personally to acquire an international research experience, while the School Director Prof. A. Senthil Kumar helped with his kind recommendation.

I would fail from my duty if I do not thank Prof Mark Taylor, Product Accelerator, University of Auckland, for supporting my scholarship through the MBIE subcontract to AUT University. I also feel quite indebted to the Head of School of Engineering, AUT University for the scholarship support, waiving the tuition fee, and free access given to all the labs and other facilities of the school. Thanks are also due to the office staff of the school, the technical support staff in machine shops, materials testing labs, and SEM labs of both at AUT and University of Auckland. Special thanks are due to Mr Joe Crowther of Progressive Castings Ltd for allowing undertaking casting trials whenever needed. It was great pleasure to work with undergraduate students, Stuart Dow, MinWoo Kim, and Graham Versefield as part of their industrial projects during the course of my study.

Last but not the least, I would like to thank my father, mother, sister, brothers and their families, my wife's family and other relatives for their constant support, and also I would like to express my sincere thanks to my spiritual father and humble servant of god, Pastor. Viki Vignarajah Selvaraja, who is having the passion for dying souls fed me with homemade food with love and affection every week without missing a week for the past four years along with spiritual feed, and Mr. Anton and his family all the way to come to my place to pick me up and drop me back on every Sunday to Church for the past four years, and our worship team leader Mr. Prem and members of the worship team and also each and every believers of "Elim Tamil Ministry", Elim Christian Centre, Botany, Auckland, New Zealand for their prayers, love and support. All my friends, especially Dr Rani Rajesh and my flat mates deserve to be mentioned for their support.

Finally, I would like to give all the glory and honour to Him only and His name alone must be glorified through this. Amen.

## **Abstract**

Casting is an age old process, but finds wider applications even in modern manufacturing in a variety of ways. Significant importance is associated with the process considering that it often feeds the initial forms within the supply chain of the overall manufacturing realm. However, it is plagued with several drawbacks due to the inherent weaknesses of different techniques evolved over the past many years. One of the major issues is the time to market, which is usually quite high in this case. Considering the global competition and the time-to-market race, this becomes an important issue. Addressing this, quite a few new developments occurred, mainly in the form of rapid prototyping, tooling and of late, manufacturing. While most traditional manufacturing methods have benefited from the developments in 3D printing, rapid prototyping and tooling, casting processes in particular were the earliest to adopt these new technologies as part of the continuous efforts always attempted at improving some of the time-consuming steps.

Beginning with the early application of rapid prototyped parts used as patterns for sand and investment casting, there were other developments such as application of selective laser sintering for the direct production of sand moulds by fusing either coated or uncoated sand particles and production of metal dies by selective laser melting direct from CAD files. Employing polymer parts made by stereolithography, fused deposition modelling, selective laser sintering, and even

the laminated object manufacturing as patterns for mould making by different means is a definite saving in the overall production time, but it is still only one step that is improved, while the rest of the process still remains the same. Direct production of moulds from CAD files is a much better option, but the laser sintering or melting technologies are generally expensive and not within the operational ranges of small to medium scale enterprises.

The ceramic 3D printing process commercially developed by Z-Corporation (Z-Corp) made available a material option that can be used for direct printing of complex moulds for sand casting of non-ferrous alloys. This is relatively a cheaper solution and readily available for small to medium scale production. While proved to be an effective solution for small scale production casting of certain non-ferrous metals and alloys, the main limitations include non-availability of suitable data for the selection of appropriate material and process conditions and also not being suitable for casting ferrous alloys. The Z-Corp technology was later procured and commercially implemented more elaborately by both Voxeljet and ExOne. Several new material alternatives including those suitable for ferrous castings have evolved, but the proprietary nature of material systems continues and the systems are also very expensive.

Overall, the 3D printing of moulds for sand casting is an effective means of achieving the much needed savings in the production time in small scale manufacturing. However, the current solutions are commercial, very expensive and do not allow much insight into the science of the materials involved and the

mechanisms of material consolidation and performance characteristics. The literature available also is mainly around the application of the technology to specific cases or evaluation of the properties of the moulds in general or the castings in certain cases. Other than a few patent documents, where limited information on specific systems is available, the science of ceramic 3D printing elucidating the mechanisms and mechanics of powder consolidation with different material systems has attracted very limited research attention. On the other hand, there has been a vast collection of recorded scientific research on the chemical and physical changes taking place with traditional foundry sand mixtures based on plaster or clays. There exists a gap also between the material systems developed for 3D printing and those used in the traditional foundry practices. The current research is based on the hypothesis that the material consolidation methods achieved through traditional foundry practices can also be used to further benefit the 3D printing of moulds.

The hypothesis is tested by experimental means involving different material systems developed for 3D printing and the integration of the knowledge from traditional foundry practices to evaluate the enhancements possible. Both plaster and resin bonded systems are developed and evaluated together with specific treatments such as soaking in sodium silicate. With each system, the mechanisms and mechanics of material consolidation, roles of the basic ingredients and their variations have been evaluated through systematic scientific investigations. While the outcomes are positive, each material system

needed application of specific knowledge of certain mechanisms as reported in the literature in the context of traditional methods, other than 3D printing.

First, a plaster based system is developed and evaluated considering the effective adaptation of the hydration mechanisms to achieve the necessary bonding under the 3D printing conditions. Pre-moisturisation of the plaster is used as the technique to achieve accelerated hydration and proved it to be effective within the 3D printing time constraints. While this paves way for a relatively simple and cheaper material option, the mechanisms of bonding and the variations ensuing from varying material and process conditions allowed significant insights into the internal material structures. The overall mechanical strengths achieved for the final mould material in the baked state is lesser relative to the traditional foundry materials.

A plaster-clay-sand composite is considered next, attempting better refractoriness through the clay component, while the plaster still serves to initiate the bonding in green state. The sodium silicate treatment, commonly used to strengthen sand moulds is integrated with this material system to achieve better mechanical properties after baking. The mechanisms of bonding are understood and the mechanical properties of the printed moulds evaluated in both green and baked states. Compressive strengths of the baked moulds are found to improve substantially over the simple plaster based system as a result of the sodium silicate crystallization.

The electrolytic bonding action based on kaolinite clays for the green strength and the polymerization reaction of resin bonds for the baked strength are evaluated next in the third material system. The dispersion of the clay particles within the silica flour matrix and the plastic flow, necking and solidification of the resin, resulting in an intricate network of cross linked polymer substrates giving rise to the green and baked strengths respectively are clearly evident. The mould strengths after baking are high volume errors within limits, satisfying all the conditions as per the standards of the American Foundry Society.

Casting trials are also conducted evaluating influences of both material and process parameters on the volume errors, surface quality and tensile strength levels. The mould-metal interactions are also very encouraging in particular with the second and the third material system, as the refractoriness appears to be high and no adverse chemical or physical changes are evidenced. While further refinements are necessary improving specific attributes, the experimental research conducted as part of this research allowed better understanding of how combinations of different ingredients at varying levels influence the quality of 3D printed moulds.

# Chapter 1

## Introduction

### 1.1 Metal casting

Casting is almost a six thousand year old process. The oldest surviving casting is a copper frog from 3200BC [1]. It is a manufacturing process by which a liquid material is usually poured into a mould, which contains a hollow cavity of the desired shape, and then allowed to solidify. The solidified part is also known as a casting, which is ejected or broken out of the mould to complete the process. Casting materials are usually metals or different cold setting materials that cure after mixing two or more components together such as epoxy, concrete, plaster and clay. Casting is most often used for making relatively complex shapes that would be otherwise difficult or uneconomical to make by other methods.

Different processing methods as employed by the foundry normally include green and dry sand casting, no-bake, resin shell, permanent, die, and investment casting, expendable pattern, vacuum ("V") process and centrifugal casting variants. The choice is based on the application, design complexity, part quality, and the material system. Of all these methods, sand casting is the most widely used technique in manufacturing to produce a variety of forms with different metals and alloys. Almost all common metals and alloys can be sand cast. Sand castings can range from very small to extremely large sizes. Some examples of items

manufactured in modern industry by sand casting include engine blocks, machine tool bases, cylinder heads, pump housings, and valves, etc.

Currently, the metal casting process has become integral to the manufacturing industry and can be used to create relatively complex geometric parts with relative ease, irrespective of the size of the part. Cast metal products are found in 90% of manufactured goods and equipment, from critical components for aircraft and automobiles to home appliances and surgical equipment. Also, the process is very economical and generates little waste, which can be reheated and used again. Ingenuity and new technological advancements are transforming the metal casting industry that has become innovative, high-tech, challenging, clean, and safe. Multiple processes have been developed in the industry where each process is specific to the metal used and the results desired. Within each process, there are several variables that impact the design of the final product. Today, castings are used in a number of markets and in a variety of applications, ranging from manufacturing to home decor. Applications of casting technologies in different sectors are listed in Table 1, which is reproduced from the Handbook of Mechanical Engineering by Grote [2].

While the wide use of different casting techniques in different application areas is readily evident, it may also be noted that casting takes up a major share of the overall market generated by the manufacturing sector in any industrialised country. It was reported that USA alone roughly shipped over 14 million tons of castings worth more than US\$ 33 billion in the year 2005, while it was \$37.67 billion in the

year 2008 and it is projected to increase to \$42.6 billion in 2015 [3, 4]. In essence, most of the manufactured goods and all manufacturing machinery have casting processes used at some stage.

**Table 1: A sector-wise application of the casting technologies [2]**

<b>Sector</b>	<b>Type</b>
<b>Transport</b>	Automobile, Aerospace, Railways and Shipping
<b>Heavy Equipment</b>	Construction, Farming and Mining
<b>Machine Tools</b>	Machining, Casting, Plastics moulding, Forging, Extrusion and Forming
<b>Plant Machinery</b>	Chemical, Petroleum, Paper, Sugar, Textile, Steel and Thermal plants
<b>Defence</b>	Vehicles, Artillery, Munitions, Storage and Supporting equipment
<b>Electrical Machines</b>	Motors, Generators, Pumps and Compressors
<b>Hardware</b>	Plumbing industry pipes, Joints, Valves and Fittings
<b>Household</b>	Appliances, Kitchen and Gardening equipment, Furniture and Fittings
<b>Art Objects</b>	Sculptures, Furniture, Lamp stands and Decorative items

Considering the process economy, casting is generally cheaper for mass production. However, it becomes uneconomical when used for small job production or for making one-off parts. Sand casting leaves a rough surface which needs machining in most cases, adding to the overall production costs. It has poor dimensional accuracy and involves design and use of complex tooling when the intricate shapes with re-entrant sections are cast. Cast parts perform well under compressive loads but could be relatively poor under tensile or shock loads. Pattern making is usually quite involved and also often requires additional maintenance, adding up to the overall production time and cost. While many solutions evolved during the course of time, the time to market issues and other bottlenecks are still at large. Relatively recent developments in rapid prototyping and tooling eventually helped to resolve some these issues to varying degrees.

## 1.2 Rapid prototyping and tooling

Rapid prototyping (RP) is layer-by-layer fabrication of three-dimensional physical models directly from a computer-aided design (CAD) file. The additive manufacturing process provides designers and engineers the capability to literally print out their ideas in three dimensions. The RP processes provide a fast and inexpensive alternative for the conventional route for part production. The advantage of building a part in layers is that it allows building of complex shapes that would be virtually impossible to machine, in addition to achieving more simple designs. RP can build intricate internal structures, parts inside of parts and thin-wall features just as easily as building a simple cube.

RP was a breakthrough technology for prototyping but as is the case with any good technology, it rapidly evolved as a useful tool in numerous applications, including casting, tooling, reverse engineering and direct hardware fabrication. Rapid tooling became available, integrating RP with other traditional processes which also led the way for the development of specific new material solutions. With foundry processes in particular, plaster and resin based new materials and process enhancements emerged over the past two decades with the advent of the ever growing RP techniques.

Early applications of RP for casting processes include the replacement of the wax patterns for investment casting by polymer prototypes printed directly from CAD files. This was followed by the production of moulds and cores for sand casting through Selective Laser Sintering (SLS) of the mould sands. Further, selective

laser sintering and Direct Metal Laser Sintering (DMLS) systems also allowed production of moulds directly from metal powders for die-casting or injection moulding. RP has the freedom to produce moulds with conformal cooling channels which is highly complicated or impossible by conventional methods. Moulds with conformal cooling channels are widely used in injection moulding to reduce the cycle time and to increase the part quality. Subsequently, 3D printing made it possible to print sand moulds directly from CAD files, allowing for metal prototypes to be produced without the need for patterns and other complex tooling.

Further, both money and time could be saved by eliminating traditional casting tooling for making prototypes or low volume production castings. The cost involved in modifying a poorly designed component and the numbers of iterations required before finalising a design are also reduced through rapid casting solutions. Casting tooling does not need to be ordered until the design is finalized and frozen. Optimising the gating and runner system design is often a major task in normal foundry activities. The use of RP patterns for trial run castings facilitates the optimization of the gating system before ordering the production tooling. RP allows the foundry to cast components of more complex geometries and intricate internal details, which are either too expensive or almost impossible to achieve by conventional casting methods. Overall, the RP assisted and pattern-less casting approaches help reduce both production costs and the time to market.

### 1.3 Rapid casting

The RP processes rapidly evolved into technologies used for direct production of end use parts in specific cases, apart from the wider prototyping applications. Currently being called Additive Manufacturing (AM), these improvements in both materials and processes also allowed for increased applications in casting. The application of AM in a metal casting process, primarily targeting reduced production times is now regarded as rapid casting (RC). In sand casting, the most time consuming step is the design and production of patterns. Further, designing and preparation of core boxes and gating systems upon which the overall quality of a casting depends are also equally time consuming and expensive, especially with complex castings. The use of AM technologies in the creation of casting patterns allows a foundry to manufacture a metal part without the use of tooling for small quantities. In particular, patterns, cores and cavities for metal casting can be obtained through AM. Rapid casting based on the application of AM to produce patterns, cores, and other tooling made it possible to produce the first batch of castings in a matter of days, as against a few months needed by the traditional manufacturing methods.

In the sand casting process, use of the Laminated Object Manufacturing (LOM) method to produce the layered patterns replacing the traditional wooden patterns was the start of rapid casting. Polymer parts made by Stereolithography (SLA), Fused Deposition Modelling (FDM), and SLS could also be used as patterns for a

few runs. Direct production of pattern-less moulds using polymer coated sands in selective laser sintering followed next, directly fusing sand particles. Considering the cost of the equipment, and the fact that it is only one step of the overall process, the pattern making that was simplified in some of these approaches, the 3D printing of moulds based on the ink-jet method became the most economical of all the rapid casting approaches.

#### **1.4 Three dimensional (3D) printing**

Three Dimensional (3D) Printing, a patented MIT process, refers to the process of using an ink-jet print head to lay down a liquid adhesive on a layer of powder, binding the powder particles together. First, a thin distribution of powder is spread over the surface of a powder bed. From a computer model of the desired part, a slicing algorithm computes information for the layer. Using a technology similar to ink-jet printing, a binder material joins particles where the object is to be formed. This 3D printing is the cheapest and the simplest process to produce sand moulds directly from powders. The cost of the printer is cheaper compared to the other RP process like SLS and DMLS. Dimensional accuracy and strength of the mould is reasonably high.

The 3D printing approach eliminates the pattern creation phase of the traditional sand casting process in a revolutionary way, resulting in a drastic reduction of the process lead time from weeks to days. Parting line and excessive cost problems are eliminated, and there will be no design limitations to make complex moulds,

and no complexity-cost ratios encountered. Considering all these benefits, the process is expected to play an important role in future rapid casting endeavours. The erstwhile Z-Corporation made the commercial 3D printing systems available and developed a proprietary material system, ZCast 501 for non-ferrous casting applications. The mechanism of bonding depends on the plaster hydration and allows to achieve the necessary green and dry strengths. A binder solution, predominantly constituted of water injected through a print head strikes the powder bed and initiates the gypsum hydration reaction. This process is repeated as layers of powder are added one over the other, and the 3D part is built.

While the material system consists of a binder and a sand together with some form of accelerators, the actual mechanisms of bonding are quite involved and need to be balanced effectively within the specific constraints of time. For example, an excessive seepage results in a loss of definition and dimensional quality. Also, a premature binding action could lead to insufficient coalescence within and across the layers. Also, the hydration and dehydration mechanisms often involve volume changes and may require special attention. Considering the proprietary nature of commercial material solutions, the science of 3D printing materials is not reported substantially. The limited information available from patent documents allows only a narrow window to visualise the widely varying processes occurring internal to the material system.

Despite the recent hype and the significant attention 3D printing enjoyed, research efforts were mainly diverted towards evaluating either the application potentials or

the comparative quality aspects of non-ferrous castings produced due to reasons stated above. Numerous case studies followed, exemplifying the process capabilities, while in most cases, the time and cost savings were the most critical responses. Being able to produce more complex shapes attained some attention, but the ability to cast in thin shell type moulds became an attractive feature. Apart from this, the literature does not allow much insight into the material interactions or possible influences of varying material and process conditions.

On the other hand the nature and hydration of gypsum plaster and the possible dehydration mechanisms have been studied quite extensively in different contexts, from building materials to geological transformations. The classical colloidal theory explains the internal changes and the physical and chemical interactions taking place. Further, different forms of clays and the electrolytic bonding actions resulting from the interactions with water added to the clay-sand composites were also investigated and reported in the past. Special treatments such as sodium silicate soaking and subsequent baking resulting in inter-granular solid crystal formation and the consequential dry strengths achieved for the mould sands are well known. Mechanisms of bonding yielding the much needed higher compressive strengths in moulding sands based on clay and resin coated sand composites are also significantly investigated and applied in the industry. However, the science of 3D printing is not widely investigated and reported, which is hindering further developments of these solutions and increasing their applications. This is identified as the research gap and the current research is structured to answer the overarching question; what are the specific mechanisms

and mechanics of bonding in 3D printing and how do specific mechanisms extracted from traditional foundry practices respond to the requirements of processing by 3D printing?

### **1.5 Objectives, methodologies and the structure of the thesis**

The overall objective is to evaluate the hypothesis that some of the mechanisms commonly used with the traditional mould material systems can also be made effective in the 3D printing context. The plaster bonding, enhanced by the pre-moisturisation as possible means of accelerating the crystallisation process, the bentonite clay bonding together with the sodium silicate treatment, and the clay-resin coated sand systems allowing for higher mechanical strengths from the polymerisation reactions have been chosen as specific aspects to be evaluated. Consequently, the objectives of the work include verification of the possible means of integrating all these mechanisms into the context of a 3D printing system and evaluating the mechanisms and mechanics of bonding in each case.

The research methodology is predominantly experimental, as different material compositions are first identified, tested for preliminary responses and the working systems are further investigated identifying the critical material and process parameters and the most promising ranges for the constituent factors. The mechanisms of bonding and the possible roles of varying experimental factors in each material system are then identified based on scanning electron microscopy. The mechanics of bonding in specific systems are then evaluated by means of

empirical models developed for the critical responses based on statistical experimental designs.

Chapter 2 presents a detailed review of literature available on the past work done in rapid casting and related topics leading to the identification of the research gap. Specific research questions are formulated and presented, followed by a discussion of the specific methods to be employed to achieve the objectives set for the research. Each chapter following this addresses a specific aspect identified above as part of the proposed research domain.

Chapter 3 presents the experimental research evaluating the plaster based material system for 3D printing. The premise that small quantities of di-hydrate pre-mixed with hemihydrate could help develop nucleation and accelerate the hydration process will be tested and experimentally proved to be applicable in 3D printing, while processing a plaster-silica sand composite treated with different levels of pre-moisture. Mechanisms and mechanics of bonding and influences of varying process parameters will be established, based on photo-micrographic and mechanical testing results using printed samples. The maximum volume errors resulting from the gypsum crystal growth and the compressive strengths attained with different material compositions will be evaluated completing the cycle of material-structure-property relationships. It will be noted that the maximum compressive strength achieved after baking is within the range of strengths essential for casting non-ferrous metals such as aluminium as per the ASTM standards.

Chapter 4 presents the experimental work evaluating the mechanisms and mechanics of bonding resulting from the use of clay-sand composites together with sodium silicate treatments in a 3D printing system. Bentonite-sand composites of varying compositions will be used for 3D printing and evaluated establishing the bonding mechanisms. Differing amounts of  $\alpha$ -hemihydrate will be employed as the binding material, together with varying quantities of terra alba as the seeding agent. The effects of impregnation by sodium silicate and subsequent baking at suitable temperatures will be evaluated. The gypsum crystallisation will be noted as the predominant mechanism of bonding in the green state. The sodium silicate soaking and impregnation will also be found to be essential and effective to achieve the required strength after baking, through inter-particle loading and crystal growth.

Chapter 5 includes experimental research and the ensuing results considering the clay-resin coated sand composites for 3D printing and evaluating the mechanisms of bonding and mechanical attributes of specimens made. The moisture from the print head will be proved to be effective in terms of initiating the clay bonding through electrolytic forces generated from the diffuse double layers and the dispersion of clay and silica flour particles. Further to baking, the plasticisation and flow of the resin and subsequent polymerisation, establishing the networks of interconnected neck regions, developing the necessary consolidation and mechanical properties will be discussed.

Chapter 6 includes the experimental results from the casting trials considering the three material systems investigated in Chapters 3 to 5. Apart from allowing to understanding of the mechanisms and mechanics of bonding, establishing the roles of critical parameters and identifying the most favourable combinations of material and process parameters for the best mould material responses in each case, the material systems will also be shown to perform while casting different metals. The higher refractoriness achieved through the use of clay-sand composites will be demonstrated through the ability to cast stainless steel.

Chapter 7 presents the conclusions drawn based on the results of the current research work. Apart from projecting an overall perspective of the research work done and the general trends of results observed, the most significant results obtained will be listed in a proper sequence.

## **Chapter 2**

### **Literature review, research questions, hypotheses, objectives and methodologies**

#### **2.1 Traditional Casting and Time Constraints**

Foundry processes play vital roles in the time-to-market capabilities of many manufacturing activities, considering that they are often the methods used for creating primary parts. In order for a supply chain to be effective, foundry processes need to be efficient in terms of product lead times. Generally, the main stumbling block in any casting process is around the production of the necessary tooling, whether it is the dies for injection moulds and die casting or the patterns, cores, and moulds in sand casting. Production of prototype models of a small batch size using the traditional investment casting process is costly and time consuming, going from fabrication of master pattern to the final casting. Also, the cost of the metal moulds though dependent on the size and the design complexity of the part, are typically in the range around US \$5000 - \$100000 with 8-24weeks long lead times [38]. As a result, utilisation of innovative production methods becomes an essential component of sustaining competitive manufacturing demands.

There have been some early variants developed and widely used in the industry as rapid tooling processes, much before the advent of rapid prototyping by the

layered manufacturing approaches. Spin casting with vulcanised rubber moulds, and applications of silicone rubber, resin and ceramic and plaster moulds are some examples. With the advent of rapid prototyping, rapid tooling became an important means of achieving some saving in manufacturing lead times. Indirect methods evolved combining RP and metal casting in order to be able to save manufacturing times. High quality and complex patterns could be made for investment casting in shorter times. Prototypes also became useful in a variety of other casting processes including sand casting, die casting and lost foam casting.

Substantial research has been done and reported in the past two decades concerning the application of different rapid prototyping methods in order to achieve the much needed time savings in different casting processes. While the initial research was mainly focussed on the application of different approaches in specific cases, more systematic and scientific evaluations of materials, processes and their enhancements followed in the recent years. All these developments are reviewed next, allowing for the identification of the research gaps, formulation of the research questions and objectives towards the end of this chapter.

## **2.2 Rapid prototyping solutions for casting**

While the first commercial systems for rapid prototyping emerged in the late eighties, actual research reporting the applications for casting processes appeared from the beginning of the nineties. In an early review, Thomas [5] was in fact very

sceptical about the possible benefits from the application of RP to sand casting. It was stated that there had been vague claims by several manufacturers of rapid prototyping equipment, and in reality with very little impact on the sand casting and pattern making industries. Early applications of prototypes for plaster mould casting and investment casting were noted, apart from use of RP patterns for rubber or epoxy moulds or spray metal pattern moulds. Though the conclusion was that the use of RP for casting applications was limited at the time, the review predicts a gradual increase in its use, especially with companies ready to quickly adapt to the computer aided design (CAD) tools that were also evolving at that time.

Reg [6] presented an overview of the RP processes available in the late nineties for casting related applications including fused deposition modelling, laminated object manufacturing, solid ground curing, stereolithography, 3D printing and direct shell production casting. Several case studies involving the application of one or the other RP process in different casting tasks have been presented. An FDM prototype was used as a master pattern for a C355 aluminium aircraft fuel pump inlet housing. The FDM prototype, tooling and prototype castings were reported to have been completed within 3 weeks after making the CAD drawings. Use of LOM patterns in the making of an iron disc rotor based on green sand casting was shown to reduce the production time from 9 months to 6 weeks, compared to the traditional processing routes. A SLA pattern used for investment casting of a prototype aluminium valve body was reported to be quite effective during the design stages. A selective laser sintered sand core was reported to be beneficial,

together with a pattern consisting of 40 pieces, made from LOM and CNC machining for the rapid production of an aluminium gas turbine engine fuel control system by sand casting.

Chua *et al.* [7] reviewed several rapid tooling technologies, classifying the tools into two types; soft and hard tooling, each of which was further identified to have direct and indirect methods. Use of SLA and SLS moulds for rapid injection moulding of a few parts comes under the direct rapid soft tooling category. Several material variants resulted from this approach, such as the aluminium filled epoxy resins for thin shell moulding based on SLA to the Alumide, a nylon-aluminium powder composite for processing by SLS. In indirect soft tooling, a RP model is used together with some other methods for building the tooling. Arc spray metal tooling, silicone and vulcanised rubber, resin, ceramic, and plaster moulds fall under this category. The direct hard tooling at the time of this publication were mainly the LOM process used to develop patterns and the DTM Sinterstation 2000 used for direct production of metal dies for injection moulding by sintering coated metal powders and a further infiltration treatment. The 3D Keltool method developed by 3D Systems based on SLA models and a fused powdered steel was considered as the indirect method for hard tooling. A comparative analysis presented shows the hard tooling methods provide longer tool lives, but at higher costs. When it comes to lead times, the direct soft tooling methods score the best, at less than a week, while hard tooling methods take more than 2 weeks.

Bernahard *et al.* [8] reported the application of rapid pattern production using LOM and the effective application in a specific case. A pattern with overall dimensions 330x140x70 mm was reported to be completed in about 10 days, while the pattern making cost was reduced by 25% and the total time of producing the first casting was around 2½ weeks. In a similar report, Wanlong *et al.* [9] also stated that a 25 mm ballistic projectile casting could be produced in ductile iron within 10 days and at a cost of US \$6000, employing the LOM process for rapid tool making. It was noted that the traditional methods could have taken around 24 days, and at US \$ 11000. The rapid tooling based on LOM resulted in around 54% and 49% savings in time and cost respectively, compared to the traditional aluminium tooling.

Both RP and RT began attracting more attention by the turn of the century. While reviewing these developments, Kochan *et al.* [10] noted in particular the significance of RP patterns in reducing the lead times in casting. While being cautious as not to over-estimate, they however predicted a promising future for the RP and RT applications. This was proved to be true almost at the same time, as Rosochowski *et al.* reported a dramatic impact of RP and RT on the engineering environment [11]. While re-establishing the classification as presented by Chua *et al.* [7], this review presents some advances in materials for both FDM and SLS allowing for the direct production of sacrificial patterns with minimum residues and some interesting case studies. An investment cast exhaust manifold for a Chrysler car made from wax patterns, an SLS polycarbonate pattern for the investment casting of a cylinder head and an engine intake manifold made from 3D printing using the Direct Shell Production Casting (DSPC) process are notable examples

reviewed. Apart from emphasising the RP and RT technologies to play vital roles in manufacturing engineering in general, the casting technologies in particular were noted to be significantly benefited.

Highlighting the significance of the design and manufacturing of dies and moulds in the entire production chain, Taylan *et al.* [12] reviewed the implementation of the latest technologies for these tasks. One of the major issues of the economics of die/mould making was identified to be the need to carefully control costs while reducing the build times by 50%. The role of RP and RT in achieving the much needed cost and time reductions was clearly emphasised, apart from the other benefits such as the use of conformal cooling lines around mould cavities. Use of FDM, and SLS parts made of proprietary materials as sacrificial patterns for investment casting and the direct printing of large scale sand moulds were noted to have gained significant applications. Bauer *et al.* [13] extended this evaluation further, projecting that it is profitable to use rapid prototyping processes in the cost-intensive and time-consuming manufacturing of miniaturised micro-patterned ceramic components.

Presenting an overview of the layer manufacturing technologies, Levy *et al.* [14] insisted on the concurrent engineering and contemporaneous free-form fabrication approaches to shorten the time-to-market. The data reviewed indicates the time to produce approximately 80% of the moulds took between 6 to 20 weeks, 35% of moulds between 6 to 10 weeks, and 40% of the moulds between 11 to 20 weeks. Cost analysis based on alternative RT polymer technologies indicated 20% and

50% cost and time savings respectively. Identifying RP and RT as the key enabling technologies for Rapid Manufacturing (RM), Pham *et al.* [15] classified different RP processes and identified the commercial impact of the technologies. While considering applications in different sectors, RP patterns used for investment and vacuum casting were noted to be cost effective with small scale production of up to 50 parts, when shape complexities and prohibitively high tooling costs were involved. Inserts for die casting of a wind screen wiper arm, injection moulding the cap of a nose hair trimmer, and direct production of a car seat frame were presented as case studies employing the Rapid Tool process based on SLS. It was concluded that the developments of the time had been indicative of very promising prospects for the future of rapid manufacturing.

Brian *et al.* [16] presented two case studies involving the use of RP techniques for rapid casting. The master pattern of around 960mm length of the A-posts of a Volvo safety concept car was fabricated by Stereolithography and aluminium castings could be produced within 7.5 weeks, at a cost of 18260 pounds. While the time taken was similar to machining, it was reported that Volvo was satisfied with the elimination of the residual stresses achieved from the rapid casting process compared to the machining methods. Selective laser sintering of sand for direct production of moulds was used for producing the V6 cylinder heads for a UK based car manufacturer. The moulds were reported to be suitable for aluminium, iron and compacted graphite iron castings and were produced much faster than the traditional methods, as the first castings could be made within 3 weeks.

While reviewing the state of the art of rapid manufacturing and tooling with layer manufacturing technologies, Gideon *et al.* [17] presented a systematic material based classification together with specific examples and applications. The market for rapid tooling and manufacturing was reported to be still developing, while also finding numerous real applications in both soft and hard tooling. Bernard *et al.* [18] reported a study carried out by the SMC Colombier Fontaine company reducing the time and cost of product development by sand casting. Rapid patterns were generated using the Optoform technique based on UV curing. Sand moulds were produced using the UV cured patterns and the rapid tooling was reported to be effective up to 500 runs. Ferreira points out those foundries, being the primary suppliers, are vital links in the time-to-market chain and will be perceived as valued customers when castings are produced rapidly [19]. The significance of RP in achieving the much needed time savings was established through several case studies, including fabrication of sand cores through epoxy resin SOMOS 3100 prototypes, an RT core-box for sand casting by SLS of polymeric powder Dura Form GF, and a massive core box printed in epoxy resin SL5170. Esposito *et al.* [20] presented a method to build moulds based on silica powder suspended in a photo reactive resin processed through stereolithography. Further heating to 500°C for pyrolysis and sintering at 1100°C were reported to result in flexural strengths at around 53MPa and three successful castings. Other researchers also emphasised the effective utilisation of several RP techniques to achieve rapid casting solutions [21, 22].

Dimitrov *et al.* [23] considered four process chains based on either 3D printing of moulds and cores or polymer pattern making and evaluated the process capabilities based on the critical aspects of a benchmark part. The dimensional accuracy of the moulding tool was reported to be within  $\pm 0.8$  mm over 100 runs. The tooling equipment was noted to be within normal limits of the European standards for the production of sand moulds and cores. It was concluded that the ability to produce equipment for patterns with close tolerances and shorter lead times establishes the possible enhancements layered manufacturing technologies could bring to traditional foundry practices.

Dineshh *et al.* [24] generated a database of RT process capabilities based on benchmarking experiments of an impeller pattern considering a variety of RP processes. A robust evaluation and decision making tool was developed based on overall process compatibility indices calculated using quality function deployment and analytic network process. The methodology was reported to be effective while testing with an industrial example of a separator body casting. They identified the accumulation of dimensional errors at each stage of the rapid tooling schemes as an important aspect to be considered.

A comparative analysis of wax patterns produced using a rapid prototyping approach against the traditional methods used for investment casting established time and cost savings of 50% and 60% respectively [25]. Zhang *et al.* [26] reported the successful use of LOM for rapid prototyping the die pattern for the clutch house of a diesel engine. It was noted that the tooling was effective up to 100

castings, with drastic reductions in both time and cost of manufacturing. Haihua *et al.* [27] reported the investment casting of hollow turbine blades based on stereolithographic models, while Zhou *et al.* [28] also reported the direct fabrication of integral ceramic moulds using stereolithographic moulds. Stankiewicz *et al.* [29] presented the possible roles of different RP techniques for the rapid production of casting tools. Block diagrams were developed elucidating the extent to which production of single and multiple use tooling for traditional casting methods could be influenced by rapid prototyped patterns or sand moulds. While reiterating the use polymer and wax patterns made of SLA, SLS, FDM and the jetting systems, direct production of sand moulds using the Z-Corp, VoxelJet, and the ProMetal RCT processes scored better in terms of cost, time, part complexity and tolerances achieved.

Chabra *et al.* [30] presented a comprehensive review of the application of different RP processes employed to assist casting technologies, mainly to reduce tooling times. Referring to the approaches as rapid casting solutions, the review covers all aspects of applying rapid prototyping to different casting operations. Apart from cost and time savings, process optimisation, better tolerance to part complexity, and effective use of concurrent engineering were noted as specific benefits. While specific process limitations and further enhancements to be achieved were the limitations, the need to develop cheaper and better material systems for rapid casting was emphasised. Considering the numerous benefits, rapid prototyping and manufacturing gained much recent interest as many review articles followed suit where rapid casting also drew significant attention [31 – 34].

### 2.3 Direct laser sintering of moulding sand

Based on the literature reviewed above, it may be noted that the initial application of RP techniques to benefit different moulding and casting technologies had been mainly through the use of the polymer and other forms of patterns as rapid tooling. However, the application of SLS for direct production of sand moulds also attained some attention as the laser sintering process gradually evolved and became more and more accessible. Tang *et al.* [35] used silica sand finely ground to around 50  $\mu\text{m}$  size and attempted direct printing of fused sand moulds by selective laser sintering. A small quantity of  $\text{Al}_2\text{O}_3$  was included to assist in reducing the melting temperature at the surfaces of the fine sand grains. Partly melted sand grains, partial flow into narrow inter-granular regions, formation of inter-granular necks and subsequent solid state sintering were identified as the mechanisms of bonding. The compression strength and the surface roughness of the sintered sand specimens were found to increase with increasing laser power at a given laser speed.

Klocke *et al.* [36] also reported the direct laser sintering of ceramics, considering the process to be comparable to plastic or metal laser sintering. Zirconium Silicate grades with varying grain sizes were sintered evaluating the influences of laser sintering process parameters. The mechanism of consolidation with ceramic laser sintering was noted to be transient liquid phase sintering. The favourable role of finer powder particles resulting in better sintering was noted. The role of increasing laser power in increasing the density and resulting in poor surface qualities was

understood similar to the observations by Tang *et al.* [34]. According to Wang *et al.* [37], direct sintering of silica sand without any binder, to fabricate moulds for sand casting was feasible mainly through the partial melting and bonding of low melting ingredients such as calcium, aluminium, and others. It was reported that it took about 22 hours to achieve the aluminium casting from the CAD file, including laser sintering of sand moulds and infiltration. The dimensional accuracy of the sand mould was close to 0.4mm, while the surface roughness ( $R_a$ ) was noted to be 35.6 $\mu\text{m}$  and 26.2 $\mu\text{m}$  respectively on the horizontal and the vertical surfaces. The inclined and freeform surfaces scored poorly in terms of surface quality, due to stair-step effects.

Resin coated sand material options were developed by EOS GmbH for laser sintering applications. The LASERCRON coated sand composed of 96.8% quartz sand and 3.2% resin was investigated by Casalino *et al.* [38] and reported the compressive strength and permeability characteristics of the sintered mould samples to be well above the normal limits as specified by the American Foundry Society. Bertrand *et al.* [39] used pure yttria-zirconia powder with particle sizes 1-40 $\mu\text{m}$ . The density was low at 56% before sintering. An experimental design was developed and conducted based on significant process parameters. High quality and dense ceramic components were reported to have been developed based on the evaluation of micro-structures, particle sizes and morphologies and mechanical properties. The role of the powder bed density prior to sintering in influencing the post-process sintered characteristics was evaluated based on cubic components fabricated to varying process conditions.

Song *et al.* [40] investigated the silica sand–phenol formaldehyde resin (PF resin) composite for 3D printing. The main components of the silica sand were SiO<sub>2</sub> 99%, Al<sub>2</sub>O<sub>3</sub> 0.22% and a micro-content of TiO<sub>2</sub>. The melting point was 1750 °C. The phenol formaldehyde with a 200 mesh size acts as the bonding agent, softening at around 105-115°C, while the solidifying agent was 8-12% methenamine. Bonding agents were found to be uniformly distributed and the strengths of samples were enhanced with a post-process heating at 300°C. Slice thickness and other critical process parameters were optimised for improved quality.

It may be understood that the use of RP patterns for casting is an indirect method where either the pattern or the cores are produced by means of the RP process used as a rapid tooling device. However, the problems with the remaining stages of the actual casting process such as making the mould and associated issues are still present. The direct sintering of either coated or uncoated sand answers this to some extent, but the process is not very efficient. Also, the SLS systems being more expensive are not readily available for small scale applications. The actual application of the direct laser sintering of sand moulds has therefore seen very limited application in reality.

The 3D printing of moulds employing plaster based materials and aqueous binders as developed by MIT and commercialised by Z-Corp offers better solutions in this regard, targeting mainly the sand casting process. The moulds can be directly printed, and then used for casting after baking to the necessary extent. This saves considerable amount of time in specific applications as the moulds are directly

printed and also allows for more complex moulds being produced. There is also the possibility to build these moulds as thin shells, paving the way for the direct printing of thin shell pattern-less moulds from CAD files and produce relatively complex castings within short lead times. Considering these advantages, the process also attracted significant research attention as presented next.

#### **2.4 3D Printing of moulds for sand casting**

Consolidating ceramic powder substrates into freeform 3D forms based on inkjet printing began with Esterman [41] investigating the ceramic material system used for the traditional investment casting process for 3D printing. The effects of the binder volume and raster line spacing on the quality of the printed moulds were assessed based on factorial experiments. The experimental results allowed second order models to be built for strength, flatness, surface finish and dimensional control as critical responses. Emmanuel *et al.* [42] employed a mixture composed of Aluminium Oxide and 30wt% of colloidal silica nano particles for 3D printing of moulds. Further to printing, the entire powder bed was to be transferred to a kiln and fired at 900°C for 2hours. The loose powder was removed by shaking and the dried shells could be used for direct pouring of high melting point alloys such as nickel super alloy, Inconel, and Co-Cr. The porous printed shells were reported to have properties similar to the traditional counterparts. The maximum dimensional deviation was estimated to be around 0.020mm, while the average shrinkage upon firing was at around 0.002mm over the mould dimension of 38.10mm. In a further study, Emmanuel *et al.* [43] also evaluated the 3D printed

shell moulds casting hollow shapes with Inconel 718 and cobalt chrome. The average surface roughness of the cast parts was estimated to be around 12µm.

Further, Emanuel *et al.* [44] also presented the build characteristics, process physics, mechanisms of bonding, and related issues with 3D printing. Considering the rate at which the 1600 nozzle commercial print heads deliver the binder, they envisioned the 3D printing process to be suitable for production purposes. As the print head jets the binder, the ejected liquid penetrates the powder bed coating the particles. The attempt to minimise the area of liquid/vapour interface results in the densification of the powder particles and subsequent drying further compresses the particles together. The ballistic impact of the binder droplets ejected on to the powder bed may disrupt the dispersion of the solid particles over the substrate, if the cohesive strength is insufficient.

One of the early applications of 3D printed ceramic moulds based on alumina powder and silica binder was to cast the ingrowth surfaces of Co-Cr (ASTM F75) alloy and a tin-lead alloy. The 3D printing process was utilised to be able to reliably generate orthopaedic prostheses with porous surfaces and high flexibilities and relative ease. It was reported that 3D printing helped production of small surface features with an average porosity of 45% and pore sizes varying from 200-800µm, well within the specifications for orthopaedic applications. The authors also reported printing features reliably as small as 350µm (L) x 200µm (W) x 175µm (D) with a maximum deviation between 12-51µm, depending on the part orientation.

The 3D printing process was later commercially made available by Z-Corp and a specific material system evolved for casting purposes, named ZCast 501, mainly suitable for non-ferrous castings. Clay *et al.* [45] reported a comparative assessment of the merits of the ZCast direct mould metal casting process based on 3D printing of ceramic moulds with other more traditional approaches. It was noted that the ZCast process allowed aluminium castings to be made in less than 12 hours for just a few hundred dollars of raw materials costs. The breakeven quantity for the ZCast process was identified to be between 3 and 10 pieces. The ZCast moulds scored the best in terms of achieving complex shapes and lead times.

While reviewing rapid prototyping and production, David Bak [46] considered 3D printing as moving manufacturing processes towards the latter. The tolerances and accuracies of parts made by the ZCast methods were pronounced to be closer to the traditional sand casting results. Minimum wall thicknesses of 3.0mm and minimum core sizes at around 3.5-4.0mm were ascertained to be achieved in non-ferrous castings through 3D printing. Dimitrov *et al.* [47] reported 3D printing as a competitive process in terms of cost and time involved in fabricating moulds and cores. Several aspects related to 3D printing including material and process improvements, expansion of the range of application and customer satisfaction have been reviewed. The 3D printing technology being based on the simple drop on bed ink-jet principles and with no major physical changes involved in the materials was identified to be associated with relatively low equipment, material and overall process costs, compared to the use of the other RP techniques.

Budzik [48] reviewed the typical attributes of the ZCast 3D printing process used for sand casting. While emphasising the effective utilisation of 3D printing to produce shell moulds as thin as 12mm, the limitation on the maximum allowed pouring temperature at around 1100°C was noted. The procurement of the Z-Corp technology by the ExOne Company and subsequent development of 3D printing materials suitable for ferrous castings was also reported. The competitive advantages of rapid casting allowing for short manufacturing lead times was further reiterated by Elena *et al.* [49] They produced moulds for a test piece using two different methods; a 3D printed starch pattern used to build the mould for casting steel in the investment casting route and then direct printing of ZCast moulds for casting aluminium. Cast parts were used to evaluate the porosities and the surface qualities comparing the two approaches.

Considering the chemical bonding of the critical ingredients in 3D printed moulds, the nature of the metal-mould interactions will become important as the molten metal at elevated temperature comes in contact with the mould walls. Rebros *et al.* [50] presented a comparative thermal distortion analysis of the silica sand and furan resin composite used on a ProMetal S15 rapid casting machine and the Phenolic Urethane Cold Box (PUCB) system at an aluminium fill temperature. It was noted that the PUCB system exhibited a greater thermal distortion. It was noted that the major contribution to distortion in the 3D printed specimens occurred due to expansion, while the PUCB specimens distorted due to expansion as well as plastic deformation. The mass losses due to thermal loading were noted

to be similar though, as both material systems appeared to undergo considerable heat induced thermo-chemical reactions.

As an alternative processing route for medical applications, Ben *et al.* [51] attempted 3D printing of alumina powder particles in the range of 18-26 $\mu$ m mixed with acetate alumoxane in a 95:5 ratio. Distilled water with isopropanol was used as the liquid binder, activating the inter-particle bonding upon striking the powder bed through the print head. Based on experimental results with varying compositions, it was established that 5% of powdered Acetate Alumoxane as binder with 5% water resulted in a ceramic yield of 95%. The authors also considered a range of alumina powders and their mixtures with zirconia for printing using alumoxane as the binder and did a comparative evaluation with commercial dental ceramics. A further experimental investigation allowed them to identify a binder system for the ProMetal print head system, predominantly based on distilled water, with around 20% of isopropyl alcohol.

Singh *et al.* [52] evaluated the possibility to reduce the shell thickness with 3D printed moulds, produced using the ZCast 501 powder bonded by the zb56 liquid glue. It was shown that shell moulding with thicknesses much smaller than the recommended values could be possible for the successful casting of non-ferrous alloys. A shell thickness of 5mm was reported to improve the hardness of the castings produced by around 3.79%, while production cost and time were reduced by 54.6% and 55.4% respectively.

Elena *et al.* [53] attempted to optimise the mechanical performance of moulds produced by the ZCast process varying the post-printing thermal treatment parameters. Based on the optimised settings, the International Tolerance (IT) grades were calculated by means of a specific dimensional evaluation scheme applied to the printed parts. The results indicated that heating at 150°C with baking time varying from 4 to 6hrs has negligible effect on the compressive strength, while varying the baking temperature had some significance. Based on dimensions measured in all three directions it was established that the IT tolerance grades achieved with printed parts were independent of the direction as well as the heat treatment conditions. Overall, it was noted that the 3D printed samples based on the ZCast method could be classified within the IT15 tolerance grade.

Gill *et al.* [54, 55] attempted a comparative assessment of the ZCast and the investment casting methods as applied to the production of aluminium castings. The patterns for the investment casting were produced using both the starch based (zp14) and the plaster based (zp100) materials and the printed patterns were further treated infiltrating wax and acrylate, eventually resulting in four different material systems. Initial experiments allowed identifying a layer thickness of 0.127mm, horizontal part orientation, post-curing time of 60 minutes and curing temperature at 110°C as the most favourable parameter settings for the ZCast process. The acrylate infiltration was done for 10 minutes in both the starch and the plaster patterns which were then cured at 105°C for 30 minutes. The wax infiltration was done using commercial wax heated at 60°C for 10 minutes. While

the hardness values of castings produced by both methods were closer, the ZCast method was reported to result in relatively higher surface roughness values.

Singh *et al.* [56, 57] analysed the possibilities to reduce the thickness of 3D printed shell moulds for casting brass and lead alloys. Mechanical property measurements and microstructural evaluations ascertained the quality of castings produced. The ZCast 501 powder was used for printing the moulds that were heat treated at 110°C for one hour. The shell thickness was varied from 12 to 0.5mm. Based on microstructural evaluations, 2mm and 1mm shell thicknesses were identified to be better for the moulds used for casting brass and lead respectively. This was reported to be equivalent to a cost and a time saving of up to 54.75% and 43% respectively with the casting of the lead alloy. Similarly, the brass castings showed 40.05% and 32.84% savings in cost and time respectively. It was also noted that effective production of sound castings with thin shell moulds depends on the pouring temperature and the weight density of the liquid metal.

Singh *et al.* [58] analysed the role of the thickness of 3D printed shell moulds made of the ZCast 501 material option while casting zinc alloys. A hybrid method was developed combining both 3D printing and the traditional casting methods, as the thin shell moulds were supported by different types of sands; dry, green, and molasses mixed. The best dimensional accuracy was obtained with a shell thickness of 3mm. The surface roughness of castings was reported to be around 6.5-7.0µm, while the shelf life of the moulds was not affected by the shell thickness. Similar results were also reported elsewhere [59-61].

Drokina *et al.* also investigated thin shell moulds made of the ZCast process, but subjected to post-printing impregnation and calcination at 400°C for 1 hour [62]. The tensile strength of the impregnated mould with a shell thickness of 7mm was reported to be better than that of the 15mm thick shell mould without any impregnation. However, the shell mould strengths were found to reduce with increasing calcination temperature and time, which was even more pronounced further to impregnation. Also, the thinner the mould walls, the faster the cooling rates and the finer the grain structure of the solidified castings.

Markowski *et al.* [63] analysed the geometrical quality of moulds printed using the 3D printing method and found that several factors influence the overall dimensional accuracies of printed moulds, including layer thickness, mould handling methods, condition and calibration of the print heads, slides, and guides, and file preparation methods. A gear shaped mould cavity was printed using 0.0875 mm thick layers and a coordinate measuring machine was used to evaluate the dimensional variations. The Z-Corp material system zp130 was employed, with a post-printing infiltration by the Z-Max™ epoxy resin. The laminar structure of material consolidation was noted to be the main source of dimensional errors, especially in the Z-direction. It was also stated that the location of the part on the build platform has an influence on the dimensional variations too.

While casting aluminium cellular structures in moulds 3D printed to varying conditions, Nicholas *et al.* proved the process to be effective in achieving the geometry with minimum loss of material. However, the castings produced were

noted to be too porous and could only withstand a maximum compressive force of around 64kN [64]. The porosity could have occurred due to improper casting procedures, rather than any inherent problems with the printed moulds. Considering the proprietary nature of the ZCast materials and the limited opportunities to vary the constituencies to suit different applications such as both ferrous and non-ferrous castings, Koltygin *et al.* [65] attempted mixing certain local ingredients to be used on a 3D printing system to construct sand moulds. While the primary ingredients used for achieving the refractory and the binding characteristics were not fully disclosed, the authors evaluated the use of iron sulphate and dolomite as accelerator and moisture absorber respectively and the indigenous material systems were reported to perform similar to the commercial alternatives.

Chabra *et al.* [66] reported a 50% savings in both time and cost while using the direct printing of 3D moulds as compared to the use of LOM patterns. The authors investigated the effects of casting volume, pouring temperatures of different alloys and the thickness of the shell moulds on the surface roughness of the castings produced. The analysis based on the Taguchi method indicated the pouring temperature as the most significant factor in influencing the surface roughness, while the shell thickness of the mould scored next. The optimum surface roughness achieved was at around 6.47µm.

Snelling *et al.* [67] comparatively assessed a no-bake traditional silica sand material against two commercial 3D printing options, ViriCast™ and ZCast® while

casting the aluminium A356 alloy. The tensile strengths of moulds were reported to be at around 0.56 MPa, 0.16MPa, and 0.06MPa respectively, with the no-bake silica sands, ViriCast, and ZCast material options while the average surface roughness ( $R_a$ ) values of the aluminium castings produced varied at 12.14 $\mu$ m, 13.62 $\mu$ m, and 15.62 $\mu$ m in the same order. All these values are within the range of surface qualities expected of traditional sand casting, i.e., 12.5-25 $\mu$ m. In a further study, Snelling et al. [68] emphasised the specific benefits of using 3D printing technologies for cellular sand moulds and compared the effectiveness of the two commercial material systems, ZCast and ExOne. Cellular moulds were printed using the two commercial systems and aluminium (A356) castings were produced. It was reported that the ZCast moulds resulted in relatively poor filling of the thinner sections compared to the ExOne solution probably due to excessive gases released from the liquid binder. The ExOne system was reported to have better filling with the overall compressive force of the resulting casting to be at 123.18kN.

## **2.5 Research gaps, hypotheses, and questions**

Summing up the literature reviewed above, casting processes are often at the core of the manufacturing supply chain. The tool making tasks are time consuming and costly, which makes casting impractical for small to medium scale production applications. Rapid prototyping and tooling solutions evolved assisting different manufacturing methods both directly and indirectly, and made marked impressions on different casting techniques too, helping to reduce both time and cost of production. Most preliminary research was based on applications replacing the

traditional pattern making with either wax or polymer patterns printed using SLA, FDM, and SLS systems [5-7, 10-19, 25, 27-34], or the layered patterns made of LOM [8, 9, 26].

There was some attention paid evaluating process capabilities, including dimensional stability [23] and tolerance limits[24]. Direct production of sand moulds by laser sintering silica sand [35], zirconia powder [39], and ceramic based materials with binders [34, 36] and without binders [37], and polymer resin coated sands [39] followed next. The laser sintering applications scored better in terms of geometrical accuracies, but the need to invest in costly equipment and equally expensive material solutions deterred the wider application and uptake by smaller industries, typical customers for the rapid casting solutions. The inkjet technologies referred to as 3D printing and initially made available by the erstwhile Z-Corp offered relatively better solutions.

Initial research into 3D printing emerged considering aluminum oxide as the candidate material [42, 47], followed by the evaluation of the process physics [44]. The results paved ways to researching other ceramic material systems [41], shell mould printing [43], and commercially viable solutions [45]. As the printed moulds and their properties were not too far from traditional material systems, commercial interests and developments followed, with Z-Corp launching the plaster based silica sand composite for 3D printing of moulds for non-ferrous castings. Considering the proprietary nature of the material the research that followed on 3D printing mainly centred around issues such as dimensional tolerances of moulds

[46], evaluation of optimum post-printing baking conditions [53] and effective shell thickness when used as pattern-less shell moulds [48, 49, 52, 56-58, 59-62, 66], and other aspects like thermal distortions or comparisons with traditional methods such as investment casting [54, 55]. Comparative evaluation of traditional, and different commercial material systems [67], application of the method to other areas, including medical [51] and cellular structures [68] were also noteworthy research developments.

However, the proprietary nature of the material systems and the reduced freedom allowed by commercial systems meant there was very little research reported considering the actual science of 3D printing. There was also very limited effort in the direction of investigating alternative material systems though the need for simpler and better materials systems was identified [65]. Other than the limited information reported in the patent documents, systematic scientific research into the mechanisms of bonding and the evaluation of the roles of different ingredients on the final mould material characteristics are seriously lacking. Nevertheless, the literature available is full of examples around the application of RP to facilitate rapid casting solutions and associated investigations. There has also been quite an amount of abstract information reported on how effective rapid casting solutions could be in achieving the much sought after time and cost savings.

While the commercial 3D printing material solutions developed by ExOne and Voxeljet are still available, the ZCast system ceased to exist since 3D systems took over the Z-Corp process. However, the proprietary nature of these solutions

continues and there is a dearth of scientific knowledge available to understand how these different material systems actually function. It is important that the actual science of printing moulds for rapid casting solutions is explored and reported so that the research interest widens and leads to better and more economical material solutions for the future.

On the other hand, there has been considerable amount of scientific research on different aspects of various ingredients used in traditional foundry practices, both individually and combined. Mould material ingredients, including sands, clays and other additives used for moulds and cores and their chemical, physical and thermal influences together with metal mould interactions have been well studied and reported during the past few decades. While this kind of scientific research and reporting is yet to happen with most 3D printing research, considering the limited freedom available for researchers, an intriguing aspect that attained less research importance in particular with 3D printing of moulds is that there is a lack of application of the knowledge already gained through traditional casting to the benefit of rapid casting solutions through printed sand moulds.

The plaster based 3D printing solutions heavily rely on the hydration mechanism of the plaster powder when reacting with the aquatic binder solution. In traditional foundry sand mixing, different types of clays play this role, and the electrolytic bonding helps achieve the required plasticity and inter particle bonding. There has been no reported literature indicating any efforts made towards integrating these different mechanisms for the benefit of 3D printing of ceramic sand moulds.

Further, different ingredients are used to achieve different attributes for the sand moulds and cores, while methods such as sodium silicate treatment and applications of resin coatings are quite popular and time tested solutions. Notwithstanding the information hidden behind commercial material solutions, there is hardly any scientific research reported exploring the possibility of integrating these traditional approaches with the 3D printing of sand moulds. The current research is focussed on filling this gap, based on the hypothesis that specific systems evolved through the traditional processing routes can be effectively integrated with the 3D printing of ceramic sand moulds.

The overarching research question is: How do specific mechanisms of bonding initiated by selected combinations of materials as employed in related traditional processing methods perform within the constraints of a 3D printing approach?

While there are many aspects and methods from the traditional foundry practices that can be utilised to bring some benefits to 3D printing, four specific aspects from the existing literature are considered for evaluating the current hypothesis; pre-moisturisation of hemihydrate as an accelerating mechanism, possible roles of foundry clays, the sodium silicate bonding, and the effects of resin coatings. Sub questions presented arise next based on these four aspects of research interest.

Literature on hydration mechanisms of plaster contains many suggestions on how to accelerate the hydration of plaster into gypsum. One of the simplest methods is

to add a certain amount of moisture to the plaster, before the actual hydration process. While this was proved to be true in the traditional plaster processing methods, it will be interesting to investigate whether this works fine within the 3D printing timeframes. Secondly, different forms of clays are often used to achieve bonding between different particles of a traditional sand mould material. Sand, clay and water mixtures are thoroughly mixed in order to generate electrolytic forces developing inter-particle attractions and consolidation of the material. Subsequent heating or baking drives the moisture out and leaves the interlocked sand particles within the matrix of the dried clay behind, giving rise to the strength, porosity, collapsibility and other essential characteristics. It will be intriguing to investigate, if these mechanisms also become effective when used in a 3D printing situation.

Further, traditional sand moulding practice also includes sodium silicate treatment to achieve high mould strengths. Sodium silicate as water glass (jell form) is usually combined within the mould material mixture and allowed to form the inter particle bonds through solidification, crystallisation and subsequent vitrefication. It is yet unknown, if these aspects can be employed in a 3D printing system to achieve further improvements. Lastly, various forms of resin coatings are often applied to sand particles and processed to achieve the mould material characteristics. Though similar systems are made available by the current commercial 3D printing systems, the actual science of material consolidation is not reported and how a specific type of coated sand actually will respond to varying process conditions of a 3D printing system is interesting to evaluate.

Based on these aspects of research interests, the following are the sub questions which will be answered through the research proposed:

- How does pre-moisturisation of plaster help accelerate the hydration mechanism within a 3D printing context?
- How effective are foundry clays as possible binding ingredients in a mould material to be processed on a 3D printing system?
- How does the sodium silicate treatment method affect 3D printed moulds?
- How can resin coated sands perform within a 3D printing system with varying process conditions?

## **2.6 Objectives of the current research**

The proposed research requires moulding materials with varying ingredients to be tested within a 3D printing system in order to be able to evaluate and understand the mechanisms and mechanics of interactions between different phases. The commercially available material systems are too proprietary and do not allow any freedom of insight or alteration. As a result, the proposed research requires development of working material systems in order to be able to conduct experimental research and evaluate different aspects, searching for answers to the questions raised. Considering the four main aspects proposed to be investigated, the overall research is designed to achieve the following objectives, focussing on the mechanisms and mechanics of binding in each case:

- Evaluate different binder options and identify a solution that works within the limits of the 3D printing system available at the time of beginning this research
- Evaluate different mould material options and develop a method to construct working material solutions.
- Experimentally investigate a working plaster-based material system assessing the role of pre-moisturisation together with other factors in influencing the bonding mechanisms and mechanics.
- Develop a working material system based on traditional foundry ingredients and evaluate the possible role of a selected clay
- Use the clay and sand composite material system and evaluate the role of the sodium silicate treatment within a 3D printing system
- Experimentally evaluate a resin based system establishing the roles of different 3D printing process parameters on the mould material consolidation and performance.

## **2.7 Methodologies**

General procedures followed for achieving different requirements of the tasks of the proposed research are presented here. Where necessary, more specific details and are included in the chapters to follow, within the context of the actual experimental work done. The material and binder systems and the initial testing procedures are the first steps in this research. Once working material and binder

systems are established, the next step is to conduct systematic experimental evaluation of structures and properties.

### ***2.7.1 Development of experimental material systems***

It may be noted that different material systems are required to be composed for 3D printing, in order to be able to conduct the experimental research proposed, investigating the roles of specific ingredients. For this, the process development steps reported by Utela et al. are employed for developing new material systems for 3D printing [69]. While they presented a series of steps, for the current research, the most important stages include formulation of working powder and binder systems and establishing the most suitable process and post-process parameters. Within these, the powder system offers more freedom considering that it will not interfere much with the sensitive working systems of the actual printing system. Different mould material options are attempted as required for this research and will be discussed more closely in different chapters that will follow.

However, the binder solution is very critical, as it needs to satisfy prerequisite conditions to be able to pass through the print head system available for the research. There is limited freedom in this as too widely varying characteristics of the liquid could lead to damage to the print head system. Many different solutions are initially tried and at times, major problems and consequent delays were faced due to lack of compatibility of different solutions with the print head system.

Further to these experiences, a working, relatively simple composition is established for the binder solution composed of around 96% of distilled water and a small amount of glycerol and other surfactants. This composition for the binder is kept constant for all the experimental trials conducted next with different material systems. As a result, the material systems developed for moulding in the current research are based on achieving the required powder-binder interactions and the green strength for the consolidated powder through this binder solution.

With each material system investigated, preliminary trials are conducted testing the compatibility of the binder and powder systems [69]. These are bench-top tests examining the powder-binder interactions, outside the actual 3D printing system. Small quantities of powders of different compositions are taken in plastic trays with rectangular pockets and the binder solution is injected through a syringe, simulating the 3D printing process. Successful combinations of powder systems are subjected to further testing, varying the process parameters and post-process baking and testing conditions. The most favourable process conditions are then applied in the actual experimental analyses that followed.

### ***2.7.2 3D Printing***

Compression test specimens as well as the moulds for further testing of all the experimental work conducted as part of this research have been printed using the ZPrinter® 310 plus from the Z-Corp, USA, a photograph of which is presented in Fig 2.1. After the initial tests are passed, each material system is first manually

mixed in a container with dry powder materials used in the appropriate compositions. A food mixer is then used for thoroughly mixing all the ingredients. The mixed sand composites are then sieved using a 250-230 $\mu$ m standard sieve, in order to avoid any particle conglomeration. The powder material is then loaded into the storage chamber of the machine, just before commencing the printing of test pieces. In all cases, powder mixing is usually taken up as and when needed, so as to avoid moisture pick-up if any, during long storage times.



***Fig 2.1. The ZPrinter® 310 plus***

## **2.7.3 Mould material characterisation**

### **2.7.3.1 Metallographic evaluation**



**Fig 2.2. HITACHI E-1045 magnetron sputter ion**

Several types of samples will require coating prior to investigation in the SEM or analysis with EDS or EBSD. Coatings increase the electrical conductivity of insulating specimens, reduce microscope beam damage and sample charging and improve the 'return' or emission of secondary electrons from specimens that have low atomic number elemental matrices (e.g. biological samples). The E-1045 ion sputter coater shown in Fig 2.2 can produce high resolution, continuous films with precise thicknesses at controlled temperatures. The available coating materials are Gold (Au), Platinum (Pt) and Carbon (C) and in this research Platinum was coated.



***Fig2.3. The Hitachi SU-70 Schottky field emission SEM***

The Hitachi SU-70 Schottky field emission SEM shown in Fig 2.3 allows for high magnification and ultra-high resolution imaging at low and high accelerating voltages was used to analyse the photomicrographs for both green and baked samples.

#### *2.7.3.2 Compression tests*

Compressive strength of the mould material is used as the basis to evaluate the general strength of the moulds printed with different material combinations both in green and baked states. Cylindrical and rectangular test specimens shown in Fig 2.4 are printed as per ASTM standards [38] with both diameter and height at 50mm. Both green and baked specimens are stored in desiccators with silica gel so during the period from printing and baking to the actual compression tests, so

as to avoid moisture pick-up, if any. Sample test pieces printed and the storage in a desiccator are depicted in Fig 2.5.

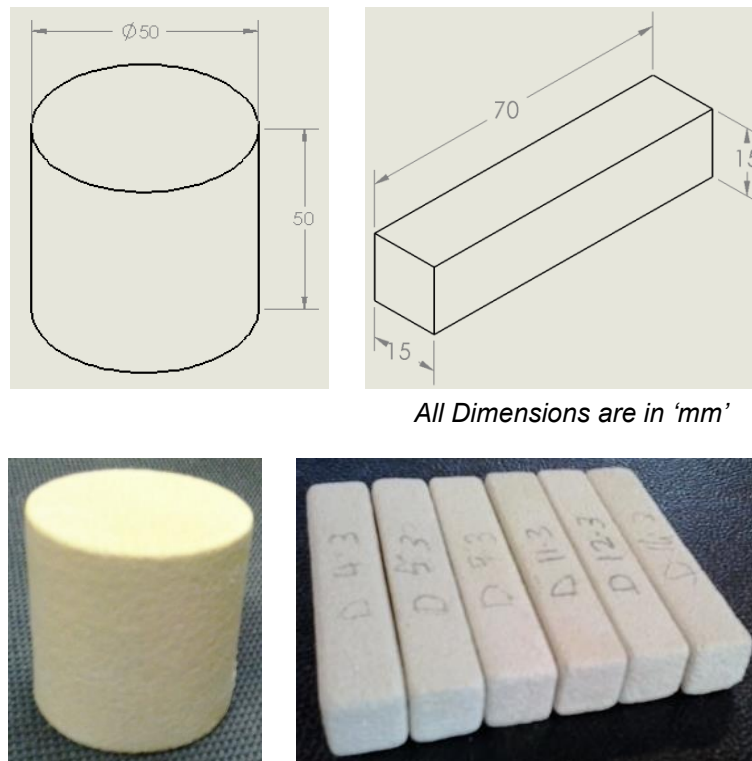


**Fig 2.4. CAD drawings and printed samples of compression and 3-point bending test pieces**



**Fig 2.5. Test specimens printed for compression tests as per the ASTM standards and preserved in the desiccator**

The Hounsfield tensile testing equipment 0162 Model H10KS was employed for the compression testing of the printed sand samples. The maximum load capability is 10000N, and a loading rate of 5mm per minute was employed for both green and dry compressive strength evaluation. A compressive test in progress on a standard sand specimen and the fractured specimen are shown in Fig 2.6. It may be observed that the fractured surfaces are almost at 45°, indicating shear failure of the specimens, which has been consistent with all the specimens tested.

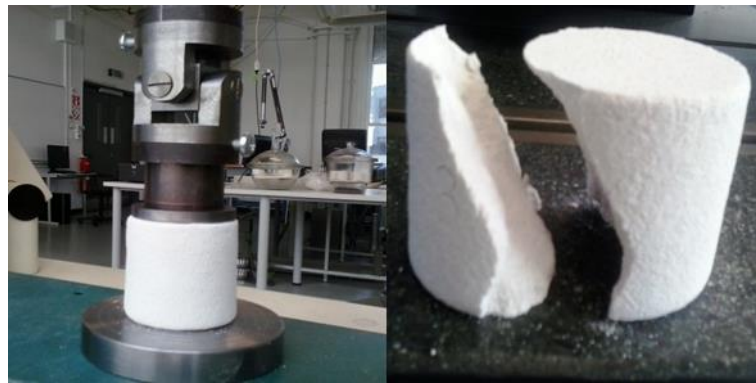


***Fig 2.6. The compression test in progress and a test specimen fractured on 45° shear planes.***

### *2.7.3.3 Printed moulds*

The mould design is developed in order to test the effectiveness of the printed moulds for the actual use in casting. It includes a cylindrical cavity for the casting, a runner and a sprue at one end and a riser at the other end, as depicted by the CAD drawing shown in Fig 2.7. The main body of the mould is printed in two pieces split at the centre, so as to facilitate easy removal of unbound powder. The two parts are later assembled and glued together. The pouring cups are also

printed separately and glued to the main mould at the end. CMS mould bonding agent was used for gluing all parts of the mould together, after baking to the necessary extent, it is a polymer based self-setting adhesive suitable for gluing or bonding of mould joints and cores. Images of some of the moulds and the pouring cups printed and in waiting for casting are shown in Fig 2.8.

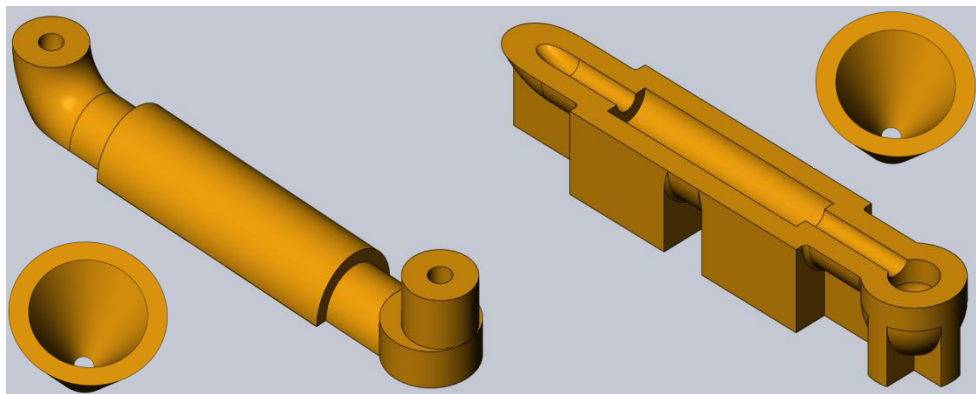


**Fig 2.7. CAD model of the mould**



**Fig 2.8. Printed Moulds and pouring cups waiting to be cast**

The moulds are stacked first, glued and then clamped together by means of a steel wire, in order to avoid any separation under the buoyant forces of the molten liquid. For each casting trial, a number of moulds are printed, naked assembled and stacked on the floor with additional foundry material as backing material. All moulds are gas torched to remove any residual moisture, before pouring the molten metal.

#### ***2.7.4 Casting trials and characterisation***

All casting trials including both aluminium and stainless steel casting were conducted at Progressive Castings, one of the local foundries in Auckland. The foundry assisted in ensuring proper degassing of metals before pouring so that sources of porosity could be avoided. Further to pouring and cooling to the room temperature, the moulds are broken and the solidified casting is taken out. A sample cylindrical casting together with the runner, riser and the gating system is shown in Fig 2.9. It may be noted that the castings came clean off the moulds and there was no evidence of any mould-metal interactions or unwanted reactions.



***Fig 2.9. A finished casting***

The cylindrical specimens are trimmed of the unwanted metal portions and subjected to surface roughness measurements first. Once this is done, each cylinder is carefully turned on a lathe, reducing the form and dimensions down to the standard specimens as per ASTM standard E8. The dimensions of the drawing and some of the specimens are shown in Fig 2.10.

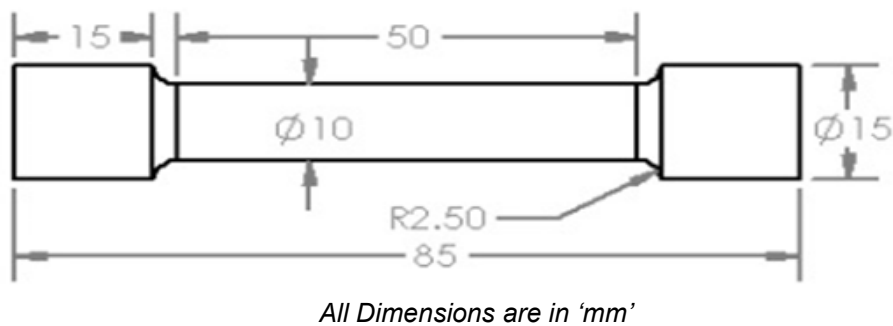


**Fig 2.10 Tensile test specimens prepared as per the ASTM E8 standard**

### **2.7.5 Tensile testing**

The Hounsfield tensile testing equipment is used with the force range of 50kN shown in Fig 2.11.

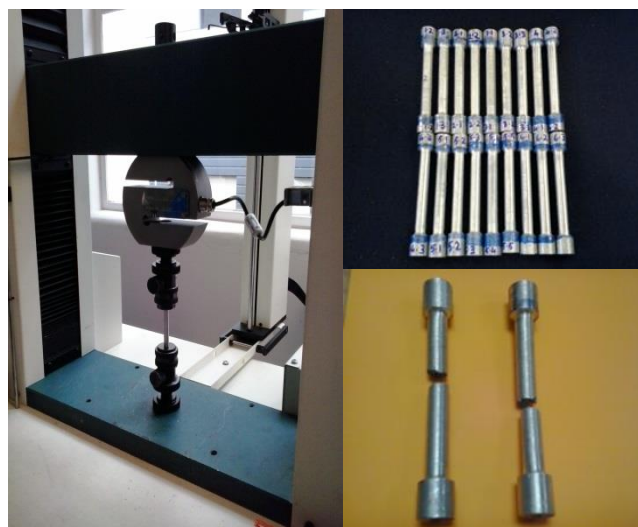


**Fig 2.11. The Hounsfield Tensile Tester and the specimens before and after testing.**

### **2.7.6 Surface roughness measurements**

The Taylor Hobson Talysurf shown in Fig 2.12 is used for measuring the average surface roughness ( $R_a$ ) values of the castings produced. The sampling length and cut-off lengths were 20mm and 5mm respectively.



**Fig 2.12. The Taylor Hobson Talysurf surface roughness tester**

### **2.8 Nomenclature of material systems used**

The three material systems used in the current research will be referred as follows in the thesis:

- i. Plaster based material system*
- ii. Sodium silicate treated plaster-clay material system*
- iii. Resin coated sand material system.*

## Chapter 3

### Plaster based material system

#### 3.1 Printing sand moulds

The ZPrinter 310 Plus system is used as the test bed for the current experimental research involving different mould material options. Like any other RP process, the input is a CAD model often converted into the .stl format. The CAD model is then sliced into layers of 0.08 - 0.23mm and then printed layer by layer. Powder feeding between two cylinders, controlled by the movement of two pistons allows the layer deposition and consolidation. The mixed powder composition filled in the supply chamber is levelled and allowed to be spread as a uniform layer over the build platform by means of a roller, while the excess powder is collected into the over flow chamber.

A drop-on demand (hp) print head selectively dispenses the liquid binder solution over the powder bed to initiate the bonding in specific areas. The rate of bonding reaction and the spread of the glue within the powder substrate depend on various factors, including the type of additives and activators used in the powder and liquid systems. The seepage can be controlled by controlling the viscosity of the liquid binder and the size of the powder particles. The level of control over the seepage directly relates to the dimensional accuracy of the printed part. Once all the layers

are printed, the part is allowed varying amounts of curing times for achieving the necessary green strengths depending on the material system.

The printed part in green state though attains some mechanical strength, must be handled with care and is often subjected to post-printing baking. The part strength often varies directionally, as it is the stronger along the x-and y-directions, the strength along the z-axis is less. The dimensional accuracies and surface qualities will depend on the powder system employed. During baking, which is at around 200°C and for a few hours, the free moisture content is removed and with further heating, chemically bound water is also removed, leaving behind a porous mould material structure with sufficient dry strength and permeability.

While different commercial material and binder systems were offered for use on a Z-Corp 3D printing system, the plaster-ceramic composite ZCast 501 had been the material solution for printing moulds and cores that could be used to cast non-ferrous metals and alloys. This material system, though discarded currently, could be used to print the pattern-less shell moulds with the wall thickness varying from 12.5mm to 25.4mm and a furnace baking at around 180-230°C for 4-8 hours based on the volume of the moulds. The mould and casting qualities were claimed to be almost equal to those of the regular sand casting, though the surface roughness is a little higher than the normal sand casting.

### **3.2 Basic ingredients and the bonding mechanisms**

As already noted in the previous chapter, there is very little information reported on the science behind these material solutions and the mechanisms of bonding at play. The US Patent filed by James et al. throws some light on how the system actually works [70]. When the aqueous binder fluid jetted by the print head strikes the powder bed, some of it is absorbed by the plaster powder and begins to migrate, while the rest evaporates. When sufficient moisture reacts with the plaster, gypsum crystallisation initiates due to the rehydration mechanism. The rate of rehydration, the expansion and the migration of the droplets will influence the effectiveness of the bonds while there are other additives in both the particulate material as well as the binder that will bring into effect the necessary controls. One of the issues is that the bonding mechanism in this case needs to be accelerated as against the conventional processing of plaster water composite; thoroughly mixing to form a slurry and then giving enough time to initiate and complete the gypsum crystallisation. Some forms of accelerators are often used.

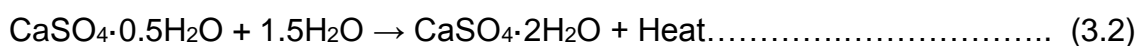
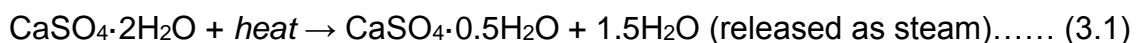
Further to printing, the mould strength is increased substantially by removing the excess moisture through drying naturally or by heating. An adhesive or a combination of adhesives is included either in the base material or the binder or both for additional strength of the printed moulds. The bulk of the strength of the article is achieved through the gypsum crystals interlocking the loose powder particles together. It was noted that the choice of the specific type, grade, and particle size of the adhesive employed play significant roles in contributing to the

mechanism of bonding and the additional strengths. A synergic interaction between the aqueous binder and the adhesive was reported, where the viscosity and migration of the binder solution vary with time, allowing for the reactions to be properly timed and the effects of the glue localised.

James *et al.* [70] considered small quantities of sodium chloride, sodium sulphate, and potassium sulphate as the possible accelerators of the rehydration mechanism. While there were also unknown quantities of citric acid, acetate, and boric acid used as retarders for controlling the swelling. While the actual composition is not fully known, this material system is too rigid in terms of experimentally evaluating the roles of different material and process parameters. Further, pre-moisturisation of the plaster phase was mentioned as a possible mechanism for acceleration, which is relatively very simple and economical, but was not used earlier. The experimental work presented in this chapter addresses these issues. A review of the hydration and dehydration mechanisms of plaster together with the possible means of accelerating the reaction are reviewed first and then a working system is developed making use of the pre-moisturisation as the means of accelerating the gypsum reaction rate. The working plaster-sand composite is then evaluated to understand the mechanism and mechanics of bonding in 3D printing.

### 3.3 The plaster hydration, dehydration, and accelerated crystallisation

From ancient times, plaster has been used for arts, architecture, medicine, and as fire protecting walls, etc. The chemical compound is calcium sulphate hemihydrate, but is often referred to in several names such as plaster, gypsum, and plaster of Paris. It is a finely ground white powder produced by heating the calcium sulphate di-hydrate or gypsum at 150°C in accordance with Eq. 3.1 [71]. The reaction product with half a molecule of water is calcium sulphate hemihydrate and commercially, this is what is known as plaster or plaster of Paris. The hemihydrate form, when treated with sufficient water, will be transformed again back to the di-hydrate form, following the exothermic hydration reaction given in Eq. 3.2. The hydration reaction begins by dissolving hemihydrate partially, establishing an absorbed layer and the  $\text{Ca}^{+2}$  and  $\text{SO}_4^{-2}$  ions passing into the liquid solution [89]. Theoretically, 18.6g of water is required for every 100g of plaster for the hydration process to complete for the transformation of gypsum and this water is said to be the chemically bonded water. The excess water remains as free water and occupies the inter-planar regions, providing the plasticity and flow characteristics for the slurry and also leaves behind porosity when dried off.



The dehydration process involves removing the excess water first and reducing the general mobility. It was known that heating at around 150°C will result in the removal of the free water. At this stage, the hemi-hydrate is formed from the di-hydrate. Further heating beyond 200°C removes the bonded water also, leaving behind the dry and anhydrous plaster. There are two types of plasters; 'α' and 'β' hemihydrates, depending on the forms of their crystal structures. The α-hemihydrate crystals are long and needle-like while the β-hemihydrate crystals are short and wider. The formation and final forms of the crystal structures are dependent on the heating cycle of the di-hydrate gypsum [72]. The strength of the α-hemihydrate is higher than that of β-hemihydrate [73]. It is possible to achieve hydration from any of these forms by treating with water again. In traditional mould making processes, plaster is mixed with cement, fibre glass, sand, clay, etc. for the best green and dry strengths, refractoriness and permeability to cast light metal alloys. It is well known that the castings produced by plaster moulds have good surface and dimensional qualities [73,74].

Mc Cartney *et al.* evaluated the effects of different additives on the crystallisation of calcium sulphate [75] and observed a correlation between the solubility of the calcium sulphate and the presence of organic anions, particularly from malic, citric, fumaric, glycolic, and succinic acids. Sung-Tsuen *et al.* [76] evaluated the kinetics of gypsum crystal growth, adding varying amounts of di-hydrate crystals to super saturated calcium sulphate solutions of varying compositions, with temperature varying from 15-45°C. As already noted, the rate of gypsum crystal growth is

controlled by an absorbed layer of calcium and sulphate ions around the seed crystals. The mass of the di-hydrate crystals growing was noted to be two to three times the weight of the seed crystals, increasing the surface for the ionic activity substantially. An induction period in the growth was observed when the concentration of the seed crystals was reduced. At higher super-saturation levels of the slurry and when the number of growth sites added was not sufficient to accommodate the required amount of crystal deposition, spontaneous crystallisation within the bulk of the solution was noted. Overall, the rate and extent of gypsum hydration depends on both the number of seed crystals and the concentration of the solutions and varies interactively.

Smith *et al.* [77] also conducted a comprehensive evaluation of the crystallisation of calcium sulphate di-hydrate considering both seeded and unseeded solutions of varying super saturations. Based on a dilatometric study, the gypsum crystallisation in the absence of seed crystals was observed to be heterogeneous, with the growth rate proportional to the crystal surface area and the square of the super-saturation. Dehydration of calcium ions was noted to be the controlling factor for the rate of crystal growth. According to them, stirring has a slight influence on the rate of crystallisation. With increased stirring, the crystal growth was noted to stabilise, indicating the growth rate was not diffusion controlled at higher speeds of stirring. Further research in similar lines by Nancollas *et al.* [78] considering a wider temperature also reaffirmed these results.

A comparative evaluation of the nature of gypsum crystal growth in bentonite clay and sodium silicate gels was considered by Cody *et al.* [79]. Plaster in silica gel at 40°C and pH 7.5 resulted in elongated prisms of relatively smooth crystal faces and often twinned, while tubular crystals with a variety of kinks, steps and pits without any twinning resulted in bentonite clay solutions under similar conditions. It was noted that sodium montmorillonite stimulates the process, allowing for large gypsum crystals to grow. Klepetsanis *et al.* [80] observed that the pH of the solution has a marked influence on the electrophoretic mobility of the calcium sulphate di-hydrate particles. This might affect the crystal growth of the internally formed calcium sulphate di-hydrate crystals due to variations in  $\text{Ca}^{+2} / \text{SO}_4^{-2}$  ion ratios.

Considering the dehydration of gypsum, thermal dehydration process of synthetic gypsum was considered by Strydom *et al.* [81]. While the overall dehydration was found to proceed in multi-step reactions, the main dehydration of calcium sulphate was observed to occur as Eq. 3.3 between 95 and 107°C by means of an activation energy. A second reaction as given in Eq. 3.4 follows this, resulting in a calcium sulphate compound with 0.15 water molecules. It was reported that the calcium sulphate-water bonds are strong and sustain even until heating up to around 450°C.



In a further work, Lamb *et al.* [82] also compared the dehydration of natural and synthetic forms of gypsum. It was reported that both forms decompose into the anhydrous calcium sulphate via the formation of  $\text{CaSO}_4 \cdot 0.15\text{H}_2\text{O}$ . The natural gypsum was found to have certain amount of anhydrite and that it increased slightly at 60°C. At 170°C, both hemihydrate and anhydrite contents were noted to increase with a possible coexistence of  $\text{CaSO}_4 \cdot 0.62\text{H}_2\text{O}$  and  $\text{CaSO}_4 \cdot 0.15\text{H}_2\text{O}$ . When heated to 240°C, more  $\text{CaSO}_4 \cdot 0.15\text{H}_2\text{O}$  was noted than hemihydrate in natural gypsum, while the synthetic form showed an increasing amount of anhydrite, but almost equal quantities of hemihydrate and  $\text{CaSO}_4 \cdot 0.15\text{H}_2\text{O}$ . At 450°C, the synthetic dihydrate was noted to be completely transformed to anhydrite, while the natural gypsum still showed traces of hemihydrate.

Nakamura *et al.* [83] proposed that the dielectric and mechanical strengths directly correlate in hardened gypsum, while both strengths decreased with increasing water content, which could be attributed to the porosity resulting from excess water. Badens *et al.* [84] based on controlled transformation rate thermal analysis observed that the dehydration of gypsum varies with the pressure under which the reaction takes place. The intermediate formation of the hemihydrate was observed to be absent with pressures ranging from 1 to 500Pa, while pressures beyond 900 Pa resulted in its formation.

Finally, it is also necessary to understand how the hydration mechanisms can be altered by means of other ingredients. Badens *et al.* [85] investigated the

crystallisation of gypsum in the presence of different acids considering changes to the kinetics of crystallisation and the gypsum crystal morphologies. Low concentrations of carboxylic acids were found to have no significant effects either on the habit or the morphology of gypsum crystals. D, L-malic acids were found to result in extremely rough faces and more twinning for the crystals.

Singh *et al.* [86] observed that accelerators promote the hydration of plaster by increasing the nucleation through a seeding action and changing the rate at which calcium and sulphate ions are transported into the dihydrate crystal lattice. Dihydrate, depending on the amount and the surface area, was found to be an effective accelerator of the gypsum crystallisation.  $K_2SO_4$  was found to increase the gypsum crystal growth in both the [001] directions and the directions normal to the axis of the needle resulting in much larger needle like crystals but with lesser mechanical strengths. Soderberg *et al.* [87] also noted the positive role of dihydrate seeding to promote gypsum crystal growth. It was reported that strong inorganic acids and salts of strong acids and bases act as accelerators, while weak organic acids and their salts with strong bases work as retarders of the gypsum nucleation.

The role of dihydrate as a seeding material, promoting accelerated gypsum reaction has also been confirmed by Maritas *et al.* in a plaster composite constituted of  $CaCO_3$ , vermiculite and mica [88]. An accelerating effect on the kinetics of gypsum crystallisation was observed with the introduction of dihydrate

germs. The setting time was found to reduce to half when 20% by weight of dihydrate used as a seeding material. However, the effect was not equally pronounced, with a commercial hemihydrate, and was attributed to the role of the particle size. Consequently, a commercial plaster sieved to 10 microns was found to reduce the setting time from 40 to 10 minutes with dihydrate germination.

### **3.4 The material system**

Summarising from above, when treated with water, plaster first dissolves and gypsum precipitates after attaining the equilibrium solubility limits, as its solubility limit is exceeded considerably [72]. The hydration process proceeds with the hemihydrate partially dissolved, forming an absorbed layer and  $\text{Ca}^{+2}$  and  $\text{SO}_4^{-2}$  ions going into the solution [89]. When the absorbed layer reaches a limit, cracks will form, more water comes in contact with fresh hemihydrate, forming di-hydrate nuclei. Partially dehydrated gypsum can exist in two forms;  $\alpha$  and  $\beta$ -hemihydrate plasters and considering their abilities to rehydrate and form rigid and porous moulds, both are widely used in the production of moulds for slip casting. Needle like crystals grow forming a network and crystals pile-up one over the other resulting in internal forces and displacements in the setting mass, overall setting expansions, and exertion of pressure on the container walls [90].

When used as a mould material in plaster mould casting, gypsum is dried and furnace heated before pouring liquid metal. Kelly et al. noted that alternate layers

of water and calcium sulphate molecules constitute gypsum, giving rise to the easy cleavage of this mineral [91]. On the other hand, the structure of hemihydrate has water molecules arranged in channels within the network of the calcium sulphate chains. As a result, the induction period for the dehydration of gypsum is considerably higher compared to that of the hemihydrate. The water molecules get easily removed without disrupting the solid structure, when anhydrites are formed from hemihydrates.

Commercial 3D printing systems made available by Z-Corp earlier and the 3D systems continue utilise a specific form of plaster together with olivine sand as a possible material system for rapid production of pattern-less moulds for non-ferrous casting. An aqueous glue delivered through an ink-jet nozzle system consolidates the powder particles through initial spreading by capillary action, dissolving the plaster and crystallising, essentially through hydration and giving the necessary green strength. It was noted by Yu *et al.* [92], that different grades of hemihydrates need different amounts of water for the hydration which begins slowly through an initial incubation period and takes about 9 minutes to complete. Accelerators of some form are used within the 3D printing material system to expedite the process as the rate of crystallisation and final setting are paramount. As a result, the accelerators play a significant role. Singh *et al.* [86] noted that strong inorganic acids and salts of strong acids and strong or weak bases can accelerate the hydration of plaster by increasing the nucleation through a seeding action and modifying the rate at which calcium and sulphate ions are transported to be incorporated into the lattice of the growing di-hydrate phase. Martias *et al.*

[88] observed that as the presence of di-hydrate germs increases, the kinetics of the hydration process is accelerated.

While the plaster hydration, dehydration and the possible addition of accelerators and retarders are now known from the preceding discussions, most of the knowledge generated is based on widely varying conditions. From natural geological processes to building material systems, and in between the mould material applications, the common theme however is the addition of sufficient water and thorough mixing and development of a slurry-like consistency. Once this is achieved, the mechanisms from the classical theories of gypsum hydration and dehydration can be considered to be working. As already highlighted, the conditions are completely different in a 3D printing situation and it is not clear how the plaster-sand composites perform with powder spreading and binder jetting methods. These aspects are experimentally investigated and presented in this chapter, investigating the timely formation and growth of gypsum crystals to develop the necessary green and baked strengths of moulds produced by 3D printing with varying material compositions and process parameters. Pre-moisturisation of hemihydrate is considered as the possible means of accelerating the gypsum crystal growth.

Based on these constraints, a working material system is attempted to be developed initially. First, a series of plasters and silica sands are mixed in different proportions, and tested in ice trays, with the binder liquid injected by means of a

hand pressed syringe. The small rectangular blocks set to different times are shown in Fig 3.1. These blocks are manually tested for the possible green strengths achieved. A clay-sand combination resulting in reasonable green strength is shortlisted from these preliminary studies.



**Fig. 3.1 Initial trials manually printed in ice-trays**

Victor Superfine Utility Plaster ( $\text{CaSO}_4 \cdot 0.5\text{H}_2\text{O}$ ), a  $\beta$ - hemihydrate from Australia is used as the binder and New Zealand's high purity (99.32%) silica sand (AFS fines No. 60 - 65 grain size & clay content 0.3%) is used as the refractory material. The aqueous solution based on glycerol is the common binder solution. Initially, the thoroughly mixed sand and hemihydrate composite is used in a 3D printer without any further conditioning and attempts are made to produce rectangular test specimens. The resulting specimens came out to be too fragile, with almost negligible transformation of the plaster into gypsum. Evidently, there is insufficient moisturisation of the plaster, resulting in weak nucleation and lack of formation and

growth of gypsum. The difference between these trials and the initial trials on the ice-trays lies in the fact that the syringe disposes relatively high quantities of the binder liquid and the relatively small quantity of powder constrained in a small volume gets completely soaked with the binder solution. Further, the time allowed for each set of samples helps the gypsum reaction to proceed sufficiently. Following the observations by Martias *et al.* [88], a small quantity of water is thoroughly mixed in the plaster-sand composite to provide a certain amount of dihydrate, resulting from the presence of pre-moisture, before loading the powder mixture on the printing system. The pre-moisturised powder composite is then loaded on the 3D printer system to print small rectangular test pieces of specific dimensions as shown in Fig 3. 2. It may be noticed that these blocks are already able to be produced with sufficient dimensional stability and green strengths.



**Fig. 3.2 Printed and baked rectangular samples**

The rectangular blocks are then subjected to baking to different temperatures and times to achieve varying dry strengths. Both green and dry strengths of the blocks are then subjected to a simple loading similar to the three point bending, but on a make-shift arrangement where the loads are applied by means of masses added to a hook at the centre of the specimen supported on either ends. Volume errors are also estimated in both green and dry states by measuring the critical dimensions. Based on the *a priori* data thus generated, a working material system with narrow ranges of plaster, sand and pre-moisture could be identified.

Based on a gradual improvement in the dimensional stability and overall sample strength, the hemihydrate content within 33% to 53% and baking temperature and time in the ranges 200°C to 400°C and 2 to 6hours respectively could be ascertained. The effects of varying the pre-moisture content from 1% to 15% are investigated. Considering dimensional stability, mass, density, and porosity, pre mixing of water in the range 2% to 5% is ascertained to be the most favourable range, while moisture levels beyond 5% resulted in excess water and plasticity [93].

When the right amount of moisture is pre-mixed with the material system, a small quantity of plaster is converted into gypsum and accelerates the hydration process. Subsequently, when the glycerol based aqueous liquid binder strikes the surface of the material system, the water contained in the liquid binder begins to evaporate and diffuse away from the printed location. When sufficient water content is made available, based on the composition of the mould material

mixture, the plaster to gypsum conversion initiates and further assisted by the di-hydrate, completes the crystallisation process.

### **3.5 Mechanism of gypsum bonding with varying levels of pre-moisture**

The mechanisms of bonding in both green and dry states were assessed based on test pieces printed with varying compositions and then baked to different conditions. SEM photomicrographs with varying levels of pre-moisture, mould material with 33%  $\beta$ -hemihydrate and 67% silica sand with varying pre-moisture levels immediately after mixing and before printing are presented in Fig 3.3. It is noted that the plaster is beginning to show crystal growth with additions of moisture. Comparing the photomicrographs of Fig 3.3 (b) and (f), there is a clear morphological change in the form of the plaster aggregates. There is evidence of the needle like growth of gypsum crystals in pockets, indicating the formation of the nucleation sites. However, the binder is still in fine powder form when it is introduced into the printing system. The spreading and distribution by the roller breaks any growth in the existing crystals, but the material is ripe for the conversion of the plaster into gypsum.

SEM photomicrographs of green samples printed with 33%  $\beta$ -hemihydrate and 67% silica sand and varying levels of pre-moisture treatments are presented in Fig 3.4. Formation and growth of di-hydrate crystals is evident in all samples, but with increasing intensity, as the pre-moisture level increases from 2 to 4% as seen in Fig 3.4 (a), (c), and (e). All photomicrographs at higher magnifications as

presented in Fig 3.4 (b), (d), and (f) clearly demonstrates the needle or plate like growth of gypsum crystals from  $\beta$ -hemihydrate. It is interesting to note that the accelerated needle or plate like growth developed from 3D printing is very similar to the structures obtained after 28 days of curing  $\beta$ -hemihydrates, together with retarders such as carboric acids, as reported by Singh *et al.* [86]. While the formation of needle like gypsum crystals is a common feature for all the samples, there are minor variations, probably due to the varying contents of pre-moisture. It was also reported by Singh *et al.* [86] that seed crystals while enhancing the crystallisation rates, will also change the crystal growth rate and morphologies. Nevertheless, the gypsum crystal growth is quite needle-like and very intricate in the case of 2% pre-moisture as compared to the other samples.

It is to be noted that Fig 3.3 represents samples of plaster sand mixtures before being loaded on to the printer and moisturised with the binder jetted through the print head. The presence of pre-moisture helped develop partial crystal growth to varying degrees depending on the amount of pre-moisturisation. Fig 3.4 presents the growth of gypsum crystals as a strengthening mechanism in the green state. Fig. 3.5 is a collection of SEM photographs of the baked samples. Considering the time lapses between different stages of the development from mixed powder to the final baked samples, and also due to the varying nature of the crystal growth, different magnitudes were used for these three sets of photomicrographs.

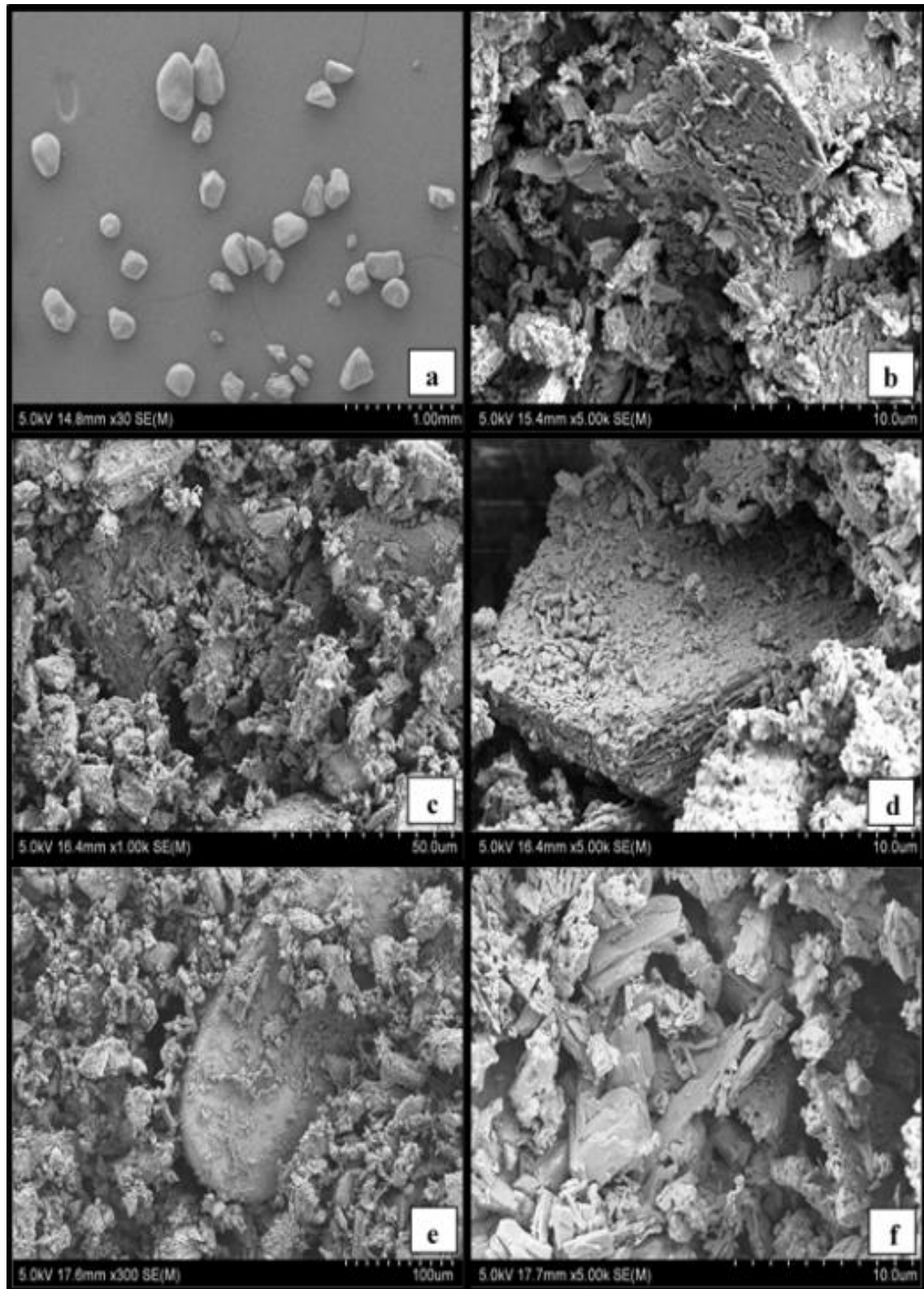


**Fig. 3.3 (a) Spherical silica sand particles, (b)  $\beta$ - hemihydrate, mould material mixtures with 33% plaster and 67% silica sand and varying pre-moisture levels; (c&d) 2% and (e&f) 4%**

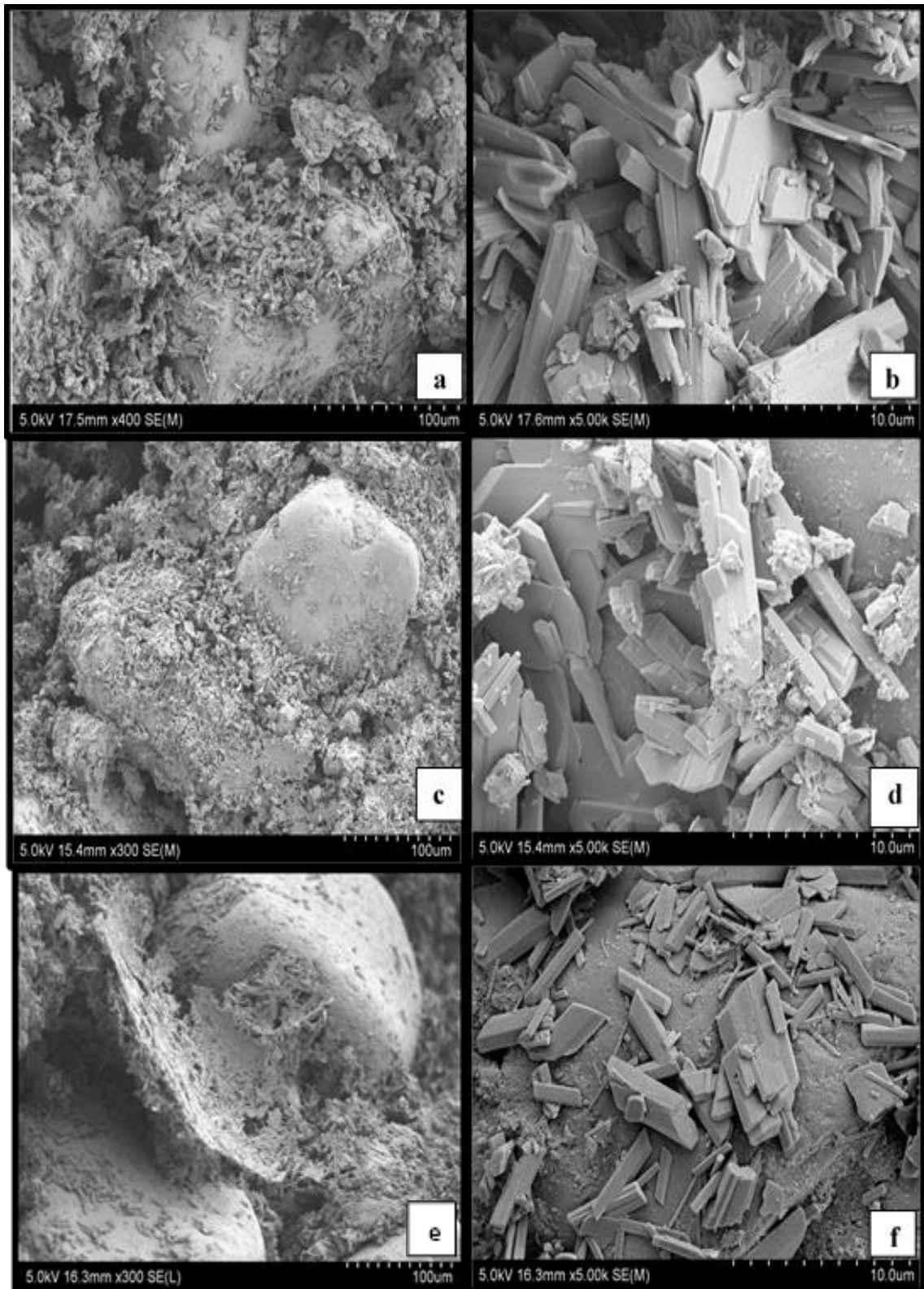


**Fig 3.4 Di-hydrate nucleation and growth in green printed samples with 33% plaster, and pre-moisture levels at 2% (a&b), 3% (c&d), and 4% (e&f).**

Green samples printed with varying levels of pre-moisture are subsequently baked at 200°C and 300°C, for about 10 hours. Previous studies show that the dehydration of gypsum is slow below 95°C and then accelerates between 95°C and 170°C [81]. The water absorbed between layers or in structural channels is either in zeolitic form or bound to exchangeable cations or directly to the clay mineral surfaces, while both forms can be removed by heating. As reported by Mondal *et al.* [94], heating gypsum to about 90°C will result in a loss of 3/2 molecules of water, resulting in hemihydrate with a hexagonal symmetry. Further heating does not allow the remaining water to be removed until about 300 to 350°C, where the strongly held water molecules are also removed, resulting in an orthogonal anhydrate.

Ideally, it would appear that the samples need to be heated to around 300 - 350°C in order to achieve complete drying. However, the results are mixed, as evident from the photomicrographs of Fig 3.5, from which it is clear that the effects of heating at different temperatures will also be influenced by the amount of pre-moisture and the level of gypsum crystallisation. Fig 3.5 (a) and (b) show a marked difference in the crystal structures resulting from heating to 300°C. Compared to the structures in Fig 3.4 (a) and (b), the needle like appearance is changed to relatively smoothed and rounded structure, filling the inter-sand particle regions and forming a continuous matrix structure in which the sand particles are embedded. The 3% moisture samples shown in Fig 3.5 (c) and (d) show this formation to a relatively lesser extent, while the 4% samples did not seem to be filling the inter sand particle gaps sufficiently.

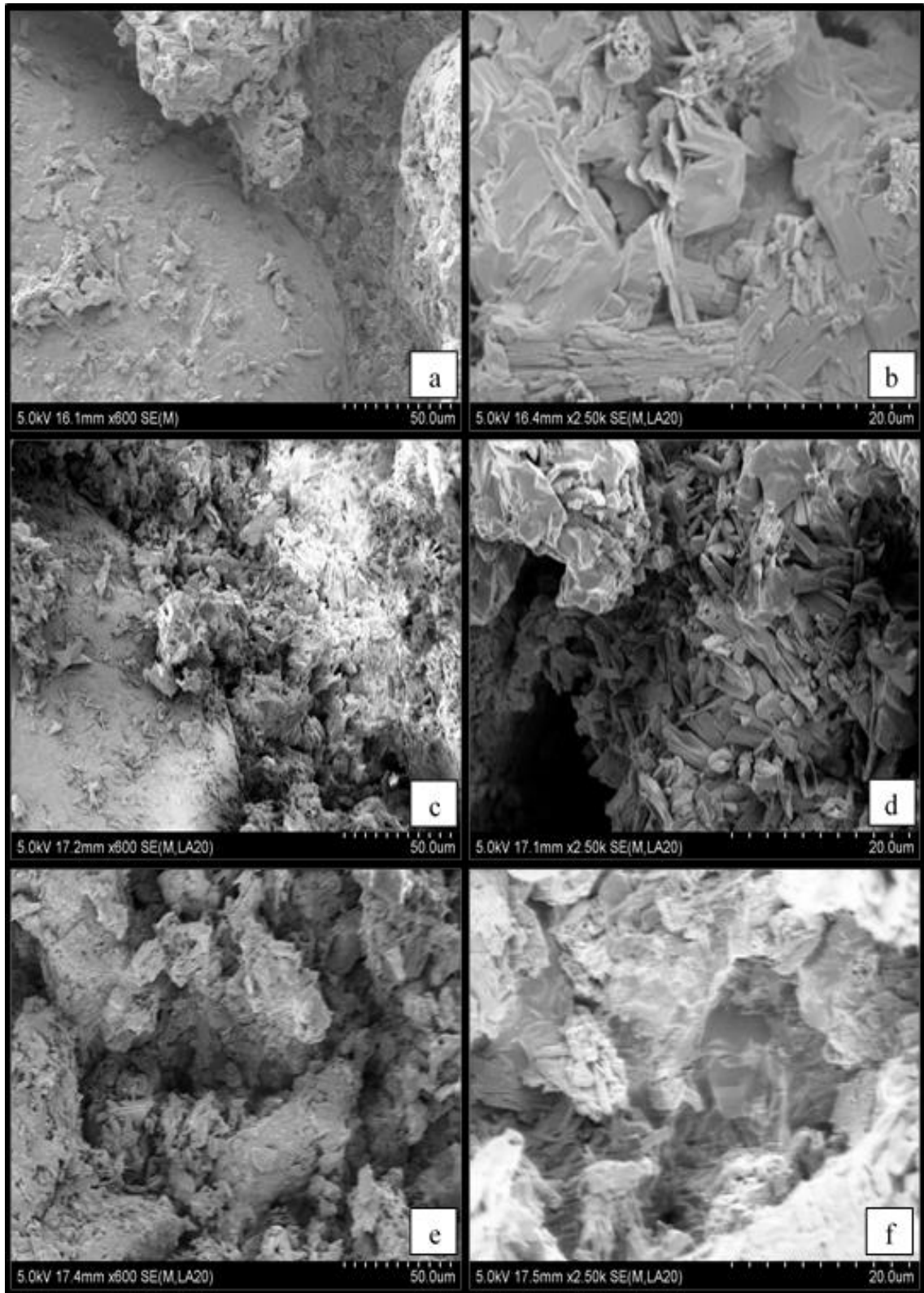


**Fig 3.5 Crystallographic changes due to baking: samples with 33% plaster, and pre-moisture levels at 2% baked at 300°C (a & b), 3% baked at 200°C (c & d), and 4% baked at 200°C (e & f).**

### 3.6 Mechanics of bonding

As evident from the photo micrographic evaluation, adding a small quantity of water to pre-moisturise the plaster allows  $\beta$ -hemihydrate to be effectively used as a binder to hold sand particles together in 3D printing applications. However, the extent of gypsum crystallisation and subsequent responses to baking at different temperatures vary with composition and process conditions. In order to be able to understand the true nature of the binding system, empirical models are developed based on a statistical experimental design.

The three level design developed by Box and Behnken combining  $2^k$  factorial with incomplete block designs is used for this purpose [95]. Specific advantages of this design include; highly efficiency in terms of the number of runs, and being rotatable or nearly rotatable. Further, the Box-Behnken design is either spherical or cuboidal, and in spherical form, all points lie on a sphere of radius  $\sqrt{2}$ . While there are three levels for each factor, the cubic design does not use the points at the vertices of the cube, which could be advantageous when experiments with combinations of extreme levels of factors involved are difficult to conduct. Compared to the central composite designs, the Box Behnken design necessitates lesser number of trials for any number of experimental factors. In the current case, with four factors, Box-Behnken design yields a total of 27 trials, as against 31 in the case of central composite designs. Further, the design is relatively more reasonable in terms of capturing the roles of the factors as majority of experimental points are in the middle of the ranges.

Multiple linear regressions conducted to evaluate the relationships between the key responses and the experimental factors as well as predict the values of responses with specific combinations of factors [95]. The critical experimental factors considered and the ranges of each of them as established from the preliminary studies detailed above are presented in Table 3.1. The quadratic response model given in Eq. 3.5 is used considering up to second order interactions. Dimensional volume error and compressive strength of both green and baked samples are considered as key responses and the design matrix and experimental responses are listed in Table 3. 2.

$$Y = \beta_0 + \beta_1 X_1 + \beta_2 X_2 + \beta_3 X_3 + \beta_4 X_4 + \beta_{11} X_1^2 + \beta_{22} X_2^2 + \beta_{33} X_3^2 + \beta_{44} X_4^2 + \beta_{12} X_1 X_2 + \beta_{13} X_1 X_3 + \beta_{14} X_1 X_4 + \beta_{23} X_2 X_3 + \beta_{24} X_2 X_4 + \beta_{34} X_3 X_4 \dots \dots \dots (3.5)$$

where, Y is the response, X<sub>1</sub>, X<sub>2</sub> ... are the factors and β<sub>1</sub>, β<sub>2</sub>... are the coefficients

It may be noted that the responses from the green samples are only affected by the plaster (X<sub>1</sub>) and the pre-moisture (X<sub>2</sub>) levels, which results in repetitions of certain trials shown in Table 3.2. In such cases, the average values of responses from repeated trials are used and the second order models involving factors X<sub>1</sub> and X<sub>2</sub> only are developed using experimental arrays with nine different trials. With each response, ANOVA is conducted and the most significant variables are identified comparing the P-values (P<0.15) at 85% confidence level. Response surface models are finalised, discarding the insignificant factors in most cases and the results obtained based on these models are discussed next.

**Table 3.1 Process parameters and their levels**

Parameters	Low Level (-1)	Mid-Level (0)	High Level (+1)
<b>β-hemihydrate (X<sub>1</sub>)</b>	33%	43%	53%
<b>Percent pre-moisture (X<sub>2</sub>)</b>	2%	3%	4%
<b>Baking Temperature (X<sub>3</sub>)</b>	200°C	300°C	400°C
<b>Baking Time (X<sub>4</sub>)</b>	2hours	4hours	6hours

**3.6.1 Percent volume error**

Percent volume error is calculated in the green state, X<sub>2</sub>, X<sub>1</sub><sup>2</sup>, X<sub>2</sub><sup>2</sup>, and X<sub>1</sub>X<sub>2</sub> are identified to be the most significant variables. Further ANOVA reconfirmed that these variables are really significant in influencing the response on green percent volume error. There is improvement in adjusted R-square values from 90.92% to 91.24%. The second order quadratic model for percentage green volume error is written as,

$$Y_{GVE} = 7.9348 + 9.6954X_2 - 0.0111X_1^2 - 2.9492X_2^2 + 0.1595X_1X_2 \dots\dots\dots (3.6)$$

where, Y<sub>GVE</sub> is the green volume error.

**Table 3.2 Box-Behnken experimental design and key responses with plaster based system**

Trial No.	Coded Variables				Un-Coded Variables				Volume Error (%)		Compressive Strength (KPa)	
	X <sub>1</sub>	X <sub>2</sub>	X <sub>3</sub>	X <sub>4</sub>	% β-Hemihydrate	% Pre-Moisture	Baking Temp. (°C)	Baking Time (hrs.)	Green	Baked	Green	Baked
1	-1	-1	-1	-1	33	2	200	2	16.29	13.95	276.88	219.34
2	-1	-1	0	1	33	2	300	6	14.59	13.95	436.13	169.60
3	-1	-1	1	0	33	2	400	4	11.1	13.95	312.54	182.16
4	-1	0	-1	1	33	3	200	6	13.79	14.17	403.53	322.05
5	-1	0	1	-1	33	3	400	2	15.08	14.17	429.68	154.32
6	-1	1	-1	0	33	4	200	4	9.01	8.48	93.71	106.44
7	-1	1	0	-1	33	4	300	2	9.01	8.48	65.36	65.19
8	-1	1	1	1	33	4	400	6	7.59	8.48	75.55	76.90
9	0	-1	-1	0	43	2	200	4	6.87	8.70	142.6	109.33
10	0	-1	1	-1	43	2	400	2	8.31	8.70	205.42	104.92
11	0	-1	1	1	43	2	400	6	9.55	8.70	95.41	112.05
12	0	0	0	0	43	3	300	4	9.37	10.51	72.49	159.75
13	0	0	0	0	43	3	300	4	11.1	10.51	99.65	153.47
14	0	0	0	0	43	3	300	4	9.72	10.51	37.35	128.85
15	0	0	0	0	43	3	300	4	12.12	10.51	95.41	128.68
16	0	0	0	0	43	3	300	4	12.12	10.51	91.67	131.23
17	0	1	-1	-1	43	4	200	2	6.13	6.42	80.78	84.71
18	0	1	-1	1	43	4	200	6	4.63	6.42	86.45	67.74
19	0	1	1	0	43	4	300	4	6.49	6.42	78.6	52.80
20	1	-1	-1	1	53	2	200	6	1.58	1.22	69.77	40.06
21	1	-1	0	-1	53	2	300	2	1.77	1.22	58.91	30.56
22	1	-1	1	0	53	2	400	4	1.58	1.22	71.3	30.22
23	1	0	-1	-1	53	3	200	2	3.13	4.63	120.7	48.21
24	1	0	1	1	53	3	400	6	3.69	4.63	106.44	60.61
25	1	1	-1	0	53	4	200	4	1.39	2.13	169.26	65.02
26	1	1	0	1	53	4	300	6	3.13	2.13	141.08	68.59
27	1	1	1	-1	53	4	400	2	3.69	2.13	222.73	51.10

Fig. 3.6 presents the variation of the green percent volume error in printed samples with varying plaster and percent pre-moisture levels. In all the cases, the percent volume error increased initially, attained a peak and then gradually dropped as the percent moisture level is increased. Also, the volume error values decreased as the amount of hemihydrate is increased, at all levels of pre-moisture. Generally, addition of moisture to hemihydrate results in a volume expansion as the gypsum crystals start growing, with accumulation of water molecules. Hydration of plaster is reported to be associated with around 30-50% increase in volume [96]. In the 3D printing situation, volume errors also arise due to excessive flow and seepage of the binder, thus resulting in overall increased dimensions. While the initial expansion could be attributed to either of these, the volume expansion resulting from gypsum crystal growth is the most likely cause, but to the extent of the hydration in each case.

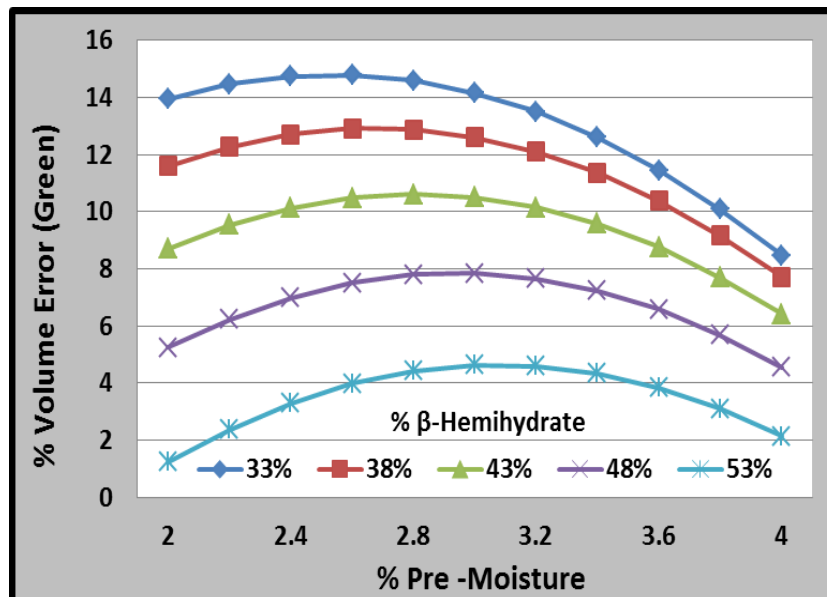


**Fig 3.6 Percent Green volume error Vs percent pre-moisture at different levels of  $\beta$  hemihydrate**

Pre-moisture, while helping promote gypsum crystal growth acting as seeds, the effective role within the seeding mechanism varies with the amount of moisture as well as the amount of plaster. While the variations arising with increasing pre-moisture levels are relatively minor, the plaster content has a significant effect on the volume errors, as the situation changes from higher expansions at lower (33%) limits of plaster to lesser expansion at upper (53%) limits. Generally, addition of moisture first results in a volume contraction during the early stages of the mix. Nucleation and subsequent growth of gypsum crystals results in volume expansion [97]. In the present case, the regaining of the lost volume is dependent on the amount of gypsum recrystallization. Apparently, at higher plaster contents, there is an initial contraction resulting from the early setting, but considering the less moisture and higher plaster content, the overall amount of gypsum crystallisation is limited, thus resulting in the lower contraction from its expansion at the upper (53%) limit.

The volume errors obtained based on the baked samples are listed in Table 3.2 and the ANOVA results using this data yielded adjusted R-Square values 81.75% and 78.11% for the full model and the model with the significant factors respectively. Since there is no improvement in the adjusted R-Square value in the model with significant factors, the full model is used and the second order quadratic equation developed is as given in Eq. 3.7.

$$Y_{BVE} = 40.1529 - 2.4695X_1 + 11.2383X_2 + 0.0505X_3 + 2.7484X_4 + 0.0193X_1^2 - 2.4840X_2^2 - 0.0001X_3^2 - 0.3718X_4^2 + 0.1098X_1X_2 - 0.0002X_1X_3 + 0.0125X_1X_4 - 0.0038X_2X_3 - 0.0842X_2X_4 + 0.0003X_3X_4 \dots (3.7)$$

where  $Y_{BVE}$  is baked volume error.

The volume errors predicted by Eq. 3.3 are plotted for varying hemihydrate with different combinations of the other parameters, as shown in Fig 3.7. There is a slight volume contraction in all cases, clearly demonstrating consistent decreases in volumes of all samples at all ranges, as compared to the results in Fig 3.6. Further, in all the cases, the volume error gradually decreased, with increasing hemihydrate. Though not to the same scale, this is in accordance with the report by Azam [98] that dehydration of gypsum is usually associated with around 39% decrease in volume. However, Joanna [99] stated that this may have alterations depending on the nature of ingredients, and further photomicrographic evaluation is essential to establish the real cause. Further, the higher the plaster, the lesser the volume error is also proved to be true, after baking.

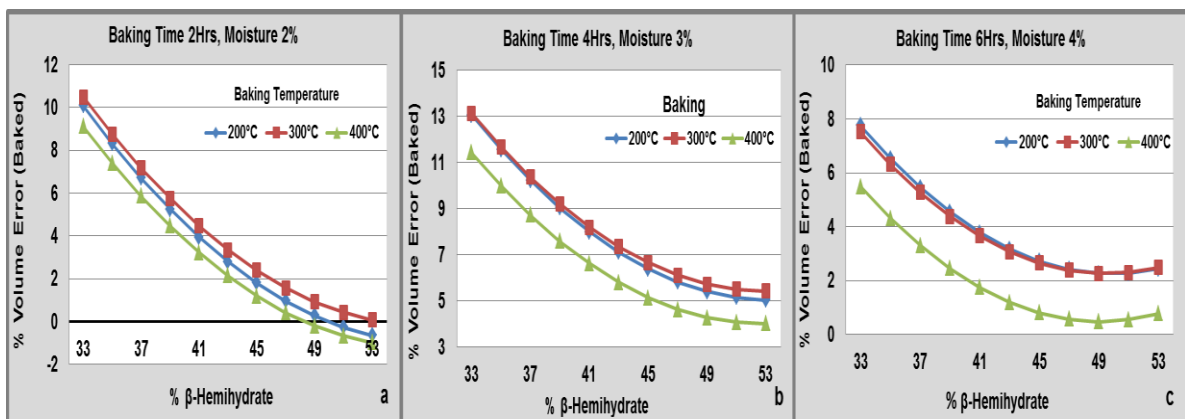


**Fig. 3.7 Percent volume error after baking Vs β –hemihydrate percent at different levels of pre-moisture and baking times**

### 3.6.2 Compressive strength

While transformations of plaster to gypsum and vice versa are micro level changes, bulk material properties such as compressive strengths of green and baked samples should allow verification of the role of pre-moisture on the nature of consolidation of gypsum as a binder in 3D printing. Compression tests on the mould samples are conducted using the compression testing equipment (Tinius Olsen, England) described and shown in section 2.7.3 and Fig. 2.6 respectively. The specimen shape is based on ASTM standards [100] and fracture propagation on the 45° plane is clearly evident in Fig 2.6, indicative of shear failure [101].

ANOVA based on the compressive strength results obtained with the 3D printed test specimens in the green state allowed identification of significant factors, but as the adjusted R square value (69.76%) of the full model and model based on the significant factors being the same. The full model as given in Eq. 3.8 is considered for further evaluation. The positive correlation observed between  $X_1$  and  $X_2$  with a value of (+1) shows the relation between these two factors to be very strong.

$$Y_{GCS} = 3261.2776 - 120.5620X_1 - 229.6965X_2 + 0.9928X_1^2 - 34.9151X_2^2 + 9.3668X_1X_2 \dots\dots\dots (3.8)$$

where,  $Y_{GCS}$  is the green compressive strength

The variation in green compressive strength with varying process conditions based on the model in Eq. 3.8 is depicted in Fig. 3.8 (a) and (b). While the printed

samples are in the green state, the gypsum crystals holding the sand particles together is the predominant mechanism providing the necessary compressive strength and resistance to shear failure. With increasing pre-moisture content, as shown in Fig 3.8 (b), the green compressive strength gradually decreased when the plaster content is varied from 33 to 43 percent, but gradually increased with the 53% plaster case. It is difficult to correlate these results with the crystal structures observed from the SEM photomicrographs of Fig 3.4 but, the needle like gypsum crystal growth is more predominant at lower pre-moisture levels; with 33% plaster sand mixture. With increasing plaster levels, the green compressive strength gradually decreased and either stabilised at lower values or slightly increased. Essentially, the amount of binder liquid supplied to the powder substrate is the same irrespective of the composition of the powder. Considering the general trend, it would appear that the pre-moisture and the additional moisture supplied can only hydrate a certain amount of plaster [93, 102]. When excessive plaster is used, there will be unbound loose fine powder phase, resulting in relatively weak powder consolidation.

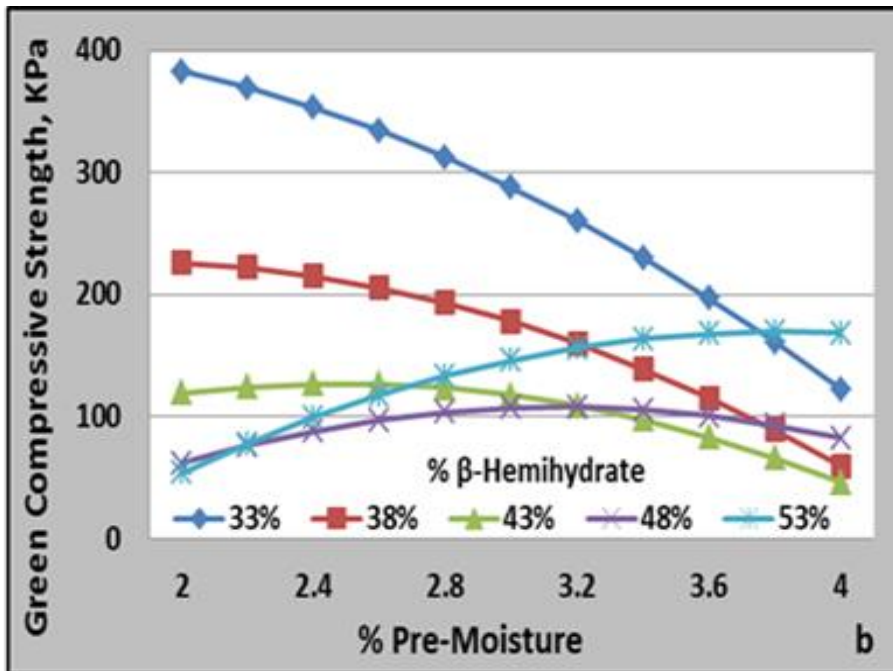
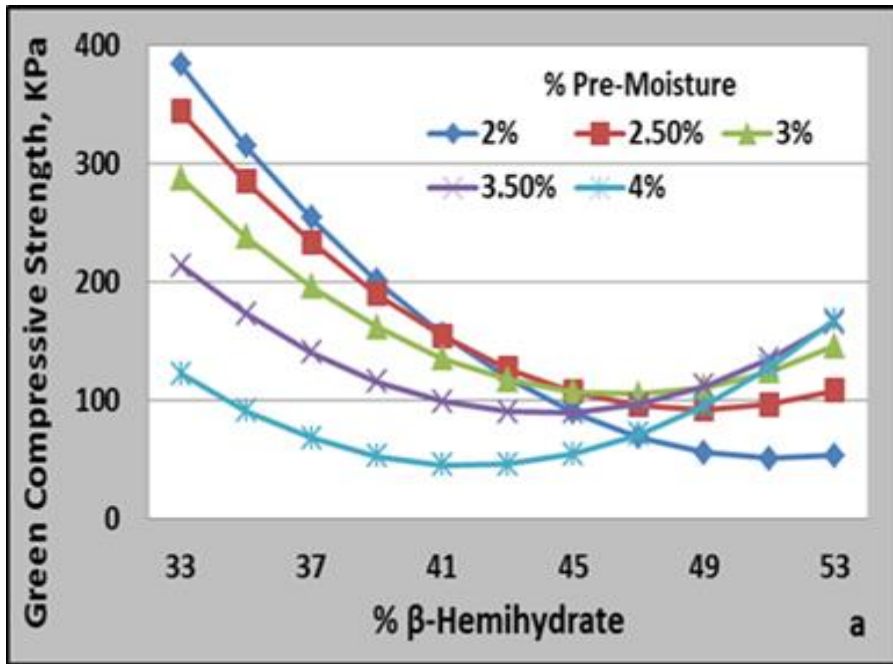


Fig 3.8 Green compressive strength vs (a) percent  $\beta$ -Hemihydrate and (b) percent pre-moisture

Further, the baked sample attributes are governed by the dehydration resulting from heating. ANOVA based on the compressive strength responses of baked samples established no improvement in the adjusted R-squared values of the model based on the factors significant at 85% confidence level. Consequently, the full model with all the factors, the square and first order interactions is considered as presented in Eq. 3.9

$$Y_{BCS} = 664.9815 - 23.8412X_1 + 171.7934X_2 - 1.1041X_3 + 30.7588X_4 + 0.0462X_1^2 - 56.6986X_2^2 + 0.0007X_3^2 + 0.2535X_4^2 + 3.3868X_1X_2 + 0.0186X_1X_3 - 0.3763X_1X_4 - 0.0239X_2X_3 + 1.8886X_2X_4 - 0.0576X_3X_4 \dots \dots \dots (3.9)$$

where,  $Y_{BCS}$  is baked compressive strength.

The variations in compressive strengths of baked specimens calculated based on Eq. 3.9 are plotted against varying critical parameters and presented in Fig 3.9. At any moisture level and a given baking temperature, the baked compressive strength decreased with increasing plaster content as evident from Fig 3.9(a-i). On the other hand, with increasing moisture content, the compressive strength decreased substantially with all baking temperature and plaster content conditions. Increasing baking temperature also consistently resulted in a loss of the mould compressive strength. Based on the dehydration theory, as the samples are heated, part of the moisture is driven off first, converting gypsum crystals into hemihydrate form. With further heating, and beyond 300 - 350°C, the remaining moisture is also driven off; leaving behind anhydrite crystals [81, 95] and consequently, the strength reduces.

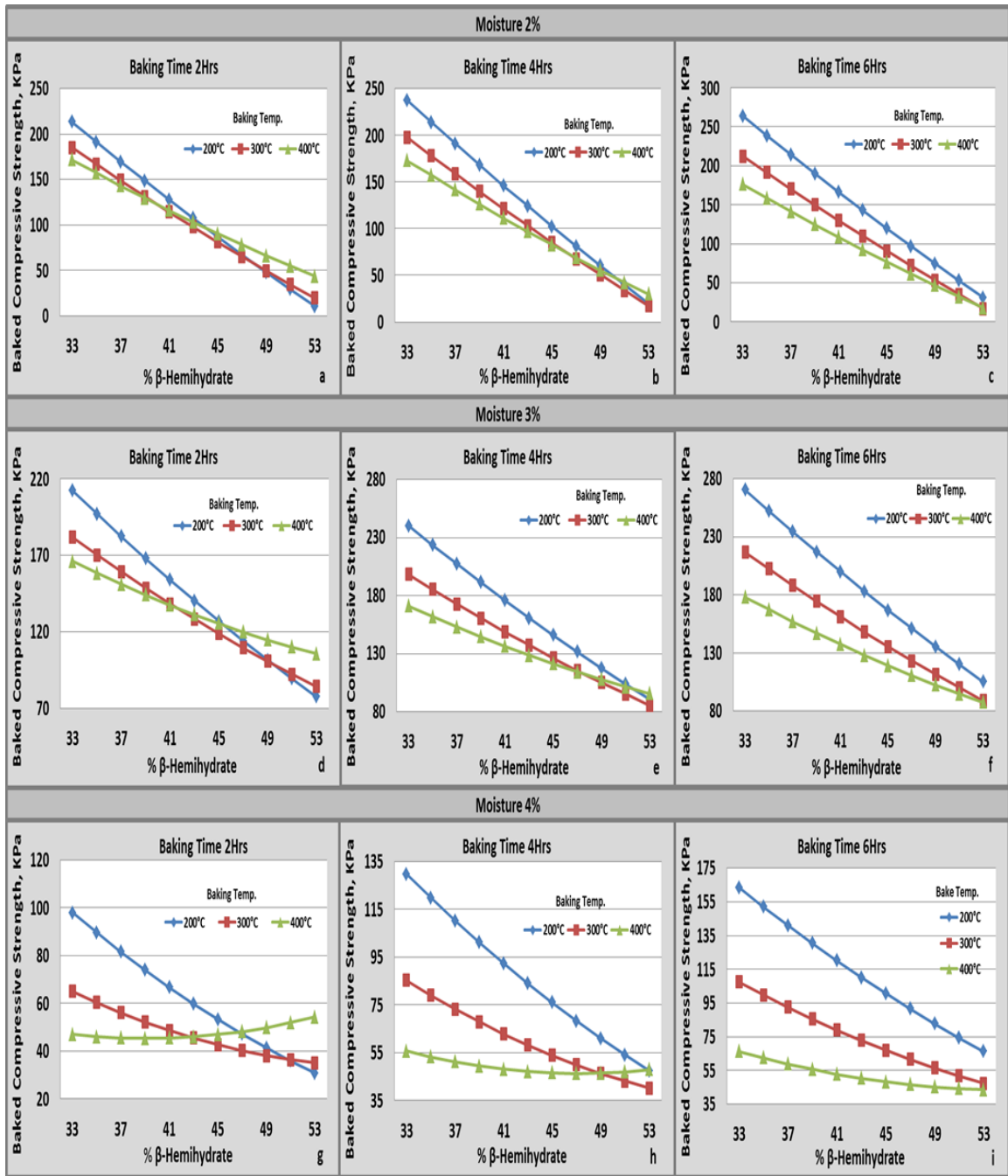


**Figure 3.9** Variation in compressive strengths of baked samples with varying (a-c) 2% pre-moisture (d-f) 3% pre-moisture, and (g-i) 4% pre-moisture keeping other variables are fixed at same levels

The effect is more pronounced at lower plaster levels, perhaps also due to the fact that the gypsum crystallisation is limited, and results in loose and dry binder particles weakly holding the sand particle structure together, and eventually giving very poor mechanical strength further to baking. Comparatively, the overall green compressive strength values are higher than the compressive strengths obtained after baking. Structurally, hemihydrate and anhydrate are weaker than di-hydrate, and based on experimental results, Yu *et al.* [103] also reported about 50% reduction in both compressive and flexural strengths resulting from baking to around 220°C.

### **3.7 Summary of pre-moisturised plaster system used for 3D printing**

Pre-moisturisation of  $\beta$ -hemihydrate is proved to be effective in accelerating the hydration mechanism when used in 3D printing. Photomicrographic evidence suggests varying levels of crystal growth with varying quantities of pre-moisture and plaster. Semi-empirical relationships developed based on statistical design of experiments allowed evaluation of the mechanics of bonding with varying levels of critical material factors. The volume errors in green state varied from +6% to -6%, with varying plaster contents, as a result of the differential contraction and expansion effects of initial setting and subsequent gypsum nucleation and growth respectively. All samples showed 0 to 10% isotropic volume expansion after baking. Shear failure is noted to be the predominant failure mechanism of compression test samples. The green compressive strength gradually decreased or increased depending on the plaster content while there is a more complex

variation in the baked compressive strength. Overall, the green compressive strengths are higher compared to the baked samples.

## Chapter 4

### Sodium silicate treated plaster – clay material system

#### 4.1 Clay and sodium silicate treatments in sand casting

In traditional green sand moulds bentonite clays are used as binders for both ferrous and non-ferrous casting applications. When a small amount of water is added to the clay, the hydration reaction takes place resulting in an electrolytic bonding and associated plasticity and green strength for the clay-sand composites. Special additives are often used to alter the nature and the rate of the hydration reaction depending on the casting materials and the size of the mould. Bentonite clays are capable of withstanding the pressures and retain the bonding strength when the molten metal is introduced into the cured moulds. While there may be some slight variations in the permeability, but the surface quality of castings improves due to the finer clay particles within the mould material. There is hardly any reported literature on the application of traditional foundry clays within a 3D printed mould material system.

In traditional foundry practice, 5-10% clay is often used to develop the bonding forces around the silica sand particles. Water is added in sufficient quantities and the whole aggregate is thoroughly mixed or stirred allowing for the water molecules uniformly attaching to the clay particles and develop the electrolytic forces. In a 3D printing context, the clay-sand composite is required to be in a fully

dry and powder form within the powder bed, until the time the aqueous binder is injected. As already experienced with the plaster based binding mechanisms presented in Chapter 3, the critical issue is the time. The rate of reaction should be high enough to initiate the bonding reaction and substantiate the consolidation of a layer at least partly, by the time a few layers are built upon one another. Further, the mere sweeping and spreading of the powder together with the jetting of small quantities of the binder should be sufficient in developing the electrolytic bonding forces.

Apart from developing the green strength, the moulds must also gain sufficient dry strength, so that the mould wear and pressure failures under the action of the molten metal are avoided. If the clay bonding generates sufficient green strength, the next stage is to evaluate the possible mechanisms of achieving the baked strength. In traditional foundry practices, sodium silicate is often employed to achieve additional bonding strengths for the moulding sands and may also be employed in the 3D printed cases. All these aspects are experimentally investigated and reported in this chapter. First, the clay bonding mechanisms are reviewed from the literature, before identifying the experimental material systems and plans.

## 4.2 Clay hydration and dehydration mechanisms

When Kaolinite is treated with sufficient water, unsaturated points on the crystals adsorb ions or molecules of the suspended medium. The adsorbed water may be planar water, the hygroscopic moisture mechanically held in the interstitial spaces or the water molecules attached to the particles on the edges due to free valencies [104]. Depending on the amount of water added, the clay-water composites may exhibit different types of rheological behaviours. Due to hydration, the viscosity of dilute clay slips is usually quite high as compared to the volume of the clay particles used. The adsorbed water was reported to be subdivided into planar and broken bond water forms that will be lost at 150°C and 400°C respectively upon further heating and baking.

As water is added to the clay, it will displace the air between the clay particles and increases the inter-particle cohesion to the maximum when the plastic limit is reached. The resulting plate-like morphologies of the clay mineral particles sliding one over the other, as water acts as a lubricant gives rise to the plasticity of clays. As the water content is increased, at a certain stage, called the liquid limit, the clay begins to transform from a paste to a slurry form. The difference between the two limits expressed as the plasticity index is influenced by both clay- and process-related factors [105].

The nature and extent of the adhesion mechanisms in clay-water composites are usually complex, and there may also be changes as different types and grades of

clays are employed. Luckham *et al.* [106] recently reviewed all the existing literature and presented an outline of the colloidal and rheological properties of clay suspensions. Electrical double layers of both positive and negatively charged ions are formed on the surfaces of clay particles suspended in a medium. Counter ions are attracted towards the surface due to the unbalanced charges on the surfaces of particles. The counter ions also have a tendency to go into the relatively less dense parts of the surrounding solution. The result is an excessive concentration of counter ions near the surface of the clay particle. Due to electrostatic repulsive forces, there will also be a deficiency of the same charges. When the concentration of the electrolyte increases, the diffuse double layer gets compressed. At the edges of the clay crystals, however, as mentioned above, the double layer is formed by ions attached to the broken bonds of the tetrahedral silica or octahedral alumina sheets, and different studies indicated that the edges are positively charged.

Based on the DLVO theory [107, 108], the interaction between clay particles suspended in a medium depend on the combination of inter particle repulsive energy and the Van der Waals attractive energy. When two clay particles approach each other due to Brownian motion, the ions are repositioned in the diffuse double layers and the work done to bring them to a given distance apart is the repulsive energy. The Van der Waals forces constitute of three components; the dipole-dipole interaction, induced dipole-dipole interaction and interactions between nonpolar molecules. The total interaction energy is the sum of the repulsive and attraction potentials and was found to be maximum when the

particles are at a specific distance. If this maximum energy barrier is overcome, the particles can come together. Also, an increase in the electrolyte concentration or the temperature was found to reduce this energy level and allow the particles to agglomerate. The coagulation of particles varies with the concentration of the electrolyte and at very high concentrations; a continuous gel structure is formed.

When it comes to the dehydration mechanisms, the plasticity was noted to increase initially when heated up to 60°C. Further heating between 100°C and 110°C was found to remove the planar water, resulting in a decrease in the plasticity. Heating beyond 110°C and up to 250°C was found to have no effect probably due to the retention of the broken-bond water, while the plasticity steadily reduces beyond this. After heating between 300°C and 400°C, the clay becomes fully dry, and like fire clay, as was observed based on the similarities in the value of the modified Pfefferkorn number (mP) [109].

However, there are different opinions on the dehydration of clays, as [110] notes that the chemically bound water is removed only after heating to 500-600°C. While heating to 500°C was reported to decrease the plasticity number to a range from 1 to 3, upon further heating the plastic properties were noted to be completely lost at 600°C. Clays dehydrated at 450°C were also noted to exhibit a reduction in the shaping moisture content as well as shrinkage problems. Also observed that most clays are completely loose the combined water at around 430°C, other than bentonites, which dry at 530°C [111]. The decomposition was noted to proceed

through nucleation and when the growth is to the extent that individual fronts impinge on one another, the reaction ceases.

Evidently, the bonding mechanism within clay-water composites is electrolytic in nature. The Van der Waals forces are relatively weak and may require substantial processing such as thorough mixing or stirring of the ingredients and sufficiently long reaction times. Both are quite difficult to be provided within the 3D printing environment. As a result, the initial experimental trials with varying amounts of different types of clays were not successful as reported in subsequent sections. The plaster based bonding reported in Chapter 3 is eventually combined with the clay system, to further substantiate the green strength to the necessary extent as will be discussed later in the section on initial experimental methods and material systems. Further, the baked strengths of the resulting clay-sand composites also proved to be insufficient and a further strengthening mechanism such as the sodium silicate treatment as reviewed next became necessary.

### **4.3 Sodium silicate as a foundry sand binder**

Apart from bentonite clays, other forms such as fire, kaolin, and ball clays are also commonly used as binding agents in sand-clay composite materials used as the moulding materials [112]. Na-bentonites have higher fusion temperatures and dry strengths while Ca-bentonites allow for the better release of the castings from the mould. It is often customary that different forms of clays are used targeting different casting goals. Different treatments of clays are also in use to achieve

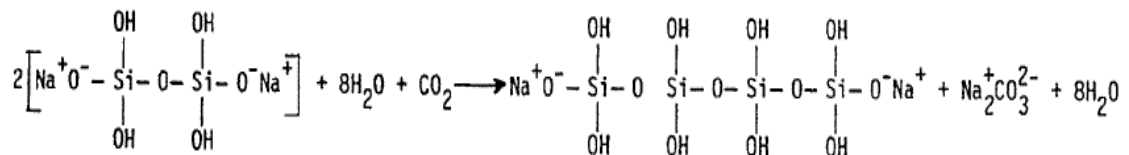
different end results. Calcium and magnesium bentonites when treated with sodium carbonate were noted to convert into sodium and calcium forms, enhancing the binding behaviour. While comparing the traditional resin bonding methods with the green approach using sodium silicate, [113] confirmed from both TGA and DMA tests that the sodium silicate method gives better results.

Sylwia *et al.* [118] reported that the water stored in the montmorillonite leads to swelling, allowing bentonites to attain the colloidal and mechanical properties. Use of sodium carbonate was found to produce calcium carbonate with a significant increase in the water absorption and an improvement of mechanical properties. XRD and FTIR analyses, together with the copper complex adsorption method Cu (II)-TET allowed establishing the enhancements possible with the sodium carbonate treatment.

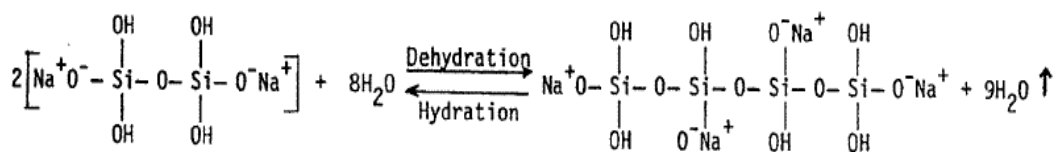
Sodium silicate has been in use as a foundry sand binder since the early fifties and is often cured by the use of CO<sub>2</sub> gas or heating, apart from using a few other catalysts including ferrosilicon, di-calcium silicate and cements [115]. The ability of sodium silicate to form bonds in foundry sands is associated with the formation of a precipitate gel, sodium silicate, and silicic acids. Yaw reviewed the manufacture, physical and chemical properties, the colloidal nature, and the mechanisms of condensation polymerisation and other aspects of sodium silicate [115]. Sodium silicate solutions consist of water, the positive sodium ions, and the negative silicate ions and the ionic micelles of colloidal silica.

In sodium silicate solutions, the unbalanced surface charges attract water molecules towards the surface of the solid substance formed reducing the general mobility of the water phase. In addition, the solid phase undergoes the cross-linking of the constituent phases, leading to overall stiffening and the formation of a gel structure, characterised by a cohesive coexistence of numerous colloidal particles. The  $\text{SiO}_2$  molecules in sodium silicate have a tendency to polymerise into chains and networks due to the nature of the tetrahedral unit  $\text{SiO}_4$ . Giant molecules are likely to form as the tetrahedral groups polymerise sharing an oxygen atom between two units.

The colloidal silicic acid gel is formed by the condensation polymerisation reaction of the silicic acid into poly-silicic acid structure. Two monomers combine to form a dimer, the di-silicic acid, which then joins with another monomer to form the tri-silicic acid. As a result, the silicate acid, its ions, poly-silicic acid and the gel are in equilibrium in a sodium meta-silicate solution. The poly-silicic acid turns into a gel, and hardens by syneresis, through curing by  $\text{CO}_2$  treatment or heating. The amount of water present in the solution has a bearing on the rate of gelation and the final strength of the mould. The chemical reactions representing the  $\text{CO}_2$  curing and the hot-air curing are reproduced from the paper by Yaw et al [115] as follows. It was noted that the Si-O-Si bonds are far stronger than the  $\text{Na}_2\text{CO}_3$  or the hydrogel bonds formed during the  $\text{CO}_2$  process, and hence the bonding by the hydration method gives better strength results.



**Sodium silicate reacting with CO<sub>2</sub> gas [12]**



**Dehydration of sodium silicate solution [12]**

Yaw *et al.* [115] also proposed a mechanism for the bonding within a moulding sand mixture. The sodium silicate gel adheres to the surfaces of the sand grains through physical adsorption and formation of multiple Van der Waals bonds. As the sodium silicate is dispersed in the sand mixture, the surface tension forces and the viscosity of sodium silicate lead to the formation of the inter particle neck regions. Subsequently, the CO<sub>2</sub> treatment or heating of the moulds will result in the formation of the Si-O-Si linkages, water, sodium carbonate and sodium hydro carbonate compounds, giving rise to the hardening and strengthening of the moulds.

McDonald *et al.* [116] observed that sodium silicates possess high surface tension and the penetration and adhesive qualities are possible to be improved by adding suitable surfactants and wetting agents. More interestingly, the total water loss of sodium silicate was reported to be not affected by the presence of clay, while it allows the formation of a tougher and a coherent film, free of cracks. While assessing the strengths of moulding sands prepared by different methods, Major-Gabrys *et al.* [117] micro-wave hardened moulding sands with water glass and glassex additives to perform better.

#### **4.4 Mechanisms of clay bonding in 3D printing**

##### ***4.4.1 Initial printing trials with bentonite clays***

Based on the literature reviewed above, in the clay-sand composites, the component that controls the binding attributes is montmorillonite, which swells with the addition of water, allowing colloidal and mechanical properties to develop in moulding sands [118]. The positive ions of the montmorillonite diffuse ionic layers, resulting in electrostatic repulsions, but when heated, the clay particles agglomerate due to the reduction in the potential energy [119]. A gel structure gradually sets in, as particles assume minimum energy configurations effective from the Brownian motion. While bentonite clays are very popular as binding media in traditional sand casting, there is no readily available literature on their applications in 3D printing. Considering the wide-spread usage, and the time-tested attributes, it is interesting to investigate the possible use of the traditional bentonite and sand mixtures to be processed by 3D printing. The experimental

research reported in this chapter attempts this, evaluating the mechanisms and mechanics of bonding with materials of varying compositions, while also allowing the superior thermal resistance and strength of bentonite at elevated temperatures [120] to be integrated into the relatively simple mould material systems for 3D printing.

Varying amounts of bentonite clays are mixed with silica sand particles, making sand–clay composites of different compositions. The dry powder composites are then loaded on to the printing system and simple rectangular blocks are attempted to be printed. However, the sand and bentonite mixture did not work together to develop the necessary green strengths. All the trials failed as the mechanism of clay bonding could not be triggered within the 3D printing method of jetting the aqueous binder on the finely spread powder bed. After trying a few different combinations and possible alterations, the plaster bonding mechanism as presented in Chapter 3 was found to work well with the clay-sand composites too. At the end of the initial trials, a plaster-clay-sand composite could be identified with sufficient green strengths developed during printing. Further experimental work is based on this combination of material ingredients.

#### ***4.4.2 The clay-plaster combination and the mechanism of bonding in the green state***

As stated above, a certain amount of plaster became essential to be used in the powder mixture, in order to be able to achieve the necessary bonding and green strength while implementing the 3D printing scheme with clay-sand composites. The mechanism of bonding in this material system is primarily dependent on the initiation and growth of gypsum crystals from the plaster component of the powder mixture [121]. Both  $\alpha$  and  $\beta$ -forms of hemihydrate possess properties suitable for this application. However, considering the mechanical strength,  $\alpha$ -hemihydrate is selected for the purpose [86] as against the  $\beta$ -version used in the previous chapter.

Different compositions of sand, bentonite and  $\alpha$ -hemihydrate are then attempted on a 3D printing system, but the plaster hydration rate posed some problems. Accelerators of gypsum reaction are essential and as already stated in Chapter 3, either pre-moisturisation [122] or addition of a certain quantity of di-hydrate [121] are possible solutions. In the current research, small quantities of terra alba, a commercial form of di-hydrate is used as the seeding material. Preliminary trials employing different amounts of terra alba resulted in promising results in terms of green strengths achieved in the printed specimens. Table 4.1 presents the basic ingredients of the mould material system used as the basis of the experimental work that follows. The compositions are identified based on the a priori data

generated from a number of repeated trials printing small rectangular specimens subjected to green strength evaluations.

The mechanisms of bonding achieved with varying compositions are first evaluated in order to be able to assess the effectiveness of the materials composed for 3D printing. Photomicrographs of 3D printed green samples of varying compositions are presented in Fig 4.1 with terra alba and bentonite remaining at similar levels, the gypsum crystallisation generally increased with increasing  $\alpha$ -hemihydrate from 25% to 75%. This is due to availability of more plaster for a given amount of water added to the system [92]. While the crystals are shorter and plastered around by bentonite at lower levels of hemihydrate, sharp needle-like crystals grew, forming intricate networks as the hemihydrate content increased, as may be observed comparing photomicrographs of the first and the last rows of Fig 4.1 in pairs vertically. The role of terra alba is to promote formation of gypsum crystals [123]. This is clearly evident comparing the photomicrographs of Fig 4.1 (i) (a) & (d), (ii) (b) & (d), and (iii) (a) & (d); each pair representing the effects of increasing terra alba content, while the other contents remain at similar levels.

**Table 4.1 The mould material system**

S. No	Material	Chemical Formula	Supplier	Weight	% Level
1	Silica Sand (AFS fines No. 60 – 65)	SiO <sub>2</sub>	Industrial Sands Ltd, NZ.	100%	100
2	USG Hydrocal FGR95	CaSO <sub>4</sub> . 0.5H <sub>2</sub> O	United States Gypsum Company.	50% of Sand	25-75
3	Terra Alba	CaSO <sub>4</sub> . 2H <sub>2</sub> O	Winstone Gypsum, NZ.	50% of $\alpha$ -HH	12.5 - 37.5
4	Calcium Bentonite	Al <sub>2</sub> O <sub>3</sub> .4(SiO <sub>2</sub> ).H <sub>2</sub> O	Industrial Minerals (NZ) Ltd.	50% of Terra Alba	6.25-18.75

Cody *et al.* [124] proposed that gelling clays such as montmorillonite and Wyoming bentonite allow for large crystals of gypsum to grow. It was identified that bentonite resembles natural sediments in terms of promoting gypsum crystal growth. While it is to be accepted that the presence of bentonite allows gypsum crystal growth, it does not necessarily mean that the higher the bentonite, the higher the growth of gypsum crystals as other ingredients such as hemihydrate are likely to interact. For example, it is clearly evident that the gypsum crystal growth considerably increased from Fig 4.1(i.b) to (i.c) as the bentonite is increased from 6.25% to 18.75% at the same level of terra alba and 25% of hemihydrate. This effect is less pronounced in Fig 4.1 (ii.a) and (ii.b) at 50% hemihydrate, while there is hardly any effect of increasing bentonite on the samples obtained with 25% terra alba and 75% hemihydrate. The excess bentonite is only able to disperse inter-granularly, cushioning the gypsum crystals. It is oversimplifying to say that the higher crystal growth results in higher strength. Bentonite also plays a role through ionisation and forces of attraction and repulsion between molecular components. The dispersion of bentonite together with the size, shape and distribution of the gypsum crystals will dictate the final mechanism of the green strength achieved. The DLVO theory reviewed earlier [108] identifies a certain energy barrier to be overcome in order for the clay particles to be attached together. As also already pointed out, an increase either in the electrolyte concentration or the temperature or both were found to reduce this energy level and allow the particles to stick together. In the current case, the amount of plaster and the extent of the hydration depending on the moisture content could result in both the increased concentration of the binding fluid as well as the temperature, due to ionisation of

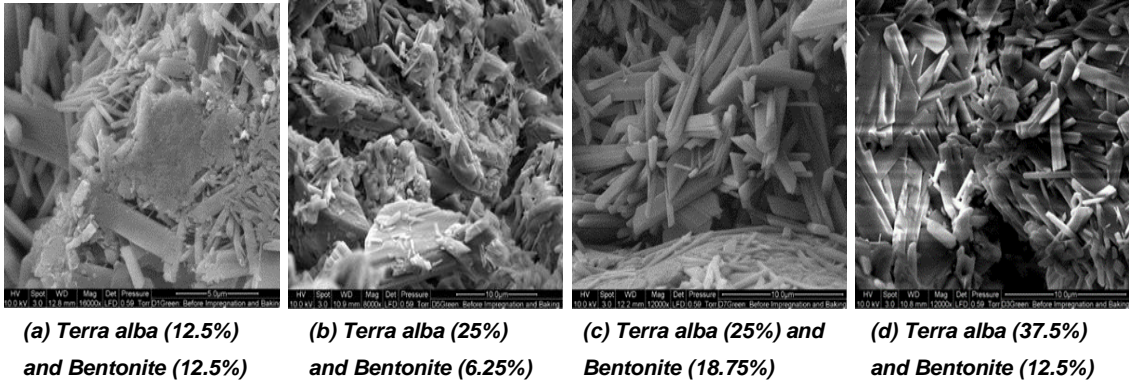
plaster and clay particles [115] and the exothermic nature of the plaster hydration process [86] respectively.

However, two clay particles do not need to come intimately close together in order to develop cohesive forces resulting in the green strength. In the current situation, there are gypsum crystals, either fully or partly formed, loose plaster particles, ionised clay particles and the viscous binding fluid gradually diminishing within the inter-particle spaces and the relatively larger sand particles embedded in this matrix. The actual mechanism of bonding in the printed samples gets quite involved and perhaps sensitively varying with different conditions.

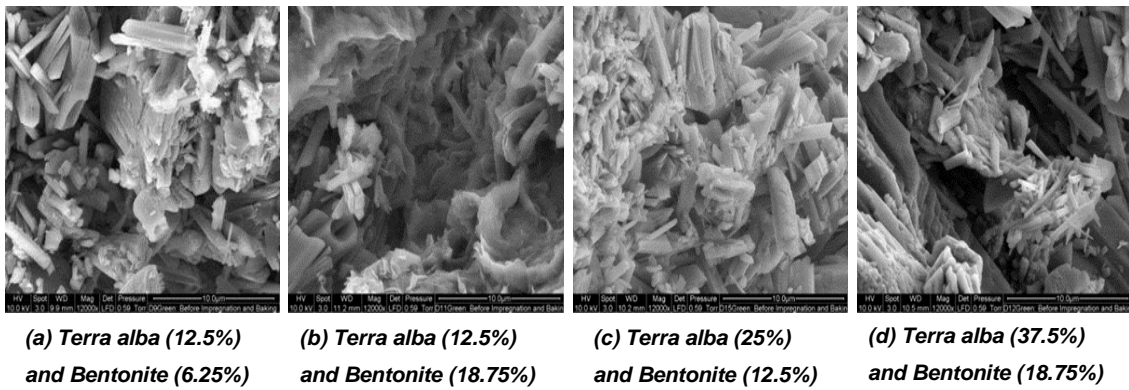
#### ***4.4.3 Post baking concerns and the sodium silicate treatment***

It was noted that the printed specimens when directly heated become quite fragile and friable and do not attain any solid strength or shape. This is due to the evaporation of the water and subsequent loss of the electrolytic forces developed by the bentonite clays. The dehydration of gypsum crystals gives rise to varying levels of strength depending on the temperature to which the moulds are heated, as noted in [103]. However the easily friable clay content probably results in relatively weaker material sections, resulting in an overall loss of dry strength.

**(i)  $\alpha$ -Hemihydrate (25%)**



**(ii)  $\alpha$ -Hemihydrate (50%)**



**(iii)  $\alpha$ -Hemihydrate (75%)**

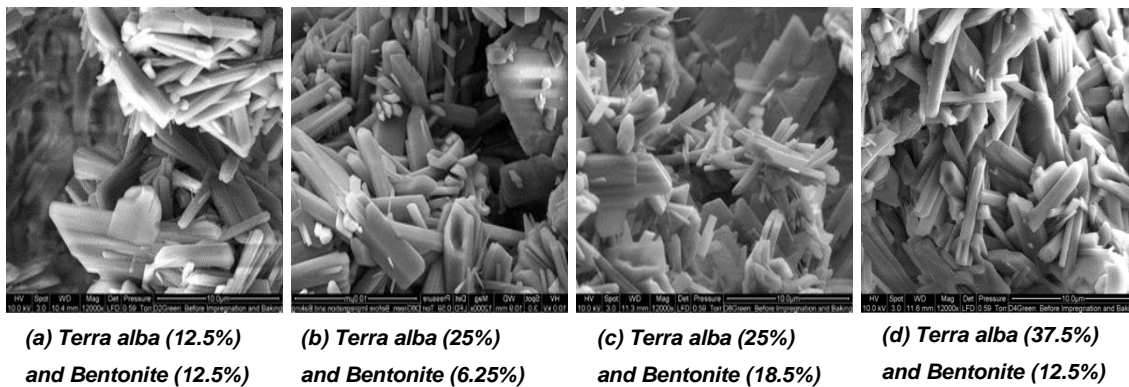


**Fig. 4.1. SEM Photomicrographs of green samples 3D printed with varying compositions**

To overcome this problem, the sodium silicate treatment as used in the traditional foundry practices is considered next. As reviewed above, sodium silicate acts as a foundry binder through the ability to form bonds by a precipitated gel. The semi-solid substances bond sand grains into continuous 3D arrays. As explained by Yaw [115], sodium meta-silicate solutions are in equilibrium with silicate acid and its ions, polysilicic acid and the gel. The silicic acid under suitable pH conditions form polysilicic acid. The polysilicic acid in turn transforms into a gel, which will eventually harden due to shortening of the Si-O-Si distances and build-up of tension within each chain by a suitable mechanism. Based on the dispersion and mechanical compacting, sodium silicate covering individual grains form bonds between adjacent sand grains due to necking, resulting from surface tension forces [115].

However, in the current case, this mechanism resulting from the use of sodium silicate soaking will be more complex due to the fact that there are gypsum crystals already grown around sand grains from the moisture added from the print head. The sodium silicate solution does not affect the gypsum crystals much, other than the excessive water probably promoting further growth or even stabilisation at some stage. The mechanical compaction factor is absent, but the soaking of the printed sand specimens for sufficient time allows wide dispersion of the binder within the matrix of sand particles stuck together by means of gypsum crystals and bentonite spread in between, cushioning other ingredients. Pure water could have resulted in a loss of the printed structure as excess moisture takes inter-lamellar spaces, softening the gypsum [86]. Considering that the sodium silicate is already

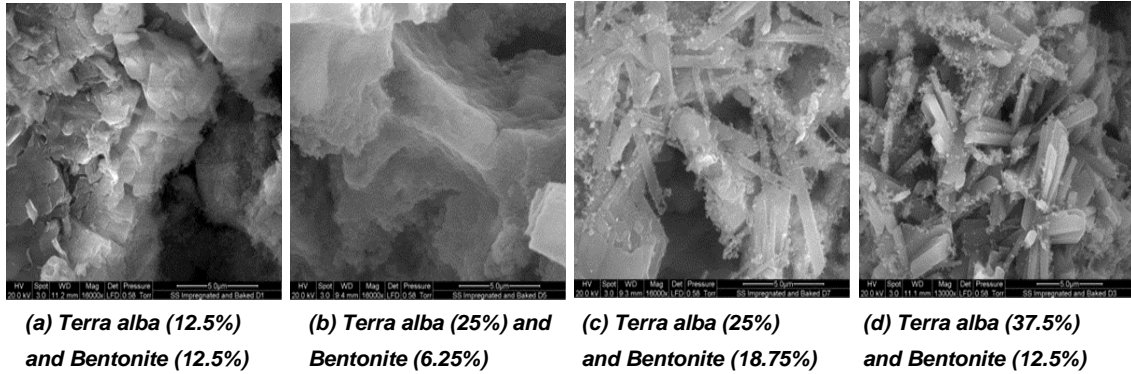
in a gel like structure, the H<sub>2</sub>O component can either promote further gypsum crystal growth or just leave it as it is.

Evidently, all the photomicrographs of Fig 4.2 presenting the microstructures of 3D printed samples soaked in sodium silicate solution after baking show the original gypsum crystals and the sand grain structure coated in a white layer of the glassy solidified gel. Again referring back to the work of Yaw [115], sodium silicate does not act as a structure filling mortar, but stretches at the contact points of adjacent sand grains, bridging them through necks formed due to surface tension forces and viscosity. Inter-granular bonding through necking and subsequent solidification is clear in some cases, such as Fig 4.2 (i.b). In cases where there is already a fine needle-like growth of gypsum crystals, the sodium silicate helped by coating the crystals first and then providing an overall strength through the formation of a network of inter-granular bonds.

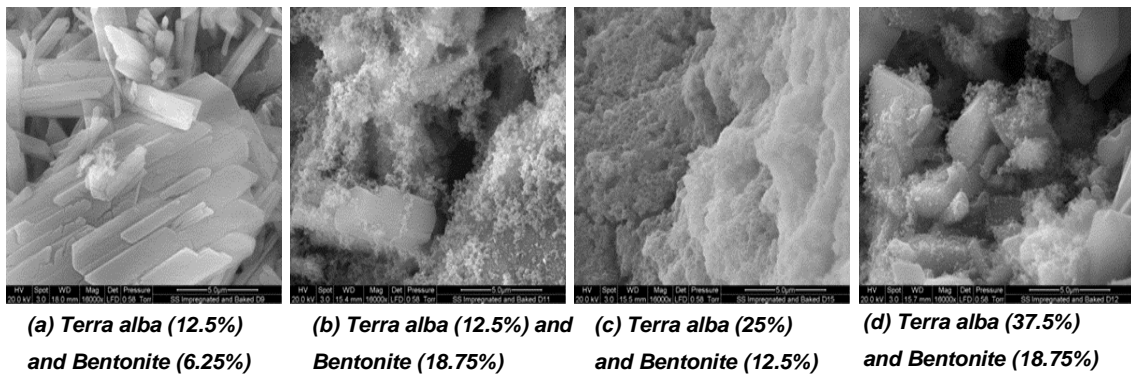
When the original structure is made up of short and compressed gypsum crystals, the final resulting structure is predominantly constituted of a wide network of continuously distributed layer of solidified sodium silicate gel as observed in Fig 4.2 (ii.b and ii.c). Also, the plate-like growth of the gypsum remained as coated plates, bonded inter-granularly, as may be observed in Fig 4.2(ii.a), (iii.a), and (iii.c). Both needle and plate-like crystals are connected through intricate networks of vitrified sodium silicate bonds, compared to the wide-spread dispersion of the glassy gel matrix seen in Fig 4.2 (ii.b and ii.c). Presumably, the structures with

wider network of solidified sodium silicate bonds could have achieved higher mechanical strengths compared to the other forms, which will be verified later.

**(i)  $\alpha$ -Hemihydrate (25%)**



**(ii)  $\alpha$ -Hemihydrate (50%)**



**(iii)  $\alpha$ -Hemihydrate (75%)**

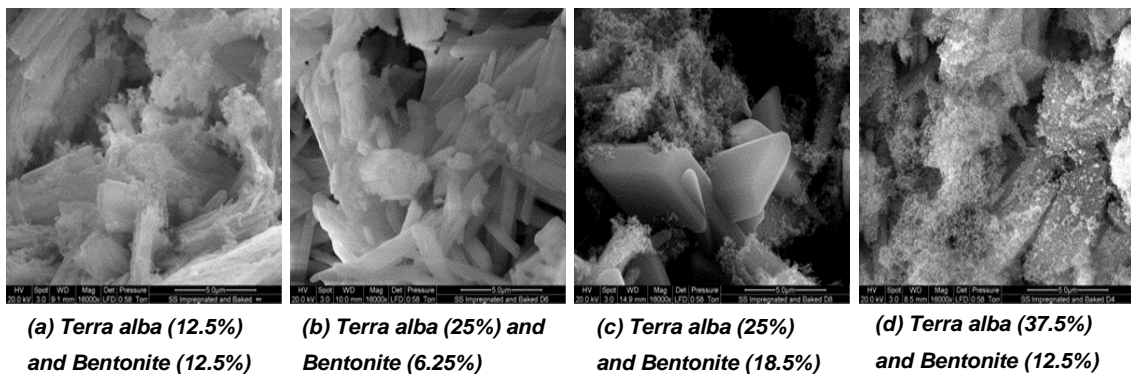


**Fig. 4.2. SEM photomicrographs 3D printed and sodium silicate soaked samples after baking**

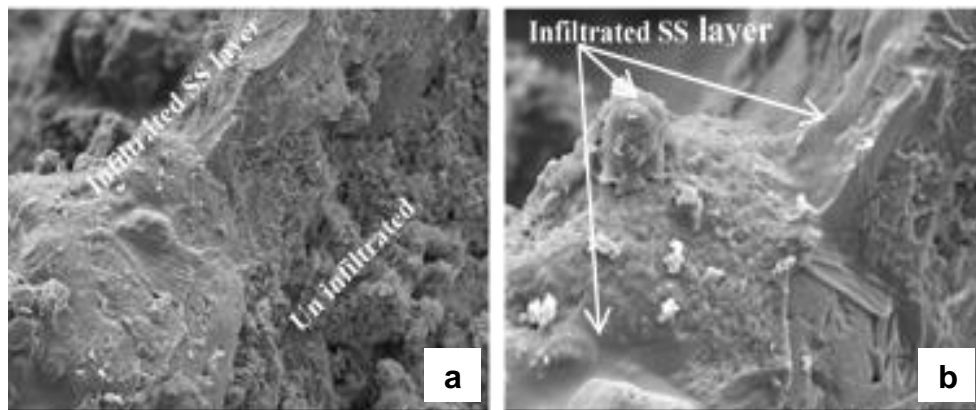
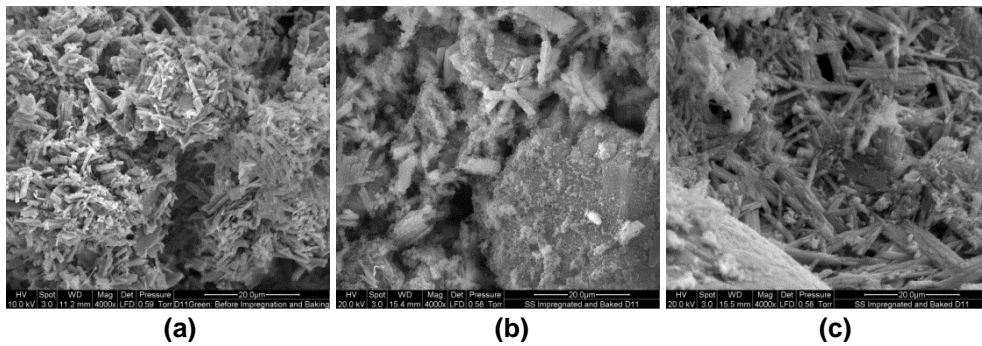


**Fig. 4.3. Variations in sodium silicate infiltration in the green state (terra alba 12.5%,  $\alpha$ -hemihydrate 50% and bentonite 6.25% )**

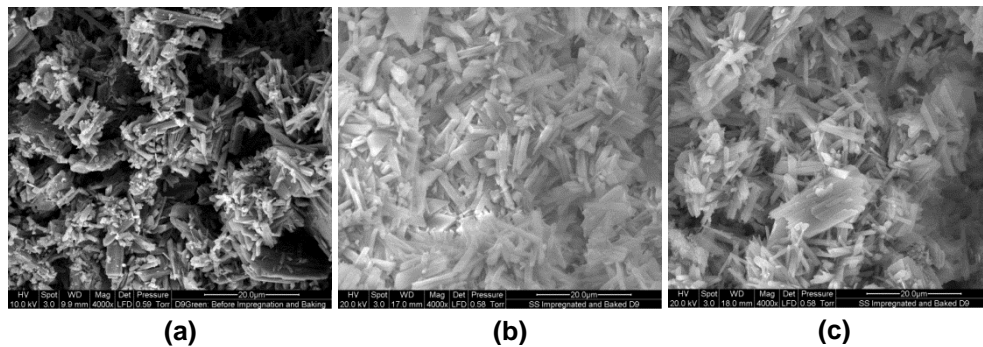
Further, there is also a variation in the level of infiltration of sodium silicate from the surface to the interior depending on other ingredients such as bentonite. The interior of the mould wall received relatively lesser sodium silicate presence as seen in Fig 4.3 (a), compared to the exterior. The surface layers are representative of fully soaked sand grains, and gypsum crystals connected by clearly distinguished neck regions of sodium silicate. Similar observations may be made from the photomicrographs of Fig 4.4, where green samples are juxtaposed against sodium silicate treated and baked samples from the interior and the surface of the mould.

It may be observed that the interior of the sample shown in Fig 4.4(ii)(a) received better dispersion of sodium silicate than the same location of the other sample in Fig 4.4(b)(ii). The reasons for this are first, the intricate network of the crystals grown in the green state of the sample in Fig 4.4(b) and then the excessive bentonite, both contributing to a greater resistance to the infiltration of sodium

silicate in the second case, resulting in relatively lesser verification in the central portions. Overall, the sodium silicate treatment and subsequent baking allowed the structural components of the mould material to be blanketed by the glassy substance resulting from the condensed siloxane bonds and the network of intergranular connections, the extent of which varies with the location. The resulting influences of these treatments on the final dimensional variations and mechanical strengths of the specimens printed need to be verified experimentally, by looking at the mechanics of bonding as discussed next.



**(i) Terra alba 12.5%,  $\alpha$ -hemihydrate 50% and bentonite 6.25%**



**(ii) Terra alba 12.5%,  $\alpha$ -hemihydrate 50% and bentonite 18.75%**

**Fig 4.4 Mechanism of bonding at various states green (a), after impregnation and baked and at the mould centre (b), and at the surface (c) with varying bentonite, but terra alba and  $\alpha$ -hemihydrate fixed at 12.5 % and 50% respectively**

#### 4.5 Mechanics of bonding 3D printed plaster-clay-sand composites together with the sodium silicate treatment

Considering the total number of factors and their possible interactions, statistical design of experiments became necessary again, to capture the overall trends economically. In order to establish the mechanics of bonding in 3D printed mould materials based on  $\alpha$ -hemihydrate and ionised clay as the preliminary sources of bonding followed by a sodium silicate treatment prior to baking, a statistical design based on the Box-Behnken approach is chosen again. This allowed three material factors;  $\alpha$ -hemihydrate, terra alba, and calcium bentonite to be considered at three levels each.

The levels of the factors are shown in Table 4. 2 and the general form of the regression models to be developed is as given in Eq. 4.1 to evaluate the variation of specific responses; volume error, compressive and flexural strengths both in green and baked states. Three factors varied at three levels each as per the Box-Behnken design resulted in 15 trials in total, and the key responses measured in terms of volume errors, flexural and compressive strengths in both green and baked states are shown in Table 4.3. A detailed discussion of these results follows next.

**Table 4.2 Factors and their levels**

<b>Variables</b>	<b>-1</b>	<b>0</b>	<b>+1</b>
<b><math>\alpha</math>-Hemihydrate</b>	25%	50%	75%
<b>Terra Alba</b>	12.5%	25%	37.5%
<b>Calcium Bentonite</b>	6.25%	12.5%	18.75%

**Table 4.3 Experimental factors and critical responses with sodium silicate treated plaster-clay material system**

Run	% $\alpha$ – Hemi Hydrate	% Terra Alba	% Calcium Bentonite	Volume Error (%)		Flexural Strength (MPa)		Compressive Strength (MPa)		
				Green	Impregnated & Baked	Green	Impregnated & Baked	Green	Not Impregnated but Baked	Impregnated & Baked
1	25	12.5	12.5	0.60	1.21	0.39	0.36	0.25	0.08	0.33
2	75	12.5	12.5	4.87	3.40	0.76	1.02	0.3	0.11	1.23
3	25	37.5	12.5	1.60	2.80	0.15	0.37	0.05	0.02	0.34
4	75	37.5	12.5	6.11	8.20	0.70	0.60	0.37	0.13	0.77
5	25	25	6.25	5.07	6.74	0.37	0.66	0.24	0.10	0.48
6	75	25	6.25	7.57	10.33	0.80	0.55	0.62	0.31	1.05
7	25	25	18.75	2.00	3.00	0.27	0.29	0.19	0.08	0.17
8	75	25	18.75	3.81	5.69	0.50	1.39	0.28	0.12	0.6
9	50	12.5	6.25	5.69	7.37	0.69	1.36	0.49	0.19	1.3
10	50	37.5	6.25	3.64	9.05	0.47	1.22	0.4	0.15	0.46
11	50	12.5	18.75	4.65	6.12	0.81	0.66	0.49	0.23	0.78
12	50	37.5	18.75	5.08	6.12	0.53	0.82	0.27	0.16	0.43
13	50	25	12.5	3.64	6.32	0.67	0.38	0.48	0.27	0.9
14	50	25	12.5	8.20	10.55	0.64	0.28	0.53	0.19	0.68
15	50	25	12.5	7.57	8.20	0.71	0.34	0.5	0.24	0.66

$$Y = \beta_0 + \beta_1X_1 + \beta_2X_2 + \beta_3X_3 + \beta_{11}X_1^2 + \beta_{22}X_2^2 + \beta_{33}X_3^2 + \beta_{12}X_1X_2 + \beta_{13}X_1X_3 + \beta_{23}X_2X_3 \dots \dots \dots (4.1)$$

#### **4.5.1 Volume errors**

Mould materials made of multi-material mixtures are likely to go through changes in dimensions due to structural variations and distribution of constituent phases. In particular, the hydration and dehydration of both plaster and clay systems are often associated with volume changes. While the infiltration by sodium silicate is likely to cause swelling, subsequent baking could balance this to some extent. It is important to establish the possible overall volume errors in order to be able to predict the ability to reproduce drawing dimensions. It is also important to understand the possible implications of post-printing treatment and baking on the final dimensional variations. The total volume errors estimated as differences between theoretical and the actual printed sample volumes before sodium silicate treatment and after baking are considered here to represent the overall dimensional aspects of the process.

The volume error values obtained measuring the dimensions of the green samples after printing and taking out of the printer as recorded in Table 4.3 allowed to estimate the coefficients of the model developed as given in Eq. 4.2, Analysis of variance validated the model at 95% confidence level and the resulting R-Square value is 66.42% establishing all variables to be significant.

$$Y_{GVE} = -6.79879 + 0.340712X_1 + 0.381456X_2 - 0.14794X_3 - 0.00266X_1^2 - 0.00968X_2^2 - 0.00494X_3^2 + 0.000196X_1X_2 - 0.0011X_1X_3 + 0.007907X_2X_3 \dots (4.2)$$

where,  $Y_{GVE}$  is Green Volume Error,  $X_1$ ,  $X_2$ , and  $X_3$  are the factors

Considering the mechanism of bonding, the mould material first absorbs water during the printing process and expands [124]. Further, the formation of gypsum crystals involves volumetric changes, depending on the extent of nucleation and growth [123]. The results presented in Fig 4.5 showing the variation of the percent volume error with varying process conditions validates this, as the volume error increased with increase in  $\alpha$ -hemihydrate, indicative of the possible increase in the nucleation and growth of the gypsum crystals. This can also be verified from the photomicrographs of Fig 4.1, where the gypsum crystal growth directly proportional to the  $\alpha$ -hemihydrate content is clearly evident.

However, beyond a certain limit, the volume error either stabilised or even reduced to some extent, considering the level of moisture available for the gypsum crystals to form. When excessive gypsum powder is available, part of the growth of the crystals is likely to be accommodated within the soft powder phase, resulting in an overall reduction in the volume change. Plausibly, the reduction in the volume error observed in all cases of Fig 4.5 with increasing bentonite could also be due to the same reason. Also, the observations noted above discussing the possible role of bentonite on the crystal growth referring to Fig 4.2 propose that the more the bentonite, the more is the possibility to accommodate the growing gypsum crystals within the confines of the packed material, and the lesser the chances of

volumetric expansions. The relatively less volumetric deviations noted with increasing bentonite in all cases of Fig 4.5 are probably in accordance with these observations.

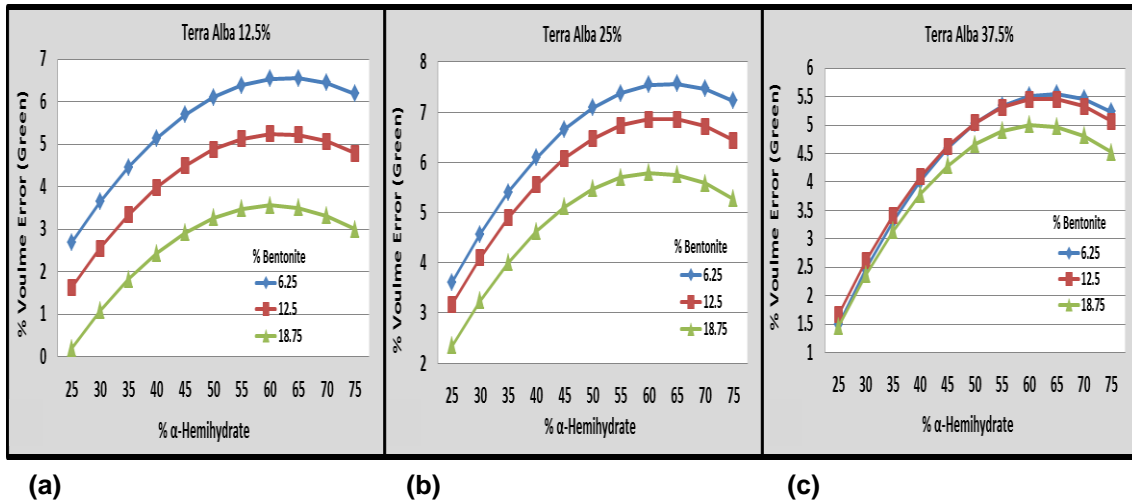


**Fig 4.5** Variation of volume error in the green state

Next, the volume errors further to sodium silicate treatment and baking are considered. The green printed samples when soaked in sodium silicate for four hours, the viscous solution tries to penetrate into the inter-granular pores, cavities and other areas through capillary action. The depth of penetration depends on the concentration of the solution as well as the porosity of the printed sample. The excess solution absorbed within the specimen leads to an overall expansion either due to further gypsum crystallisation or through capillary filling and the associated buoyant or surface tension forces. Subsequently, the baking process results in the formation of the Si-O-Si polymer chains a gradual reduction in the inter-molecular spacing [115] and contraction to some extent as the gel solidifies into a glassy brittle substance. Samples produced after sodium silicate solution treatment for 8

hours, and subsequent baking by heating at 150°C temperature for 1 hour are measured to estimate the volume errors as noted in Table 3. The empirical model developed based on this data is of the form given in Eq. 4. 3

$$Y_{IBVE} = - 8.48772 + 0.437675X_1 + 0.616116X_2 - 0.47577X_3 - 0.00414X_1^2 - 0.01193X_2^2 + 0.017231X_3^2 + 0.002565X_1X_2 - 0.00144X_1X_3 - 0.00537X_2X_3 \dots\dots\dots (4.3)$$

Where,  $Y_{IBVE}$  is volume error after sodium silicate impregnation and baking

ANOVA suggests the model to be valid at 95% confidence level and the R-Square value is 86.91% and all variables are significant. Considering the accumulation of additional material during soaking, there is a general absorption and increase in the volume compared to the post-printed green stage. All the graphs of Fig 4.6 showing variations in the percent volume errors of baked samples with varying compositions clearly show higher volume errors compared to the results from the post-printed green samples presented in Fig 4.5. However, the variations resulting from varying other factors remained almost similar to the patterns in Fig 4.5. This is natural to expect as there are relatively less changes in the constituent phases and internal structures resulting from the sodium silicate treatment or the subsequent baking.

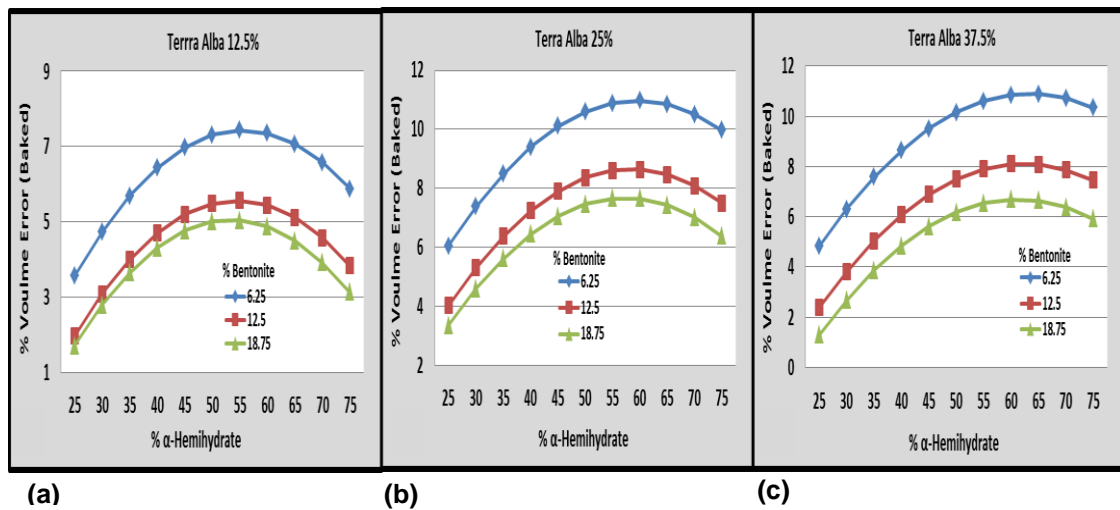


**Fig 4.6 Variation in the percent volume error further to sodium silicate soaking and baking with varying %  $\alpha$ -hemihydrate**

Another interesting observation to be made from Fig 4.6 is the effect of terra alba on the % volume error. Comparing the corresponding diagrams of Fig 4.5 and 4.6, it may be observed that the higher the terra alba, the higher is the volume error in the baked samples. Terra alba is mainly the seeding agent in the mould material and when it is more abundantly available, there is a chance of more nucleation of gypsum crystal formation at numerous places, and whether they fully grow or not, will lead to possible formation of micro cavities. When such samples are finally soaked in sodium silicate, there is a possibility of a larger solution penetrating through the well-connected networks of porous structures, leading to a better absorption and subsequent solidification, resulting in an overall expansion. Also, a closer look comparing the photomicrographs of Fig 4.2 in pairs; (i.a) with i.d) and (iii.a) with (iii.d), clearly elucidates the spectacular sodium silicate deposition and growth within the narrow spaces between relatively small crystals allowing for the

dendritic growth in the samples with higher terra alba. This is indicative of a better absorption of the silicate solution and the consequent higher volume errors.

#### **4.5.2 Flexural strength**

Both green and baked flexural strengths are evaluated as per the AFS standards using three-point bending test pieces of dimensions 70mm x 15mm x 15mm. The Hounsfield tensile testing equipment reported in Fig 2.6 of Chapter 2 is again employed for these tests. Fig 4.7 presents a typical sample under the three point bending load. All samples are loaded using a speed of 1mm per minute in both green and baked cases. The flexural strength values established based on the green samples are listed in Table 4.3. The model predicting the variation of the green flexural strength, built based on this experimental data is presented as Eq. 4.4. All the coefficients are statistically validated at 95% confidence level.

$$Y_{GFS} = - 0.3604 + 0.033315X_1 - 0.00778X_2 + 0.036815X_3 - 0.00025X_1^2 - 0.00011X_2^2 - 0.0008X_3^2 - 0.000145X_1X_2 - 0.00033X_1X_3 - 0.00018X_2X_3 \dots\dots\dots (4.4)$$

where,  $Y_{GFS}$  is Green Flexural Strength.

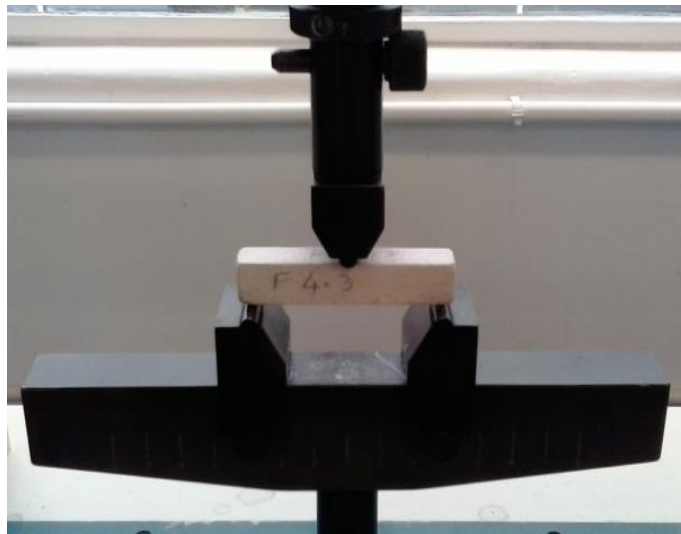


**Fig 4.7 Flexural strength measurement**

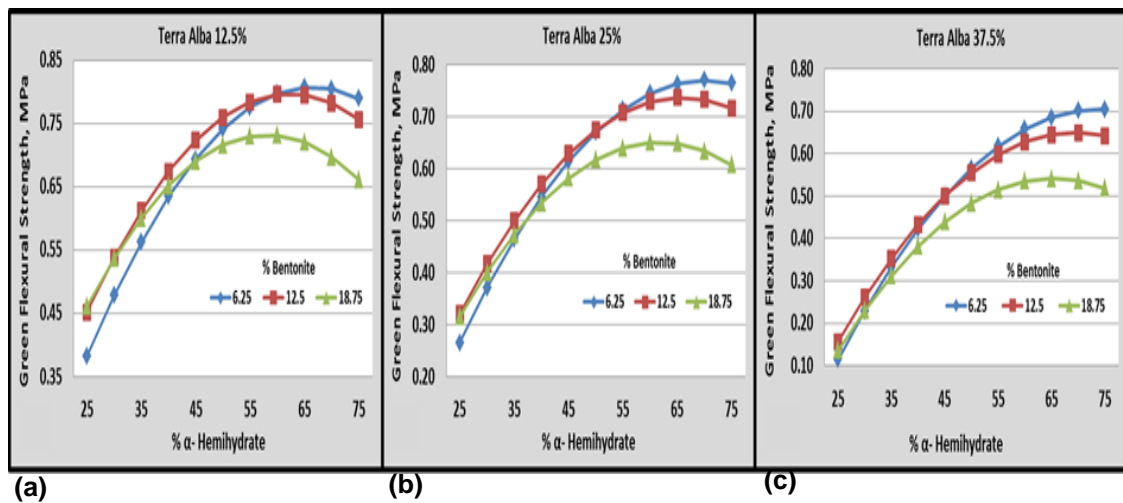


**Fig 4.8 Flexural strength in the green state with varying  $\alpha$ -hemihydrate**

The green flexural strength results based on the model in Eq. 4.4 are plotted for varying compositions as shown in Fig 4.8. A quick look at the general trends clearly shows that the green flexural strength increases with increasing  $\alpha$ -hemihydrate. Naturally, the higher the hemihydrate, the more the crystallisation resulting in the increased flexural strengths. However, the flexural strength

reduced with increasing contents of terra alba. Again, the role of terra alba as a seeding agent results in finer more randomly oriented and distributed gypsum crystals as its content increases. The decrease in the flexural strength is probably due to these widely dispersed random grains giving opportunities for the intergranular crack formation and growth, eventually allowing for an easier failure, leading to the reduced flexural strengths. The bentonite content seems to have relatively lesser impact on the flexural strength in the green state.

Further to sodium silicate soaking and baking, the flexural strength values measured are listed in Table 4.3. The model developed and validated at 95% confidence level with all the factors to be significant is of the form presented in Eq. 4.5

$$Y_{IBFS} = 3.845587 - 0.00325X_1 - 0.08583X_2 - 0.394X_3 - 3.20005X_1^2 + 0.001748X_2^2 + 0.010442X_3^2 - 0.00034X_1X_2 + 0.001941X_1X_3 + 0.000929X_2X_3 \dots \dots (4.5)$$

where,  $Y_{IBFS}$  is the flexural strength of the impregnated and baked specimen.

The flexural strength values further to impregnation and baking as predicted by Eq. 4.5 are presented in Fig 4.9, with varying combinations of experimental factors. The results indicate relatively less variations with varying terra alba. However, variations of differing nature and degree in flexural strength are evident with increasing hemihydrate, at different levels of bentonite, indicating strong interactions between the two factors. The increase in the flexural strength with increasing hemihydrate as noted with the 12.5% and 18.75% bentonite is natural,

but there is a slight reversal at lower levels of bentonite, possibly due to variations in crystal habit and surface topographies resulting from reacting with sodium silicate and the bentonite clay, as also noted by Cody and Shanks [124].

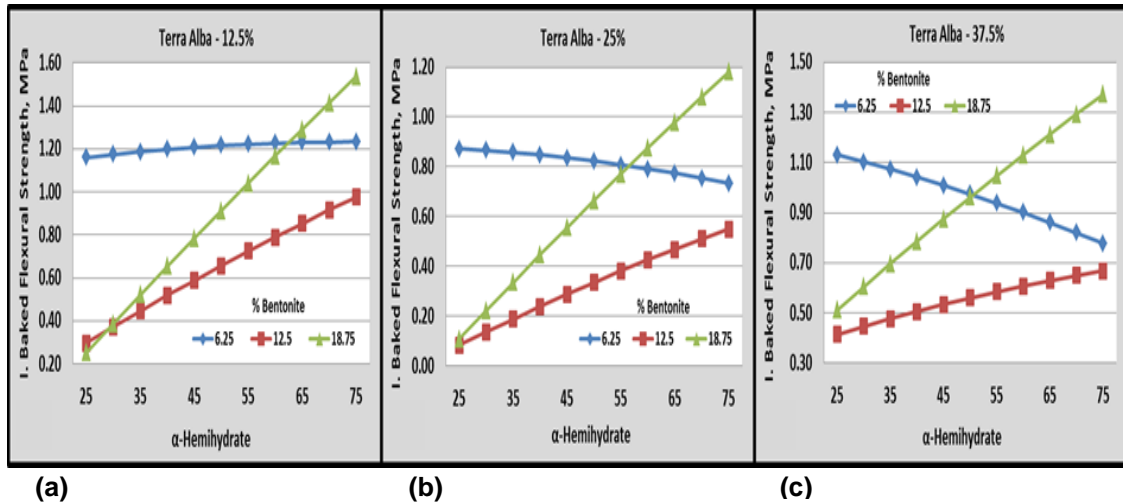


**Fig 4.9 Flexural strength further to sodium silicate treatment and baking with varying  $\alpha$ -hemihydrate percentage**

### 4.5.3 Compressive strength

Compressive strength tests are conducted based on AFS standards using cylindrical specimens of diameter 50 mm and height 50mm using the Hounsfield Compressive Testing equipment. The specimen loading method and rates are similar to the ones discussed in chapter 2. The green compressive strength values are presented in Table 4.3, and the model developed based on these results is given in Eq. 4.6. Analysis of variance validated the model at 95% confidence level and the R-Square value is 95.01% indicating all variables, their quadratic effects

and the first order interactions are significant in controlling the variation of the compressive strength in the green state.

$$Y_{GCS} = - 0.6597669 + 0.0314106X_1 + 0.0196108X_2 + 0.0235895X_3 - 0.0002704X_1^2 - 0.0005982X_2^2 - 4.382005X_3^2 + 0.0002215X_1X_2 - 0.0004566X_1X_3 - 0.0004009X_2X_3 \dots\dots\dots (4.6)$$

where,  $Y_{GCS}$  is Compressive Strength in the green state.

Fig 4.10 presents the variation in the compressive strength of the printed samples in the green state for varying compositions and combinations of other critical factors. In almost all the cases, the green compressive strength gradually increased, attained a peak and then reduced either substantially or to varying extents in specific cases. Again, in the green state, the strength of the printed sample can be attributed to the nucleation, growth, and the final form of the gypsum crystal growth. As the percentage of  $\alpha$ -hemihydrate increases, the crystal growth and the gypsum bonding of the sand and clay masses increases, thus giving better compressive strengths. However, beyond a certain limit, the crystal growth is restricted by the amount of the moisture available, while at the same time, the unaltered plaster powder, together with bentonite forms relatively softer zones promoting easier shear failures, resulting in an overall lesser compressive strength.

These aspects may also be physically observed from the photomicrographs taken at a relatively lower magnification and presented in Fig 4.11. The gypsum crystals

are grown into wider areas and are well connected laterally at 50% of plaster, as against the weakly connected dispersion of finely grown crystals at 25% and 75% plaster levels. Understandably, there is an optimum level of  $\alpha$ -hemihydrate at around 50% which seems to be effective in developing the necessary bonds in the green state, for the amount of moisture added through the print head, for each combination of the other parameters. Also, at higher terra alba and low to mid-range of bentonite, the compressive strength continuously increased with increasing hemihydrate, as depicted in Fig. 4.10 (c). SEM photomicrographs presented in Fig 4.12 confirm steady rise in the growth and the intricacy of the crystal network with increasing hemihydrate. The higher terra alba promotes better seeding and relatively high chances of the gypsum crystal growth with the moisture levels made available through the printing process.

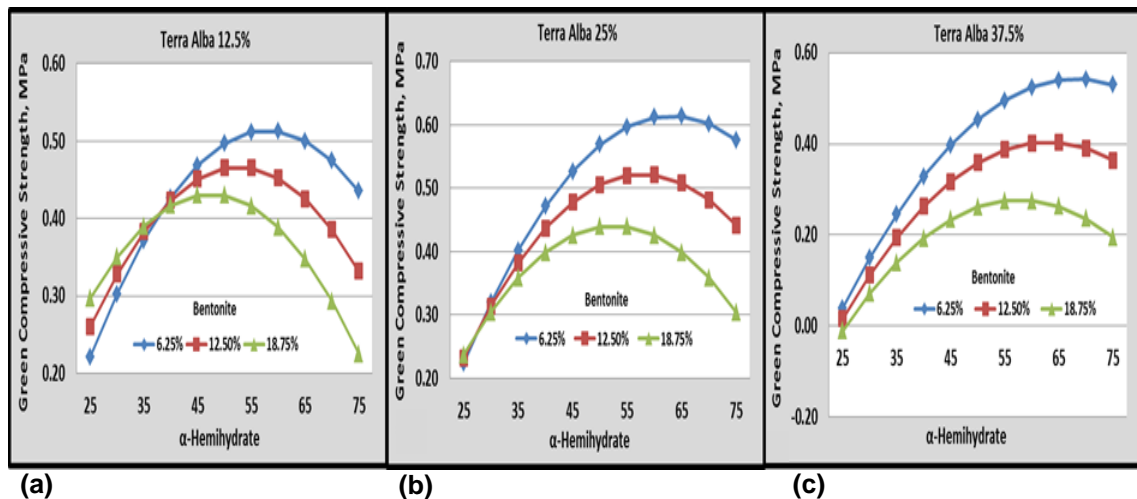
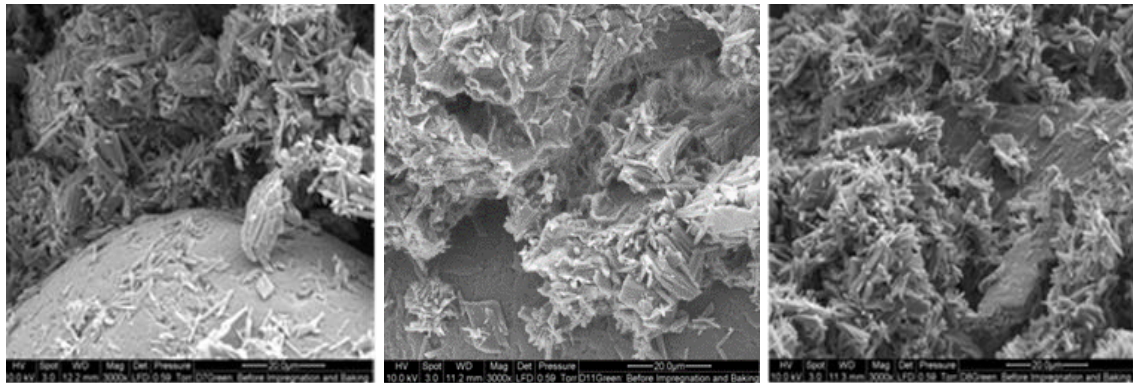


**Fig 4.10 Variation in the green compressive strength with varying  $\alpha$ -hemihydrate**

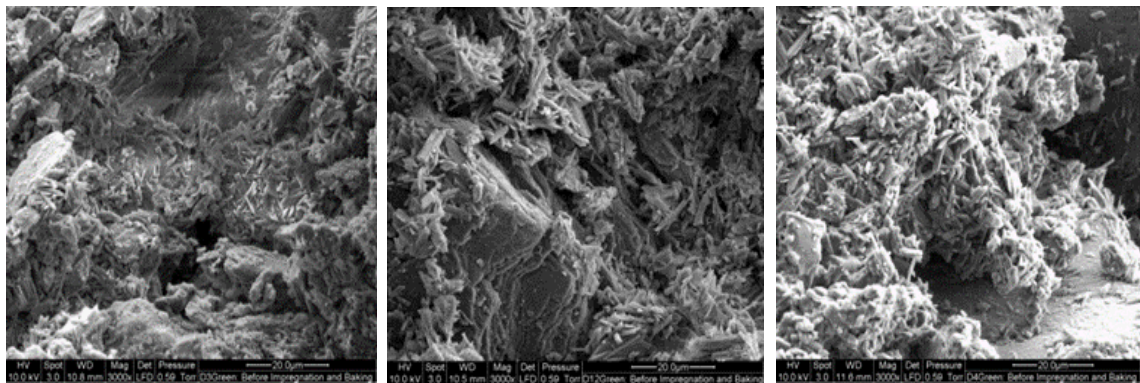


(a)  $\alpha$ -Hemihydrate 25%

(b)  $\alpha$ -Hemihydrate 50 %

(c)  $\alpha$ -Hemihydrate 75%

**Fig 4.11 The role of plaster on the extent of gypsum crystallisation at 18.75% bentonite**



(a)  $\alpha$ -Hemihydrate 25%

(b)  $\alpha$ -Hemihydrate 50%

(c)  $\alpha$ -Hemihydrate 75%

**Fig 4.12 Gypsum crystal growth increases with increasing  $\alpha$ -hemihydrate, at 37.5% bentonite**

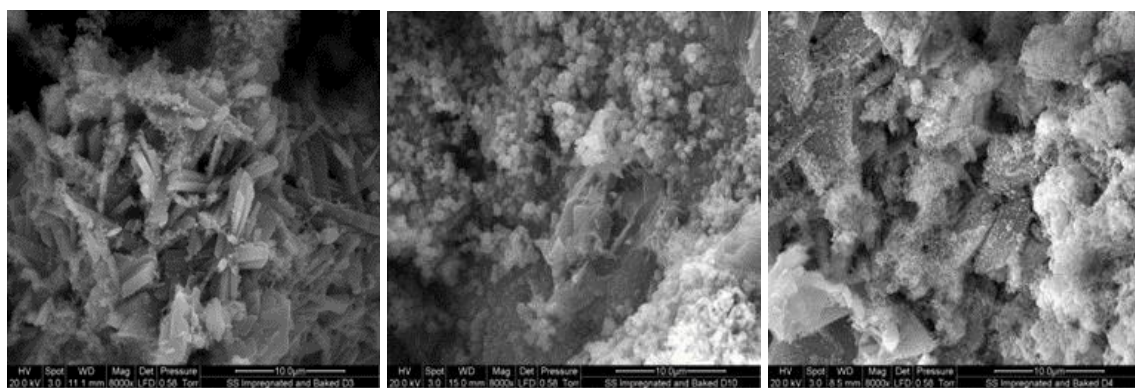
It is interesting to note that the higher the bentonite, the lower is the green compressive strength predicted as seen in all the cases of Fig 4.10. This indicates that the electrolytic bonding action of the clay has significantly less effect on the overall strength achieved in the printed samples. Consequently, the higher contents of clay actually result in wider areas of unconnected ingredients, leading to easier shear failures and lower compressive strengths.

The regression model based on the compressive strength results of samples soaked in sodium silicate and then baked is given in Eq. 4.7. ANOVA validated the model at 95% confidence while an R-squared value at 92.13 % indicated all factors to be highly significant.

$$Y_{BCS} = 0.2699548 + 0.0436652X_1 - 0.0314921X_2 - 0.0225901X_3 - 0.0001994X_1^2 + 0.0002829X_2^2 - 0.001264X_3^2 - 0.0003746X_1X_2 - 0.0002225X_1X_3 + 0.0015727X_2X_3$$

..... (4.7)

where,  $Y_{BCS}$  is the compressive strength after impregnation and baking.



(a)  $\alpha$ -Hemihydrate 25%

(b)  $\alpha$ -Hemihydrate 50%

(c)  $\alpha$ -Hemihydrate 75%

**Fig 4.13 Crystal structures post soaking and baking show increasing sodium silicate bonding with increasing  $\alpha$ -hemihydrate at terra alba 37.5% and bentonite 12.5%.**

Further to soaking in sodium silicate and baking, the compressive strength is expected to generally increase with increasing  $\alpha$ -hemihydrate. Fig 4.13 presents SEM photomicrographs of baked samples, showing evidence of increasing sodium silicate growth with increasing hemihydrate. With other conditions remaining the same, the increased gypsum crystallisation and the consequent wider and more

intricate dispersion of the sodium silicate indicates better compressive strength values. The predictions by Eq. 5.7 and as presented in Fig 4.14, also show the same trends, as the compressive strength values gradually increased with increasing contents of the plaster. While the role of terra alba appears to be almost negligible, compressive strength values after sodium silicate treatment and baking decreased to some extent with increasing bentonite. Lower  $\alpha$ -HH (50%) together with the lowest Terra alba (12.5%) and Bentonite (6.25%) resulted in the highest green (144.7g) and baked (149.2g) masses and also the highest (1.3MPa) compressive strength further to baking, as shown in Fig 4.14.

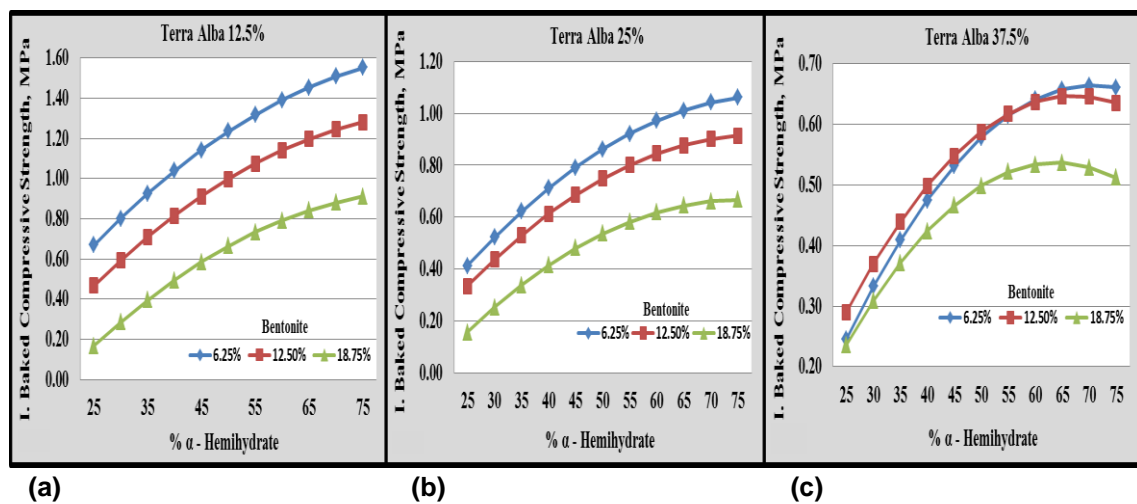


**Fig 4.14. Variation in the compressive strength further to sodium silicate soaking and baking with varying  $\alpha$ -hemihydrate**

Finally, for a comparative assessment, measured values of compressive strengths obtained for all the 15 material compositions used in the Box-Behnken design as listed in Table 4.3 are obtained and plotted in Fig. 4.15 for the three cases; green, directly baked, and sodium silicate treated and then baked. It may be noted that the samples directly baked from the green state resulted in very low compressive

strengths, and close to zero values in some cases. Once baked, the electrolytic bonding forces vanish, as the moisture content is driven out. The only bonding force is that due to the dehydrating gypsum crystals, whose strength keeps fluctuating depending on the baking temperature.

However, all the samples showed higher compressive strengths after the sodium silicate treatment and baking. While the final compressive strength values obtained varied quite widely, the average values are higher than the ones obtained with the plaster bonding methods used in Chapter 3. Also, there are a couple of peaks that are above the 1.0MPa mark, indicating the suitability of the material system for casting a variety of metals, as per the standards of the American Foundry Society.

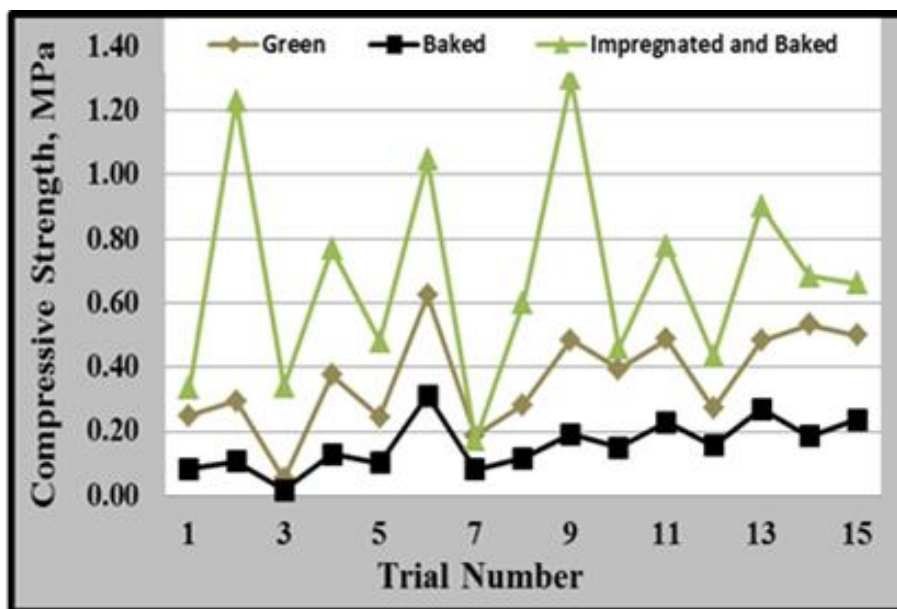


**Fig 4.15 Comparative compressive strengths; green, directly baked, and sodium silicate impregnated and baked states.**

#### **4.6 Summary of clay and sodium silicate treatments**

Traditional foundry materials composed of bentonite and silica sand are experimented for 3D printing of moulds and proved to be effective together with specific amounts of plaster and terra alba. The mechanism of bonding in green state is achieved predominantly through gypsum crystallisation triggered by the plaster reacting to the moisture injected from the print head and assisted by terra alba as the seeding component. The clay helps in the dispersion of phases as well as developing electrolytic bonding forces. Sodium silicate soaking and impregnation are found to be essential and effective to achieve the required strength further to baking, through inter-granular loading and crystal growth, apart from vitrifying gypsum crystals.

## Chapter 5

### Roles of clay and resin bonding mechanisms in 3D printing

#### 5.1 Clays and resin coated sands; the ingredients for high refractoriness

As already explained in Chapter 4, clays are the principal constituents of a traditional moulding sand system, helping achieve the necessary strength and plasticity. Often used in the range 2%-50% by weight, clays allow binding of the sand particles together when treated with sufficient moisture [125]. Generally classified as either primary or secondary minerals, Kaolin is the primary form located onsite as feldspar, while secondary clays result from the weathering action of wind and water and are transported from the geological formation sites [126]. Plastic clays usually consist of three key minerals; kaolinite, mica, and quartz, apart from other minerals and carbonaceous ingredients derived from ancient plants and tend to be quite refractory. Wide variations are often common and the characteristics may vary from one source to the other.

Kaolinite clays considered for the work presented in this chapter have been used as binders in the traditional sand mould and core making for many years. The high refractoriness allows them to cater to the needs of ferrous castings. Small quantities of clay, as low as 1% mixed with other ingredients, predominantly sand, were noted to give sufficient permeability and strength before and after baking [127]. Complex interactions between water and the clay particles control the rheology of the slurries and the final drying processes [128]. When heated

sufficiently in a kiln, the water molecules attached to the clay particles are driven off, resulting in a compound of silica and alumina, which is a monolithic substance with specific physical and mechanical properties [126]. Different forms of Kaolinite clays have been employed as foundry sand binders, exploiting some of these attributes, achieved through varying process conditions.

Both organic and inorganic resins also became widely used as bonding agents in sand casting [129]. Chemically bonded quartz sand by the reaction between furan resin and sulphuric acid is an example. Depending on the basic ingredients, the reaction mechanisms may vary from vapour cured to no bake or heat cured types [130]. Resin bonded moulds were reported to result in better casting quality compared to the clay bonded counter parts [131]. Often the sand to resin ratio is very high, as the amount of resin used is very small, at around 1-3%, which is enough to achieve the required cohesion and strength. The shape retention of the moulds is high and the moulds also resist pressure, temperature and erosion under the action of the flowing metal.

Evidently, the science of clay and resin bonding is well known, but it is not generally known as to how they may interact and perform in a 3D printing situation. Commercial systems and ready solutions are on offer, but the basic science and the mechanisms at play and more intriguingly, the roles of specific components and varying compositions are not made available yet. The experimental research and the results presented in this chapter attempt this considering clay and resin coated sand mixture as the working material system

and evaluating the mechanisms of bonding and mechanical attributes of specimens made in a 3D printing approach. A brief review of the specific clays to be used and the mechanisms of bonding achieved through the use of resins in traditional foundry approaches is considered first, before developing the material compositions and experimental plans.

## **5.2 Refractory clays**

The mechanism of bonding is essentially based on the electrolytic forces generated within the clay-water slurry, whichever form of clay is actually employed. The literature reviewed in Section 4.2 in the previous chapter applies to the clays employed here with some variations. However, the focus is on achieving better refractoriness, targeting probable application to ferrous castings. The strength of sodium bentonite bonded sand was noted to be gradually lost when heated to around 621°C, while that of the calcium bentonite suffers beyond 316°C [132].

Mariusz *et al.* [133] noted that montmorillonite; belonging to a mineral group called smectites is the component deciding the binding properties as well as the thermal resistance of bentonite clays. Under the action of the heat of the molten metal, montmorillonite undergoes various transformations such as dehydration, dihydroxylation, decomposition, and recrystallisation, at different temperatures that vary with the actual composition of the clay. The endothermic dehydration and

dihydroxylation processes occur at around 155-169°C and 519-672°C respectively. While temperatures up to 500°C do not cause any changes, montmorillonite begins to lose structural integrity at around 600°C, while heating beyond 700°C results in a complete decomposition.

Kaolins are secondary clays and are used in different forms; ball, stoneware, fire, earthenware, slip and volcanic clays. While investigating the possible use of foundry wastes in the ceramic industry, Furlani et al. [134] studied the sintering characteristics of kaolin clays and their blends. It was noted that even after heating up to 1100°C, kaolin retained a certain amount of quartz, revealing mullite and a silica rich glassy phase. While it remains the same after heating to 1200°C, the amount of mullite was noted to increase. Firing at 1300°C resulted in amorphous mullite and the quartz transformed into tridimite and cristobalite. No significant shrinkage, water absorption and phase changes were noted.

### **5.3 Resin bonding**

Phenolic resins are the oldest technical plastics to be used as binders of foundry sands. The basic mechanism of bonding is the poly-condensation reaction resulting in the cross-linking of phenolic and formaldehyde. Water is the by-product of this reaction and needs to be removed by some means. Different acids or heating can be used as the catalysts for the reaction to take place [135]. The

hydroxyl-aromatic phenolic monomers are repeatedly linked with aldehyde chemicals to synthesize phenolic resins.

The Phenol-Formaldehyde (PF) monomers are cross linked into a three dimensional network when polymerised through energy supplied in different forms. Most thermo-setting resins can exist in three different stages; Stage A: no cross linking yet and the base components of the resin sit around for some time without any changes, Stage B: The transition period during which the cross-linking occurs and Stage C: Fully cross linked. While other resins are mostly rubbery and tacky, phenolic resins exist in solid form during stage B. They can be ground and used along with moulding sands to polymerise and subsequently forming resin bonds [136].

It was noted that formaldehyde exists in equilibrium with methylene glycol in an aqueous solution. Depending on the pH of the solution, either novolac or the resole resin is formed. An acidic catalyst and an excess of phenol will result in the novolac resin. The reaction basically involves creation of methylene bridges at either the ortho or the para positions of the phenolic ring. With the reaction continuing, randomly oriented and branched polymer chains of different sizes and structures form. At some stage, when the formaldehyde is finished, the reaction stops and the resin remains stable, until treated with an agent to further initiate the cross-linking. The most common cross-linking agent is hexamethylenetetramine. Called hexa, in short, blended with resin in ground form, it acts as a source of formaldehyde and leads to further cross linking when heated to the curing

temperature. A complex 3D structure results, with the polymer molecules assuming an infusible state and accounting for the hardness and the heat resistant properties. An alkaline catalyst and excess of formaldehyde result in resole resins, which are usually quite active and complete the polymerisation and cure with time, even without any additional agent. The shelf-life is hence limited depending on the type of resin and other conditions. They are water soluble to some extent [137].

Various resins are used as bonding agents in sand casting, together with different forms of hardening mechanisms [68]. The strength of the bond may vary depending on the type of resin and the nature of the catalysts used [138]. In the cold setting process, the resin is coated on the sand particles and an acid or gas catalyst leads to gradual cross linking, reduction in the viscosity and final hardening into a hard solid. Eventually, the sand particles are bonded together by cohesive forces within the shrinkage neck and adhesive forces that stick to the surfaces of the sand particles. The larger the neck or the bridge, the stronger is the resin bond. Furan resins made from furfural alcohol are commonly used for binding moulding sands and hydrochloric, sulphuric, nitric, phosphoric, tartaric, maleic and sulfonic acids are used as the curing agents. Phenolic resins containing up to 25% of potassium hydroxide are used as no-bake moulding sands that self-set at room temperature based on ester as a catalyst [139].

#### **5.4 Clay and resin based material combinations for 3D printing**

Following from the review above, it is evident that traditional foundry materials were significantly researched and the chemical and physical interactions between constituent phases and the overall science are well established and understood. Kaolinite clays, the most common binding materials in traditional foundry sands absorb ions or molecules at points of unsaturation when suspended in a polar liquid such as water. Hendricks et al noted as early as 1938 that the water layer was an extended hexagonal network of water molecules [140]. Gruner attributed the plasticity phenomena achieved from moist clays to the dipolar forces, while the cation adsorptions and hydrations caused by dipolar forces are the driving forces leading to swelling.

When baked, the dehydration processes were noted to be; an initial increase in plasticity up to 60°C [141], a decrease in plasticity with further heating from 100 to 110°C as the planar water is driven off, no major changes beyond 110°C and up to 250°C, and drastic reduction in plasticity with further heating as the broken-bond water is also lost. Heating beyond 300°C - 400°C, the clay gradually becomes fireclay [109]. It will be interesting to investigate if the nature of kaolinite clays to attain plasticity and cohesive forces could be used to achieve the bonding with necessary strengths in a 3D printing context. As already reported in Chapter 4, clays develop the electrolytic bonding forces when treated with sufficient moisture, at around a fifth by weight, but the results will vary with the particle size and nature [142].

Further, different resins have come into use as bonding agents in sand casting [143]. Quartz sand and furan resin treated with sulphuric acid as a hardener are used to produce hard moulds for sand casting. While the mould materials are chemically bonded, the binding mechanisms could be vapour cured no bake or heat-cured types. Phenol formaldehyde resins belong to the heat cured type, penetrate effortlessly into narrow spaces and adhere to the sand particles. Heating for a short duration can lead to the cross-linking and entire setting of the polymer.

Though not reported so far, the thin, layer-wise dispersion in 3D printing and subsequent reaction with the aqueous solution injected from the print head might help develop the electrolytic bonding to achieve sufficient plasticisation and green strength based on the kaolinite clay system. It may be recalled that the bentonite clays experimented in Chapter 4 did not develop these bonding forces and a certain amount of plaster became necessary to be used to gain the required green strengths. Apart from the possible higher refractoriness, this aspect is the other reason for considering the kaolinite clays. In reality, both forms of clays develop bonding forces based on similar mechanisms. However the reaction times required to reach a certain level of material consolidation is considerably high in bentonite clays, while kaolinite clays react faster and harden quicker.

Further, as also experienced with the system presented in Chapter 4, the post-printing baking may not give sufficient dry strengths and further assistance from a secondary treatment may become necessary. The bentonite clays worked well with the sodium silicate treatment, but based on the literature, resin bonding is

selected for the kaolinite clay system. Commercial systems and ready solutions in similar lines are on offer, but the basic science and the mechanisms at play and more intriguingly, the roles of specific components and varying compositions are not reported yet. The experimental research presented in this chapter fills this gap, validating the hypothesis that clay and resin coated sand mixtures will develop the necessary green and baked strengths within a 3D printing system.

Based on the literature reviewed and material selection process presented above, and after some preliminary searching and a few table-top printing trials with different combinations, a resin coated sand and a kaolinite clay combination was finally identified for the experimental work. The initial trials constituted of loading these materials one after the other and gradually converging on a working combination. The ZPrinter 310 plus system reported earlier is again used for all the printing trials. Again, considering the sensitive print head mechanisms, the binder solution is kept the same as in the previous chapters. As a result, the clay bonding and associated reaction times are necessarily dependent on the ability to react with the moisture injected through the print head.

First, the resin coated sand was loaded without any other ingredients and attempted to build consolidated layers with the 3D printing process. Evidently, the moisture had no effect on the sand as there was no green strength achieved. Even after a curing period of almost 24 hours, no evidence of any interaction between the binder and the sand particles was noted. This test clearly indicated that the resin coating has no role to play during the actual printing process and in the

green state. Varying amounts of hydrous aluminium silicate powder commonly used in foundry practice were then added to the coated sand and printing trials were conducted with the clay varying from 1 to 20%. A dramatic variation could be noticed as the samples began showing increasing green strengths. However, it was proving to be difficult to control the dispersion of the fine clay particles within the framework of the powder spreading system. Small quantities of fine silica flour were found to mitigate these problems.

Next, the green samples produced with varying amounts of clay were subjected to baking with varying temperature and time settings. Beginning with 50°C and 30 minutes, all combinations were attempted in steps of 50°C and 30 minutes, up to 200°C and 2 hours. Small rectangular specimens were printed for each combination and the green and baked strengths were qualitatively assessed by simple snap tests. The volumetric changes were also noted by measuring the critical dimensions. Based on the a priori data thus generated the final ranges of compositions were converged to be 6-12% by weight of clay, while silica flour was at either 5% or 10%. Within these limits, the swelling problems were found to be limited.

Further to identifying the working ranges for the contents of the moulding sand, experiments are designed to evaluate the roles of the clay and the resin in imparting the necessary attributes for the 3D printing of moulds and eventually achieving the required green and dry strengths, within the limits of the dimensional

variations allowed. Micrographic evaluation of the bonding mechanisms, volume errors, compressive and flexural strengths are the key responses identified. As already mentioned in Chapter 2, all photomicrographs and EDS analyses were conducted based on the Field Emission Scanning Electron Microscope, FEI (Philips) XL 30 SFEG, with 0.2-30KV, resolution 1.5nm-2.5nm, working under vacuum pressure, available at the Research Centre for Surface and Materials Science, School of Engineering, University of Auckland, Auckland, New Zealand. All the sand specimens are coated with platinum and specific settings used are; 20 kV, low vacuum pressure and a spot diameter of 3.0nm

The specimens used for compression and three point bending tests are the same as reported earlier with other material systems and so also, the equipment used and the test standards employed. Critical dimensions of all these samples are measured in both green and baked states and the total volume error is established as the percent difference between the theoretical and the measured values. The overall plan of the experimental conditions and the key responses obtained are presented in Table 5.1.

### **5.5 The clay bonding mechanism in the green state**

The samples printed with varying compositions of the mould material composite achieved varying structures in the green state depending on the effective bonding mechanisms initiated by the clay particles. An SEM photomicrograph of a printed

sample in the green state is presented in Fig 5.1, together with the results of the EDS analysis. The clay particles appear to be clinging to the silica flour particles due to electrolytic forces. The mechanism of bonding is initiated when the moisture in the glue reacts with the clay particles. The clay particles react with the moisture when the binder liquid strikes the powder bed and begin to develop electrolytic bonding forces. It was reported in the literature that the clay particles are in the form of flaky crystals, and usually do not change this form even after coming in contact with the electrolyte [144].

**Table 5.1 Experimental factors and critical responses based on the resin coated sand system**

Run	% Silica Flour	% Clay	Mass, g		% Volume Contraction		Flexural Strength, MPa		Compressive Strength, MPa	
			Green	Baked	Green	Baked	Green	Baked	Green	Baked
1	5	6	157.13	154.67	0.27	0.37	0.62	3.55	0.2	4.17
3		8	151.51	148.4	2.36	2.49	0.34	2.55	0.17	4.66
5		10	153.21	151.1	2.38	3.33	0.2	3.63	0.17	3.79
7		12	153.95	149.13	4.34	4.69	0.55	2.69	0.24	3.73
2	10	6	153.28	149.78	2.55	3.04	0.63	4.87	0.17	4.97
4		8	150.41	146.62	1.16	2.50	0.4	3.79	0.08	4.58
6		10	151.39	148.62	2.46	3.47	0.44	1.74	0.17	3.26
8		12	145.88	145.45	2.31	3.02	0.26	3.22	0.07	2.35

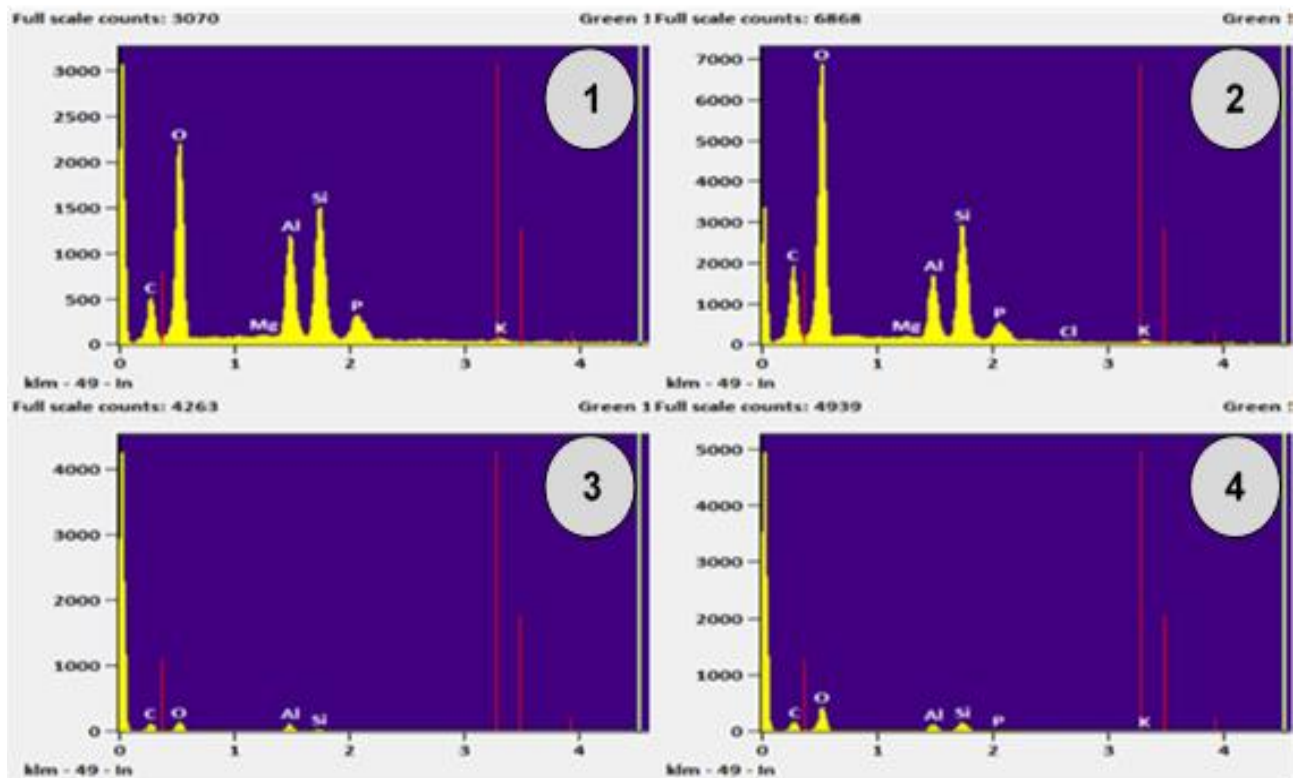
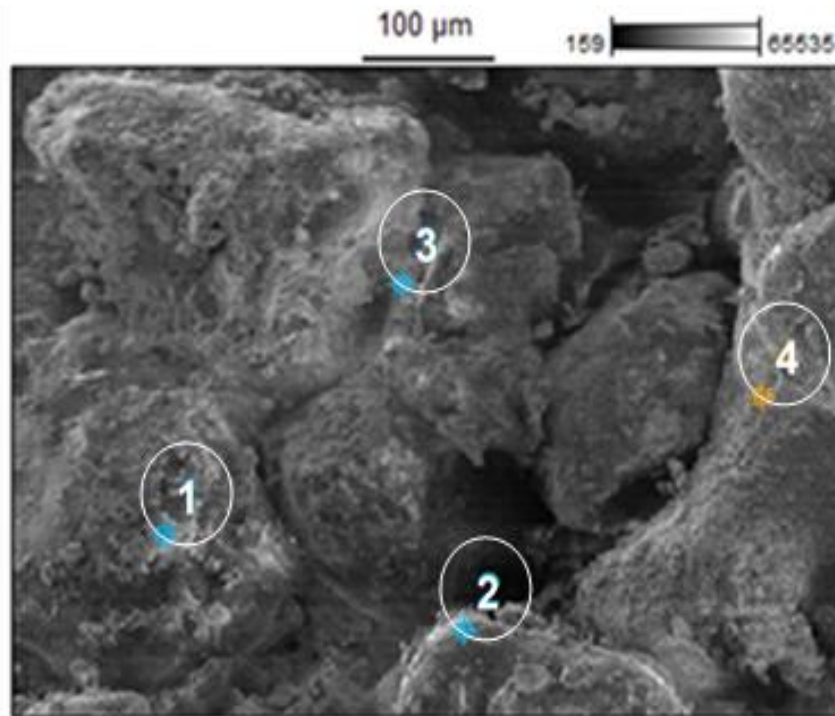


**Fig. 5.1 SEM photomicrograph and the EDS spectra of the printed samples in the green state**

The clay crystals agglomerate and form networks of solid crystals that can hold loose particles of sand together, giving the green strength to the consolidated material. Better dispersion of the silica flour also leads to better dispersion of the clay particles and an all over growth of the crystals and uniform bonding strengths. Locations numbered 1 to 4 as noted in Fig 5.1 are used for evaluating the EDS spectra. The clay crystals are formed by the agglomeration of small laminar grains ranging from 0.1-2.0 $\mu\text{m}$ . Considering the atomic concentrations, points 1 and 4 confirm the silica flour particles, point 2 confirms the silica sand particle, and the white coloured flaky substance at point 3 confirms the clay content. Similar observations were also made earlier based on EDS analysis of clay particles [145, 107]. It may be pertinent to note that the resin has no significant role at this stage of material consolidation. As a result, the green strengths must be relatively small, as will be verified later.

## **5.6 Resin bonding in baked samples**

Further to baking, the SEM photomicrographs present a clearly different arrangement of the different phases, as evident from Fig 5.2. Evidently, the heat of baking resulted in a partial softening and subsequent flow of the resin coating. While the plasticised resin begins to flow around the relatively bigger sand particles, the finer silica flour together with the clay crystals are carried forward. The higher the temperature, the higher is the viscous flow of the resin. However, the silica flour and the clay crystals enclosed within the polymer increase the viscosity and gradually restrict the freedom of movement. Eventually, the resin

sets when the temperature is reduced and usually forms a network of interconnected neck regions within the narrow gaps between the sand particles. The SEM image of Fig 5.2 clearly indicates the formation of one of the polymer necks between two large sand grains. Fine sand particles and the white clay places may also be noticed to have moved and settled impregnated over the solidified resin and entangled between narrow spaces.

The resin coating on the sand particles is in stage B, the transition period of the overall polymerisation process [136]. Alkaline catalysts and higher formaldehyde result in the resins that cure over time or with heating, even without the addition of any further catalysts. The resin employed here is similar to this and the heat from the baking accelerates the cross-linking process and allows the polymer coated over the sand and the neck regions in narrow inter-particle spaces to set hard once the polymerisation reaction is complete [137]. The baked strength of the moulds increases considering the amount of plastic flow and necking it can be observed from the photomicrograph of Fig. 5.2. An experimental verification of this observation will be considered in later sections.

The EDS spectra of the four points considered as in Fig 5.2 allowed identification of different phases based on the atomic concentrations of elements. Point 1 confirms the presence of the solidified polymer within the narrow neck zones between sand particles. Point 2 corresponds to a finer silica flour particle enclosed in a polymer coating and sticking to the surface of the larger sand particle. Point 3 is the resin coating partly melted, polymerised, and solidified around the sand

grain. Point 4 is the clay crystal still intact but carried away and finally embedded in the resin surface.

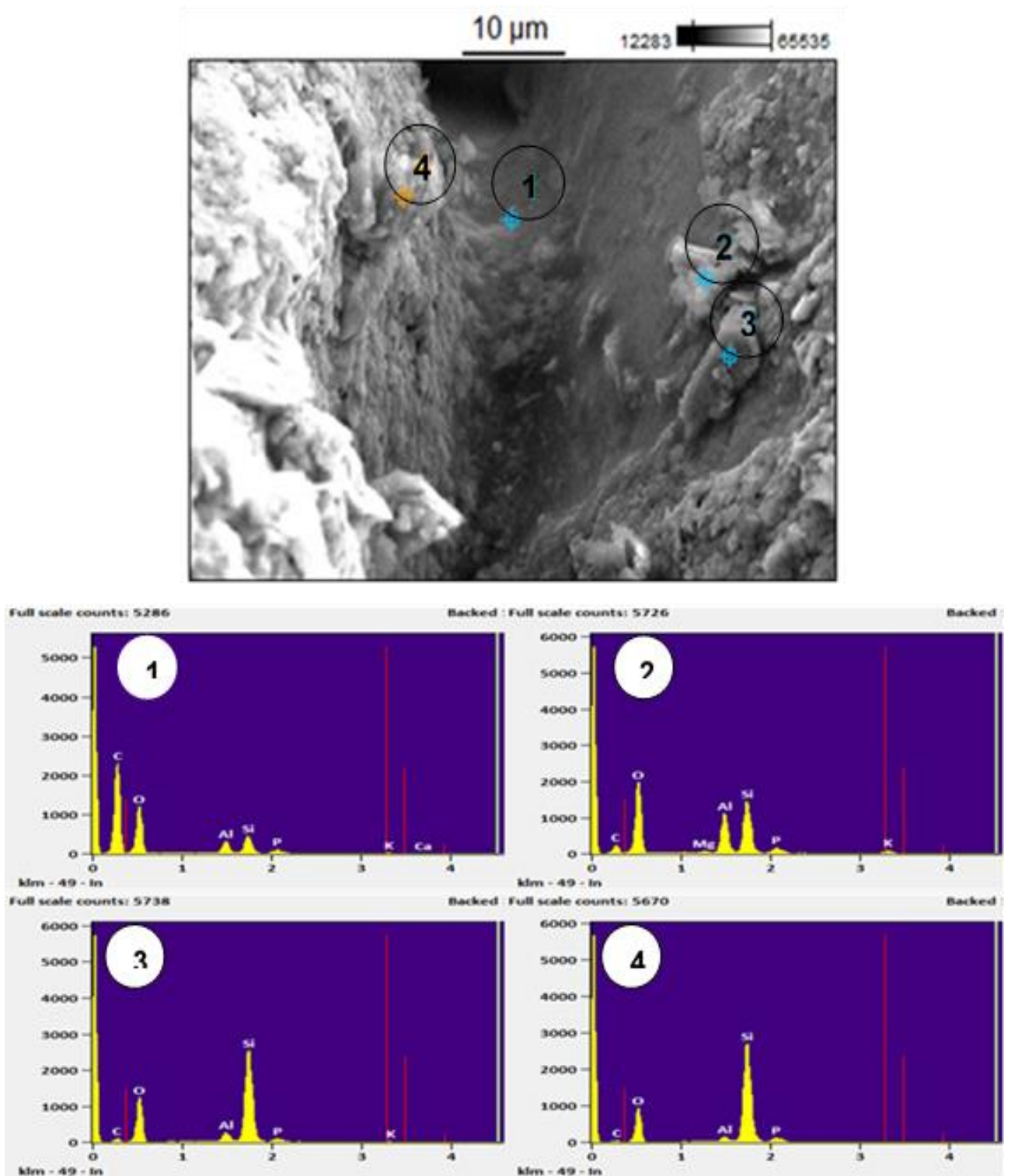
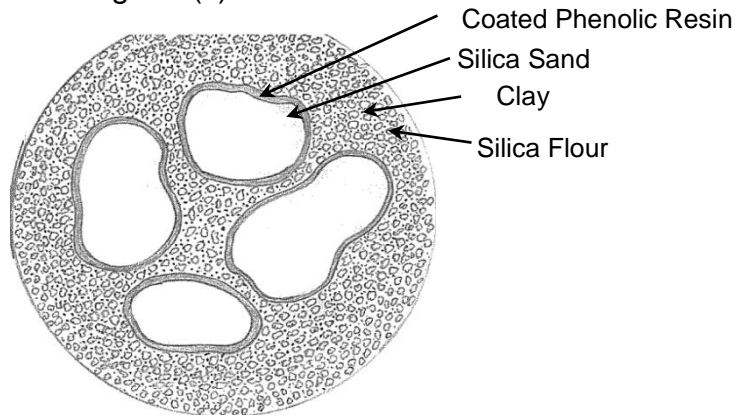


**Fig 5.2 SEM photomicrograph and the EDS spectral analysis of printed samples after baking**

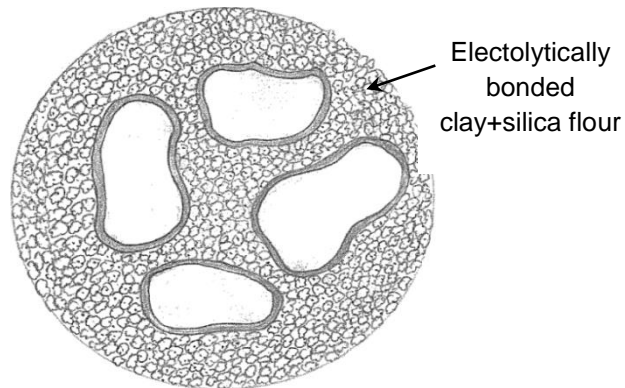
Based on these observations, the mechanism of bonding further to baking may be attributed to be predominantly due to the network of solidified resin structures, and the silica flour and clay flake components enclosed within. This is depicted schematically in Fig 5.3 and will be considered as the basis for the evaluation of the significance of varying ingredients in the mould material composition. The following is the proposed mechanism based on this schematic arrangement at various states:

- Fig 5.3 (a) shows the different ingredients of the mould material composite as it is loaded into the printer and when the sweep spreads a fine layer of the same on the print bed. There are large resin-coated sand grains and the flaky clay particles intermixed with the silica flour and occupying the narrow spaces between the larger sand particles.
- Once the binder liquid strikes the powder bed, the double diffuse layer of charges and the forces of attraction and repulsion begin to play in accordance with the DLVO theory reviewed in Section 4.2 [146, 147]. Considering the nature of kaolinite, the clay particles quickly cling to the finer sand particles and together they conglomerate and connect by the Van der Waals forces as shown in Fig 5.3 (b)
- Once baked, the resin partly softens, flows around and finally settles down coating over the sand particles. The plastic flow also displaces the clay and silica flour conglomerations and forms the bridges between narrow zones,

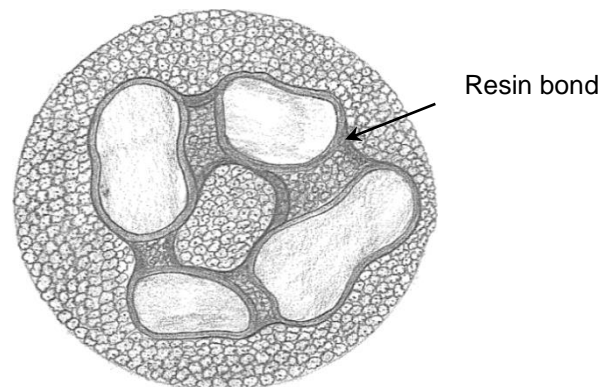
initiating and growing the neck regions [138]. With time, the cross linking is complete, and the resin hardens, bridging the gaps and giving a polymer matrix holding the larger sand grains in a network of interconnected neck regions as shown in Fig 5.3 (c).



**(a) The initial powder composite**



**(b) The green state**



**(c) Baked State**

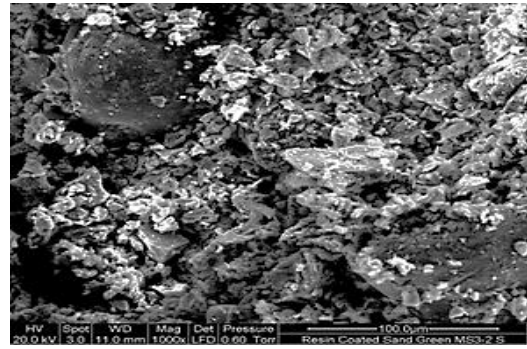
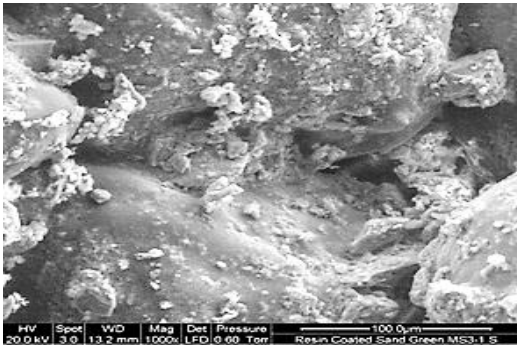
**Fig. 5.3 Schematic representation of the possible bonding mechanisms in clay-resin based moulding sands**

## **5.7 Experimental evaluation of the influences of varying compositions**

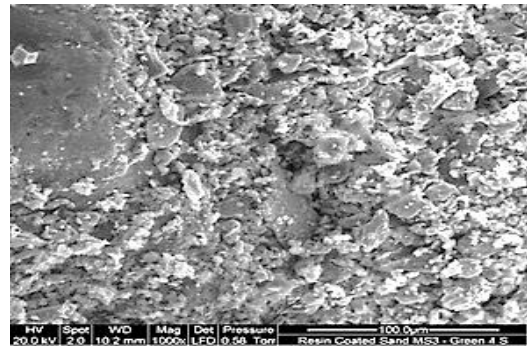
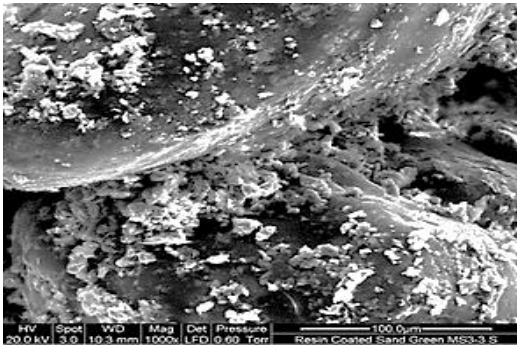
### ***5.7.1 Mechanisms of green and dry bonding***

Photomicrographs taken on the outer surfaces of green samples printed with varying compositions of sand mixtures are presented in Fig 5.4. Moving vertically downward in each column, it can be observed that the clay-silica flour bonding and agglomeration increases with increasing amounts of clay from 6% to 12 % with both 5% and 10% silica flour. Further, the dispersion of the clay particles is more uniform in almost all the samples at 10% silica flour, as compared to the 5% silica flour case. Based on these microstructures, the sample with 12% clay, and 10% silica flour might have achieved the best green strength, which will be verified later.

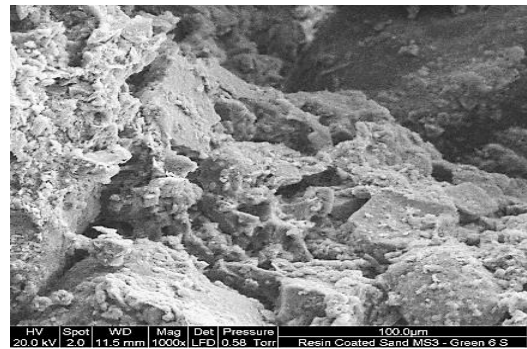
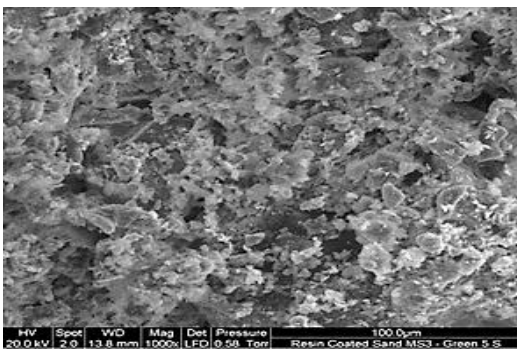
A closer observation reveals that the silica flour and the clay components interact in terms of controlling the number and size of the clay-silica flour cluster formations. The 5% silica flour though gives rise to lesser nucleation of these sites, there seems to be a better chance of the clusters sufficiently growing and connecting together. At higher silica flour content (10%), however, there is a general proliferation of the clay-silica clusters, and considering the small space, the final structure ended up being widely dispersed finer clay clusters. It will be interesting to evaluate how these microstructural changes influence the green and post-baked strengths.



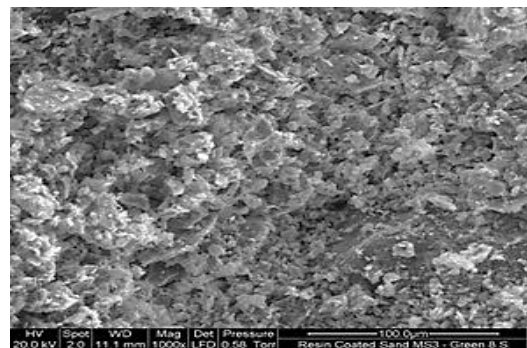
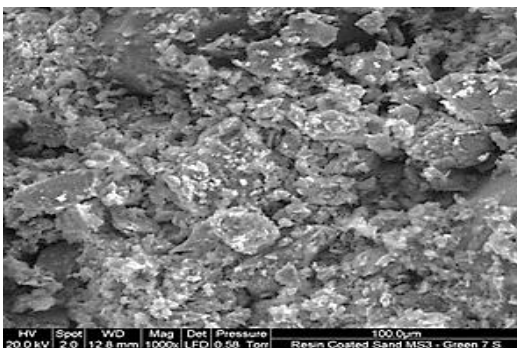
**(a). Clay 6%, Silica flour (i) 5%, and (ii) 10% at outer surface**



**(b). Clay 8%, Silica flour (i) 5%, and (ii) 10% at outer surface**



**(c). Clay 10%, Silica flour (i) 5%, and (ii) 10% at outer surface**

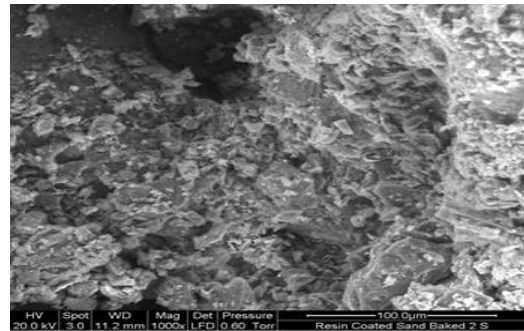
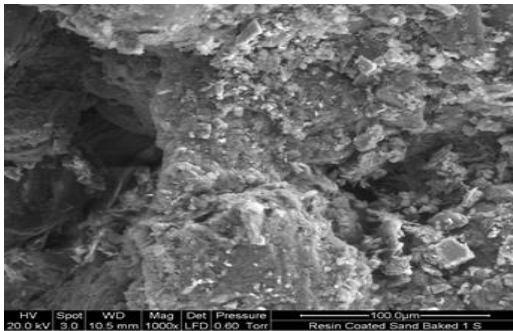


**(d). Clay 12%, Silica flour (i) 5%, and (ii) 10% at outer surface**

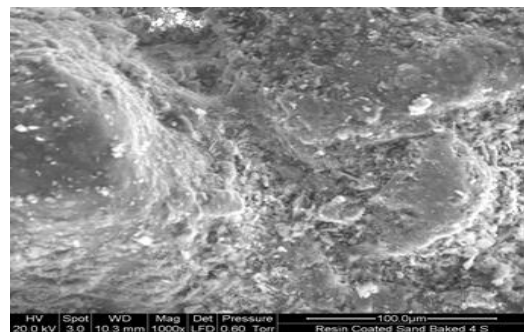
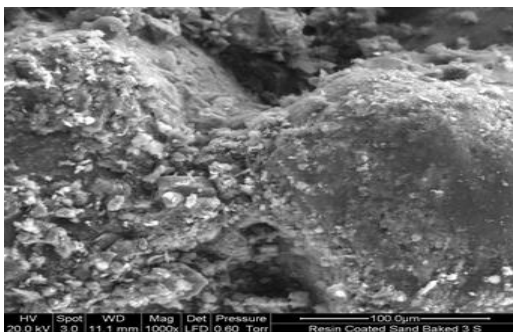
**Fig 5.4 SEM photomicrographs of green samples printed with varying compositions**

The photomicrographs of the baked samples of varying compositions are presented in Fig 5.5. The marked differences between these images and the images of the green samples presented in Fig 5.4 evidencing the plasticised resin and subsequent flow patterns may be noted. The resin spreads between grains at narrow regions, forming bridges through necking. The formation of inter-particle polymer neck regions and subsequent stretching due to surface tension forces are in particular, readily evident in Fig 5.5(b)(i) and (ii). The movement, segregation, and final settlement of the clay-silica flour clusters following the flow patterns of the resin are also different from the relatively static growth patterns of Fig 5.4.

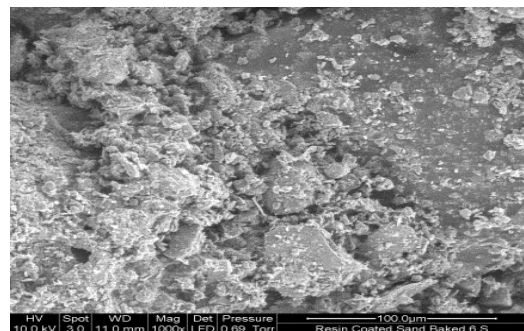
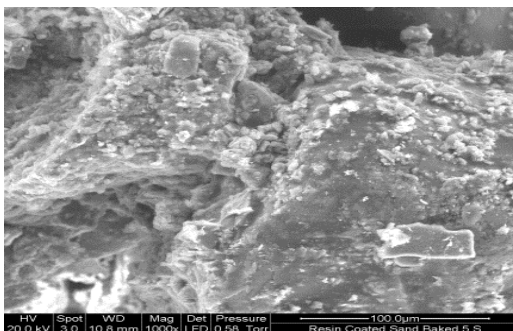
Further, Fig 5.6(a) and (b) present the photomicrographs obtained at higher magnifications based on the baked samples printed with 6% clay+5% silica flour and 12% clay+10% silica flour respectively. In both cases, the effects of heating, such as the plastic flow, and the upheavals resulting from the movement of the hot resin are evident. It is also clearly evident in particular with the case shown in Fig 5.6(b) that the clay-silica flour clusters are displaced and finally get embedded in the polymer matrix. Once baked, it may be the case that the mechanism of clay bonding is completely overshadowed by the resin bonding, effective from the flow, stretching within the narrow spaces and the formation of the continuous network of connected solid polymer phase.



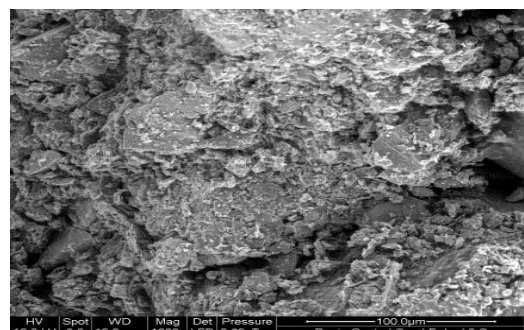
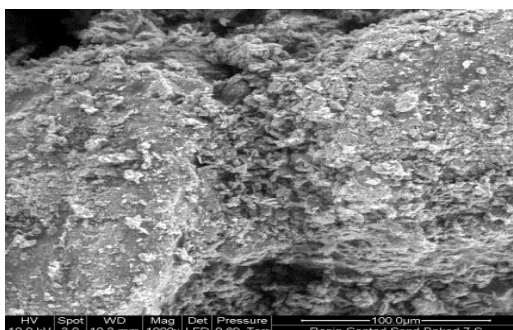
**(a). Clay 6%, Silica flour (i) 5%, and (ii) 10% at outer surface**



**(b). Clay 8%, Silica flour (i) 5%, and (ii) 10% at outer surface**

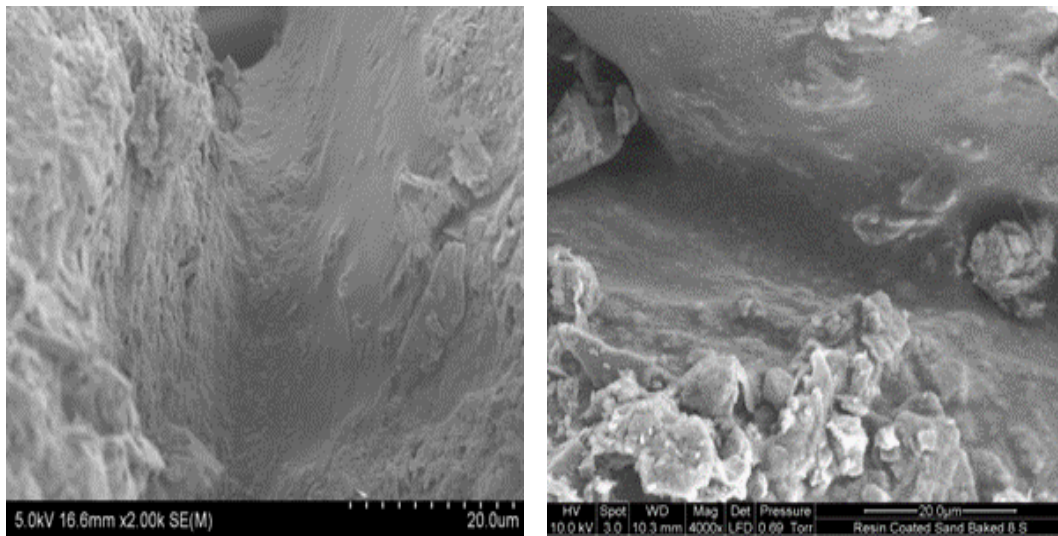


**(c). Clay 10%, Silica flour (i) 5%, and (ii) 10% at outer surface**



**(d). Clay 12%, Silica flour (i) 5%, and (ii) 10% at outer surface**

**Fig 5.5 SEM photomicrographs of baked samples printed with varying compositions**



**(a) Clay 6% and Silica flour 5%.**

**(b) Clay 12% and Silica flour 10%.**

**Fig 5.6 The inter-particle neck regions**

### **5.7.2 Volume error**

The volume errors estimated based on both green and baked samples with varying clay and silica flour contents are presented in Fig 5.7. All values reported are percent contractions compared to the original volume. It was clearly reported in the literature that the clay bonding is usually associated with a certain amount of reduction in volume [139]. Consequently, all the green samples showed a loss of volume, but the lesser the clay, the lesser is the volume contraction, as reflected in both sets presented in Fig 5.7. However, there is a slight exception in the case with 8% clay and 10% silica flour, which showed a slight increase.

It is also clearly evident that all the baked samples experienced higher volume contractions, compared to the green ones. According to Petersham [147], different clays undergo shrinkages varying from 10 to 25 percent, due to the removal of the excess moisture when baked and subsequent collapse of the material structure. Clays of finer particle size and plasticity were found to shrink more [148]. In the current case, the kaolinite clays do not exhibit high plasticity characteristics, and also considering that the overall amount of moisture added is relatively small, the maximum percent contraction did not exceed beyond 5%. This indicates closer dimensional control and no abnormality of the material mixture while used for 3D printing.

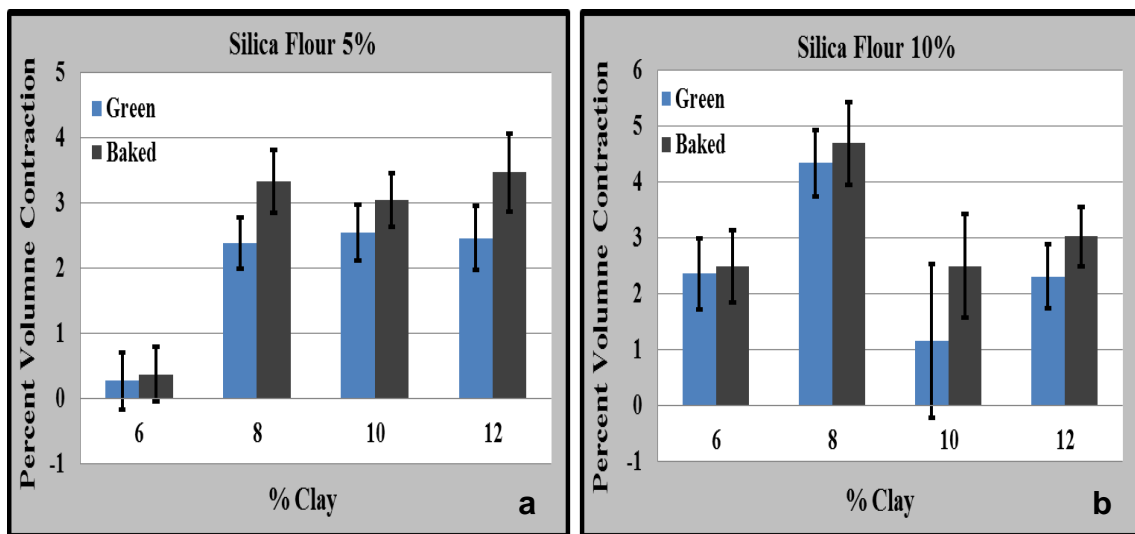


**Fig 5.7 Volume errors in printed green and baked samples**

### **5.7.3 Compressive strength**

Compressive strength results are presented in Fig 5.8, comparing responses from both green and baked samples. It may clearly be seen that the green strength of both sets of samples at 5% and 10% silica flour are very low and close. However, there is a slight reduction in the green compressive strength at 10% silica flour. At lower silica flour levels, the dispersion of the clay particles is lower and the clay-silica flour clusters are formed wide apart and have better chance to grow and strengthen the green bonds. As the clay particles attached to the silica flour grains are widely distributed with increased silica flour content, there is wide spread nucleation and lower growth of the clay flakes, which might be leaving the overall bonding mechanism slightly less effective and hence the lesser green strength. The photomicrographs of Fig 5.4 confirm these observations.

The striking result is the sharp increase in the compressive strengths of all cases after baking. Considering the wide differences it may be noted that the post baking bonding mechanism is widely different from that in the green state. The relatively weak holding forces generated in the green state by the clay flaking are completely removed and over ridden by the resin coating obtained from plasticising and associated viscous flow as also noted from Fig 5.6. The clay and fine silica flour clusters are enclosed within the polymer flow and if anything, slightly add to the strengthening mechanism in terms of varying resistance to deformation and yielding. Overall, the plastic flow of the resin and the necking phenomena in narrow zones and subsequent cross linking and hardening, along with the silica flour and clay particles displaced to varying degrees and getting

enclosed within the hardened polymer proved to be effective in achieving the necessary dry strength for the mould material.

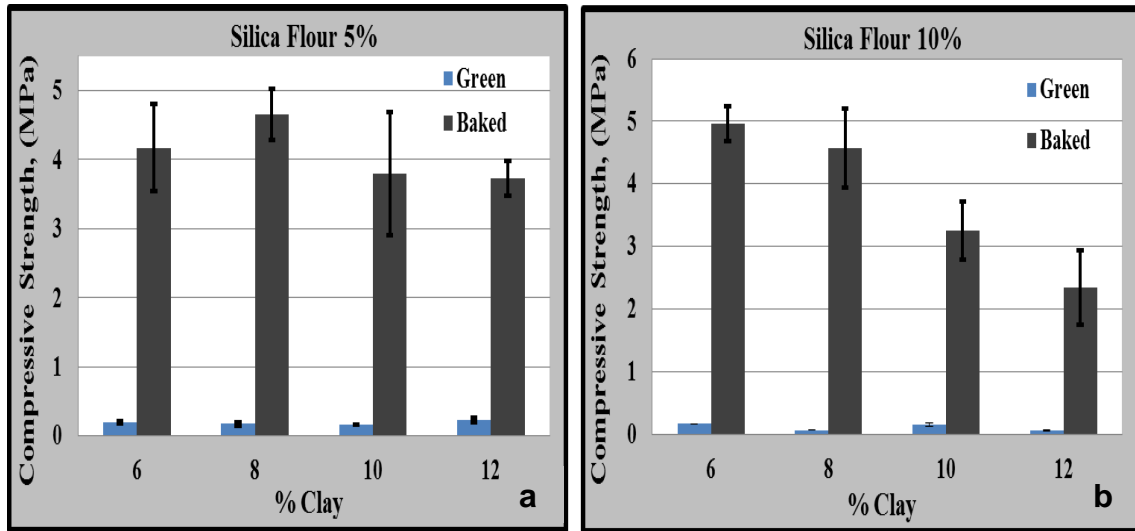


**Fig 5.8 Comparative evaluation of the Compressive Strengths in green and baked states with varying compositions**

A comparative assessment indicates that the strengths of the baked samples are similar at lower levels of the silica flour as maybe observed in Fig 5.8 (a). At higher silica flour level as shown in Fig 5.8 (b), the baked compressive strengths decreased from about 5 MPa to around 2.5 MPa as the clay content is increased from 6% to 12%. This might be due to the higher resistance offered by the higher silica flour content to the flow of the plasticised resin. Further, the formation of the clay-silica clusters is also higher at higher clay and silica flour contents. As a result, there is the added resistance from both the silica flour particles as well as the clay-silica clusters at higher levels of clay. The final strength of the baked specimens depends on the effective plasticisation of the resin coating and the

wider distribution of the matrix across the sand grain structure. The increased resistance to this flow would result in a non-uniform dispersion and solidification of the resin within the structure of the baked moulding sand mixture, leading to possible weaker areas and lower compressive strengths as witnessed in the cases presented to the right of Fig 5.8(b). Overall, the maximum compressive strength achieved is at around 5MPa, which is within the range of 0.15-25MPa specified by the American Foundry Society for the moulds to be employed for ferrous castings [131].

#### **5.7.4 Flexural strength**

The flexural strength results obtained from 3-point bending of different samples are presented in Fig 5.9 for varying compositions. The results are in similar lines to the compressive strength results as the baked strengths are very high compared to the green strengths for reasons already explained above. The general variation of the flexural strength after baking with varying compositions is also similar to the trends in the compressive strength, with some minor variations. There is a sudden drop in the flexural strength of the sample with 10% silica flour and 10% ball clay. The percent volume error also showed this difference in trend with the same case, as may be observed in Fig 5.7. It is possible that the printer settings are slightly altered at the time of printing these samples.

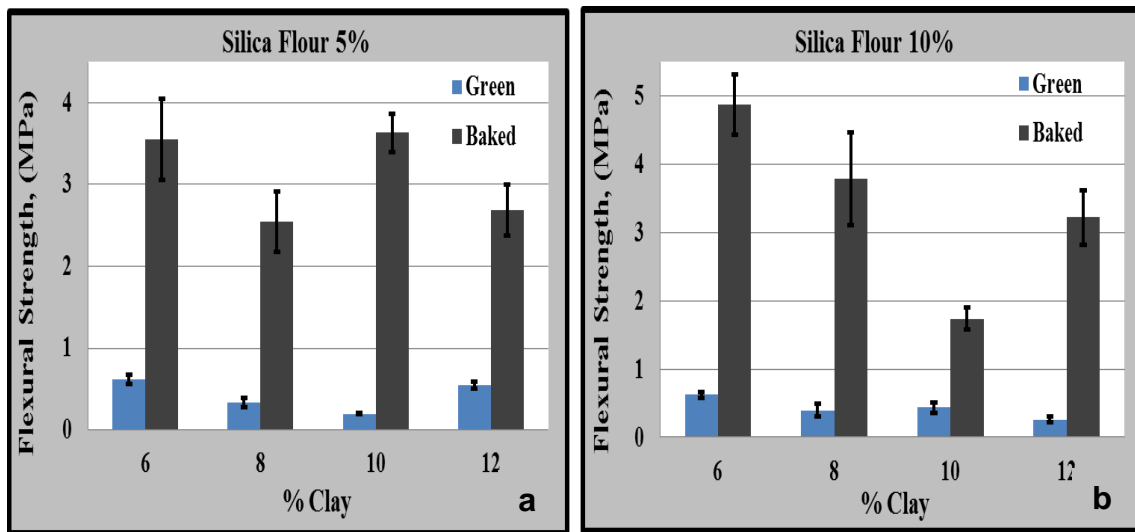


**Fig 5.9 Comparative evaluation of the flexural Strengths in green and baked states with varying compositions**

### 5.8 Chapter summary

Clay bonded resin sands are experimented for 3D printing. The results are indicative of the mechanisms of kaolinite clay bonding to be effective within a 3D printing system. Silica flour helps proper dispersion of the clay particles. The moisture from the print head is effective in terms of initiating the clay bonding. Clay crystals cling to silica flour particles and form networks of clay-silica flour clusters around the coated sand particles, providing the green strength. Further to baking, the resin polymerises by plasticising first, and then flowing and solidifying around the sand particles. The clay-silica flour clusters move with the flowing resin and gradually increase the viscosity. The polymer solidifies forming a network of inter particle neck regions, with the silica flour and clay particles embedded within the

structure, giving rise to the baked strength of the moulds. The maximum volume error is noted to be at around 5%, while the maximum compressive and flexural strengths of baked samples are at around 5MPa qualifying the material for ferrous casting as per the AFS standards.

## Chapter 6

### Casting quality evaluation

#### 6.1 Casting trials

Different 3D printing material systems have been structured and evaluated mainly in terms of the mould material characteristics as part of the research presented in Chapters 3 to 5. While all three systems scored reasonably well in terms of the mould material attributes, it is interesting to test their responses to the printing of relatively complex mould shapes. Further, casting trials based on the printed and baked moulds and the quality of the actual castings generated should be evaluated. However, it may be noted here that these material systems are primarily constructed to evaluate the internal mechanisms and the roles of varying parameters. The casting trials are also intended to further extend the understanding of the behaviour of these materials. The material systems are not optimised yet for casting purposes and so these experiments are not aimed at proving them as immediate solutions for rapid casting.

The moulds printed are designed for producing cylindrical test pieces as explained in Chapter 2. Different experimental plans are used with the three material systems as explained in the following sections. With each system, the moulds are printed following the experimental plans set, baked, and then used to cast aluminium with the first two systems and stainless steel in the third case. The

central cylindrical portions of the solidified castings are cut out and the length and diameter are measured to estimate the volume errors. The surface roughness values are obtained based on these specimens next, using the Taylor Hobson Talysurf, as explained in Chapter 2. Standard tensile test specimens are then turned out of these cylinders on a lathe and used on a tensile testing machine to obtain the ultimate strength values. Critical observations made based on the responses with castings obtained in the three cases are discussed next.

## **6.2 Moulds printed using plaster based material system for non-ferrous casting**

Following from the statistical design of experiment used to evaluate the attributes of this material system as a mould material as presented in Chapter 3, it is considered to continue with the same experimental design for understanding the casting responses. The Box-Behnken design yielding 27 experimental trials and the combinations of the experimental parameters are reproduced in Table 6.1 again, together with the critical responses measured.

### **6.2.1 Volume errors**

The Analysis of Variance (ANOVA) based on the percent volume error values yielded R-square and adjusted R-squared values of 83.95% and 65.24% respectively at 85% confidence level and the significant factors identified are  $X_1$ ,  $X_4$ ,  $X_1^2$ ,  $X_2^2$ ,  $X_4^2$ , and  $X_2X_4$ .

**Table 6.1 Mechanical properties of the Aluminium casting**

Run	X <sub>1</sub>	X <sub>2</sub>	X <sub>3</sub>	X <sub>4</sub>	Volume Error (%)	Surface Roughness, Ra (µm)	Tensile Strength (MPa)
1	33	2	200	2	18.32	40.85	101.38
2	33	2	300	6	24.34	31.95	107.97
3	33	2	400	4	30.71	39.35	103.51
4	33	3	200	6	11.83	28.78	98.48
5	33	3	400	2	9.67	36.26	107.81
6	33	4	200	4	12.91	33.68	112.49
7	33	4	300	2	23.18	41.04	94.60
8	33	4	400	6	10.97	39.2	112.36
9	43	2	200	4	11.65	35.58	90.50
10	43	2	400	2	3.00	39.08	81.55
11	43	2	400	6	15.59	41.02	85.24
12	43	3	300	4	8.26	28.38	113.13
13	43	3	300	4	8.17	27.47	102.40
14	43	3	300	4	12.10	29.83	112.94
15	43	3	300	4	7.22	28.22	95.75
16	43	3	300	4	6.36	34.13	101.38
17	43	4	200	2	8.74	37.97	87.85
18	43	4	200	6	5.50	25.14	87.79
19	43	4	300	4	4.24	19.78	82.31
20	53	2	200	6	17.45	39.29	123.73
21	53	2	300	2	17.98	54.69	125.57
22	53	2	400	4	23.48	41.38	127.51
23	53	3	200	2	11.92	30.44	129.71
24	53	3	400	6	12.10	23.97	102.08
25	53	4	200	4	15.20	33.39	108.03
26	53	4	300	6	3.97	27.89	94.47
27	53	4	400	2	12.28	41.71	87.38

A further ANOVA based on the significant factors ascertained these factors to be really significant at an adjusted R-squared value of 67.24%. The model developed based on the significant factors is presented in Eq. 6.1.

$$Y = 161.8989 - 7.8596X_1 + 12.6670X_4 + 0.0894X_1^2 + 0.7319X_2^2 - 0.8577X_4^2 - 1.9701X_2X_4 \dots \dots \dots (6.1)$$

Fig 6.1 presents the variation in the percent volume error of castings as predicted by Eq. 6.1 with varying hemihydrate for different levels of pre-moisture and baking times. In all the cases, the percent volume error represents the amount of shrinkage. In all the cases, the percent shrinkage gradually decreased initially, attaining a minimum and then gradually increased again with increasing  $\beta$ -hemihydrate. The total volume error consists of two components. The error due to the shrinkage of the solidifying metal, which is common to any casting process and the errors resulting from the faulty mould dimensions. Rafel reported 7% volumetric shrinkage for this type of aluminium alloy while changing from liquid to solid phase [149].

The main concern here is the possible additional volume error that could have been caused by the swelling effects of the mould material as described in Chapter 3 in Fig 3.7. It may be noted that the gradual decrease in the swelling of the moulds in Fig 3.7 with increase in the  $\beta$ -hemihydrate results in a gradual reduction in the shrinkage of the castings as well. This is clearly reflected in the gradual decrease in the volume error of the cast samples in all the cases in Fig 6.1 during

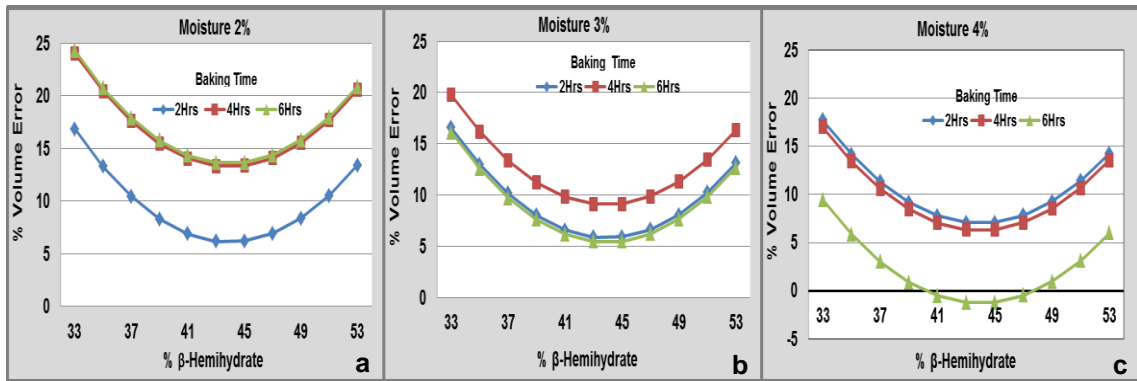


**Fig 6.1 Percent volume error of aluminium casting with varying gypsum percent in plaster based material system**

the initial stages. The percent volume error increased with further increase in the hemihydrate in all the cases as seen in Fig 6.1. It may be recalled that some of the curves showing the variation in the volume errors of baked samples presented in Fig 3.7 showed a slight increase in the error at the end. Though this may not be the only cause, both experimental and the predicted values indicate this increase in the volume errors of castings beyond 45% of hemihydrate.

Further, the baking time, at any given temperature has varying roles to play at varying moisture levels. From 2 to 3% moisture, the percent volume error increased by around 8% all around, with increasing the baking time, probably due to an increased expansion in the mould. The 4% moisture case showed a reverse trend as the baking time was increased from 2 to 6 hours. However, this deviation is more pronounced in the lower baking time case in Fig 6.1(a), while it is with the higher baking time at the higher moisture level, as shown in Fig 6.1(c). It is to be

noted that the negative volume error in castings arises due to larger dimensions than expected that result from an expansion of the mould cavity.

It is pertinent to point out that the dimensional variations occurring in a more complex case such as the moulds could be different from the simple cylindrical or rectangular shapes as used while investigating the changes in the mould materials as presented earlier. While it is interesting to investigate plausible reasons for these variations, within the limits of the current research, the most important aspect to be noted is that specific combinations of the pre-moisturised plaster based material system for 3D printing allow for producing castings of acceptable dimensional qualities. Based on the results presented in Fig. 6.1, Moulds printed with 45%  $\beta$ -hemihydrate and 2-4% pre-moisturisation baked at around 200 to 400 °C for 2 to 4 hrs will yield aluminium castings within a maximum volume error of around  $\pm 5\%$ .

### **6.2.2 Surface roughness**

Again, based on the ANOVA resulting in R-square and adjusted R-square values of 74.90% and 45.62% respectively,  $X_2$ ,  $X_2^2$ , and  $X_1X_2$  are identified to be the most significant factors at 85% confidence level. The ANOVA resulted in adjusted R-square values of 37.93% for full model and 29.83% for the model developed with the significance factors. Considering that there is no improvement, the full model is considered for further evaluation and the second order equation shown in Eq. 6.2 is the final response model for predicting the surface roughness.

$$Y_{ASR} = 101.5493 - 1.0944X_1 - 28.8385X_2 + 0.0244X_3 - 0.0317X_4 + 0.0284X_1^2 + 6.2586X_2^2 - 0.000004X_3^2 + 0.0001X_4^2 - 0.2845X_1X_2 - 0.0006X_1X_3 - 0.0012X_1X_4 + 0.0042X_2X_3 - 0.0043X_2X_4 + 0.00002X_3X_4 \dots \dots \dots (6.2)$$

Where,  $Y_{ASR}$  is average surface roughness.

Surface roughness results predicted by Eq. 6.2 with varying material and process conditions are presented in Fig 6.2. Generally, increasing plaster content is expected to increase the mould wall smoothness and eventually the surface quality of castings, as long as the temperature of the metal does not affect the stability of the plaster. In the current case, the metal is introduced into the mould at around 750°C. Literature suggests that the physical form of the plaster may not be much affected at this temperature. Hence, it may be expected that the higher the hemihydrate, the better the surface quality of castings.

However, this is not the case with all the results of Fig 6.2. At 2% pre-moisturisation, the trend is almost the other way, with the surface roughness gradually increasing with increasing hemihydrate. This could possibly be due to the insufficient formation of gypsum crystals due to the relatively small quantities of the pre-moisture available for accelerating the mechanism to the necessary extent.

The loosely bonded plaster content is likely to be eroded or dislodged under the action of the flowing metal, giving rise to increasing surface roughness with increasing hemihydrate.

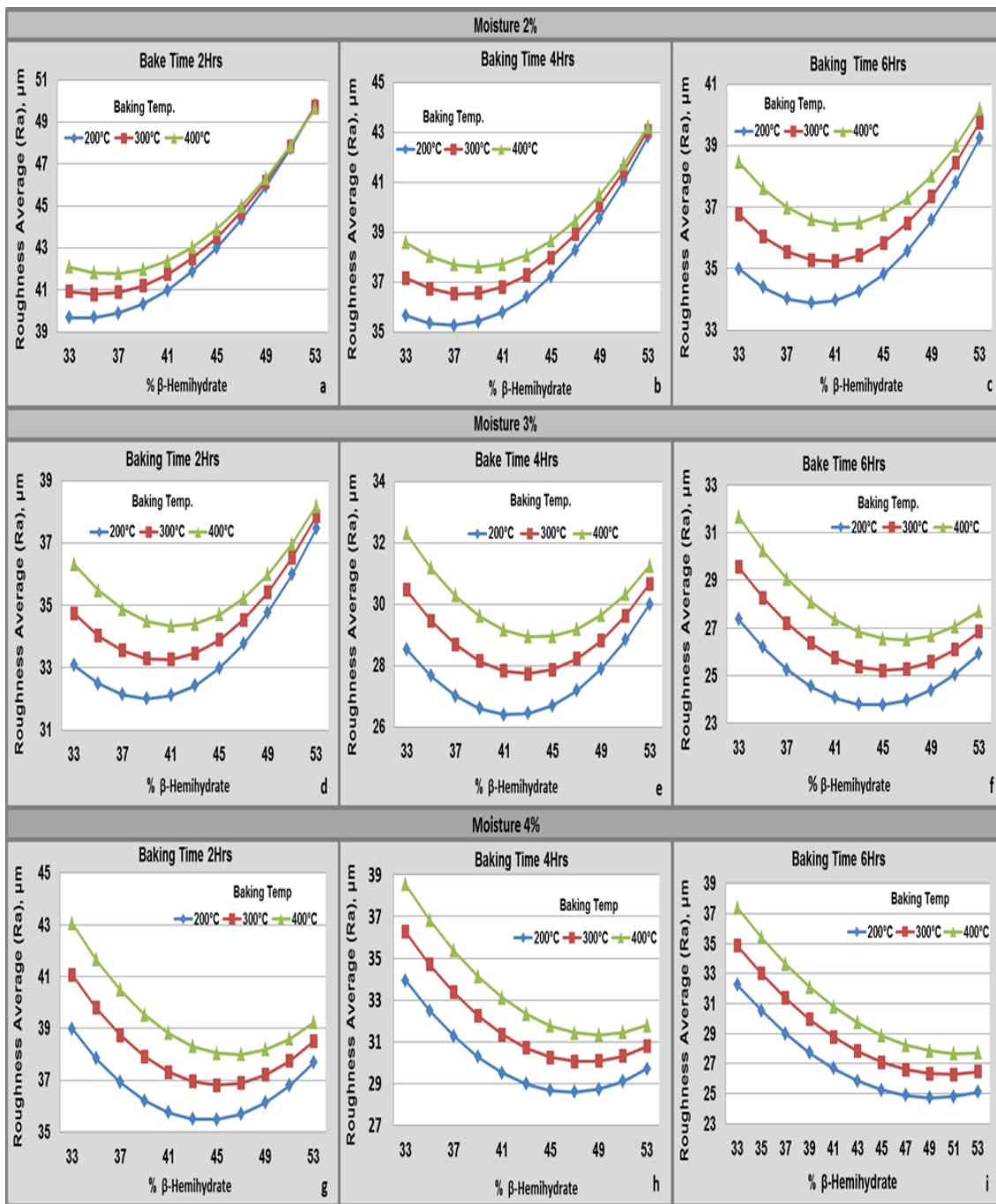


**Fig 6.2 Surface roughness (Ra) values of aluminium casting with varying gypsum percent in mould material system**

With increasing moisture content however, this trend gradually changed. With 3% pre-moisture, there is a reduction initially, a minimum value attained and then a gradual increase with further increase in the hemihydrate, as seen in Fig 6.2(d) to (f). With pre-moisture level at 4%, there is almost a continuous reduction in the surface roughness with increasing hemihydrate at all combinations of the other factors, with sufficiently long baking time, as evident from Fig 6.2(h) and (i). In all the cases, the lower baking temperature at 200°C resulted in lower surface roughness values. With increasing baking temperature, probably the moulds are becoming too dry and friable and losing grains with the action of the molten metal, resulting in a loss of the surface quality.

In normal sand casting of aluminium, the expected surface roughness values are at around 5.72 to 20.50µm [67]. In all the current cases, the surface roughness values are beyond this range. The higher hemihydrate in the range 45-50% together with higher pre-moisture, lower baking temperature and longer baking time combination as shown in Fig 6.2(i) resulted in the lowest surface roughness at around 25µm. Nevertheless, the surface roughness problems can be handled by using finer silica sand or by the application of suitable coatings.

### 6.2.3 Tensile strength

Based on the results from tensile testing of the cast cylinders, the ANOVA for the full model yielded R-square and adjusted R-square values of 84.26% and 65.91% at 85% confidence level and the most significant factors are;  $X_1$ ,  $X_2$ ,  $X_1^2$ ,  $X_2^2$ ,  $X_4^2$ ,  $X_1X_2$ , and  $X_1X_3$ . ANOVA repeated with the significant factors resulted in R-square and adjusted R-square values of 68.42% and 56.80% at 85% confidence level. Considering that there is no improvement in the model based on the significant factors, the full model as given in Eq. 6.3 is used for further evaluation of the response.

$$Y_{UTS} = 175.8681 - 12.5053X_1 + 80.6576X_2 + 0.3327X_3 + 15.0263X_4 + 0.2004X_1^2 - 8.6358X_2^2 - 0.0003X_3^2 - 1.8092X_4^2 - 0.7793X_1X_2 - 0.0047X_1X_3 - 0.1558X_1X_4 - 0.0110X_2X_3 + 0.6814X_2X_4 + 0.0133X_3X_4 \dots\dots\dots(6.3)$$

Where,  $Y_{UTS}$  is ultimate tensile strength.

The tensile strength values expected for the aluminium (A356) alloy by sand casting is  $\geq 207$ MPa [150]. If the casting process occurred normally, the test pieces obtained should have tensile strength values within this range. Variations can occur either due to thermal conditions resulting in varying cooling rates or porosities arising out of insufficient permeability or formation of excessive gases. The results presented in Fig 6.3 are based on the calculations using the Eq. 6.3.

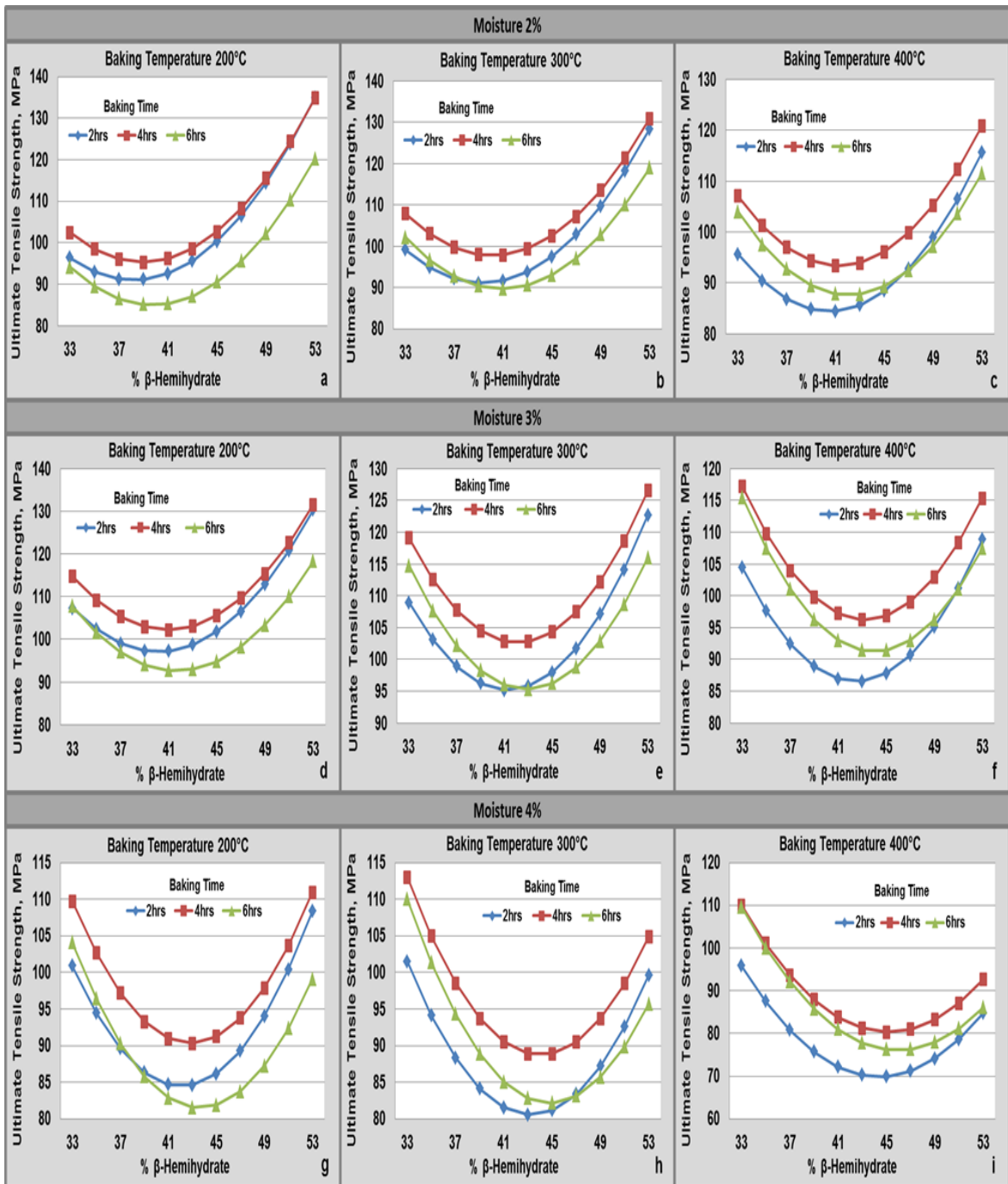


Fig 6.3 Ultimate tensile strength values of aluminium casting with varying compositions

Tensile strength values ranging from 80 to 130MPa are obtained experimentally, and are also predicted by the model built. It is difficult to connect exactly the possible reasons and the variations observed in Fig 6.3 without further experimental data, such as the possible thermal property variations with varying material and process conditions and the ensuing changes in thermal histories. Considering that such experimental work is quite involving and beyond the scope of this work, it is understood that the initial reduction in the tensile strength with increasing hemihydrate could be the result of decreasing permeability and consequent entrapment of gases. With further increase in hemihydrate, there is possible insufficient formation of the network of crystals, resulting in better permeability and formation of sound castings which is resulting in the enhanced tensile strength in all the cases.

#### ***6.2.4 Mould-metal interactions***

Further to breaking the mould and extracting the solidified casting, SEM photomicrographs are taken at different locations in both the mould material and the surface of the casting to ascertain adverse interactions if any. The photomicrographs on the surfaces of the mould directly in contact with the liquid metal are presented in Fig 6.4(a), (b) and (c). The gypsum crystal structure can be seen still intact from these photomicrographs. There is a general rounding, plastering, and discolouration of the material ingredients under the direct action of the hot metal, but no visible traces of excessive burning and loss of the material integrity is evident. There are pockets of material loss however, which could have

resulted in the porosity discussed above. Further, the SEM photomicrographs at different locations in the interior of the mould wall presented in Fig 6.4(d) to (f) are the normal gypsum crystals holding the sand particles together as presented earlier in Chapter 3. There is no trace of any metal penetration or adverse interactions.

The metal surfaces of the castings produced are photographed using SEM and presented in Fig 6.5. The photomicrographs at lower magnifications presented in Fig 6.4 (a) to (c) show general signs of the metal surface solidifying within a sand mould. The undulations and the flow patterns are indicative of the liquid metal settling down gradually and cooling, while there are also occasional rat-tail formations. While the porosity is clearly evident, which could have caused the widely varying tensile strength results depicted in Fig 6.3; there is no evidence of any mould erosion or inclusions. The occasional white specs observed are points to be verified, though, and are photographed at higher magnifications and presented in Fig 6.4 (d) to (f). EDS analysis conducted based on a two of these photomicrographs are presented in Fig.6.5 and 6.6 and evidently, the predominant element is aluminium.

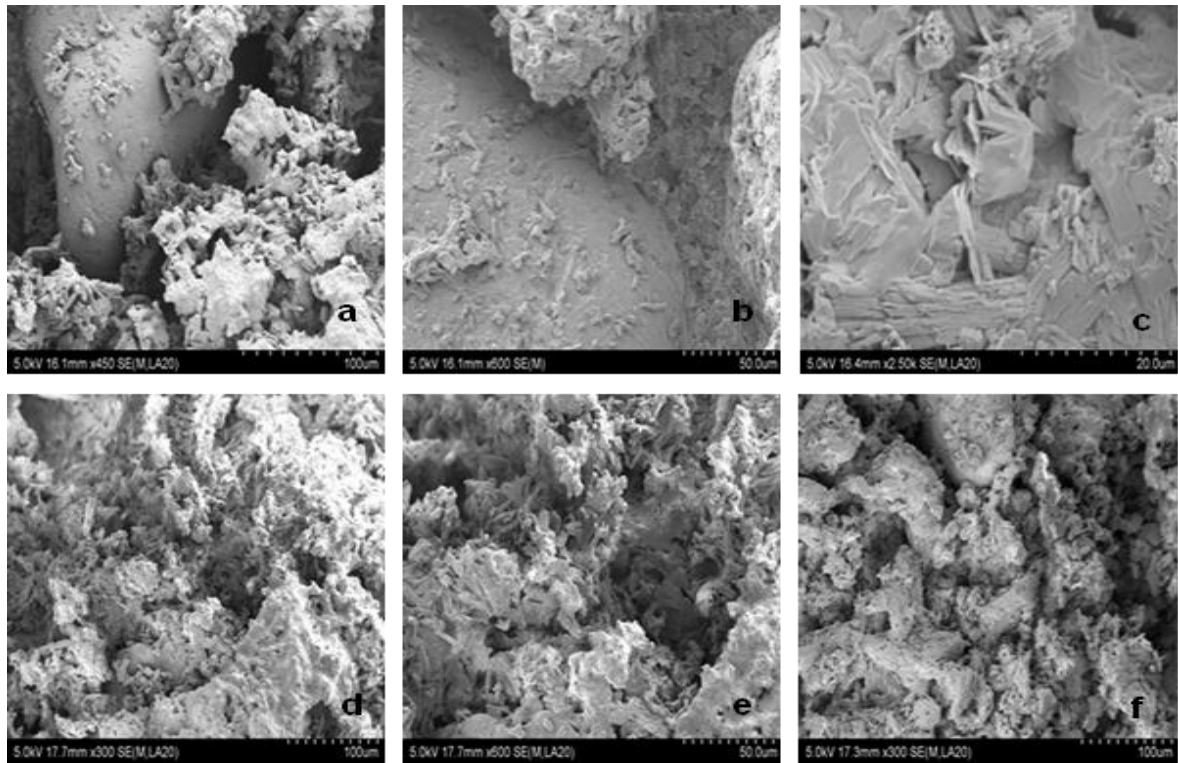


**Fig 6.4** Photomicrographs of the mould material further to casting; (a) to (c): Mould wall and (d) to (f) interior

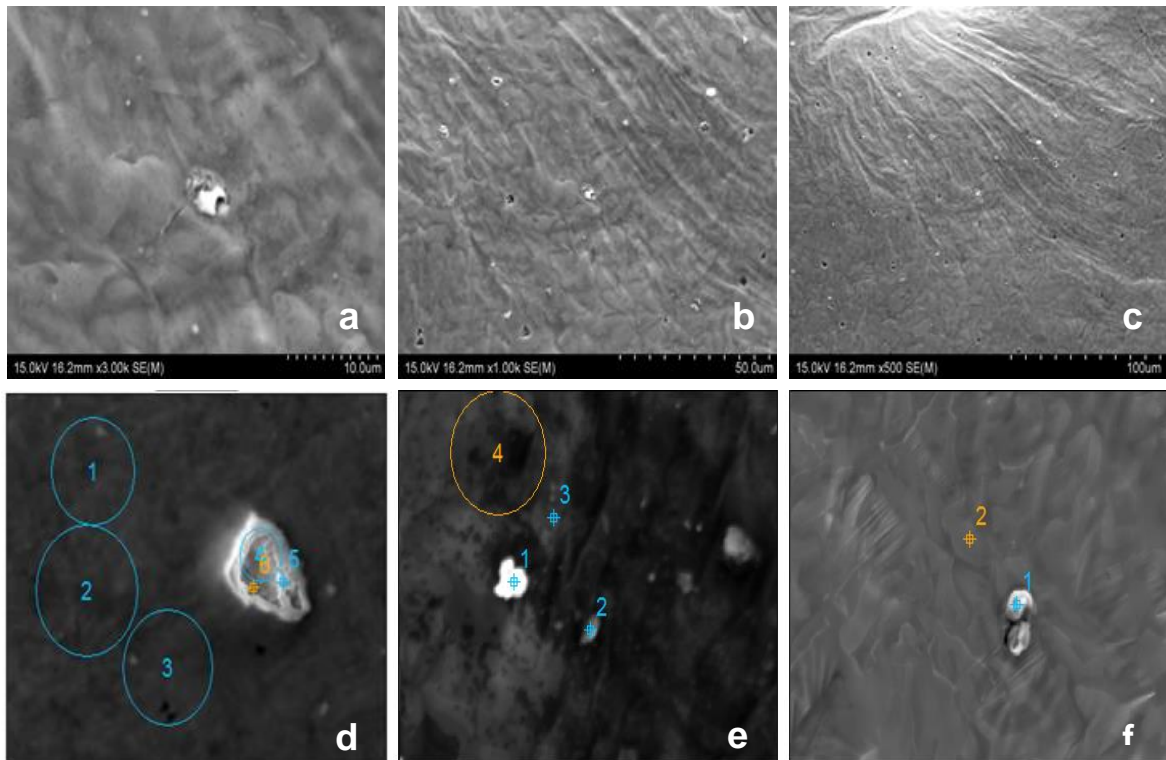


**Fig 6.5** EDS Analysis of mould metal interaction on the surface of the aluminium casting

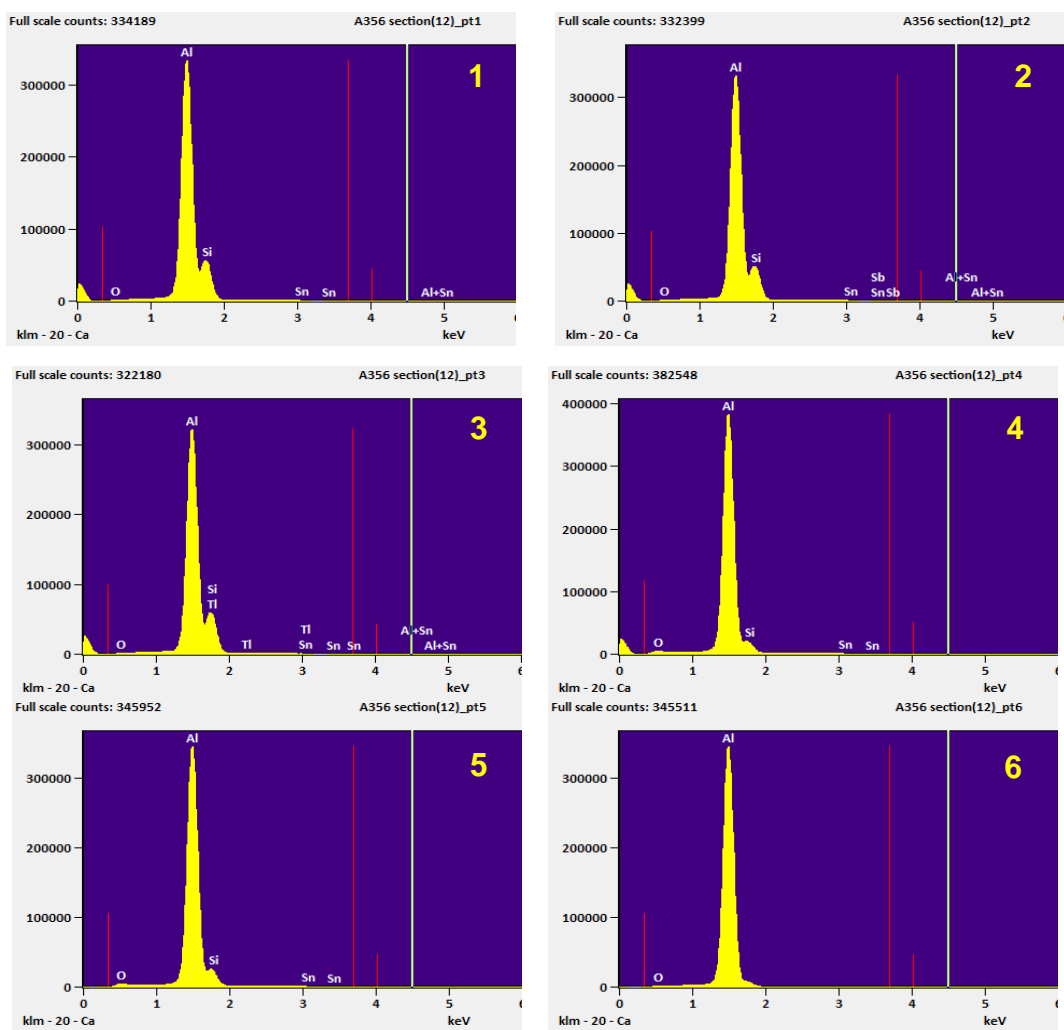
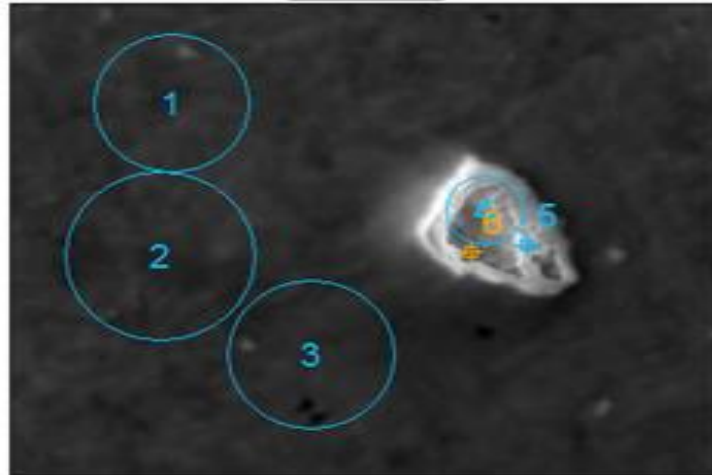


**Fig 6.6 EDS analysis of the surface of the aluminium casting based on the photomicrograph in Fig. 6.5 (d)**

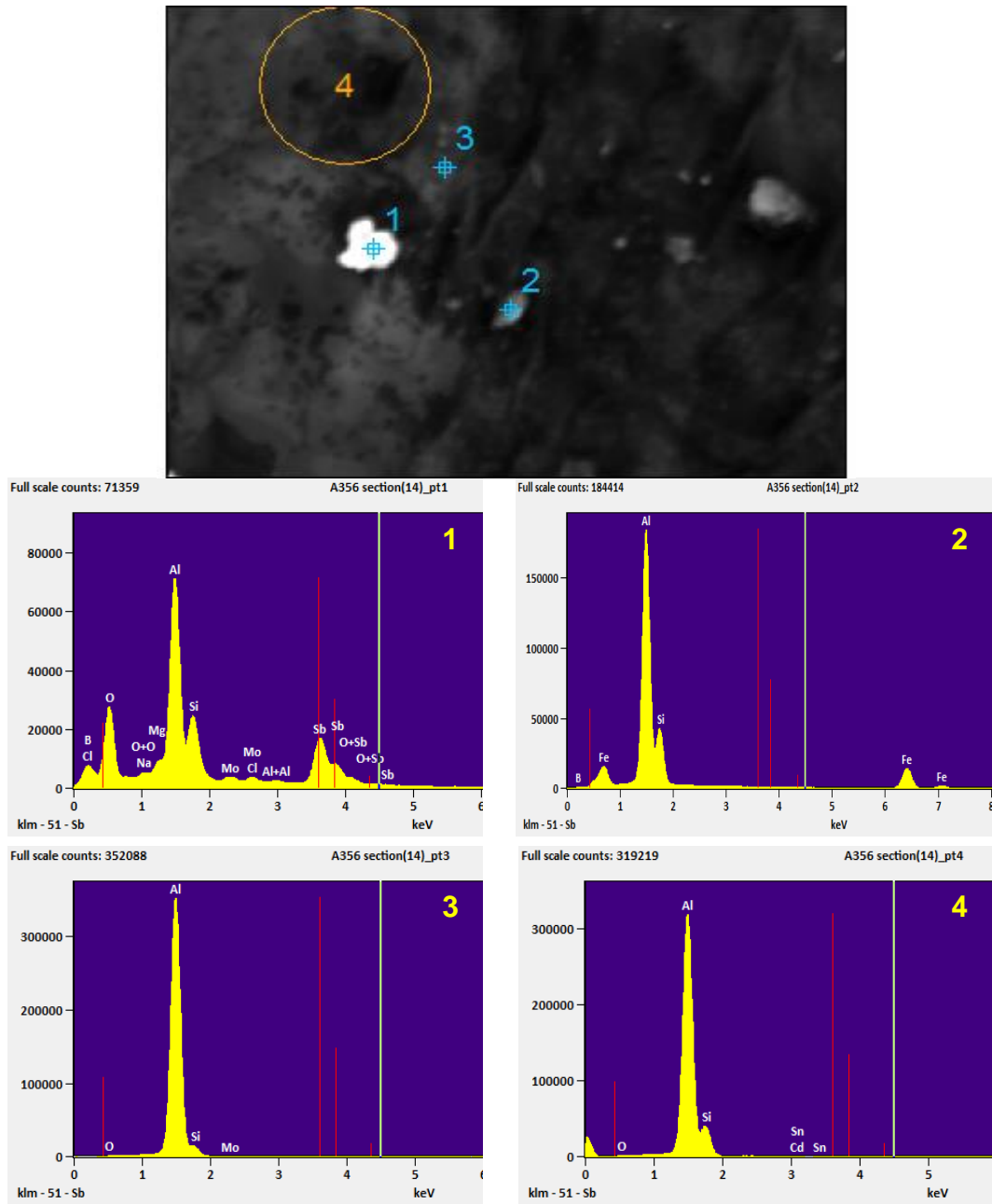


**Fig 6.7 EDS analysis of the surface of the aluminium casting based on the photomicrograph in Fig. 6.5 (e)**

### 6.3 Sodium silicate treated plaster-clay system moulds for aluminium casting

The quality of castings produced from the clay-plaster-sand composite developed and discussed earlier is considered in similar lines, also following the Box-Behnken design presented in Chapter 4. Considering the number of factors, the overall number of trials is 15. Also, the volume errors, surface roughness values and tensile strengths based on the cylindrical test pieces cast as discussed earlier are the primary responses. The experimental results together with the factor combinations for different trials are presented in Table 6.2. The response surface models developed based on these results and the general trends of variation of the responses with varying conditions are as follows.

#### 6.3.1 Percent volume error

The ANOVA based on the percent volume errors in the aluminium castings produced using the printed plaster-clay-sand based moulds resulted in no significant variation in the adjusted R-squared values further to considering the most significant factors. Hence the full model is developed as shown in Eq. 6.4 for further evaluation of the response.

$$Y_{DVE} = -12.0554 + 0.417694X_1 + 2.069758X_2 - 1.58495X_3 - 0.00652X_1^2 - 0.04809X_2^2 + 0.103978X_3^2 + 0.010588X_1X_2 + 0.008004X_1X_3 - 0.01874X_2X_3 \dots \dots \dots (6.4). \text{ where, } Y_{DVE} \text{ dimensional volume error}$$

**Table 6.2 Mechanical properties of the aluminium casting**

Run	% α-Hemi Hydrate	% Terra Alba	% Calcium Bentonite	Volume Error (%)	Surface Roughness Ra (µm)	Ultimate Tensile Strength (MPa)
	X <sub>1</sub>	X <sub>2</sub>	X <sub>3</sub>			
1	25	12.5	12.5	13.51	4.17	119.17
2	75	12.5	12.5	16.28	4.35	115.38
3	25	37.5	12.5	0.00	6.46	124.61
4	75	37.5	12.5	16.00	10.52	127.96
5	25	25	6.25	17.19	7.7	126.77
6	75	25	6.25	18.37	7.11	108.95
7	25	25	18.75	25.18	6.06	129.32
8	75	25	18.75	31.36	7.61	117.46
9	50	12.5	6.25	9.08	8.69	135.26
10	50	37.5	6.25	16.92	3.59	125.63
11	50	12.5	18.75	25.18	4.1	129.68
12	50	37.5	18.75	27.15	2.89	120.32
13	50	25	12.5	18.37	3.18	105.95
14	50	25	12.5	19.63	4.56	129.62
15	50	25	12.5	31.11	4.14	120.47

The percent volume errors predicted using Eq. 6.4 plotted in Fig 6.8, with varying hemihydrate for different combinations of the other parameters. While the overall range of variation in the volume is around 10 to 35% across all combinations, these values are again made up of the normal contraction of the liquid metal, which is common and can be compensated for. The rest of the variation is due to the loss of dimensions from the printed moulds. Based on a quick recollection of the percent volume error variation in the printed and baked moulds as presented in Fig 4.6, it may be ascertained that the volume changes in the castings follow a similar pattern. In almost all the cases, there is slight increase in volume error with increasing hemihydrate content in the mould material and a further slight reduction in some cases towards the end.

However, the overall error magnitude in many cases is much higher than the expected values. Evidently, the swelling characteristics appear to have varied effects in more complex shapes such as the mould cavities. Nevertheless, the average volume error is at around 10% with the best combination of material and process conditions; 12% bentonite, 12.5% gypsum and for any amount of hemihydrate.

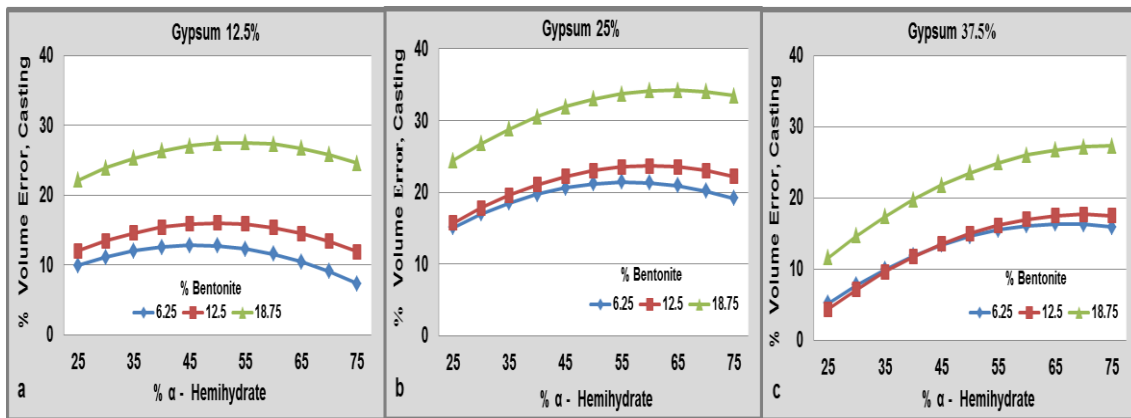


**Fig 6.8. Percent volume error of aluminium castings made using moulds printed by the plaster-clay system and treated with sodium silicate and baked**

### 6.3.2 Surface roughness

The ANOVA done based on the surface roughness values of the aluminium castings produced from the current moulds yielded a negative adjusted R-squared value, indicating that none of the variables have any significant role to play in the variation of the response. The experimental results indicate this as most roughness values are within the narrow range of variation from 4 to 10 $\mu$ m. The full model considering all the factors is developed as given in Eq. 6.5. Surface roughness results predicted by this equation are plotted for varying hemihydrate with different combinations of the other parameters as shown in Fig 6.9. Overall, the maximum surface roughness is within 10 $\mu$ m, which is the normal range for the sand casting process [67]. Within the limits of the current experimental domain the combination; hemihydrate 45-55%, bentonite 12-18% gave the best surface roughness results with 12.5% or 25% gypsum used as the seeding agent.

$$Y_{ASR} = 26.505 - 0.4718X_1 - 0.3073X_2 - 1.1238X_3 + 0.003774X_1^2 + 0.00036X_2^2 + 0.020512X_3^2 + 0.003104X_1X_2 + 0.003424X_1X_3 + 0.012448X_2X_3 \dots \dots \dots (6.5)$$

where,  $Y_{ASR}$  is average surface roughness.

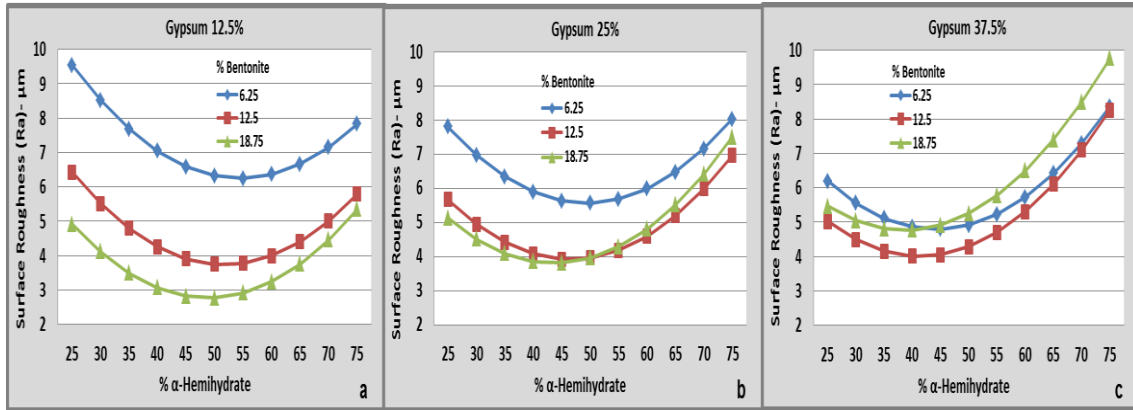


Fig 6.9 Average surface roughness (Ra) of aluminium castings with varying  $\alpha$ -hemihydrate.

### 6.3.3. Ultimate tensile strength

Again, the adjusted R-squared values based on the ANOVA of the tensile strength data is negative, indicating no specific variable having any significant role on the variation of the response. The full model with all the factors, their quadratic effects, and the first order interactions considered is constructed as presented in Eq. 6.6. The results predicted based on this model are shown in Fig. 6.10 for specific combinations of material and process parameters. While the tensile strength values varied within a very narrow range from 116 to 132MPa, the curves are also closely bunched, indicating no significant variation with any individual parameter. The best tensile strength results around 130MPa are obtained at lower hemihydrate in the range 25 to 35% and lower bentonite and lower or higher gypsum levels.

$$Y_{UTS} = 167.955 - 0.0928X_1 - 1.9377X_2 - 3.019X_3 - 0.0032X_1^2 + 0.032632X_2^2 + 0.10096X_3^2 + 0.005712X_1X_2 + 0.009536X_1X_3 + 0.000864X_2X_3 \dots \dots \dots (6.6)$$

where,  $Y_{UTS}$  is ultimate tensile strength

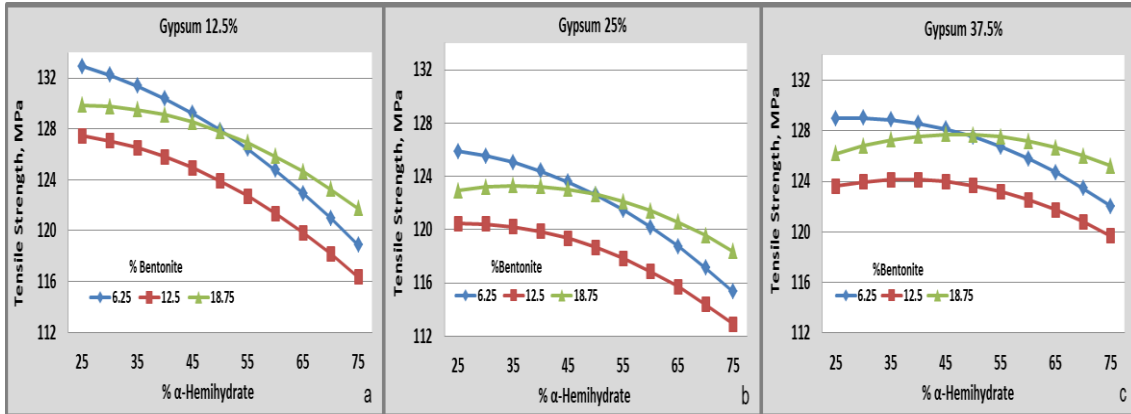


**Fig 6.10 Variation in the ultimate tensile strength of aluminium castings with varying  $\alpha$ -Hemihydrate.**

**6.3.4 Mould metal interactions in the case of the sodium silicate treated plaster-clay system**

All the moulds used for casting were found to be perfectly intact after the completion of the casting process. There was no trace of any adverse thermal effects from the molten metal. No physical changes and even the discolouration was noted to be negligibly small. The surfaces of the castings were also noted to be clean, shiny and without any damage either adverse interactions or mould erosion and inclusions. Considering these physical observations, it was understood that there were no adverse mould metal interactions in this case and no further experimental investigation was carried out. The clay content helped

increase the refractoriness, while the sodium silicate treatment increased the mould strength substantially.

#### **6.4 Ferrous casting on moulds printed using resin coated sand material system**

The casting responses of the clay-resin bonded moulds will be presented and discussed in this section. Considering the specific intention in this material system to be to increase the refractoriness based on the clay content, ferrous casting based on a stainless steel grade is attempted. Considering the high melting temperature and the overall casting difficulties, the experiments proved to be time consuming and costly currently. Due to this, a few trials are only undertaken, considering the role of varying clay content at two different levels of silica flour. Moulds are printed as per the compositions presented in Table 6.3 and subsequently baked at 200°C for 2hrs with a heating rate resulting in 50°C increases every 30 minute interval.

Stainless steel is cast into the baked moulds at Progressive Castings Ltd, one of the local foundries in Auckland. The metal filling was smooth, and the moulds withstood both the high melting temperature as well as the erosion action of the molten steel. The castings solidified without any mould cracking or other issues and could be extracted in good form and dimensional conformity. The runner, riser and other excesses are removed and the cylindrical test pieces produced as per the dimensions of 20mm in diameter and 110mm in length. These were then

measure the dimensional variations and surface roughness values. The cylindrical pieces are then turned to the form of standard tensile test specimens for further evaluation of the tensile properties. The volume errors, surface roughness and tensile strength results are listed in Table 6.3.

**Table 6. 3 Mechanical properties of the stainless steel casting**

Run	Silica Flour (%)	Clay (%)	Volume Error (%)	Surface Roughness Ra, (μm)	Ultimate Tensile Strength (MPa)
1	5	6	6.87	10.37	571.15
3		8	7.79	5.96	490.44
5		10	9.59	8.36	513.74
7		12	11.62	10.21	495.81
2	10	6	8.14	7.47	501.76
4		8	10.69	7.45	511.27
6		10	11.94	4.46	592.79
8		12	15.81	6.76	592.99

#### **6.4.1 Percent volume error**

The percent volume errors obtained from the dimensional variations in the cast steel cylinders are presented in the form of bar charts in Fig 6.11. Each test is repeated two times for establishing the statistical validity of the results obtained. The error bars in the bar chart indicates the variation noted in repeated trials. The overall range of variation and the standard deviation are very small, indicating no random errors in the experiments. The lower clay and silica flour contents at around 6% and 5% respectively scored the least in terms of volume errors, while the lower clay (6%) and higher silica flour (10%) resulted in the lowest volume error, at around 7%.

Again, considering that the volume errors in the castings are the combined result of the shrinkage of the metal as well as the dimensional variations in the printed moulds, and that the metal shrinkage part can be excluded from this discussion, the lower volume error cases should have achieved lower volume errors in the moulds. Referring back to Section 5.7.2, the percent volume errors in the baked samples presented in Fig 5.7 confirm this. The lowest volume error was obtained with the 6% clay and 5% Silica flour combination, as is also the case with the volume errors in the castings. With some micro variations, the other results also are in accordance with the volume errors noted with the moulds.

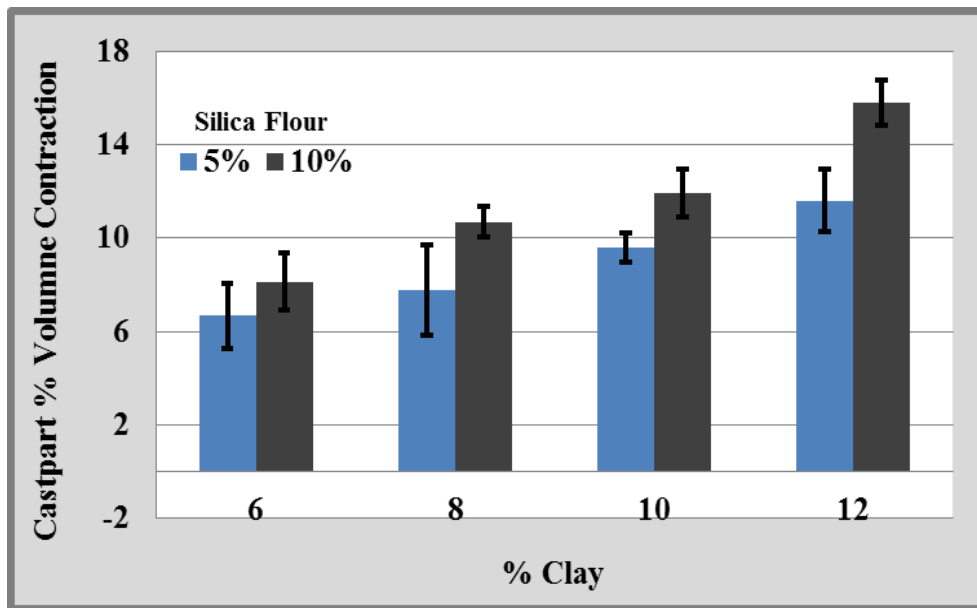


*Fig 6.11 Percent volume error of the steel casting by varying clay percent in the mould material system*

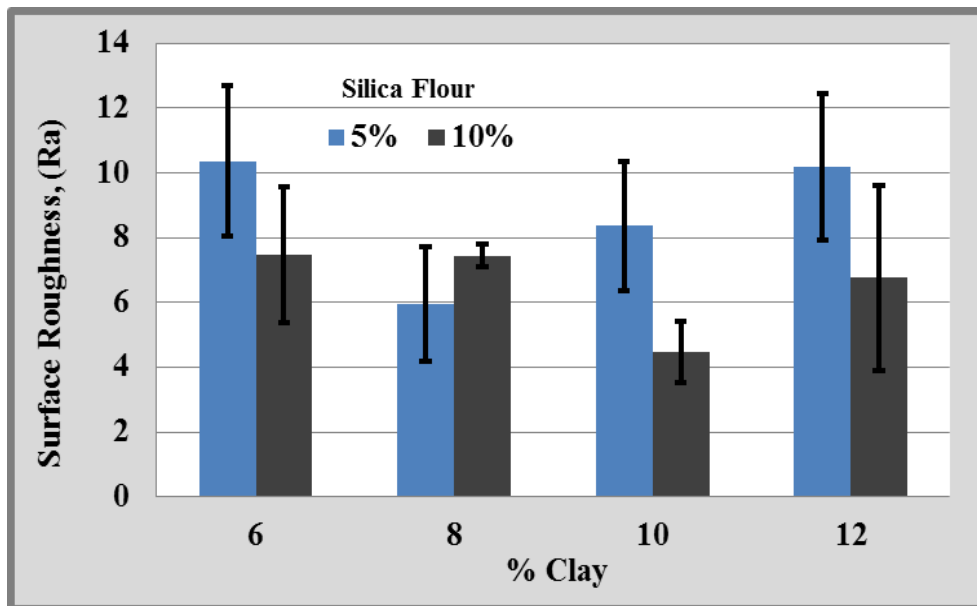


*Fig 6.12 Average surface roughness (Ra) values of the steel casting by varying clay percent in the mould material system.*

### **6.4.2 Surface roughness**

The surface roughness values are plotted in Fig 6.12 for varying combinations of clay and silica flour. Overall, the surface roughness varied within around 5-10 $\mu\text{m}$ . In general, the moulds with the higher silica flour content resulted in better surface roughness values relative to the lower silica flour ones, at all levels of clays. However, considering the wider variations noted in each measurement, it may appear that experimental uncertainty in these measurements is higher relative to the minor variations caused due to varying compositions. Hence an evaluation at the factor level is not really useful, but the average surface roughness values in all the cases are within the normal allowed limits for sand casting, and the material scores high in that sense.

### **6.4.3 Tensile strength**

The tensile test results based on the stainless steel cylinders cast in the 3D printed clay-resin bonded moulds are presented in Fig 6.13. Barring a few minor variations and notwithstanding the wider variations in measured quantities in some cases, it may be noted that most of these values average almost to the same level at around 550MPa. This is the normal range for the mechanical strengths of different grades of stainless steels [136] and so, it may be considered that the mould materials did not induce any adverse effects on the steel in terms of the mechanical properties.

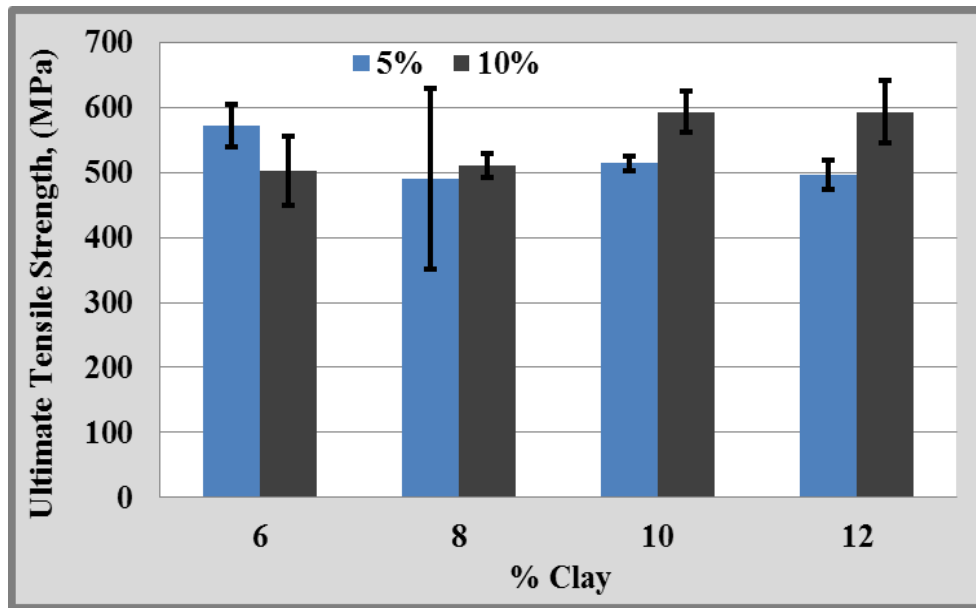


**Fig 6.13** *Ultimate tensile strength of the steel casting by varying clay percent in the mould material system.*

### 6.5 Case studies

As discussed above, the plaster based material system for the 3D printing of moulds scored the least in terms of all three responses considered; volume errors, surface roughness and tensile strength. As a result, this material is not used for the case studies considered in this section. The other two material systems are used for specific parts considered to evaluate how the systems perform in real world applications. It may be noted that the mould material attributes, in particular the volume changes may vary from a simple geometry to a relatively complex form. While this is already experienced moving from simple cylindrical forms to the moulds used for the cylindrical test pieces considered for the casting property

analysis, it will be interesting if there will be further variations with more complex forms as are necessary in the real world applications.

### ***6. 5. 1 A single cylinder engine block based on the sodium silicate treated plaster-clay material system***

A single cylinder engine block with water jackets as depicted in the CAD model presented in Fig 6.14 is considered as the case study for evaluating the performance of the sodium silicate treated plaster-clay-sand composite as the mould material through 3D printing. The mould is designed with a single runner, gating system and a couple of risers at the centre as shown in Fig 6.15. The design ensures sufficient head for the molten metal in the riser and a smooth flow and filling within the mould cavity as the metal enters from the bottom upwards through the runner branched into two gates. Considering the overall size of the mould, it is split into multiple parts and each part is printed separately, baked, assembled, and glued using an industrial moulding paste to build the complete mould. The best possible mould material composition and baking conditions are used based on the results reported in Chapter 4. Photographs of the assembled mould, the aluminium filled mould supported by backing sand, the solidified form as taken out of the mould, and the final casting are presented in Fig 6.16.

The metal filling was smooth, and there was no excessive gassing or bubbling of the liquid metal as it completely filled the mould cavity and rose on the other side

through the riser, forming a convex meniscus at the start that settled down to a concave form towards the end, considered to be indicative of a good casting in foundry practices. The solidified casting is removed from the mould after cooling down to the room temperature and both the mould and the metal surfaces did not show any signs of thermal or chemical distortions, as was the case with the trials reported above.

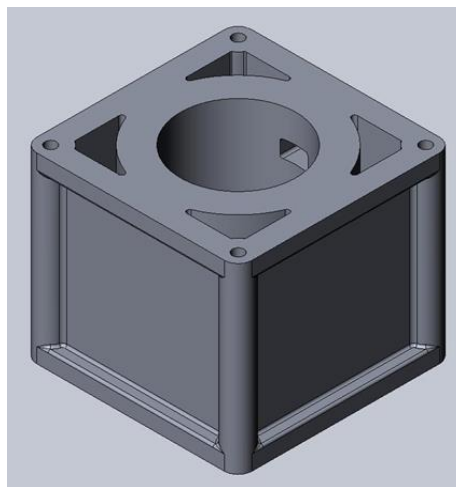


**Fig. 6.14** The CAD file of the single cylinder engine block with vertical water jackets

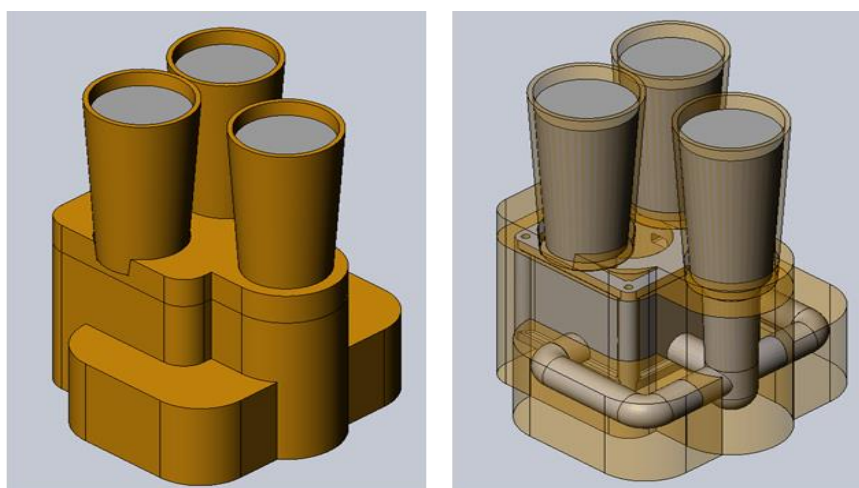


**Fig. 6.15** The CAD model of the mould designed for the single cylinder engine block



**Fig. 6.16** *The casting process and outcomes (a) assembled mould, (b) aluminium filled in the mould backed-up by foundry sand, (c) the solidified shape, and (d) final casting*

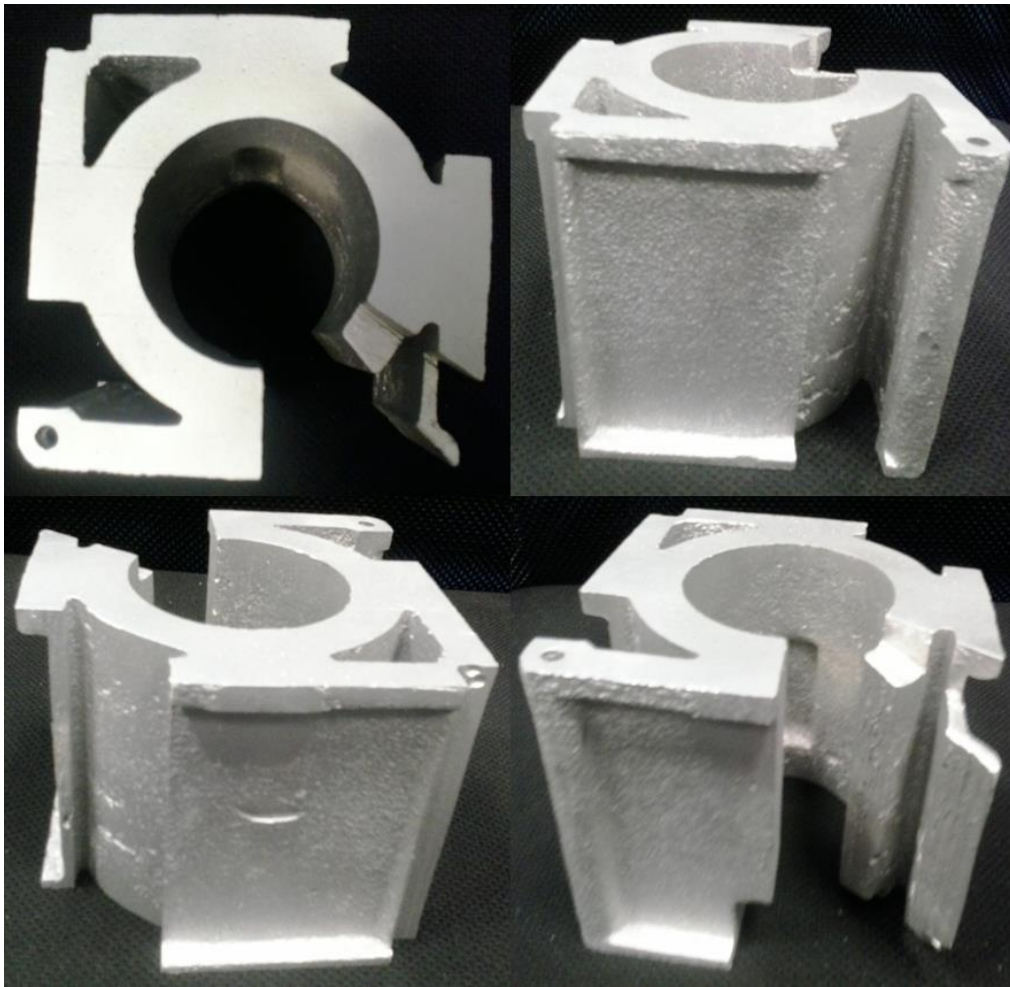


***Fig. 6.17 Aluminium casting machined for dimensional quality assessment***

The cylinder block is cleaned next and both the top and bottom surfaces are skimmed on a milling machine. A band saw is used to cut the corners as shown in Fig 6.17, and the exposed surfaces are smoothed by light milling enabling measurement of critical dimensions. Four dimensions are considered critical; the width (marked as 1 in Fig 6.16d), the length (B), and thickness (marked as 2 in Fig 6.16d) of the cylindrical wall and the overall height of the block (D). Each of the first three dimensions is measured ten times along the height, at even increments, and the height is measured at two to three places on each edge before milling the

top and bottom surfaces and the values of the percent errors measured are recorded in Table 6.4. The percent errors in the dimensions are plotted as shown in Fig 6.18. It may be noted that in most dimensions the maximum errors are within 2-3%. The thickness of the cylindrical wall by far experienced the maximum variation in dimensions, due to the swelling of the mould walls.

**Table 6.4 Percentage errors in the dimensions of the cast cylinder block**

<b>Points</b>	<b>Width</b>	<b>Length</b>	<b>Thickness</b>	<b>Height</b>
<b>1</b>	2.496	1.248	0.667	2.813
<b>2</b>	1.872	2.763	5.333	2.813
<b>3</b>	3.03	3.298	8	2.5
<b>4</b>	2.763	3.03	7.333	2.292
<b>5</b>	2.763	3.119	8.667	2.292
<b>6</b>	2.496	2.941	8.667	1.771
<b>7</b>	2.585	2.763	4.667	2.187
<b>8</b>	1.693	3.387	6.667	1.563
<b>9</b>	2.852	2.852	4.667	1.875
<b>10</b>	1.337	1.337	2	2.187

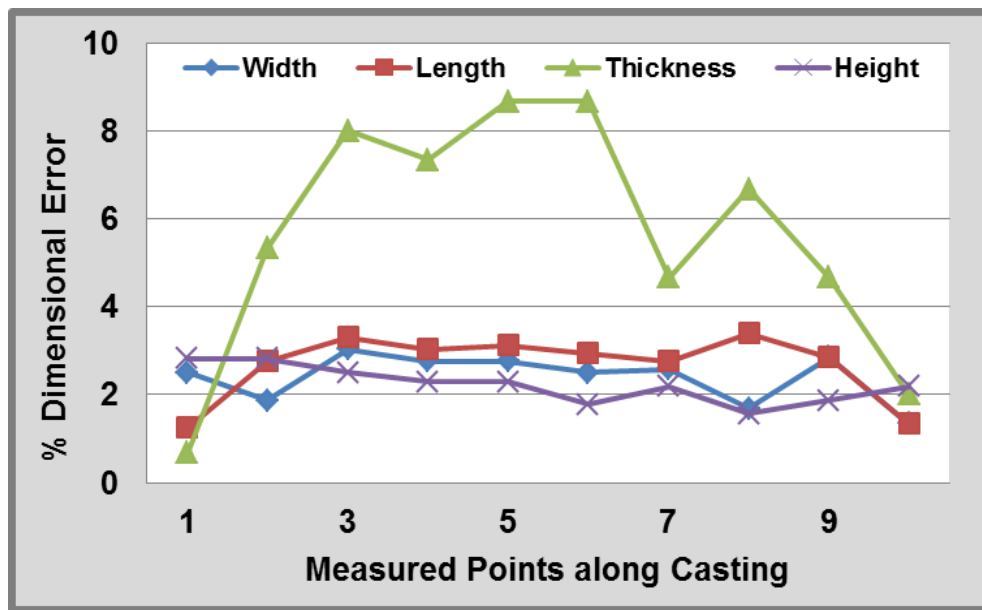


*Fig 6.18 Percent errors in dimensions plotted against locations*

### **6.5.2 Stainless steel step-cone cylinder cast in printed moulds based on the resin coated sand material system**

Step-cone test is often considered by researchers to evaluate the quality of a casting process based on both qualitative and quantitative observations [151,152]. This method is adopted here for evaluating the quality of the stainless steel casting produced based on the clay-resin coated sand moulds. The CAD image of the mould developed for casting the step cone shape as per the standards of the American Foundry Society is presented in Fig 6.19(a-c). The mould shown in Fig 6.20 is printed using the best combination of the material composition and baking conditions as presented in Chapter 5. A casting grade of stainless steel was used and the step-cone mould was filled on site at Progressive Castings Ltd in Auckland. A photograph of the stainless steel step-cone casting is presented in Fig 6.21.

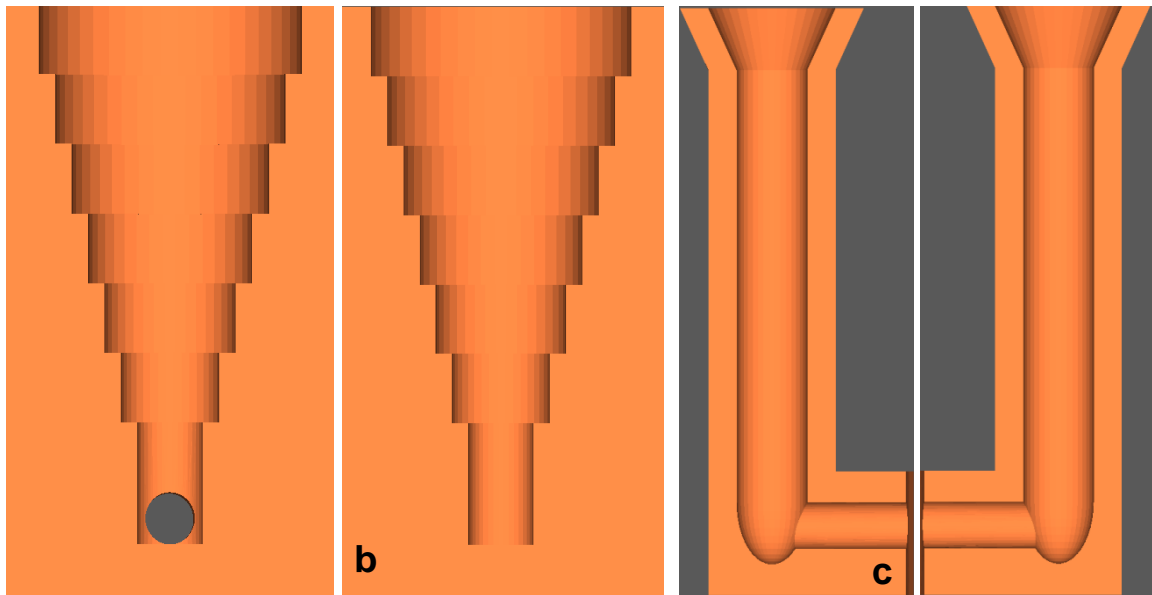
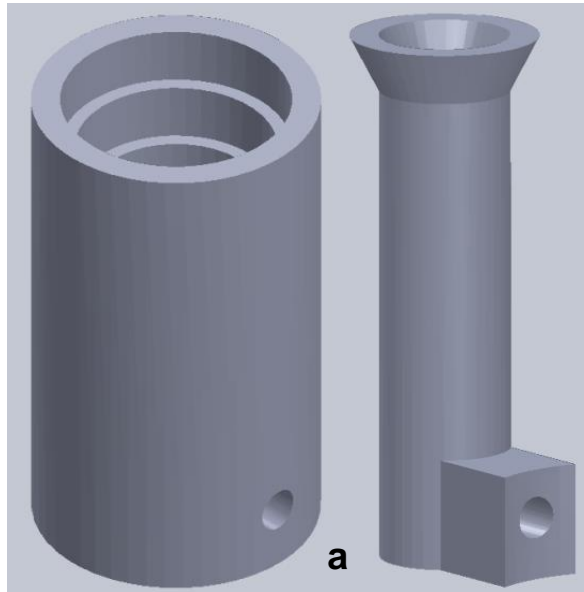


*Fig. 6.19 (a-c) The CAD model of the mould for the step-cone casting*

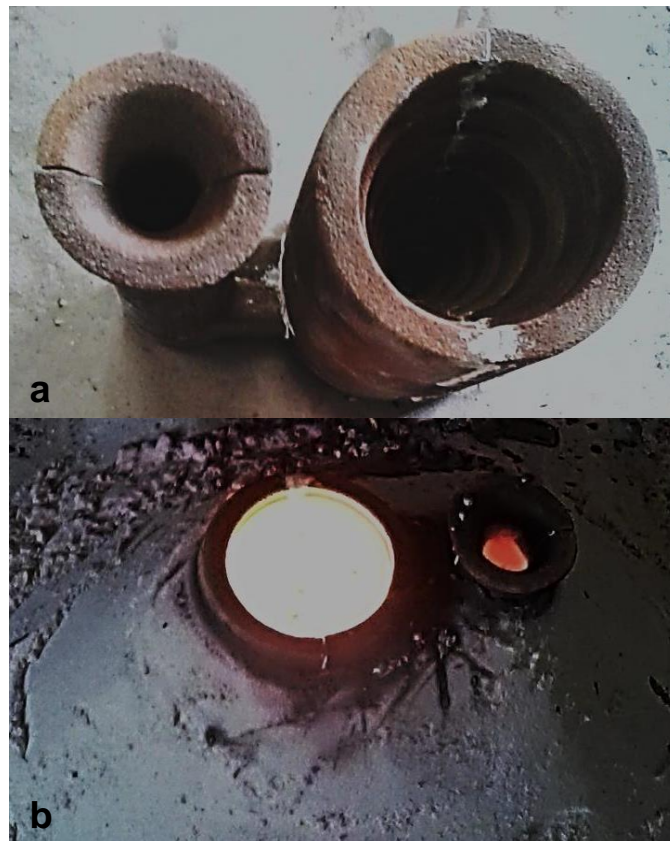


***Fig 6.20 (a) The baked mould and (b) stainless steel solidifying in the step-cone mould***

Qualitatively, the casting is successful to a large extent, in terms of reproducing the CAD model. The measured dimensions shown in Fig 6.22 and Fig 6.23 are close to the design values, as a maximum of about 5% variation is noted. The surface quality is reasonable for a first attempt and mould coatings could improve this further. Mould erosion is evident slightly at places, as extra metal deposition is observed and would need further attention. It may be observed that there is no evidence of metal penetration or the waning effect, the more serious problems observed with the step-cone tests when the moulds are not up to the required quality standards.

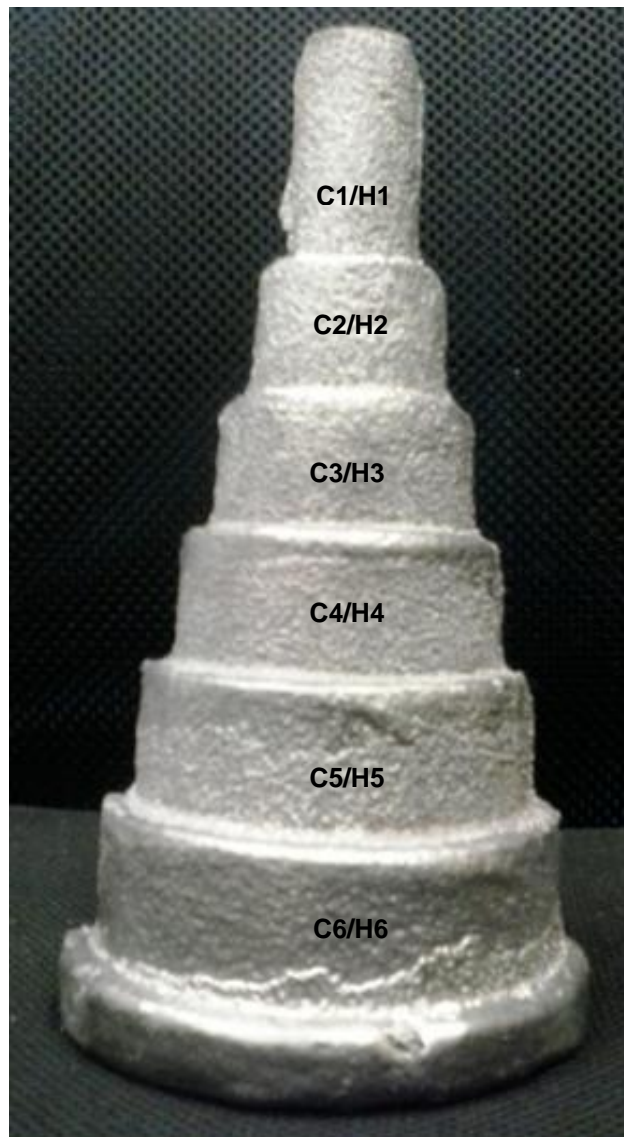


*Fig 6.21 The stainless steel step-cone casting*

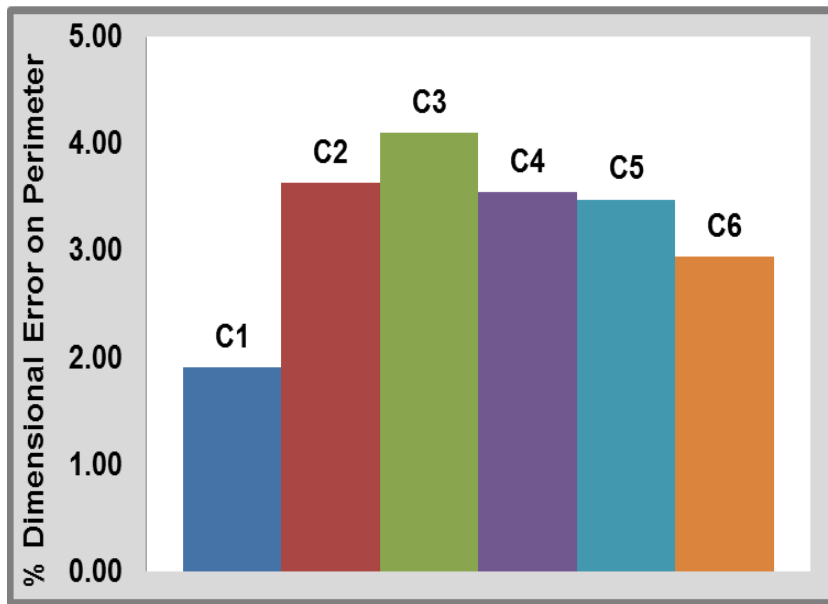


**Fig 6.22** The percent dimensional error around the periphery of the step cone casting

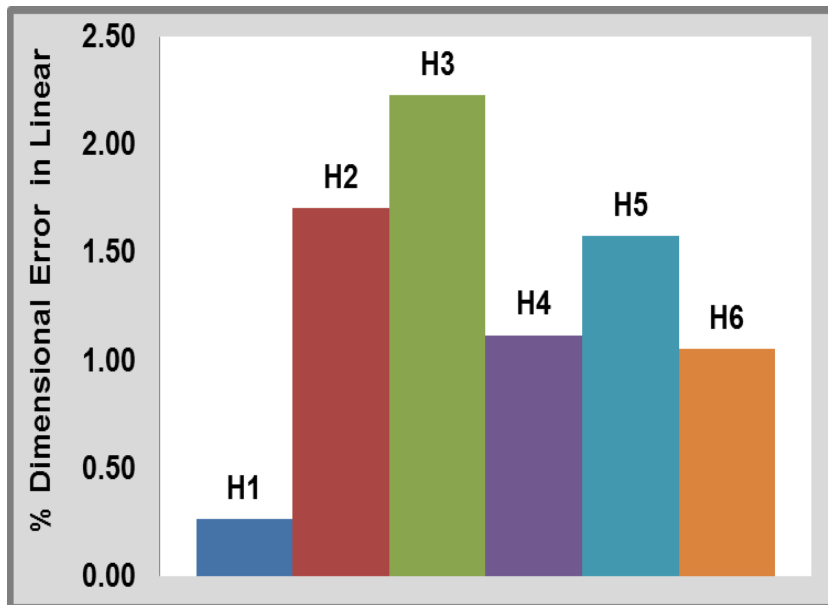


**Fig 6.23** The percent dimensional error along the axis of the step cone casting

## 6.6 Summary of casting trials and results

The three material systems presented in Chapters 3 to 5 are tested for the quality of castings, considering the production of standard test specimens using the moulds printed. Comparatively, the plaster-silica sand composite moulds scored the least in terms of the volume errors, surface roughness, and the tensile strength of the castings produced. On the other hand, the plaster-clay-sand composite moulds treated with sodium silicate performed well with aluminium castings, while the clay-resin sand composites exhibited sufficiently high refractoriness allowing casting of stainless steel to reasonable quality levels. Surface roughness, porosity and mould strength are further aspects to be considered next when these systems are fine tuned in the future. The two case studies considered with the material systems presented in Chapters 4 and 5 demonstrated that the observations made with relatively simple moulds are also true with more complex shapes.

## Chapter 7

### Conclusions

#### 7.1 The experimental research done and the overarching results

The overall objectives of the current research include evaluation of the possible use of selected material combinations and specific bonding mechanisms based on the knowledge from traditional foundry and other related processes to achieve the material consolidation within a 3D printing system and understanding the roles of varying constituents. Three material systems are considered utilising plaster, clay, and resin bonding as possible means of achieving the necessary green and dry strengths for the printed moulds. Initial responses of each material system to 3D printing conditions are first evaluated to establish the missing attributes. This is followed by supplementing with additional ingredients and alterations to achieve final bonding to the required levels. Each material system is further evaluated systematically, first ascertaining the mechanisms of bonding in both green and dry states and then establishing the mechanical properties and the roles of varying ingredients.

The hydration and dehydration mechanisms of plaster are evaluated first based on a plaster-silica sand composite for 3D printing. Initial unsuccessful trials with varying plaster contents necessitated the use of an accelerator for the hydration reaction of the plaster. Pre-moisturisation of plaster is employed as the possible

acceleration mechanism and proved to be suitable to achieve the timely reaction rates. The roles of varying amounts of plaster and pre-moisture combinations are evaluated next together with varying temperature and time conditions for post printing baking considering critical responses in both green and dry states.

Clay-silica sand composites were considered next based on the electrolytic bonding and higher refractory characteristics of clays. Initial printing trials were unsuccessful with this material combination also as green strengths attained were insufficient. The plaster hydration is used again together with terra alba as the seeding agent to accelerate the hydration reaction. The clay-plaster-terra alba composite helped achieve sufficient green strengths, but failed to sustain the subsequent baking. Soaking the printed green samples in sodium silicate solution and subsequent heating resolved the problem and resulted in better baked properties. Mechanisms of bonding at different stages were ascertained, together with establishing the influences of varying ingredients and baking conditions on the final properties of printed mould samples.

Kaolinite clays mixed with resin coated sands were evaluated to achieve the possible green strength through the electrolytic bonding action of clays. Small amounts of fine silica flour are found to be necessary to disperse the clay particles and build the bonding forces further to printing. After baking, the resin coating is effective in sufficiently covering the clay-silica sand ingredients and developing the inter particle necks and subsequent strengthening through crosslinking. The

mechanisms of bonding in the green and dry states were evaluated and the mechanical properties of moulds with varying compositions were also established.

Moulds were designed and printed using the most suitable conditions with each of the material systems investigated and cylindrical test pieces were cast. Volume changes, surface roughness and tensile strength data were generated based on the cylinders cast. The plaster based system scored the least while the clay-based sodium silicate treated material and the resin coated sand mixtures were reasonably successful in terms of the casting quality. The resin coated sand material systems are also evaluated based on the quality of castings produced using aluminium and stainless steel.

## **7.2 General observations with different material systems**

### ***7.2.1 Pre-moisturised $\beta$ -hemihydrate-sand composite***

The plaster-sand composite considered is proved to be useful as a material for 3D printing with pre-moisturisation as the acceleration mechanism. When the right amount of moisture is pre-mixed with the material system, a small quantity of plaster is converted into gypsum and helps accelerate the hydration process. Later, with sufficient moisture content made available through the print head, the plaster to gypsum conversion initiates and progresses by crystallising to varying degrees, depending on the composition of the mould material mixture. The pre-

moisture and the hemihydrate interact depending on the level of each factor in influencing the initiation and rate of crystal growth.

The formation and the growth of gypsum crystals results in swelling and volume changes in the green state. The extent of these changes depends on the amount of pre-moisturisation together with the level of hemihydrate and the effective crystal formation and growth. When heated to around 300°C for sufficient duration, the needle like gypsum crystals change to relatively smoothed and rounded forms, filling the inter-sand particle regions and forming a continuous matrix structure in which the sand particles are embedded. The extents of these transformations depend on the amount of pre-moisture added. Baking results in volume losses to varying degrees as the excess moisture is driven off. Consequently, the volume errors in baked samples are less compared to the green samples.

The gypsum crystals holding the sand particles together is the predominant mechanism providing the compressive strength and resistance to the shear failure in the green state. Consequently, the pre-moisture and the plaster level combinations promoting better crystallisation will result in better green compressive strength. Considering that both pre-moisture and the additional moisture made available through the print head are limited, only a certain amount of plaster is hydrated and the excess plaster remains unbound, resulting in weaker material consolidation. When the green samples are baked the formation of the

hemihydrate first and the anhydrite crystals next as the temperature is gradually increased result in a gradual loss of compressive strength.

### ***7.2.2 Clay-silica-sand composites with sodium silicate treatment***

In the case of the clay-plaster-sand composites, the green strength is achieved from printing due to the formation of the gypsum crystals as well as the electrolytic bonding action of the clay particles. The gypsum crystallisation helps achieve the green strength probably by both increasing the concentration of the electrolyte as well as the slight temperature raises resulting from the exothermic nature of the hydration reaction. However, these bonding mechanisms become inactive after baking, as fragile parts result, necessitating the use of secondary strengthening methods such as sodium silicate treatment and baking. The soaking of printed sand specimens in sodium silicate for sufficient time allows dispersion of the binder between particles and the formation of the inter particle neck regions.

Absorption of moisture and subsequent formation of gypsum crystals result in volume changes. Subsequent sodium silicate treatment also results in swelling due to further gypsum crystallisation as well as the absorption and crystallisation of the gel. However, the subsequent baking process results in a slight loss of volume compensating for some of the expansion caused. Both flexural and compressive strengths are attributed to the nucleation, growth and the final form of the gypsum crystal growth in the green state but the electrolytic bonding forces of the clay particle appear to play relatively minor roles. Further to sodium silicate

treatment and baking, the strength values increased as the gel solidifies around the gypsum crystals, clay and sand particles, forming a complex network of interconnected neck regions.

### ***7.2.3 Resin coated sand system***

Clay particles in the form of flaky crystals develop electrolytic bonding forces and cling to the silica flour particles when treated with the moisture ejected from the print head. The agglomeration of clay crystals, together with the Van der Waals forces between clay and silica flour particles and the overall dispersion of the two phases within the spaces between the relatively large sand particles controls the green strength. The resin coating has a negligible role in developing the green strength. However, the subsequent baking results in partial softening and plastic flow of the resin, inter-particle dispersion and necking, followed by cross linking and solidification. The final mechanism of bonding is based on the network of solidified resin structures enclosing the silica flour and clay crystals within the narrow gaps between the larger sand particles.

Photo micrographic evidence suggests better dispersion of clay with higher silica flour content. The silica flour and the clay contents interact, controlling the number and size of the clay-silica flour clusters formed which will in turn influence the strengths in green and baked states. After baking, the plasticisation and flow of the resin and the effective mechanical strength after the cross linking and solidification

depend on the size and distribution of the clay-silica flour clusters. Further to this, the clay bonding is overridden by the resin bonding mechanisms in controlling the final mechanical strength of the printed and baked sample.

The bonding mechanism based on clays is associated with contraction to varying degrees. Also, the subsequent baking leads to further contractions as the excess moisture is lost. However, the overall volume contraction is found to be limited, qualifying the material for the production of intricate parts with tighter dimensional tolerances. With lesser silica flour content, the clay-silica flour clusters are formed wide apart, grow sufficiently large and result in better compressive strengths in the green states, compared to the higher silica flour cases. The post-baking compressive strengths are much higher than those in the green states due to completely different bonding mechanisms. The final strength after baking is controlled by the plastic flow, necking, crosslinking and hardening of the resin coating and the presence and dispersion of the clay-silica flour clusters.

### **7.3 Significant conclusions based on experimental results**

The following are the most significant conclusions drawn from a quantitative assessment of the roles of different ingredients of the three material systems investigated:

### **7.3.1 Pre-moisturised plaster-sand composites**

- Preliminary results using the pre-moisturised plaster-sand composite are indicative of the best possible ranges for the key constituents to be hemihydrate 33% to 53%, pre-moisture content 2% to 5%, baking temperature 200°C to 400°C, and baking time 2 to 6 hours.
- The formation and growth of di-hydrate crystals increases as the pre-moisture level increases from 2 to 4%.
- The gypsum crystal growth is quite needle-like and very intricate in the case of 2% pre-moisture compared to the other cases
- The percent volume error in the green state increases initially, attains a peak and then gradually drops as the percentage moisture level is increased.
- Also, the volume error in green samples decreases as the amount of hemihydrate is increased, at all levels of pre-moisture.
- The plaster content has a more significant effect on the volume errors, resulting in higher expansions at lower (33%) limits of plaster and lesser expansions at upper (53%) limits.
- Further to baking all samples contracted and in all the cases, the volume error gradually decreased, with increasing hemihydrate.
- The compressive strength in the green state gradually decreased with increasing pre-moisture content, when the plaster content is varied from 33 to 43%, but gradually increased with the 53% plaster case.

- With increasing plaster levels, the green compressive strength gradually decreased and either stabilised at lower values or slightly increased.
- At any moisture level and a given baking temperature, compressive strengths of baked samples decreased with increasing plaster content.
- With increasing moisture content, the compressive strength decreased substantially at all baking temperatures and plaster content conditions.
- Increasing baking temperature also consistently resulted in a loss of the mould compressive strength.

### ***7.3.2 Clay-plaster-sand composites with sodium silicate treatment***

- Terra alba plays a significant role in promoting gypsum crystal growth. The higher the terra alba content, the higher is the hydration of the plaster and the gypsum crystallisation.
- With terra alba and bentonite remaining at similar levels, the gypsum crystallisation generally increased with increasing  $\alpha$ -hemihydrate from 25% to 75%.
- Bentonite also promotes gypsum crystal growth. Considerable increase in the growth of gypsum crystals with bentonite content increasing from 6.25% to 18.75% at the same level of terra alba and 25% of hemihydrate.
- The effect of bentonite is less pronounced at 50% hemihydrate, while it is almost negligible with 25% terra alba and 75% hemihydrate.

- Sodium silicate treatment and subsequent baking result in a network of inter-granular connections and strengthening due to condensed siloxane bonds, while the extent of these transformations vary with the location within the printed part.
- The volume errors in the green state increase with increasing  $\alpha$ -hemihydrate, but beyond a certain limit, there may be stabilisation or even a slight reduction in the error.
- The higher the bentonite content, the lower the volume errors in the green state.
- Further to baking, the volume errors are higher than in the green state but the patterns remain similar to those obtained from the green samples.
- The higher the terra alba, the higher is the volume error after baking.
- The flexural strength in the green state increases with increasing hemihydrate, but decreases with increasing terra alba.
- Further to baking, terra alba shows influence on the flexural strength, while increasing hemihydrate resulted in gradual increase at lower levels of bentonite and a slight decrease in the flexural strength at higher levels of bentonite.
- Overall, the flexural strength values increased further to baking compared to the strengths of green samples.
- The compressive strength of the green samples gradually increased, attained peak values and then reduced to varying extents with increasing  $\alpha$ -hemihydrate.

- Also, the compressive strength in the green state increased with increasing hemihydrate, at higher terra alba and lower to mid-levels of bentonite.
- Overall, the compressive strengths of samples increased after sodium silicate soaking and baking, compared to the values in the green state.
- Further, the compressive strengths further to baking showed a continuous rise with rising hemihydrate contents at all combinations of the other factors.
- The role of terra alba seems to be negligible further to sodium silicate treatment and baking but the compressive strength gradually decreased with increasing bentonite.
- Lower  $\alpha$ -HH (50%) together with the lowest Terra alba (12.5%) and the Bentonite (6.25%) resulted in the highest compressive strength 1.3MPa further to baking.

### ***7.3.3 Clay-silica flour-resin coated sand composites***

- The clay-silica flour bonding and agglomeration increases with increasing amounts of clay from 6% to 12 % at both 5% and 10% silica flour contents
- The dispersion of the clay particles is more uniform at higher silica flour content of 10%.
- More nucleation sites and finer silica flour clusters result from better dispersion at higher silica flour contents.

- After baking, the clay bonding is overridden by the resin bonding as the clay-silica flour clusters are displaced and embedded within the polymer matrix.
- All samples undergo contraction to different degrees, but the lower the clay, the lower is the volume contraction
- Baked samples undergo further volume contractions, compared to the green ones
- Considering the plasticity of kaolinite clays and the limited moisture added, the maximum percentage volume contraction after baking is around 4%.
- Compressive strengths in the green state are very low and very close in all the cases.
- The compressive strengths of all samples are much higher after baking, and are almost identical at lower levels of the silica flour.
- At higher silica flour content of 10%, the baked compressive strengths decreased from about 5 MPa to around 2.5 MPa as the clay content is increased from 6% to 12%.
- Overall, the maximum compressive strength achieved is around 5 MPa, which is within the specifications by the American Foundry Society for casting a variety of metals.
- The general variation of the flexural strength after baking followed the same trends as the variation in the compressive strength.

## 7.4 Casting trials

Cylindrical test pieces were cast based on the moulds developed with the three material systems presented earlier. Influences of material and process conditions were evaluated considering the quality of castings based on dimensional variations, surface roughness and tensile strength. The volume errors and the surface roughness values are directly related to the corresponding attributes of the moulds printed. However, the variations in the tensile strength values are the combined effects of the permeability and the effective cooling rates. The following are the specific conclusions drawn based on the results from castings using the three material systems:

### ***7.4.1 Moulds by plaster based material system for casting aluminium alloy***

- The percentage shrinkage gradually decreases initially, attains a minimum and then gradually increases with increasing  $\beta$ -hemihydrate.
- With moisture varied from 2 to 3%, the percentage volume error increases by around 8% all around, with higher baking times.
- At 4% moisture case the percentage volume error decreases as the baking time is increased from 2 to 6 hours
- Moulds printed with 45%  $\beta$ -hemihydrate and 2-4% pre-moisturisation and baked at around 200 to 400°C for 2 to 4 hrs will yield A356 castings the least volume error, at around  $\pm 5\%$ .
- At 2% pre-moisturisation, the surface roughness of castings gradually increases with increasing hemihydrate.

- With 3% pre-moisture, there is a decrease initially, a minimum value attained and then a gradual increase in surface roughness, with increasing hemihydrate.
- With pre-moisture level at 4%, there is a continuous reduction in the surface roughness with increasing hemihydrate at all combinations of the other factors, with sufficiently long baking time,
- In all the cases, the lower baking temperature at 200°C resulted in lower surface roughness values.
- The higher hemihydrate in the range 45-50% together with higher pre-moisture, lower baking temperature and longer baking time combination resulted in the lowest surface roughness at around 25µm.
- Tensile strength values ranging from 80 to 130MPa are obtained experimentally and the model predicts a gradual reduction, a minimum and then gradual increase in the tensile strength with increasing hemihydrate for all combinations of the other factors.
- No visible traces of excessive burning and loss of the material integrity is evident with the moulds after pouring and solidification of the aluminium alloy.
- No traces of mould erosion, inclusions and metal-mould interactions are evident.

#### **7.4.2 Sodium Silicate treated plaster-clay material system moulds for aluminium casting**

- An overall 10 to 35% error resulted in the volume of the castings across all combinations of experimental conditions.
- The average volume error is around 10 % with the best combination of material and process conditions; 12% bentonite, 12.5% gypsum and for any amount of hemihydrate
- The surface roughness values are within a narrow range of variation from 4 to 10  $\mu\text{m}$
- Within the limits of the current experimental domain the combination; hemihydrate 45-55%, bentonite 12-18% gave the best surface roughness results when 12.5% or 25% gypsum is used as the seeding agent.
- The tensile strengths of castings varied within a narrow range from 116 to 132 MPa
- The best tensile strength results around 130MPa are obtained at lower hemihydrate in the range 25 to 35 % and lower bentonite and lower and both higher gypsum levels.
- All moulds were perfectly intact after the completion of the casting process with no trace of any adverse thermal or physical interactions.
- The surfaces of the castings are also clean, shiny, and with no evidence of any adverse interactions with the mould walls.

### **7.4.3 Moulds for ferrous casting based on resin coated sand material system**

- The lower clay and silica flour contents at around 6% and 5% respectively scored the least in terms of volume errors, while the lower clay (6%) and higher silica flour (10%) resulted in the lowest volume error, at around 7%.
- Overall, the surface roughness varied from 5-10  $\mu\text{m}$  but the average surface roughness values in all the cases are within the normal allowed limits for sand casting.
- The average tensile strength of the castings is around 550MPa, the normal expected value for the stainless steel grade used.

### **7.5 Future work**

Three material systems have been constituted and evaluated to be used for 3D printing of moulds as part of the work done for the current research. In all three cases, the main focus is on understanding the science of material consolidation while roles of critical factors in influencing the key responses given due considerations both individually and in combinations. Underpinning knowledge from widely varying fields has been gathered and successfully applied and proved to be working within the constraints of a 3D printing system. While the mechanism and mechanics of material consolidation and further responses to real casting applications are evaluated and understood, more work is needed with each material system, fine-tuning to specific requirements.

Further casting trials are needed to fully explore the roles of different ingredients in controlling the volume errors in moulds which will subsequently influence the dimensional quality of castings. It will also be interesting to evaluate the mould coatings and related approaches as used in traditional foundry practices to achieve better surface qualities possible with the materials investigated. The tensile strength responses of cast specimens are quite varied, mainly due to the varying permeability and thermal properties of the printed moulds. Further experimental work is necessary establishing these properties and evaluating their influences on the properties of cast specimens, together with the analysis of the as cast micro-structures. Once these aspects are evaluated, the compositions of each of the material systems can be adjusted, together with addition of further elements where necessary and develop an optimisation scheme for the best performance of the materials for 3D printed sand moulds.

## References

- [1] An-Hui. Lu., Dongyuan. Z and Ying. W. (2010), "Nano Casting: A Versatile Strategy for Creating Nanostructured Porous Materials" The Royal Society of Chemistry, Cambridge, UK.
- [2] Grote and Antonsson. (2009), "Springer Handbook of Mechanical Engineering", Springer Science & Business Media. New York, USA.
- [3] Kirgin and Kenneth. H. (2005), "Casting sales forecast to grow 14% by '08: U.S. metal casting shipments are expected to continue to rebound, despite the ongoing growth of imports", The Free Library, Retrieved Sep 24 2015 from <http://www.thefreelibrary.com/Casting+sales+forecast+to+grow+14%25+by+%2708%3a+U.S.+metal+casting...-a0141294659>.
- [4] <http://fg5.eu/115-the-importance-of-iron-casting-in-the-new-automotive-industry.html>
- [5] Thomas J. M. (1992), "Using Rapid Prototyping Techniques to Prototyping Metal Castings", SAE Technical Paper 921639: 1-5.
- [6] Reg. G. (1999), "Rapid Prototyping: A Tool for Casting Design and Verification", Modern Casting, American Foundry Society: 44-47.
- [7] Chua. K. C., Hong. H. K and Ho. L. S. (1999), "Rapid tooling Technology. Part 1. A Comparative Study", International Journal of Advanced Manufacturing Technology, 15: 604-608.
- [8] Bernard. M and Detlef. K. (1999), "Laminated Object Manufacturing for Rapid Tooling and patternmaking in Foundry Industry", Computers in Industry, 39: 47-53.
- [9] Wanlong. W., James G. C and Henry W. S. (1999), "Rapid Tooling for Sand Casting using Laminated Object Manufacturing Process", Rapid Prototyping Journal, 5, (3): 134-140.
- [10] Detlef. K., Chua. C. K and Du. Z. (1999), "Rapid Prototyping issues in the 21<sup>st</sup> Century", International Journal of Computers in Industry, 39: 3-10.
- [11] Rosochowski. A and Matuszak. A. (2000), "Rapid Tooling: The State of the Art", Journal of Materials Processing Technology, 106: 191-198.

- [12] Taylan. A., Blaine. L and Yen. C, Y. (2001), "Manufacturing of Dies and Moulds", *CIRP Annals-Manufacturing Technology*, 50, (2): 404-422.
- [13] Bauer. W and Knitter. R. (2002), "Development of a Rapid Prototyping Process Chain for the Production of Ceramic Microcomponents", *Journal of materials Sciences*, 37: 3127-3140.
- [14] Levy. N. G and Schindel. R. (2002), "Overview of Layer manufacturing Technologies, Opportunities, Options and Applications for Rapid Tooling", *Proceedings of the Institution of Mechanical Engineers, Part B: Journal of Engineering Manufacture*, 216: 1621-134.
- [15] Pham. T. D and Dimov. S. S. (2002), "Rapid Prototyping and Rapid Tooling-The Key enablers for Rapid Manufacturing", *Proceedings of the Institution of Mechanical Engineers, Part C: Journal of Engineering Manufacture*, 217: 1-23.
- [16] Brain. R. (2002), "Rapid Tooling for Casting Prototypes", *Journal of Assembly Automation*, 22, (1): 40-45.
- [17] Levy. N. G., Schindel. R and Kruth. K. P. (2003), "Rapid Manufacturing and Rapid Tooling with layer Manufacturing (LM) Technologies, State of the Art and Future Perspectives", *Annals of the CIRP – Manufacturing Technology*, 52, (2): 589-609.
- [18] Alian. B., Jean. C. D., Nicolas. P and Serge. G. (2003), "Integration of CAD and Rapid manufacturing for Sand Casting Optimization", *Rapid Prototyping Journal*, 9, (5): 327-333.
- [19] Ferreira. C. F. (2004), "Manufacturing Core-Boxes for Foundry with Rapid Tooling Technology", *Journal of Materials Processing Technology*, 155-156: 1118-1123.
- [20] Esposito. C. C., Greco. A., Montagna. F., Licciulli. A and Maffezzoli. A. (2005), "Silica Moulds built by Stereolithography", *Journal of Material Sciences*, 40: 4899-4904.
- [21] Cheah. C. M., Chu. C. K., Lee. C. W., Feng. C and Totong. K. (2005), "Rapid Prototyping and Tooling Techniques: A review of application for rapid investment casting", *International Journal of Advanced Manufacturing Technology*, 25, (3-4): 308-320.

- [22] Chu. C. K., Feng. C., Lee. C. W and Ang. G. C. (2005), "Rapid Investment casting: Direct and Indirect approaches via Model maker II", *International Journal of Advanced Manufacturing Technology*, 25: 26-32.
- [23] Dimitrov. D., Wijck. V. W., Beer. D. N and Dietrich. J. (2007), "Development, Evaluation, and Selection of Rapid Tooling Process chains for Sand Casting of Functional Prototypes", *Proceedings of the Institution of Mechanical Engineers, Part B: Journal of Engineering Manufacture*, 221: 1441-1450.
- [24] Dinesh. P and Ravi. B. (2007), "Rapid Tooling route selection and evaluation for sand and investment casting", *Virtual and Physical Prototyping*, 2, (4): 197-207.
- [25] Rahmati. S., Rezaei. M. R and Akbari. J. (2009), "Design and Manufacture of a Wax Injection Tool for Investment casting using Rapid Tooling", *Tsinghua Science and Technology*, 14, (S1):108-115.
- [26] Zhang. Y and Liu. H. (2009), "application of Rapid Prototyping Technology in Die Making of Diesel Engine", *Tsinghua Science and Technology*, 14, (S1):127-131.
- [27] Haihua. W., Dichen. L and Nannan. G. (2009), "Fabrication of Integral Ceramic Mould for Investment Casting of Hollow Turbine Blade based on Stereolithography", *Rapid Prototyping Journal*, 15, (4): 232-237.
- [28] Zhou. Z. W., Li. D., Chen. W. Z and Chen. S. (2009), "Direct Fabrication of an Integral Ceramic Mould by Stereolithography", *Proceedings of the Institution of Mechanical Engineers, Part B: Journal of Engineering Manufacture*, 224: 237-243.
- [29] Stankiewicz. M., Budzik. G., Patrzalek. M., Wieczorowski. M., Grzelka. M., Matysiak. H and Slota. J. (2010), "The Scope of Application of Incremental Rapid Prototyping methods in Foundry Engineering", *Archives of Foundry Engineering*, 10, (1): 405-410.
- [30] Munish. C and Rupinder. S. (2011), "Rapid Casting Solutions: A Review", *Rapid Prototyping Journal*, 17, (5): 328-350.

- [31] Karunakaran P. K., Alain. B., Suryakumar. S., Lucas. D and George. T. (2012), "Rapid Manufacturing of Metallic Objects", *Rapid Prototyping Journal*, 18, (4): 264-280.
- [32] Priyanka. M and Mahindru. V. D. (2013), "Rapid Prototyping – Technology to Shorten the Product Design and Development Process", *International Journal of Science & Engineering Research*, 4, (8): 477-488.
- [33] Sarojrani. P., Pradeep. K. J and Benny. K. D. (2014), "A Review of Rapid Prototyping Integrated Investment Casting Process", *Proceedings of the Institution of Mechanical Engineers, Part L: Journal of Materials: Design and Application*, 228, (4): 249-277.
- [34] Malagi. R. R., Mahendra. S. B., Anil. P and Prasad. R. (2014), "Development of casting Pattern using Rapid Prototyping", *International Journal of Research in Engineering and Technology*, 3, (6): 277-280.
- [35] Tang. Y., Fuh. H. Y. J., Loh. T. H., Wong. S. Y and Lu. L. (2003), "Direct Laser Sintering of Silica Sand", *Journal of Materials and Design*, 24: 623-629.
- [36] Klocke. F and Ader. C. (2003), "Direct Laser Sintering of Ceramics", *Solid Freeform Symposium*, Austin, Texas, USA: 447-455.
- [37] Wang. H. X., Fuh. H. Y. J., Wong. S. Y and Tang. X. Y. (2003), "Laser Sintering of Silica Sand–Mechanism and Application to Sand Casting Mould", *International Journal of Advanced Manufacturing Technology*, 21: 1015-1020.
- [38] Casalino. G., De. F. C. A. L and Ludovico. A. (2004), "A Technical note on the Mechanical and Physical Characterisation of Selective Laser Sintered sand for Rapid Casting", *Journal of Materials Processing Technology*, 166: 1-8.
- [39] Bertrand. P., Bayle. F., Combe. C., Goeuriot. P and Smurov. I. (2007), "Ceramic Components Manufacturing by Selective laser Sintering", *Journal of Applied Surface Sciences*, 254: 989-992.
- [40] Song. L. J., Li. T. Y., Deng. L. Q and Hu. J. D. (2007), "Rapid Prototyping Manufacturing of Silica sand patterns based on Selective Laser Sintering", *Journal of Materials and Processing Technology*, 187-188: 614-618.

- [41] Esterman. M. (1990), "Characterization of the Powder/Binder Interaction in the Three Dimensional Printing Process", Master Thesis, MIT.
- [42] Emanuel. S., Michael. C and James. B. (1991), "Three Dimensional Printing of Ceramic Shells and Cores for Metal Casting", *Intelligent Design and Manufacturing for Prototyping*, ASME PED, 50: 61-72.
- [43] Emanuel. S., Michael. C., James. B., Alain. C., Tailin. F and David. B. (1992), "CAD-Casting : Direct Fabrication of Ceramic Shells and Cores by Three Dimensional Printing", *Manufacturing Review*, 5, (2): 117-126.
- [44] Emanuel. S., Michael. C., James. C., David. B., Jim. B., Alain. C., Tailin. F., Satbir. K., Alan. Lr., John. L and Steve. M. (1993), "Three - Dimensional Printing: The Physics and Implications of Additive Manufacturing", *Annals of the CIRP*, 4, (1): 257- 260.
- [45] Tom. C and Tom. K. (2003), "Direct Metal Casting", *Advanced Materials and Processes*, ASM International, 161, (1): 43-44.
- [46] David. B. (2003), "Rapid Prototyping or Rapid Production? 3D Printing Processes move Industry towards the latter", *Assembly Automation*, 23, (4): 340-345.
- [47] Dimitrov. D., Schreve. K and De. B. N. (2006), "Advances in Three Dimensional Printing – State of the art and future perspectives", *Rapid Prototyping Journal*, 12, (3): 136-147.
- [48] Budzik. G. (2007), "Possibilities of utilizing 3DP Technology for Foundry Mould Making", *Archives of Foundry Engineering*, 7, (2): 65-68.
- [49] Elena. B., Andrea. G., Luca.L and Maria. G. Violate. (2007), "3D Printing Technique applied to Rapid Casting", *Rapid Prototyping Journal*, 13, (3): 148-155.
- [50] Rebros. M., Ramrattan N. S., Joyce K. M and Ikonomov G. P. (2007), "Behaviour of 3D Printed Sand at Elevated Temperature, AFS Transaction, paper 07, 136, (4): 341-348.
- [51] Ben. U., Rhond. L. A and Howard. K. (2006), "Advanced Ceramic Materials and Processes for Three Dimensional Printing (3DP)", *International Solid Freeform Fabrication Symposium Proceedings*: 290-303.

- [52] Singh. R and Verma. M. (2008), "Investigations for Deducing wall Thickness of Aluminium shell casting using Three Dimensional Printing", *Journal of Achievements in Materials and Manufacturing Engineering*, 31, (2): 565-569.
- [53] Elena. B and Eleonora. A. (2009), "Direct Metal Rapid Casting: Mechanical Optimization and Tolerance Calculation", *Rapid Prototyping Journal*, 15, (4): 238-243.
- [54] Gill. S. S and Kaplas. M. (2009), "Comparative Study of 3D Printing Technologies for Rapid Casting of Aluminium Alloy", *Materials and Manufacturing Processes*, 24, 1405-1411.
- [55] Gill. S. S and Kaplas. M. (2011), "Efficacy of Powder-based Three Dimensional Printing (3DP) Technologies for Rapid Casting of Light alloys", *International Journal of Advanced Manufacturing Technology*, 52: 53-64.
- [56] Singh. R and Singh. J. P. (2009), "Comparison of Rapid Casting Solutions for Lead and Brass Alloy using Three Dimensional Printing", *Proceedings of the Institution of Mechanical Engineers, Part C: Journal of Mechanical Engineering Science*, 223: 2117-2123.
- [57] Singh. J. P and Singh. R. (2009), "Investigations for a Statistically Controlled Rapid Casting Solution pf Lead alloys using Three Dimensional Printing", *Proceedings of the Institution of Mechanical Engineers, Part C: Journal of Mechanical Engineering Science*, 223: 2125-2134.
- [58] Singh. R. (2010), "Effect of Moulding Sand on Statically Controlled Hybrid Rapid Casting Solution for Zinc alloys", *Journal of Mechanical Sciences and Technology*, 24, (8): 16898-1695.
- [59] Munish. C and Singh. R, (2011), "Experimental Investigation of Pattern-less Casting solution using Additive manufacturing Technique", *MIT International Journal of Mechanical Engineering*, 1, (1): 17-25.
- [60] Singh. R. (2011), "An Overview of Three Dimensional Printing for Casting Applications", *International Journal of Precision Technology*, 2, (1): 93-115.

- [61] Singh. R. (2012), "Effect of Workpiece Volume on statistically controlled Rapid Casting Solution of Low Melting Alloys using Three Dimensional Printing", *Materials and Manufacturing Processes*, 27: 377-382.
- [62] Drokina. V. V., Belov. D. V and Chekhonin. N. S. (2011), "Obtaining Casts of Aluminium Alloys by Foundry in Loose Moulds Fabricated on Installation of Three Dimensional Printing", *Russian Journal of Non-Ferrous Metals*, 52, (1): 24-28.
- [63] Markowski. T., Budzik. G., Kozik. B., Dziubek. T., Sobolewski. B and Zaborniak. M. (2010), "Geometrical Precision of 3DP Casting form for Foundry Gears", *Archives of Foundry Engineering*, 10, (1): 391-394.
- [64] Nicholas A., Meisel., Christopher. B. W and Alan. D. (2012), "Lightweight Metal Cellular Structures via Indirect 3D Printing and Casting", *International Symposium on Solid Freeform Fabrication, Proceedings, Texas, USA*, 162-176.
- [65] Koltygin. V. A and Bazhenov. E. V. (2012), "Development of a Substitute for ZCast Moulding Sand used on Installations of 3D Printing for Obtaining Aluminium, Magnesium, and Iron Casting", *Russian Journal of Non-Ferrous Metals*, 53, (1): 38-41.
- [66] Munish. C and Singh. R. (2012), "Obtaining desired Surface Roughness of Castings Produced using ZCast Direct Metal Casting Process through Taguchi's Experimental Approach", *Rapid Prototyping Journal*, 18, (6): 458-471.
- [67] Dean. S., Heather. B., Charles. F., Kelly. R., Andrew. W., Christopher. W and Alan. D. (2013), "The effect of 3D printed Moulds on Metal Castings", *International Solid Freeform Fabrication Symposium and Additive Manufacturing Conference, Texas, USA*.
- [68] Dean. S., Qian. L., Nicolas. M., Christofer B. W., Romesh. C. B and Alan. P. D. (2015), "Lightweight Metal Cellular Structures Fabricated via 3D Printing of Sand Cast Moulds", *Journal of Advanced Engineering Materials*, 17, (7): 923-932.

- [69] Ben. U., Duane. S., Rhonda. A and Mark. G. (2008), "A Review of Process Development steps for new Material Systems in Three Dimensional Printing (3DP)", *Journal of manufacturing Processes*, 10: 96-104.
- [70] James F. B., Timothy. C. A and David. B. R. (2003), "Three Dimensional Printing Material System and Method", ZCorporation, United States Patent, US 6610429 B2.
- [71] Text Book, (1989), "Calcium Sulfate", MAK Value Documentation, The MAK collection for Occupational Health and Safety, Willey Online Library, 2: 118-127.
- [72] Desch. C. H. (1981), "The Setting of Plaster", *Transactions and Journal of the British Ceramic Society*, 18:13-26.
- [73] Norton. F H. (1978), "Fine Ceramics: Technology and Applications", 2nd ed., Krieger Publishing Company, Florida, USA.
- [74] Piwonka. T. S. (1998), "Moulding Methods", *Metals Handbook Desk Edition*, ASM International, 736–751.
- [75] McCartney. E. R, Alexander. A. E. (1958), "The effect of Additives upon the process of Crystallization: I. Crystallization of Calcium Sulfate" *Journal of Colloidal Science*, 13: 383-396.
- [76] Sung.T. L, George H. N. (1970), "The Kinetics of Crystal growth of Calcium Sulfate Dihydrate", *Journal of Crystal Growth*, 6: 281- 289.
- [77] Smith. B. R and Frank. S. (1971), "The Crystallization of Calcium Sulfate Dihydrate", *Journal of Colloid and Interface Sciences*, 37, (3): 612-618.
- [78] George H. N., Reddy. M. M and Sai. F. (1973), "Calcium Sulfate Dihydrate Crystal Growth in Aqueous Solution at Elevated Temperatures", *Journal of Crystal Growth*, 20: 125-134.
- [79] Coddy. R. D and Shanks. H. R. (1974), "A Comparison of Calcium Sulfate Dihydrate grown in clay gels and in sodium silicate gels", *Journal of Crystal Growth*, 23: 275-281.
- [80] Klepetsanis. P. G and Koutsoukos. P. G. (1989), "Precipitation of calcium sulfate dihydrate at constant calcium activity", *Journal of Crystal Growth*, 98: 480-486.

- [81] Strydom. C. A., Hudson. L. D. L., Potgieter. J. H and Dagg. E. (1995), "The thermal dehydration of synthetic gypsum", *Thermochimica Acta*, 269/270: 631-638.
- [82] Hudson. L. D. L., Strydom. C. A and Potgieter. J. H. (1996), "The Thermal Dehydration of Natural Gypsum and pure Calcium Sulphate Dihydrate (Gypsum)", *Thermochimica Acta*, 282/283: 483-492.
- [83] Nakamura. Y., Suzuki. M., Motohira., Kishimoto. A and Yanagida. H. (1997), "Comparison between the mechanical and dielectric strength distributions for hardened gypsum", *Journal of Materials Sciences*, 32: 115-118.
- [84] Badens. E., Llewellyn. P., Fulconis. J. M., Jourdan. C., Veesler. S., Boistelle. R and Rouquerol. F. (1998), "Study of Gypsum Dehydration by Controlled Transformation rate Thermal Analysis (CRTA)", *Journal of Solid State Chemistry*, 139: 37-44.
- [85] Badens. E., Veesler. S and Boistelle. R. (1999), "Crystallization of gypsum from hemihydrate in presence of additives", *Journal of Crystal Growth*, 198/199: 704-709.
- [86] Singh. N. B and Middendorf. B. (2007), "Calcium Sulfate Hemihydrate Hydration leading to Gypsum Crystallization, Progress in Crystal Growth and Characterization of Materials, 53: 57-77.
- [87] Solberg. C and Hansen. S. (2001), "Dissolution of  $\text{CaSO}_4 \cdot \frac{1}{2}\text{H}_2\text{O}$  and precipitation of  $\text{CaSO}_4 \cdot 2\text{H}_2\text{O}$  A kinetic study by synchrotron X-ray powder diffraction", *Cement and Concrete Research*, 31: 641-646.
- [88] Martias. C., Joliff. Y., Rogez. J and Favottoe. C. (2013), "A new Composite based on Gypsum matrix and Mineral additives: Hydration process of the matrix and thermal properties at room temperature", *Thermochimica Acta*, 56: 15-26.
- [89] Sievert. T., Wolter. A and Singh. N. B. (2005), "Hydration of Anhydrite of Gypsum ( $\text{CaSO}_4\text{-II}$ ) in a Ball Mill", *Cement and Concrete Research*, 35: 623-630.

- [90] Haber. R. A and Paredes. C. A. (1998), "Slip Casting of Metals", Shaping and Consolidation Technologies, Powder Metal Technologies and Applications, ASM International, 7: 420 – 425.
- [91] Kelley. K. K., Southard. J. C and Anderson. C. T. (1941), "Thermodynamic Properties of Gypsum and its Dehydration Products", United States Bureau of Mines, Technical Paper no 625: 1–73.
- [92] Yu. Q. L., Brouwers. H. J. H and Korte de. A. C. J. (2009), "Gypsum hydration: A Theoretical and Experimental Study", Proceedings of the 17th International Conference on Building Materials, Ibausil, Weimar, Germany, 1:783 -788.
- [93] Power. W. H and Fabuss. B. M. (1964), "Transient Solubilities in the Calcium Sulfate-Water System", Journal of Chemical and Engineering Data, 9, (3): 437- 442.
- [94] Mandal. P. K and Mandal. T. K. (2002), "Anion water in Gypsum ( $\text{CaSO}_4 \cdot 2\text{H}_2\text{O}$ ) and Hemihydrate ( $\text{CaSO}_4 \cdot 1/2\text{H}_2\text{O}$ )", Cement and Concrete Research, 32, (2): 313-316.
- [95] Douglas. C. M. (2012), "Design and Analysis of Experiments", 7th Edition, Internatioanl Stusent Version, John Wiley & Sons, Inc, UK.
- [96] Pettijohn F. J. (1957), "Sedimentary rocks", 2nd Edtion, Harper & Bros, New York, USA: 718.
- [97] <http://pocketdentistry.com/chapter-4-gypsum-products/>
- [98] Azam. S. (2007), "Study on the Geological and Engineering aspects of anhydrite/gypsum transition in the Arabian Gulf coastal deposits", Bulletin of Engineering Geology and the Environment, 66: 177-185.
- [99] Joanna. J. (2012), "Crystallization, Alternation and Recrystallization of Sulphates", Advances in Crystallization Process, Edited by Yitzhak Mastai, Published by InTech Janeza Trdine, Croatia: 465-490.
- [100] ASTM International, (2010), D7012 – 10 Standard Test Method for Compressive Strength and Elastic Moduli of Intact Rock Core Specimens under Varying States of Stress and Temperatures: 9.

- [101] Casalino. G., Filippis. L. A. C. D and Ludovico. A. (2005), "A technical note on the mechanical and physical characterization of selective laser sintered sand for rapid casting", *Journal of Materials Processing Technology*, 166, (1): 1–8.
- [102] Hansen. W. C. (1963), "The Setting and Hardening of Gypsum Plasters", *Materials Research and Standards*, 3,(5): 359-362.
- [103] Yu. Q. L and Brouwers. H. J. H. (2012), "Development of a self-compacting gypsum-based lightweight composite", *Cement & Concrete Composites*, 34,1033–1043.
- [104] Kelley. W. P., Jenny. H and Brown. S. M. (1936), "The relation of crystal structure to base exchange and its bearing on base exchange in soils", *Journal of Soil Science*, 41, (5): 367-382.
- [105] Andrade. A. F., Alqureshi. A. H and Hotza. D. (2011), "Measuring the plastic of clays: A Review", *Applied Clay Sciences*, 51: 1-7.
- [106] Luckham. P. F and Rossi. S. (1999), "The colloidal and rheological properties of bentonite suspensions", *Advances in Colloid and Interface Science*, 82: 43-92.
- [107] Derjaguin. B and Landau. L. (1941), "Theory of the stability of strongly charged lyophobic sols and of the adhesion of strongly charged particles in solution of electrolytes", *Acta Physicochim, URSS*, 14: 633-662.
- [108] Verwey. E. J. W and Overbeek. J. T. G. (1948), "Theory of the stability of lyophobic colloids, Text Book, Elsevier Publishing Company Inc, Amsterdam, London.
- [109] Holdridge. D. A and Moore. F. (1953), "The significance of clay-water relationships in cermaics", *Clay Minerals Bulletin*, 2, (9): 26-33.
- [110] Lundina.G. M. (1957), "Dehydration of Clay", *International Journal of Glass and Ceramics*, 14, (9): 323-327.
- [111] Murray. P and White. J. (1954), "Kinetics of Clay Dehydration", *Transaction and Journal of the British Ceramic Society*, 53: 255-264.
- [112] Boylu. F. (2011), "Optimisation of foundry sand characteristics of soda-activated calciumbentonite," *Applied Clay Science*, 52, 104-108.

- [113] Fox. J. T., Cannon. F. S., Brown. N. R., Huang. H and Furness. J. C. (2012), "Comparison of a new, green foundry binder with conventional foundry binders", *International Journal of Adhesion & Adhesives*, 34: 38-45.
- [114] Kumon. S. Z., Holtzer. M., Olejnik. E and Bobrowski. A. (2012), "Influence of the changes of the structure of foundry bentonites on their binding properties", *Material Science (Medziagotyra)*, 18, (1): 57-61.
- [115] Yaw. A. O. (1982), "Physical–Chemical study of sodium silicate as a foundry sand binder," *Advances in colloid and Interface Science*, 18, 57-91.
- [116] Mike. M. D., Hamilton. J and Thompson. J. (2009), "Recent developments in soluble silicate based binders and coatings", *Proceedings of the 31<sup>st</sup> Biennial conference-Institute of Briquetting and Agglomeration*, San Antonio, Texas, USA, 29-40.
- [117] Gabrys. K. M., Dobosz. S. M., Jakubski. J., Stachowic. M and Nowak. D. (2012), "The influence of glasses additive on properties of microwave-hardened and self-hardened moulding sands with water glass", *Archives of Foundry Engineering*, 12, (1): 130-134.
- [118] Sylwia. Z., Mariusz. H., Ewa. O and Artur. B. (2012), "Influence of the changes of the structure of foundry bentonites on their bonding properties," *Materials Science*, 18, (1): 57-61.
- [119] Arthur. G. C and Robert. W. D. (1961), "Industrial applications of bentonite" *Proceedings of the 10<sup>th</sup> National Conference on Clays and Clay Minerals: Texas*, Edited by Ada Swineford, 272-283,
- [120] Hofmann. F. (1985), "Investigation of the effect of heat on the bonding properties of various bentonites," *American Foundrymen's Society Transactions*, 93: 377-384.
- [121] James. F. B., Sarah. C and Greeta. G. (2006), "Three Dimensional Printing Material System and Method," *United States patent*, US 7087109B2,
- [122] Yu. Q. L and Brouwers. H. J. H. (2011), "Microstructure and mechanical properties of  $\beta$ - hemihydrate produced gypsum-An insight from its hydration process," *Construction and Building Materials*, 25: 3149-3159.

- [123] Martias. C., Joliff. Y., Rogez. J and Favottoe. C. (2013), "A new Composite based on Gypsum matrix and Mineral additives, Hydration process of the matrix and thermal properties at room temperature," *Thermochimica Acta*, 56: 15-26.
- [124] Cody. D. R and Shanks. H. R. (1974), "A comparison of calcium sulfate dihydrate grown in clay gels and in sodium silicate gels," *Journal of Crystal Growth*, 23, (4): 275-281.
- [125] Tamia. Z. M. A. A. M. and Hafiz. Z. A. (2013), "Effect of clay and moisture content on the properties of moulding sand", Conference Proceedings, International conference on Mechanical, Industrial and Materials Engineering (ICMIME 2013), 1-3 Nov 2013, Rajshahi, Bangladesh, 578-582.
- [126] Chukwu. G. U and Ajuamiwe C. F. (2013), "Investigation of mechanical / physico-chemical properties kaolinite ore (clay) form Umuariage-Umudike, Abia state of Nigeria", *International Research Journal of Geology and Mining*, 3, (5): 195-205.
- [127] Sarkar. A. D. (1967), *Mould and Core Materials for the Steel Foundry*, Text Book, Pergamon Press Ltd, New York. US.
- [128] James F. Shackelford and Robert. H. D. (2008), "Ceramic and Glass Materials-Structure, Properties and Processing", Text Book, Publisher Springer, New York, US.
- [129] Ingo. E, Rainer. H and Alexander. K. (2000), "Production of casting moulds comprises depositing particulate material on support, applying binder and hardener to form solidified structure in selected region, and removing solidified structure", Patent DE 19853834 A1.
- [130] Naro. R. L. (2002), "Porosity defects in iron castings from mould-metal interface reactions", *AFS Transactions*, 110, (1&2): 839-851.
- [131] Brown R. J. (2000), "Foseco Ferrous Foundryman's Hand Book, Oxford, UK: Butterworth-Heinemann.
- [132] Vingas. G. J and Zrimsek. A. H. (1964), "Thermal stability of Bentonites in foundry moulding sand", *Proceedings of the 13<sup>th</sup> National conference on clay and clay minerals*: 367-380.

- [133] Holtzer. M., Bobrowski. A and Kumon. S. Z. (2011), "Temperature influence on structural changes of foundry bentonites", *Journal of Molecular Structure*, 1004: 102-108.
- [134] Furlani. E., Tonello. G., Aneggi. E and Maschio. S. (2013), "Possible use of waste olivine powders from a foundry process into the ceramic industry: sintering behaviour of olivine, kaolin and their blends", *Ceramic International*, 39: 1257-1263.
- [135] Wolfrum. J and Ehrenstein. G. W. (1999), "Interdependence between the curing, structure, and the mechanical properties of phenolic resins", *Journal of Applied Polymer Science*, 74: 3173-3185.
- [136] Budinski . K. G and Budinski. M. K. (2004), *Engineering materials, properties and selection*, Pearson Education, 8th International Edition. New York, USA.
- [137] <https://plenco.com/phenolic-novolac-resol-resins.htm>
- [138] Dai X., Su. G and Gao. J. (1980), "On the bonding mechanism of cold-setting synthetic resin sand mixture", *Journal of Huazhong University of Science and Technology*, 2, (1):56-70.
- [139] Hussein. S. I. N., Ayof. N. M and Mohamed. S. I. N. (2013), "Mechanical Properties and Loss on Ignition of Phenolic and Furan Resin Bonded Sand Casting", *International Journal of Mining, Metallurgy & Mechanical Engineering*, 1, (3): 223-227.
- [140] Hendricks. S. B and Jefferson. M. E. (1938), "Crystal Structure of Vermiculates and Mixed Vermiculates-Chlorites", *The American Mineralogist-Journal of the Mineralogical Society of America*, 23, (12), Part1: 851-863.
- [141] Gruner. E. (1951), "Hydrodynamic Properties of Clay minerals", *The Journal of American Ceramic Society*, 34, (4): 74-92.
- [142] Andrade. A. F., Alqureshi. A. H and Hotza, D. (2011), "Measuring the plastic of clays: A Review", *Applied Clay Sciences*, 51: 1-7.
- [143] Selvaraj. S. B and Singamneni. S. (2015), "Pre-Moisturized  $\beta$ -hemihydrate for 3D Printed Moulds", *Materials and Manufacturing Processes*, 1-11, DOI: 10.1080/10426914.2015.1037918.

- [144] Gonzalez. A. J., Carreras. C. A and Ruiz. C. D. M. (2007), "Phase Transformations in clays and kaolins produced by thermal treatment in chlorine and air atmospheres", *Latin American Applied Research*, 37: 133-139.
- [145] Hassan. H and Hameed. H. B. (2011), "Fenton-like Oxidation of Acid Red 1 Solutions using Heterogeneous Catalyst based on ball clay", *International Journal of Environmental Sciences and Development*, 2, (3): 218-222.
- [146] Verwey. E. J. W and Overbeek. J. T. G. (1948), "Theory of the stability of lyophobic colloids, Text Book, Elsevier Publishing Company Inc, Amsterdam, London.
- [147] Miska. P. (1984), "Understanding Clay Recognition and Processing, Technical paper, VITA Publication, Virginia, USA, 1-18.
- [148] [http://digitalfire.com/4sight/properties/ceramic\\_property\\_body\\_plasticity.htm#All%20Bodies](http://digitalfire.com/4sight/properties/ceramic_property_body_plasticity.htm#All%20Bodies).
- [149] Rafel. J. H. L. (2006), "Effect of cooling circuit duration of formation of solidification shrinkage in A356 casting automotive wheel", Master Thesis, AUT University of Technology, Auckland, New Zealand: 6.
- [150] Material Data Sheet, [www. Matweb.com](http://www.matweb.com)  
<http://www.matweb.com/search/datasheet.aspx?MatGUID=595aeac7a5af4446bf4d912226644759>
- [151] Eric. I., Ken. C and Jorg. K. (2002), "New Horizon in Nobake Binder Technology", *Transactions of the American Foundry Society*, 110:623-629.
- [152] Thiel. J. (2011), "Thermal Expansion of Chemically Bonded Silica Sands" *Transactions of the American Foundry Society*, 116, 369-378.

# Appendices

## Appendix 1

### Plaster based material system: Additional experimental data and results

Table A1.1 Box-Behnken design of experiment for un-coded table

$\beta_0$	$\beta_1$	$\beta_2$	$\beta_3$	$\beta_4$	$\beta_{11}$	$\beta_{22}$	$\beta_{33}$	$\beta_{44}$	$\beta_{12}$	$\beta_{13}$	$\beta_{14}$	$\beta_{23}$	$\beta_{24}$	$\beta_{34}$
$X_0$	$X_1$	$X_2$	$X_3$	$X_4$	$X_1^2$	$X_2^2$	$X_3^2$	$X_4^2$	$X_1X_2$	$X_1X_3$	$X_1X_4$	$X_2X_3$	$X_2X_4$	$X_3X_4$
1	33	2	200	2	1089	4	40000	4	66	6600	66	400	4	400
1	33	2	300	6	1089	4	90000	36	66	9900	198	600	12	1800
1	33	2	400	4	1089	4	160000	16	66	13200	132	800	8	1600
1	33	3	200	6	1089	9	40000	36	99	6600	198	600	18	1200
1	33	3	400	2	1089	9	160000	4	99	13200	66	1200	6	800
1	33	4	200	4	1089	16	40000	16	132	6600	132	800	16	800
1	33	4	300	2	1089	16	90000	4	132	9900	66	1200	8	600
1	33	4	400	6	1089	16	160000	36	132	13200	198	1600	24	2400
1	43	2	200	4	1849	4	40000	16	86	8600	172	400	8	800
1	43	2	400	2	1849	4	160000	4	86	17200	86	800	4	800
1	43	2	400	6	1849	4	160000	36	86	17200	258	800	12	2400
1	43	3	300	4	1849	9	90000	16	129	12900	172	900	12	1200
1	43	3	300	4	1849	9	90000	16	129	12900	172	900	12	1200
1	43	3	300	4	1849	9	90000	16	129	12900	172	900	12	1200
1	43	3	300	4	1849	9	90000	16	129	12900	172	900	12	1200
1	43	3	300	4	1849	9	90000	16	129	12900	172	900	12	1200
1	43	4	200	2	1849	16	40000	4	172	8600	86	800	8	400
1	43	4	200	6	1849	16	40000	36	172	8600	258	800	24	1200
1	43	4	300	4	1849	16	90000	16	172	12900	172	1200	16	1200
1	53	2	200	6	2809	4	40000	36	106	10600	318	400	12	1200
1	53	2	300	2	2809	4	90000	4	106	15900	106	600	4	600
1	53	2	400	4	2809	4	160000	16	106	21200	212	800	8	1600
1	53	3	200	2	2809	9	40000	4	159	10600	106	600	6	400
1	53	3	400	6	2809	9	160000	36	159	21200	318	1200	18	2400
1	53	4	200	4	2809	16	40000	16	212	10600	212	800	16	800
1	53	4	300	6	2809	16	90000	36	212	15900	318	1200	24	1800
1	53	4	400	2	2809	16	160000	4	212	21200	106	1600	8	800

**Table A1.2 Percentage green volume error: ANOVA table for the model based on significant factors**

Percentage Green Volume Error (Un-Coded) – Significance Model								
Regression Statistics								
Multiple R	0.962267							
R Square	0.925957							
Adjusted R Square	0.912495							
Standard Error	1.330623							
Observations	27							
ANOVA								
	<i>df</i>	<i>SS</i>	<i>MS</i>	<i>F</i>	<i>Significance F</i>			
Regression	4	487.1238257	121.781	68.781087	4.1E-12			
Residual	22	38.95229282	1.770559					
Total	26	526.0761185						
	<i>Coefficients</i>	<i>Standard Error</i>	<i>t Stat</i>	<i>P-value</i>	<i>Lower 95%</i>	<i>Upper 95%</i>	<i>Lower 85.0%</i>	<i>Upper 85.0%</i>
Intercept	7.9348	5.4242	1.4628	0.1577	-3.3144	19.1840	-0.1561	16.0257
X <sub>2</sub>	9.6954	3.7247	2.6030	0.0162	1.9708	17.4200	4.1396	15.2513
X <sub>1</sub> <sup>2</sup>	-0.0111	0.0013	-8.2339	0.0000	-0.0139	-0.0083	-0.0131	-0.0091
X <sub>2</sub> <sup>2</sup>	-2.9492	0.5441	-5.4208	0.0000	-4.0775	-1.8209	-3.7607	-2.1377
X <sub>1</sub> X <sub>2</sub>	0.1595	0.0373	4.2799	0.0003	0.0822	0.2367	0.1039	0.2150

**Table A1.3 Percentage Baked Volume Error: ANOVA table for the full model**

Percentage Baked Volume Error (Un-Coded) – Full Model								
Regression Statistics								
Multiple R	0.956969557							
R Square	0.915790733							
Adjusted R Square	0.817546589							
Standard Error	1.586262745							
Observations	27							
ANOVA								
	<i>df</i>	<i>SS</i>	<i>MS</i>	<i>F</i>	<i>Significance F</i>			
Regression	14	328.3733127	23.455237	9.3215808	0.0002106			
Residual	12	30.19475395	2.5162295					
Total	26	358.5680667						
	<i>Coefficients</i>	<i>Standard Error</i>	<i>t Stat</i>	<i>P-value</i>	<i>Lower 95%</i>	<i>Upper 95%</i>	<i>Lower 85.0%</i>	<i>Upper 85.0%</i>
Intercept	40.1529	16.2007	2.4785	0.0290	4.8546	75.4512	15.2369	65.0689
X <sub>1</sub>	-2.4695	0.6481	-3.8101	0.0025	-3.8816	-1.0573	-3.4663	-1.4727
X <sub>2</sub>	11.2383	5.0895	2.2081	0.0474	0.1492	22.3273	3.4108	19.0657
X <sub>3</sub>	0.0505	0.0526	0.9613	0.3554	-0.0640	0.1650	-0.0303	0.1313
X <sub>4</sub>	2.7484	1.9915	1.3800	0.1927	-1.5908	7.0875	-0.3145	5.8112
X <sub>1</sub> <sup>2</sup>	0.0193	0.0071	2.7170	0.0187	0.0038	0.0347	0.0084	0.0302
X <sub>2</sub> <sup>2</sup>	-2.4840	0.6922	-3.5887	0.0037	-3.9922	-0.9759	-3.5486	-1.4195
X <sub>3</sub> <sup>2</sup>	-0.0001	0.0001	-1.2439	0.2373	-0.0002	0.0001	-0.0002	0.0000
X <sub>4</sub> <sup>2</sup>	-0.3718	0.1774	-2.0958	0.0580	-0.7583	0.0147	-0.6446	-0.0990
X <sub>1</sub> X <sub>2</sub>	0.1098	0.0458	2.3986	0.0336	0.0101	0.2096	0.0394	0.1803
X <sub>1</sub> X <sub>3</sub>	0.0002	0.0005	0.3349	0.7435	-0.0008	0.0012	-0.0006	0.0009
X <sub>1</sub> X <sub>4</sub>	0.0125	0.0229	0.5478	0.5939	-0.0373	0.0624	-0.0227	0.0478
X <sub>2</sub> X <sub>3</sub>	-0.0038	0.0048	-0.7845	0.4480	-0.0143	0.0067	-0.0112	0.0036
X <sub>2</sub> X <sub>4</sub>	-0.0842	0.2290	-0.3676	0.7196	-0.5830	0.4147	-0.4363	0.2680
X <sub>3</sub> X <sub>4</sub>	0.0003	0.0023	0.1128	0.9120	-0.0047	0.0052	-0.0033	0.0038

**Table A1.4 Green compressive strength: ANOVA table for the full model**

Green Compressive Strength (Un-Coded) – Full Model								
Regression Statistics								
Multiple R	0.869347853							
R Square	0.755765689							
Adjusted R Square	0.697614663							
Standard Error	64.66465483							
Observations	27							
ANOVA								
	df	SS	MS	F	Significance F			
Regression	5	271727.5788	54345.51576	12.99660104	7.74249E-06			
Residual	21	87811.86926	4181.517584					
Total	26	359539.4481						
	Coefficients	Standard Error	t Stat	P-value	Lower 95%	Upper 95%	Lower 85.0%	Upper 85.0%
Intercept	3261.2776	535.2410	6.0931	0.0000	2148.1830	4374.3721	2461.5238	4061.0313
X <sub>1</sub>	-120.5620	23.0436	-5.2319	0.0000	-168.4839	-72.6402	-154.9937	-86.1304
X <sub>2</sub>	-229.6965	181.5466	-1.2652	0.2197	-607.2432	147.8503	-500.9622	41.5693
X <sub>1</sub> <sup>2</sup>	0.9928	0.2592	3.8296	0.0010	0.4537	1.5319	0.6054	1.3801
X <sub>2</sub> <sup>2</sup>	-34.9151	27.0205	-1.2922	0.2103	-91.1073	21.2770	-75.2889	5.4587
X <sub>1</sub> X <sub>2</sub>	9.3668	1.8667	5.0178	0.0001	5.4848	13.2489	6.5776	12.1561

Table A1.5 Baked compressive strength: ANOVA table for the full model

Baked Compressive Strength (Un-Coded) – Full Model								
Regression Statistics								
Multiple R	0.94549431							
R Square	0.89395949							
Adjusted R Square	0.77024557							
Standard Error	31.5939139							
Observations	27							
ANOVA								
	<i>df</i>	<i>SS</i>	<i>MS</i>	<i>F</i>	<i>Significance F</i>			
Regression	14	100979.7159	7212.8369	7.22602149	0.000744021			
Residual	12	11978.10473	998.17539					
Total	26	112957.8206						
	<i>Coefficients</i>	<i>Standard Error</i>	<i>t Stat</i>	<i>P-value</i>	<i>Lower 95%</i>	<i>Upper 95%</i>	<i>Lower 85.0%</i>	<i>Upper 85.0%</i>
Intercept	664.9815	322.6724	2.0609	0.0617	-38.0613	1368.024	168.725	1161.23
X <sub>1</sub>	-23.8412	12.9090	-1.8469	0.0896	-51.9675	4.2850	-43.694	-3.9878
X <sub>2</sub>	171.7934	101.3686	1.6947	0.1159	-49.0698	392.6566	15.8929	327.693
X <sub>3</sub>	-1.1041	1.0468	-1.0548	0.3123	-3.3848	1.1766	-2.7140	0.5057
X <sub>4</sub>	30.7588	39.6652	0.7755	0.4531	-55.6642	117.1818	-30.244	91.7621
X <sub>1</sub> <sup>2</sup>	0.0462	0.1413	0.3270	0.7493	-0.2617	0.3541	-0.1711	0.2636
X <sub>2</sub> <sup>2</sup>	-56.6986	13.7863	-4.1127	0.0014	-86.7364	-26.6607	-77.901	-35.495
X <sub>3</sub> <sup>2</sup>	0.0007	0.0014	0.5230	0.6105	-0.0024	0.0038	-0.0014	0.0029
X <sub>4</sub> <sup>2</sup>	0.2535	3.5331	0.0717	0.9440	-7.4445	7.9515	-5.1803	5.6873
X <sub>1</sub> X <sub>2</sub>	3.3868	0.9120	3.7135	0.0030	1.3997	5.3740	1.9842	4.7895
X <sub>1</sub> X <sub>3</sub>	0.0186	0.0091	2.0382	0.0642	-0.0013	0.0385	0.0046	0.0326
X <sub>1</sub> X <sub>4</sub>	-0.3763	0.4560	-0.8252	0.4253	-1.3699	0.6173	-1.0777	0.3250
X <sub>2</sub> X <sub>3</sub>	-0.0239	0.0962	-0.2481	0.8083	-0.2336	0.1858	-0.1719	0.1241
X <sub>2</sub> X <sub>4</sub>	1.8886	4.5602	0.4142	0.6861	-8.0472	11.8244	-5.1247	8.9020
X <sub>3</sub> X <sub>4</sub>	-0.0576	0.0456	-1.2642	0.2302	-0.1570	0.0417	-0.1278	0.0125

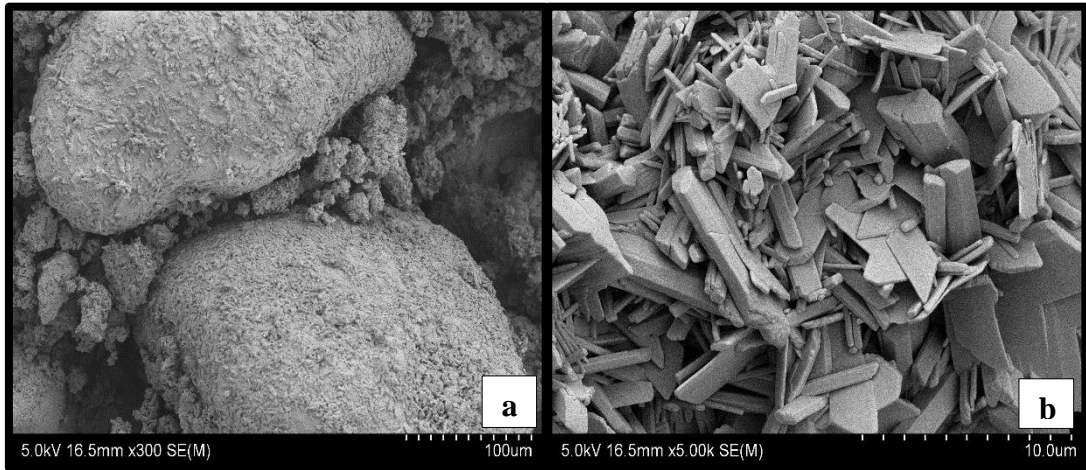


**Fig A1.1 Gypsum crystal formation in the green state:  $\beta$ -hemihydrate (33%), silica sand (67%), and pre-moisture 7%.**

## Appendix 2

### Plaster-clay material system treated with sodium silicate:

#### Additional experimental data and results

#### Box-Behnken design matrix

Table A2.1 I-optimal design with 3 factors, 3 levels and 15 runs for fitting a full quadratic

(Un-Coded) model

Un-Coded (Natural Values)										
Run	$\beta_0$	$\beta_1$	$\beta_2$	$\beta_3$	$\beta_1^2$	$\beta_2^2$	$\beta_3^2$	$\beta_{12}$	$\beta_{13}$	$\beta_{23}$
	$X_0$	$X_1$	$X_2$	$X_3$	$X_1^2$	$X_2^2$	$X_3^2$	$X_1X_2$	$X_1X_3$	$X_2X_3$
1	1	25	12.5	12.5	625	156.25	156.25	312.5	312.5	156.25
2	1	75	12.5	12.5	5625	156.25	156.25	937.5	937.5	156.25
3	1	25	37.5	12.5	625	1406.25	156.25	937.5	312.5	468.75
4	1	75	37.5	12.5	5625	1406.25	156.25	2812.5	937.5	468.75
5	1	25	25	6.25	625	625	39.0625	625	156.25	156.25
6	1	75	25	6.25	5625	625	39.0625	1875	468.75	156.25
7	1	25	25	18.75	625	625	351.5625	625	468.75	468.75
8	1	75	25	18.75	5625	625	351.5625	1875	1406.25	468.75
9	1	50	12.5	6.25	2500	156.25	39.0625	625	312.5	78.125
10	1	50	37.5	6.25	2500	1406.25	39.0625	1875	312.5	234.375
11	1	50	12.5	18.75	2500	156.25	351.5625	625	937.5	234.375
12	1	50	37.5	18.75	2500	1406.25	351.5625	1875	937.5	703.125
13	1	50	25	12.5	2500	625	156.25	1250	625	312.5
14	1	50	25	12.5	2500	625	156.25	1250	625	312.5
15	1	50	25	12.5	2500	625	156.25	1250	625	312.5

**Table A2.2 I-optimal design with 3fators, 3levels and 15runs for fitting a full quadratic  
(Coded) model**

Coded Values										
Run	$\beta_0$	$\beta_1$	$\beta_2$	$\beta_3$	$\beta_1^2$	$\beta_2^2$	$\beta_3^2$	$\beta_{12}$	$\beta_{13}$	$\beta_{23}$
	$x_0$	$x_1$	$x_2$	$x_3$	$x_1^2$	$x_2^2$	$x_3^2$	$x_1x_2$	$x_1x_3$	$x_2x_3$
1	1	-1	-1	0	-1	-1	0	1	1	0
2	1	1	-1	0	1	-1	0	1	1	0
3	1	-1	1	0	-1	1	0	1	1	0
4	1	1	1	0	1	1	0	1	1	0
5	1	-1	0	-1	-1	0	-1	1	0	1
6	1	1	0	-1	1	0	-1	1	0	1
7	1	-1	0	1	-1	0	1	1	0	1
8	1	1	0	1	1	0	1	1	0	1
9	1	0	-1	-1	0	-1	-1	0	1	1
10	1	0	1	-1	0	1	-1	0	1	1
11	1	0	-1	1	0	-1	1	0	1	1
12	1	0	1	1	0	1	1	0	1	1
13	1	0	0	0	0	0	0	0	0	0
14	1	0	0	0	0	0	0	0	0	0
15	1	0	0	0	0	0	0	0	0	0

The second order quadratic equation for Un-coded and Coded variables,

$$Y = \beta_0 + \beta_1 X_1 + \beta_2 X_2 + \beta_3 X_3 + \beta_{11} X_1^2 + \beta_{22} X_2^2 + \beta_{33} X_3^2 + \beta_{12} X_1 X_2 + \beta_{13} X_1 X_3 + \beta_{23} X_2 X_3$$

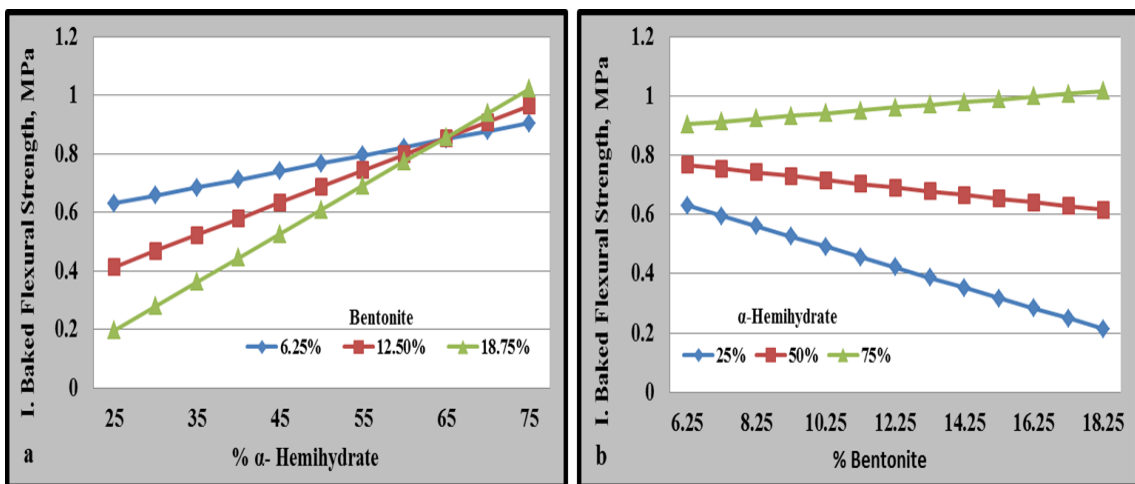
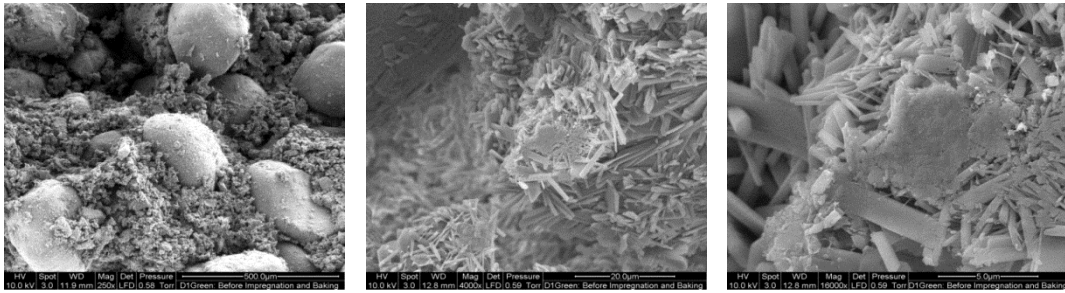
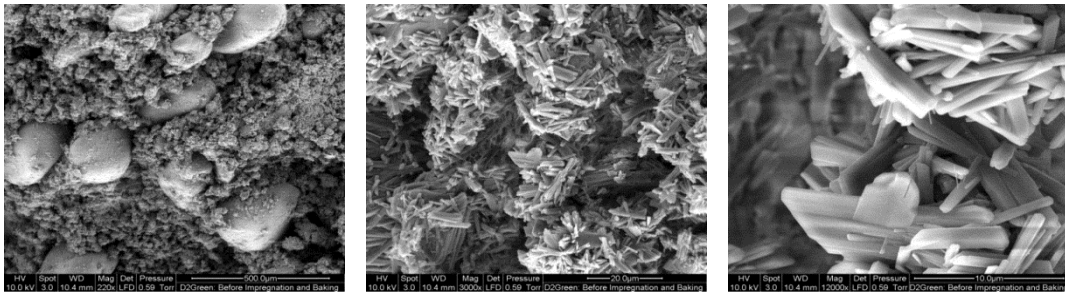


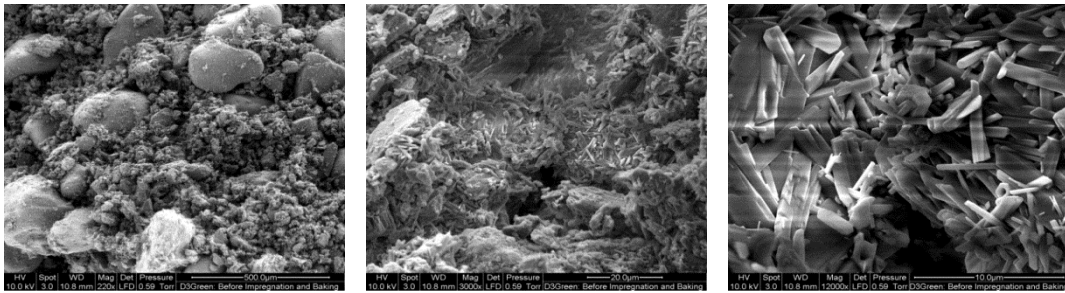
**Fig A2.1. Variation of flexural strength after sodium silicate impregnated and baking with varying %  $\alpha$ -Hemihydrate (a) and % Bentonite (b)**



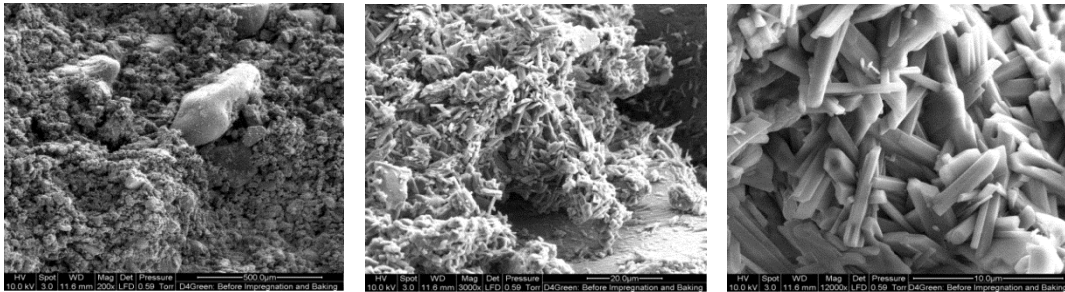
***α-Hemihydrate – 25%, Terra Alba – 12.5% and Bentonite – 12.5%***



***α-Hemihydrate – 75%, Terra Alba – 12.5% and Bentonite – 12.5%***

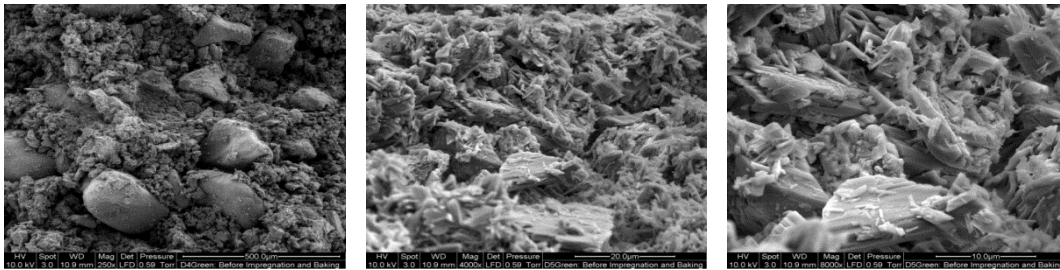


***α-Hemihydrate – 25%, Terra Alba – 37.5% and Bentonite – 12.5%***

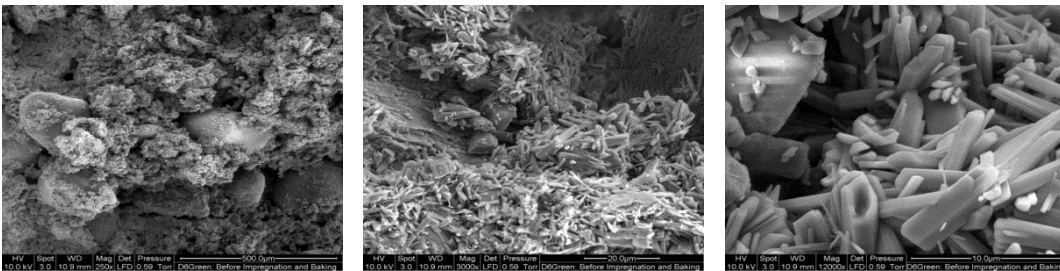


***α-Hemihydrate – 75%, Terra Alba – 37.5% and Bentonite – 12.5%***

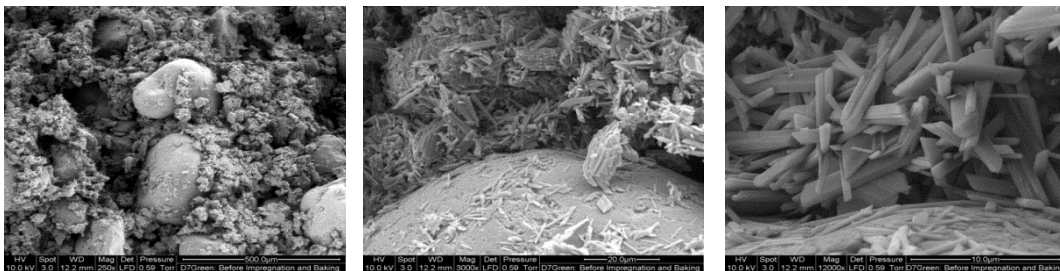
**Fig A 2.3. SEM photomicrographs of printed green samples from experimental trials 1 to 4 in Table A 2.1.**



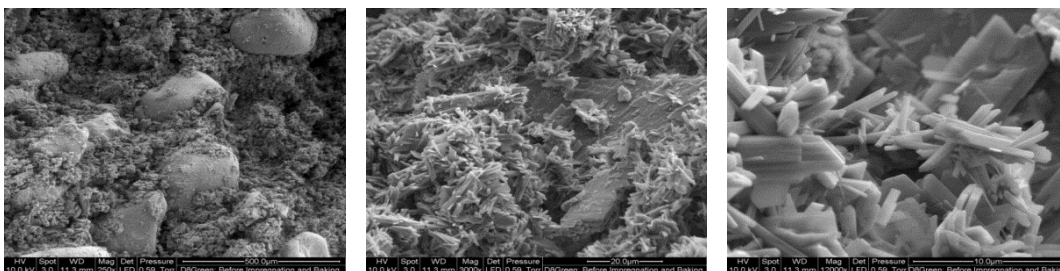
***α-Hemihydrate – 25%, Terra Alba – 25% and Bentonite – 6.25%***



***α-Hemihydrate – 75%, Terra Alba – 25% and Bentonite – 6.25%***

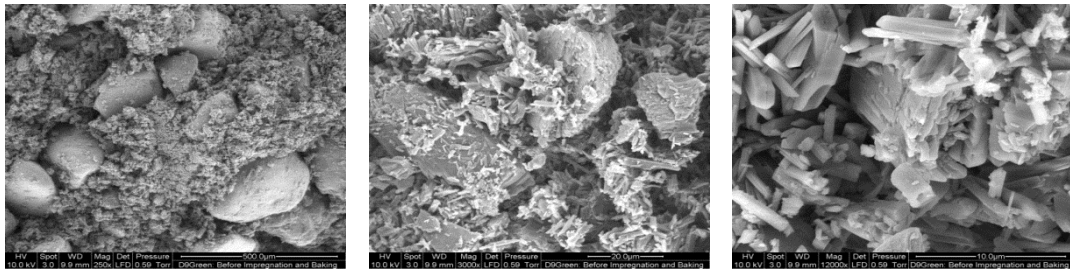


***α-Hemihydrate – 25%, Terra Alba – 25% and Bentonite – 18.75%***

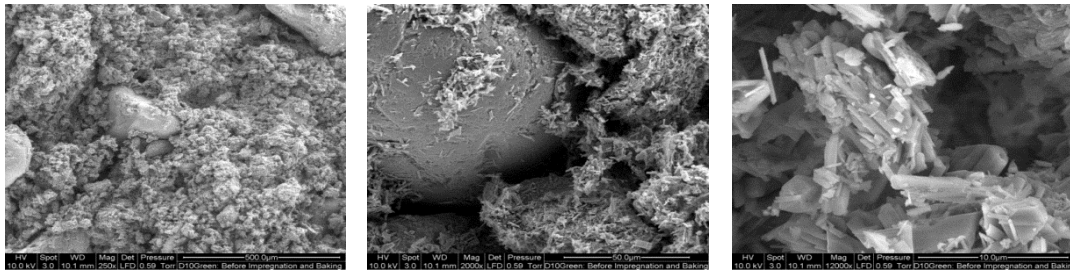


***α-Hemihydrate – 75%, Terra Alba – 25% and Bentonite – 18.75%***

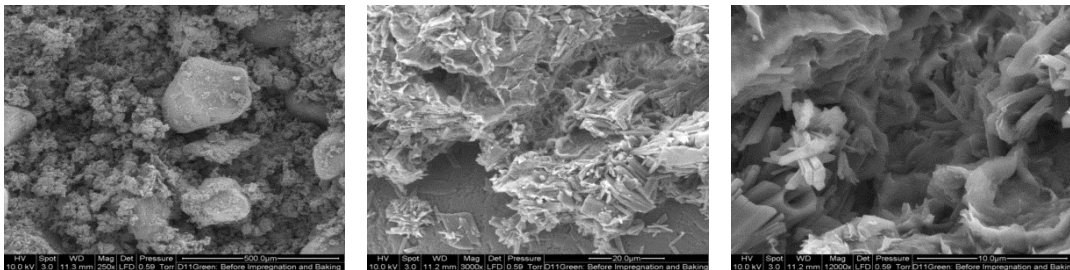
**Fig A 2.4. SEM photomicrographs of printed green samples from experimental trials 5 to 8 in Table A 2.1.**



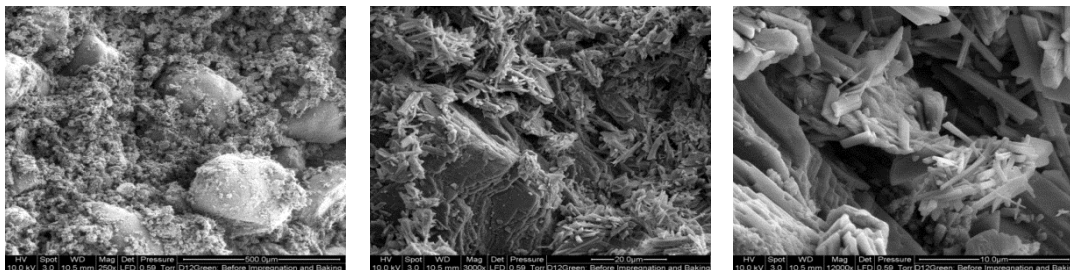
***α-Hemihydrate –50%, Terra Alba – 12.5% and Bentonite –6.25%***



***α-Hemihydrate –50%, Terra Alba – 37.5% and Bentonite –6.25%***

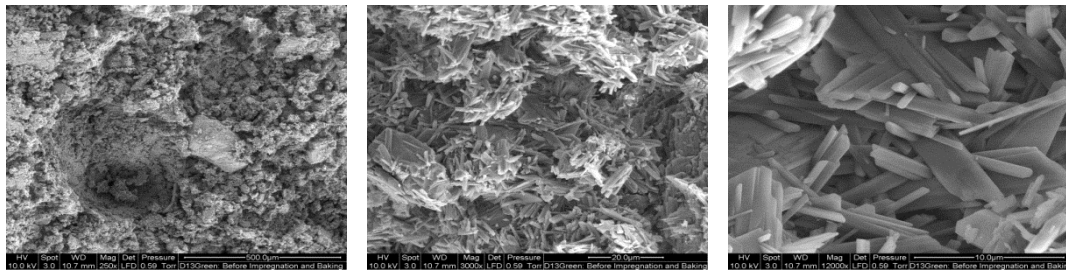


***α-Hemihydrate –50%, Terra Alba – 12.5% and Bentonite – 18.75%***

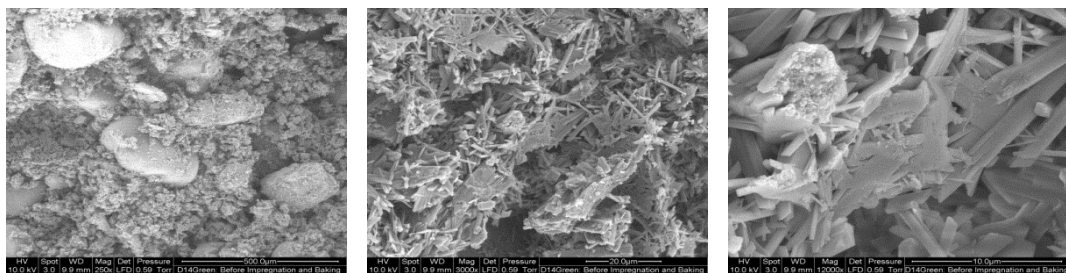


***α-Hemihydrate –50%, Terra Alba – 37.5% and Bentonite – 18.75%***

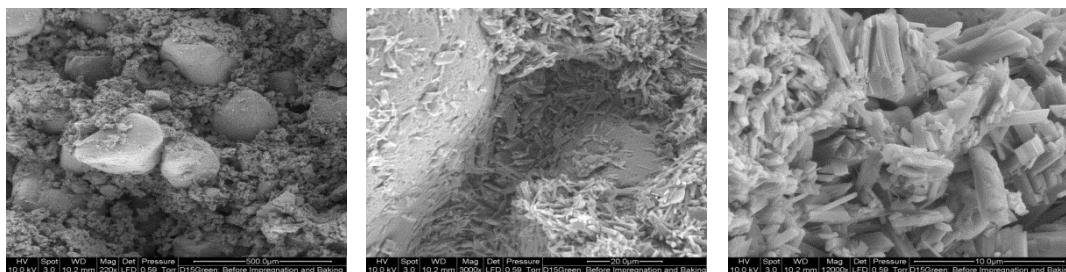
**Fig A 2.5. SEM photomicrographs of printed green samples from experimental trials 9 to 12 in Table A 2.1.**



***$\alpha$ -Hemihydrate –50%, Terra Alba –25% and Bentonite – 12.5%***

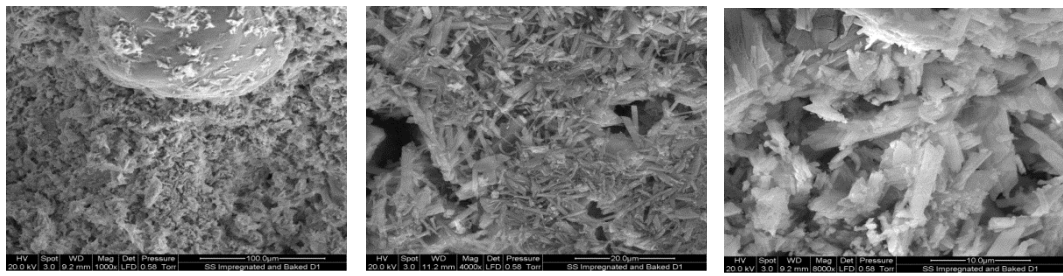


***$\alpha$ -Hemihydrate –50%, Terra Alba –25% and Bentonite – 12.5%***

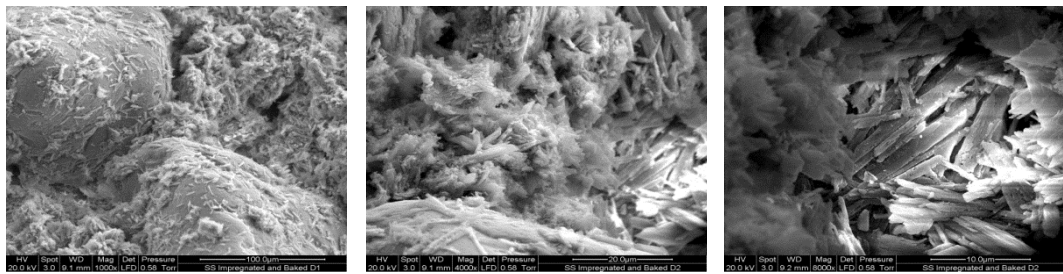


***$\alpha$ -Hemihydrate –50%, Terra Alba –25% and Bentonite – 12.5%***

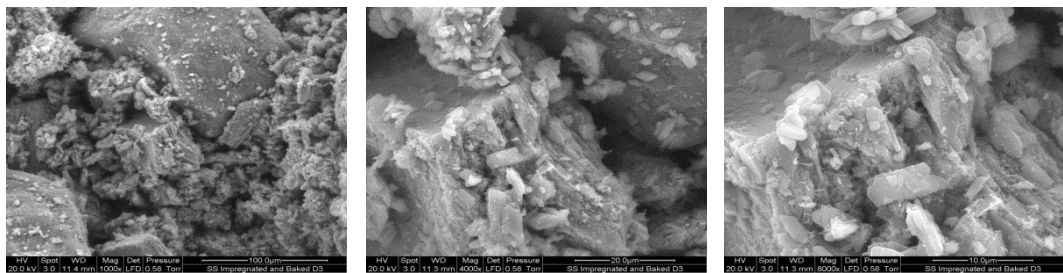
**Fig A2.6. SEM photomicrographs of printed green samples from experimental trials 13 to 15 in Table A 2.1.**



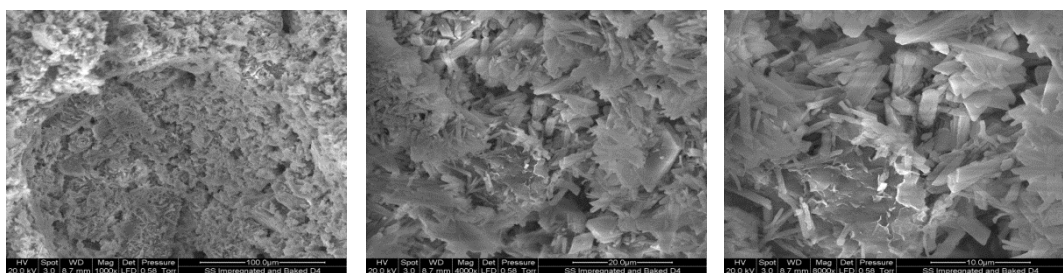
***α-Hemihydrate – 25%, Terra Alba – 12.5% and Bentonite – 12.5%***



***α-Hemihydrate – 75%, Terra Alba – 12.5% and Bentonite – 12.5%***

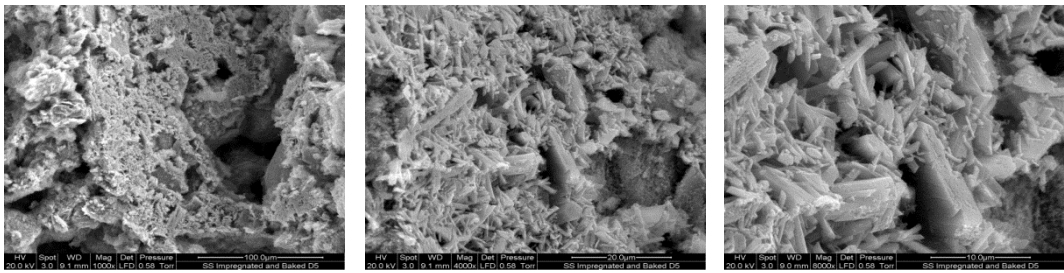


***α-Hemihydrate – 25%, Terra Alba – 37.5% and Bentonite – 12.5%***

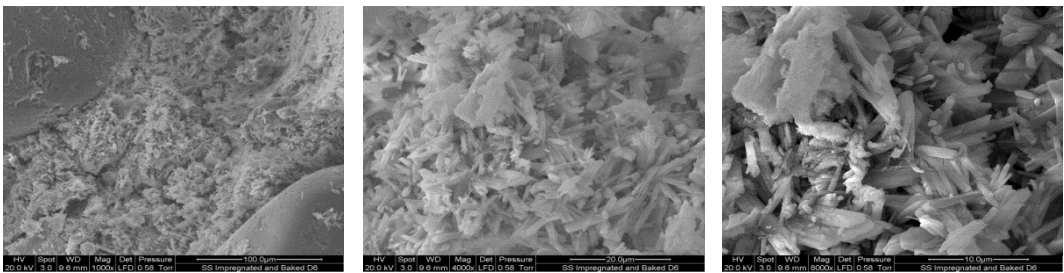


***α-Hemihydrate – 75%, Terra Alba – 37.5% and Bentonite – 12.5%***

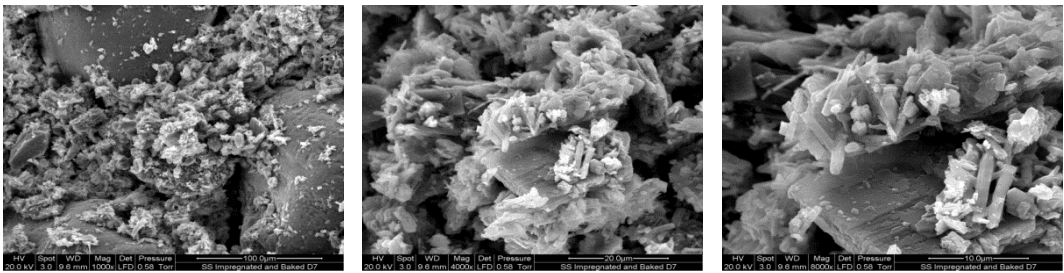
**Fig A2.7. SEM photomicrograph of printed moulds impregnated with diluted sodium silicate and oven baked samples from experimental trials 1 to 4 in Table A2.1 and measured at the centre of the mould**



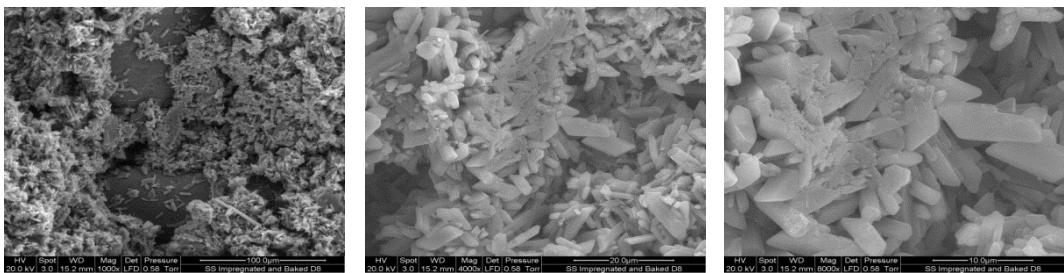
***α-Hemihydrate – 25%, Terra Alba – 25% and Bentonite – 6.25%***



***α-Hemihydrate – 75%, Terra Alba – 25% and Bentonite – 6.25%***

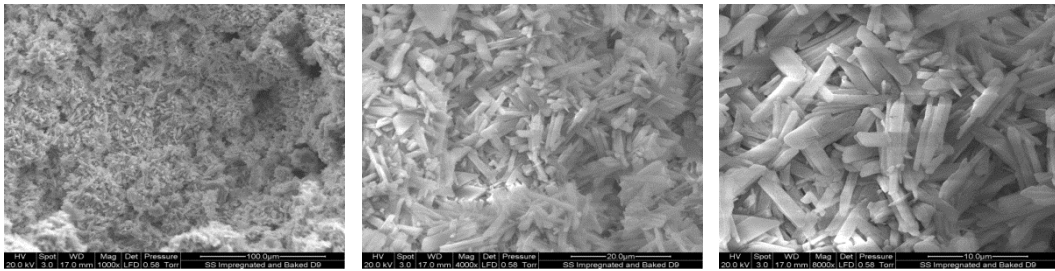


***α-Hemihydrate – 25%, Terra Alba – 25% and Bentonite – 18.75%***

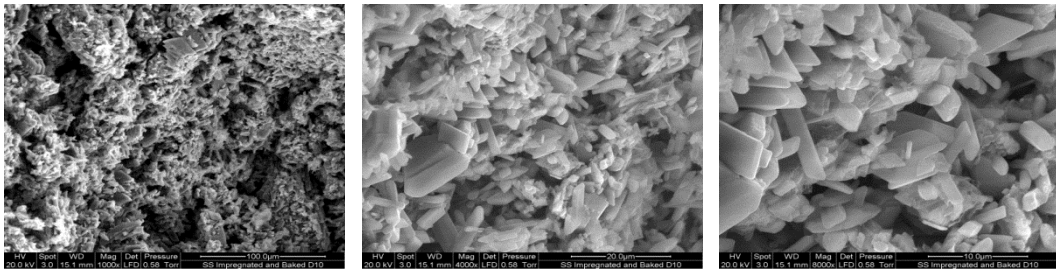


***α-Hemihydrate – 75%, Terra Alba – 25% and Bentonite – 18.75%***

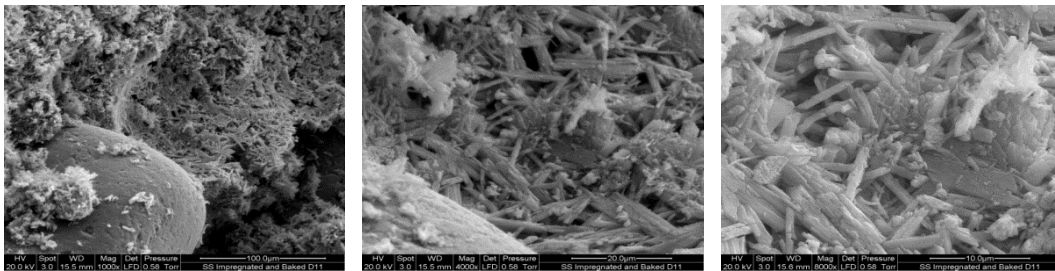
**Fig A2.8. SEM photomicrograph of printed moulds impregnated with diluted sodium silicate and oven baked samples from experimental trials 5 to 8 in Table A2.1 and measured at the centre of the mould**



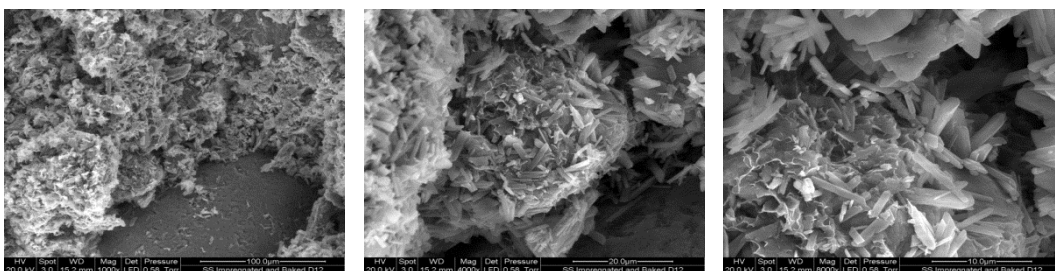
***$\alpha$ -Hemihydrate –50%, Terra Alba – 12.5% and Bentonite –6.25%***



***$\alpha$ -Hemihydrate –50%, Terra Alba – 37.5% and Bentonite –6.25%***

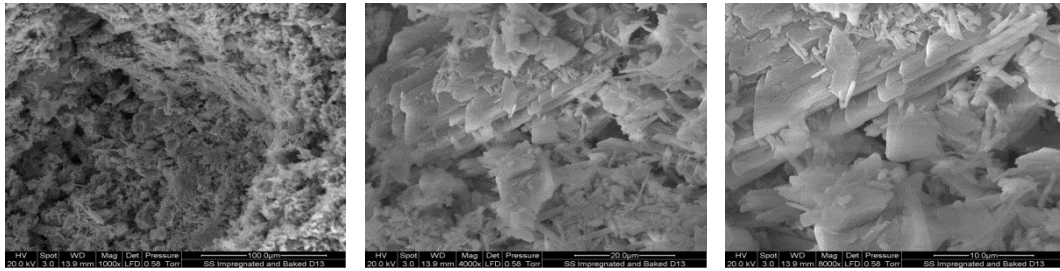


***$\alpha$ -Hemihydrate –50%, Terra Alba – 12.5% and Bentonite – 18.75%***

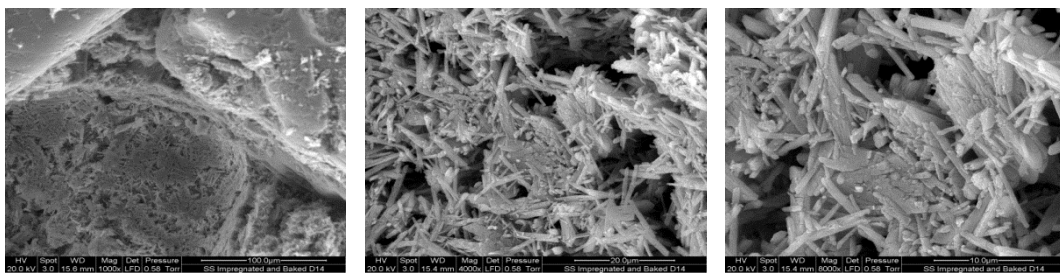


***$\alpha$ -Hemihydrate –50%, Terra Alba – 37.5% and Bentonite – 18.75%***

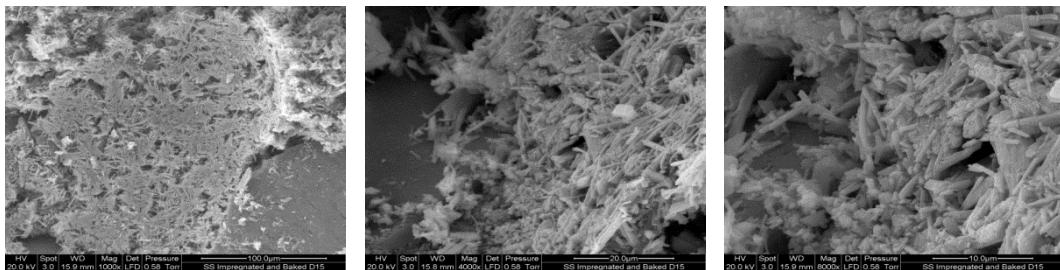
**Fig A2.9. SEM photomicrograph of printed moulds impregnated with diluted sodium silicate and oven baked samples from experimental trials 9 to 12 in Table A2.1 and measured at the centre of the mould**



***α-Hemihydrate –50%, Terra Alba –25% and Bentonite – 12.5%***

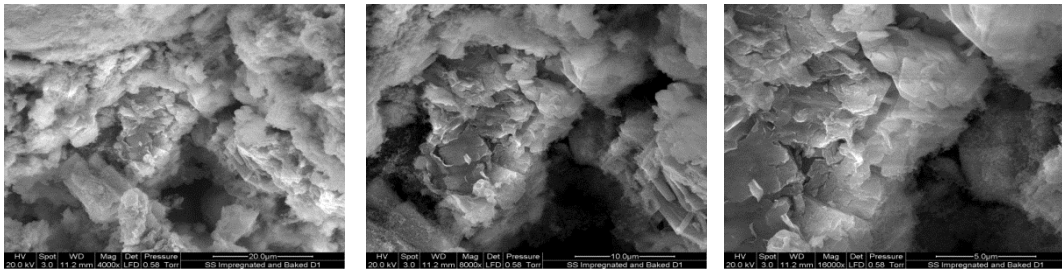


***α-Hemihydrate –50%, Terra Alba –25% and Bentonite – 12.5%***

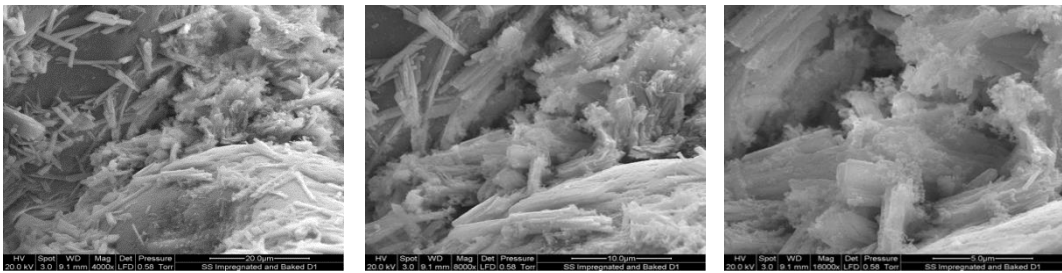


***α-Hemihydrate –50%, Terra Alba –25% and Bentonite – 12.5%***

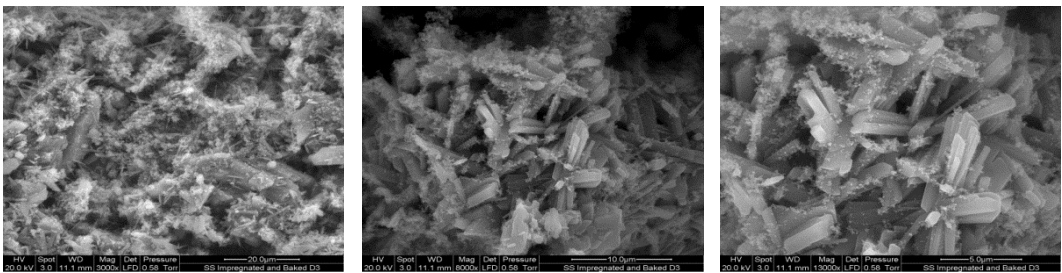
**Fig A2.10. SEM photomicrograph of printed moulds impregnated with diluted sodium silicate and oven baked samples from experimental trials 13 to 15 in Table A2.1 and measured at the centre of the mould**



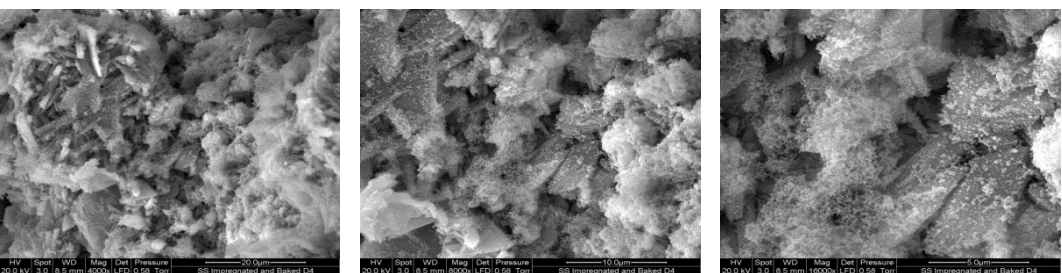
***$\alpha$ -Hemihydrate – 25%, Terra Alba – 12.5% and Bentonite – 12.5%***



***$\alpha$ -Hemihydrate – 75%, Terra Alba – 12.5% and Bentonite – 12.5%***

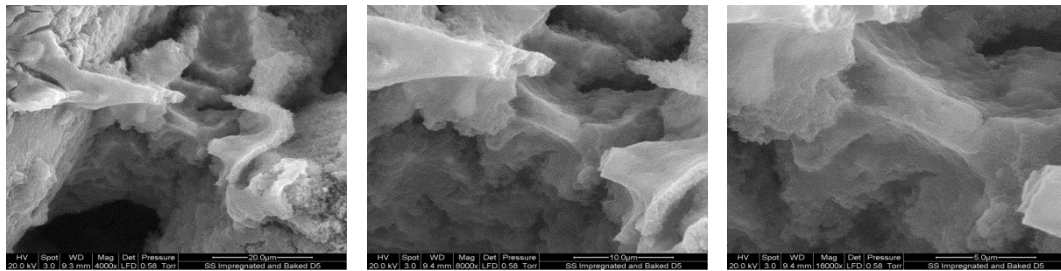


***$\alpha$ -Hemihydrate – 25%, Terra Alba – 37.5% and Bentonite – 12.5%***

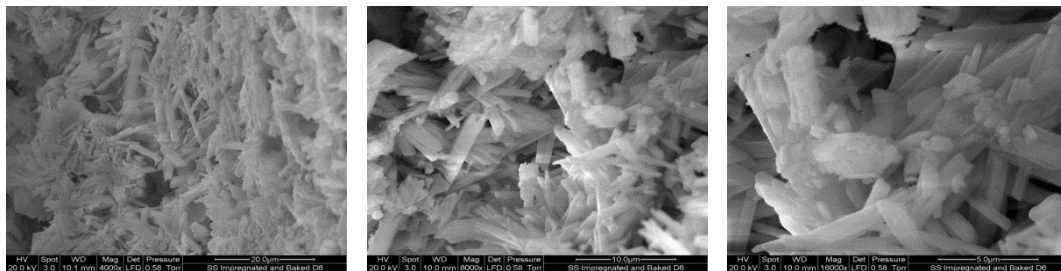


***$\alpha$ -Hemihydrate – 75%, Terra Alba – 37.5% and Bentonite – 12.5%***

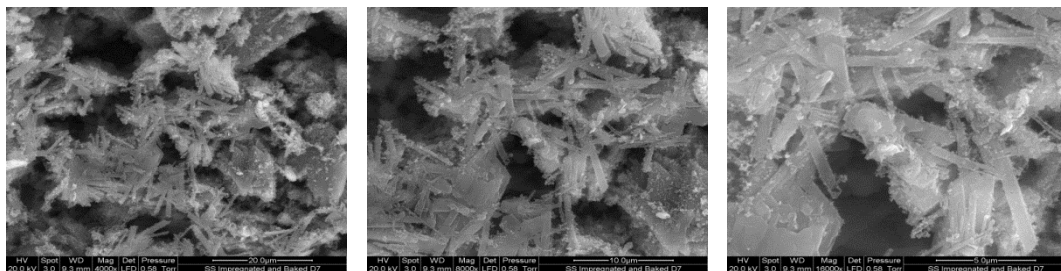
**Fig A2.11. SEM photomicrograph of printed moulds impregnated with diluted sodium silicate and oven baked samples from experimental trials 1 to 4 in Table A2.1 and measured at cavity surface of the mould**



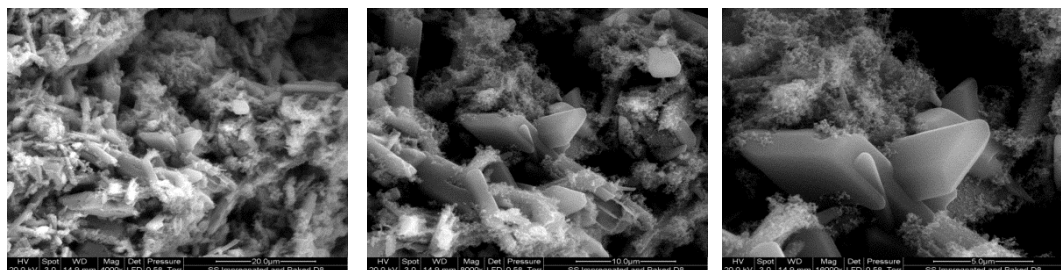
***$\alpha$ -Hemihydrate – 25%, Terra Alba – 25% and Bentonite – 6.25%***



***$\alpha$ -Hemihydrate – 75%, Terra Alba – 25% and Bentonite – 6.25%***

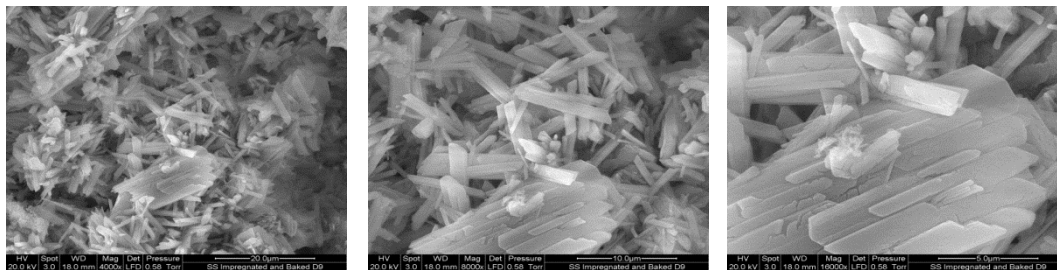


***$\alpha$ -Hemihydrate – 25%, Terra Alba – 25% and Bentonite – 18.75%***

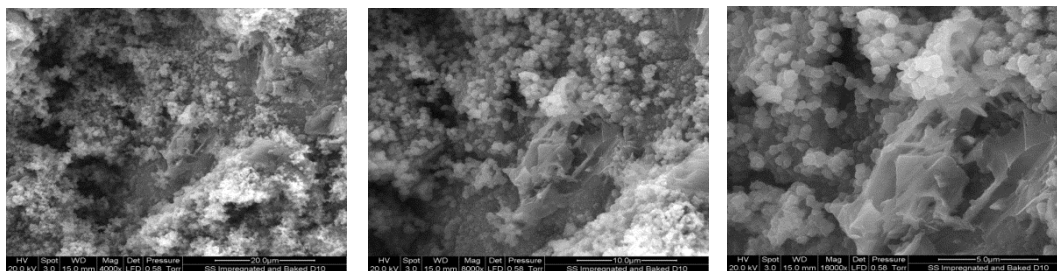


***$\alpha$ -Hemihydrate – 75%, Terra Alba – 25% and Bentonite – 18.75%***

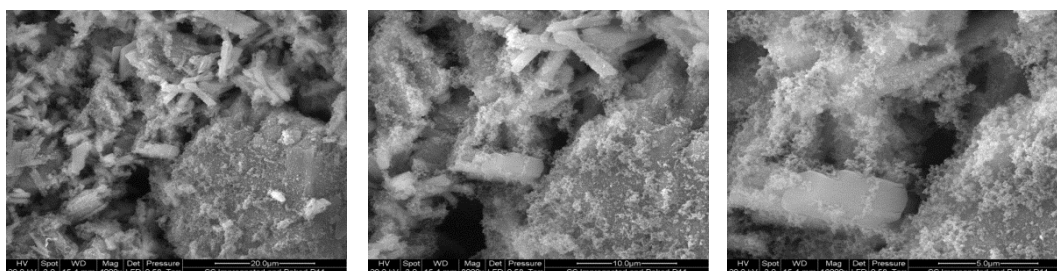
**Fig A2.12. SEM photomicrograph of printed moulds impregnated with diluted sodium silicate and oven baked samples from experimental trials 5 to 8 in Table A2.1 and measured at cavity surface of the mould**



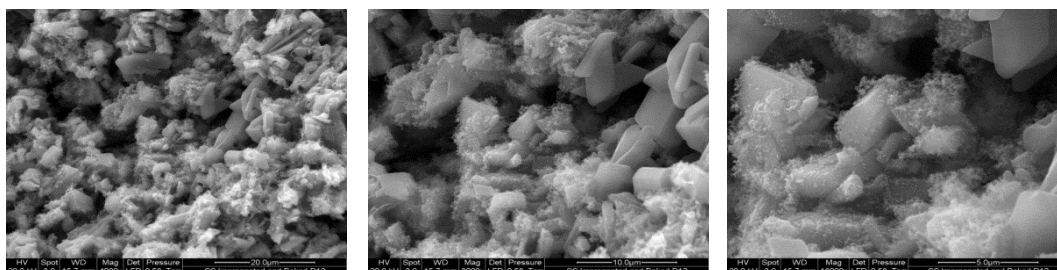
***α-Hemihydrate –50%, Terra Alba – 12.5% and Bentonite –6.25%***



***α-Hemihydrate –50%, Terra Alba – 37.5% and Bentonite –6.25%***

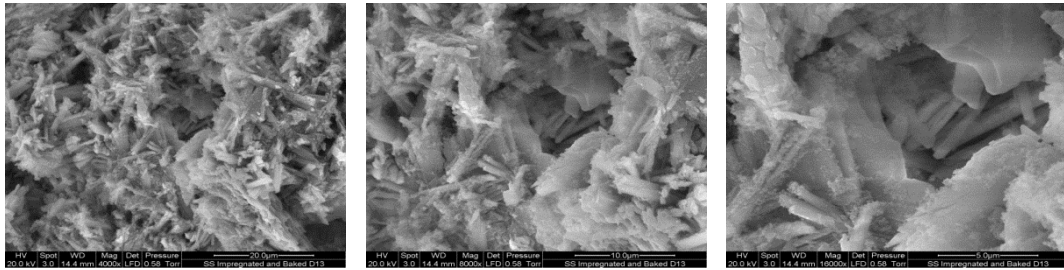


***α-Hemihydrate –50%, Terra Alba – 12.5% and Bentonite – 18.75%***

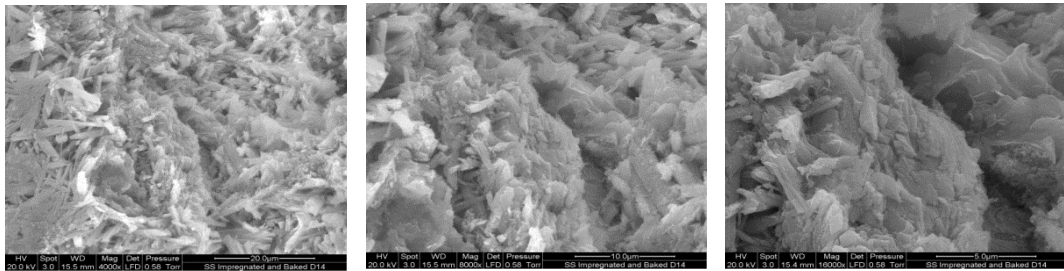


***α-Hemihydrate –50%, Terra Alba – 37.5% and Bentonite – 18.75%***

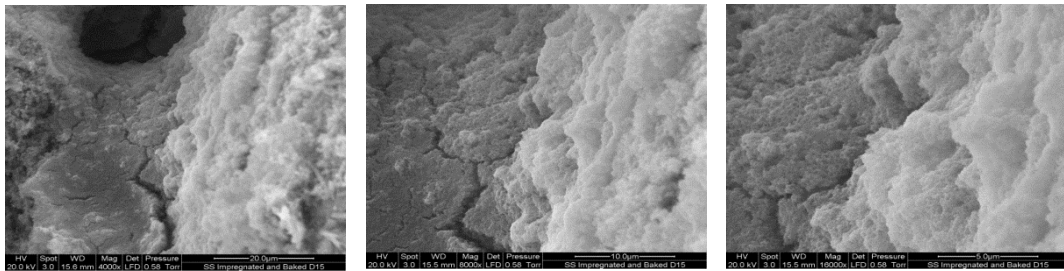
**Fig A2.13. SEM photomicrograph of printed moulds impregnated with diluted sodium silicate and oven baked samples from experimental trials 9 to 12 in Table A2.1 and measured at cavity surface of the mould**



***α-Hemihydrate –50%, Terra Alba –25% and Bentonite – 12.5%***

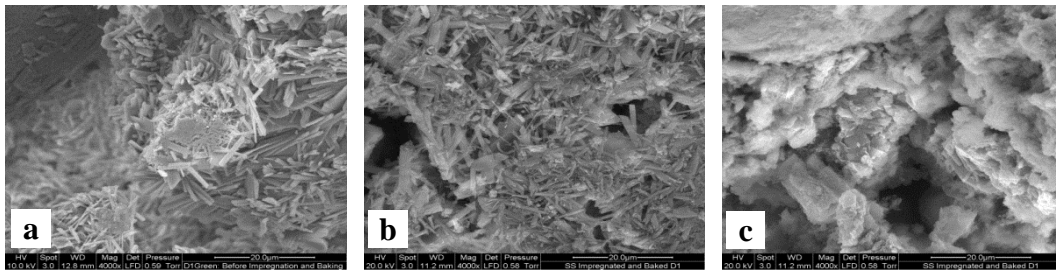


***α-Hemihydrate –50%, Terra Alba –25% and Bentonite – 12.5%***

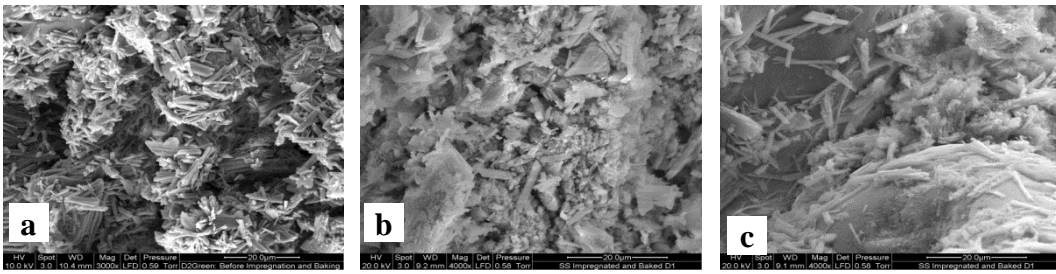


***α-Hemihydrate –50%, Terra Alba –25% and Bentonite – 12.5%***

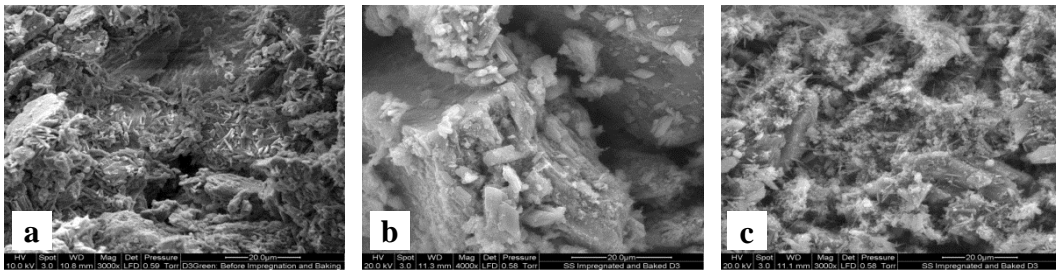
**Fig A2.14. SEM photomicrograph of printed moulds impregnated with diluted sodium silicate and oven baked samples from experimental trials 12 to 15 in Table A2.1 and measured at cavity surface of the mould**



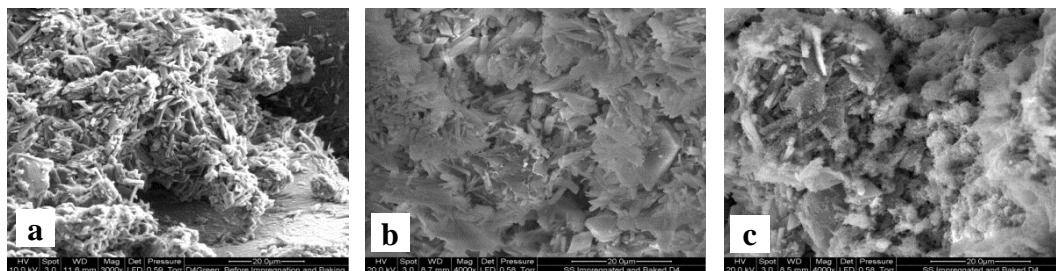
***$\alpha$ -Hemihydrate – 25%, Terra Alba – 12.5% and Bentonite – 12.5%***



***$\alpha$ -Hemihydrate – 75%, Terra Alba – 12.5% and Bentonite – 12.5%***

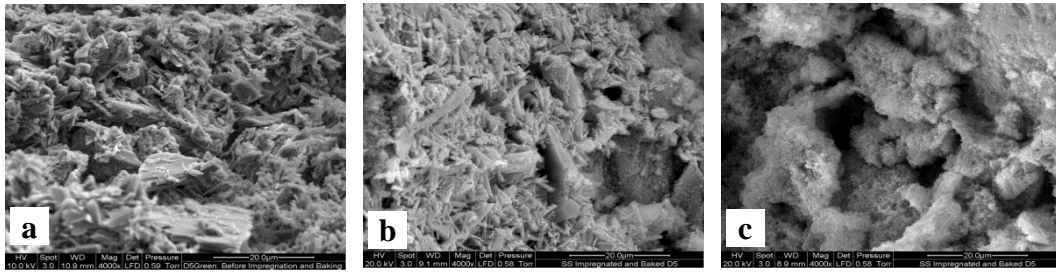


***$\alpha$ -Hemihydrate – 25%, Terra Alba – 37.5% and Bentonite – 12.5%***

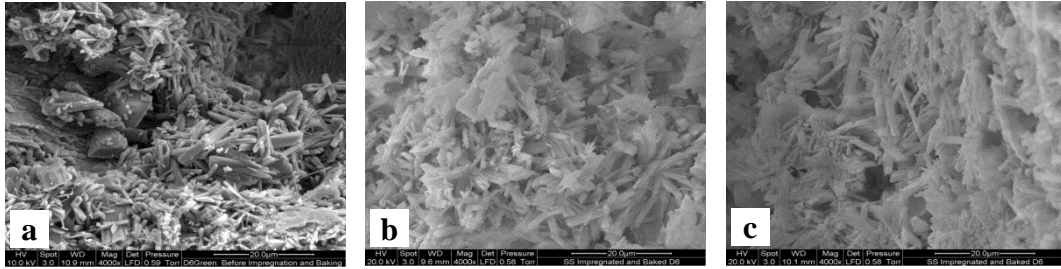


***$\alpha$ -Hemihydrate – 75%, Terra Alba – 37.5% and Bentonite – 12.5%***

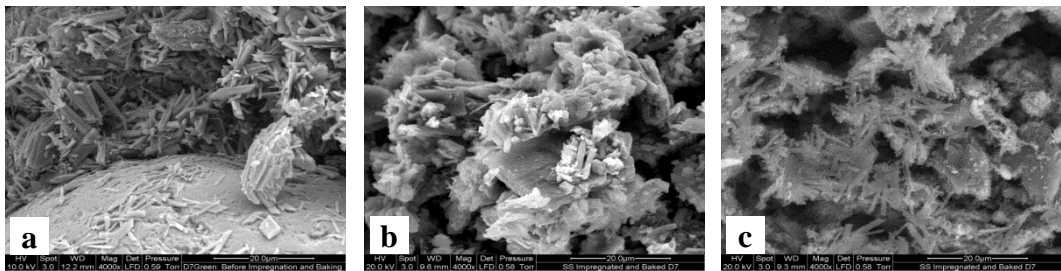
**Fig A2.15 Comparison of SEM photomicrographs of moulds at various stages, (a) Green, Impregnated and baked measured at centre (b) and at cavity (c) of samples from experimental trials 1 to 4 in Table A2.1 and measured at cavity**



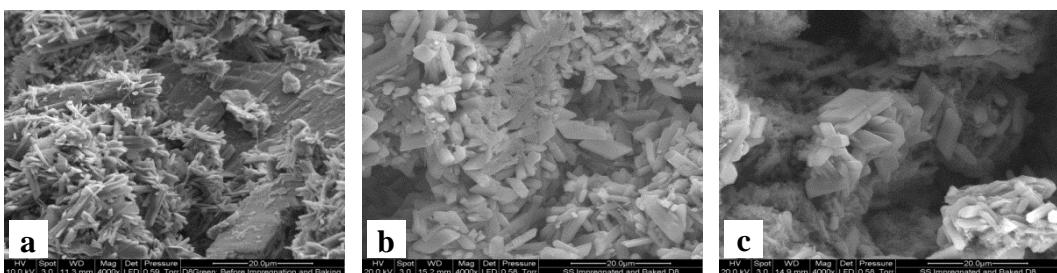
***α-Hemihydrate – 25%, Terra Alba – 25% and Bentonite – 6.25%***



***α-Hemihydrate – 75%, Terra Alba – 25% and Bentonite – 6.25%***

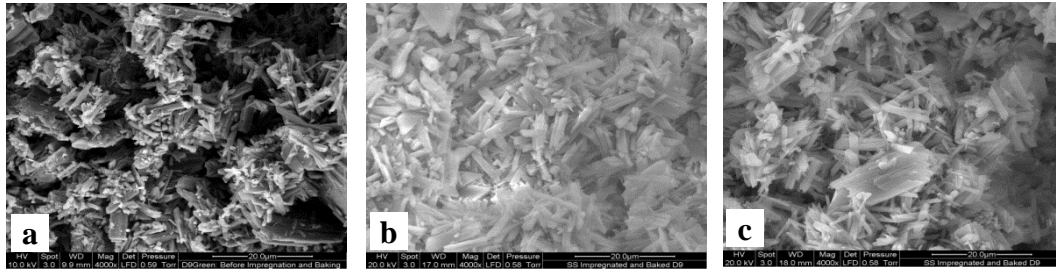


***α-Hemihydrate – 25%, Terra Alba – 25% and Bentonite – 18.75%***

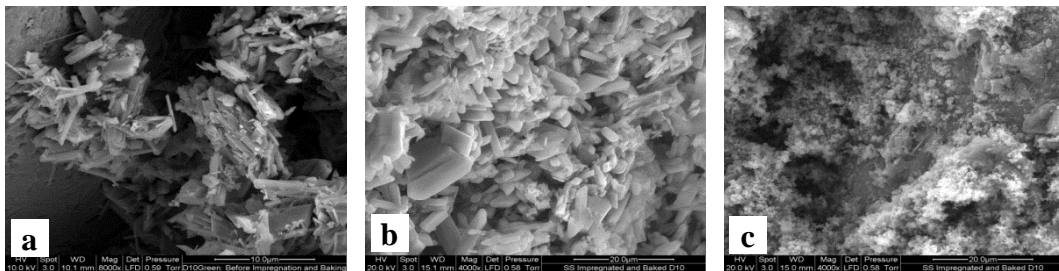


***α-Hemihydrate – 75%, Terra Alba – 25% and Bentonite – 18.75%***

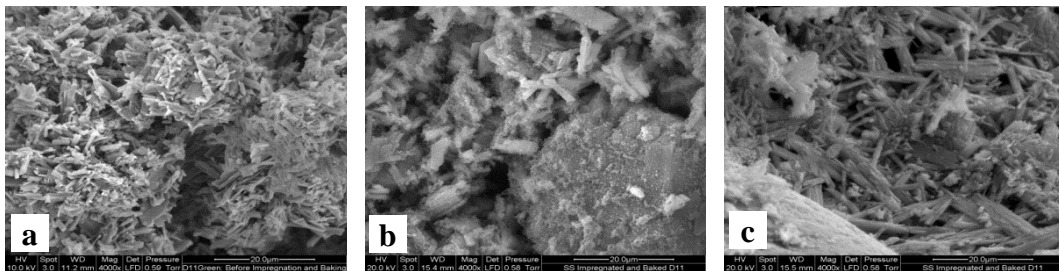
**Fig A2.16 Comparison of SEM photomicrographs of moulds at various stages, (a) Green, Impregnated and baked measured at centre (b) and at cavity (c) of samples from experimental trials 5 to 8 in Table A2.1 and measured at cavity**



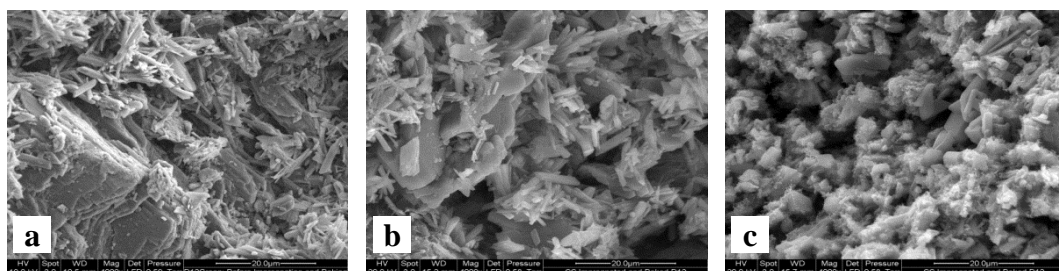
***$\alpha$ -Hemihydrate –50%, Terra Alba – 12.5% and Bentonite –6.25%***



***$\alpha$ -Hemihydrate –50%, Terra Alba – 37.5% and Bentonite –6.25%***

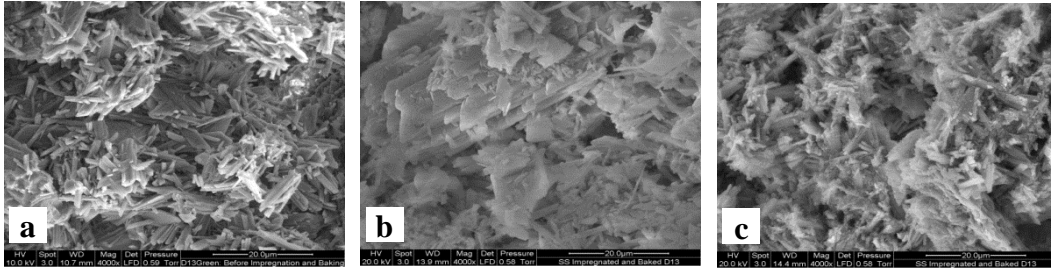


***$\alpha$ -Hemihydrate –50%, Terra Alba – 12.5% and Bentonite – 18.75%***

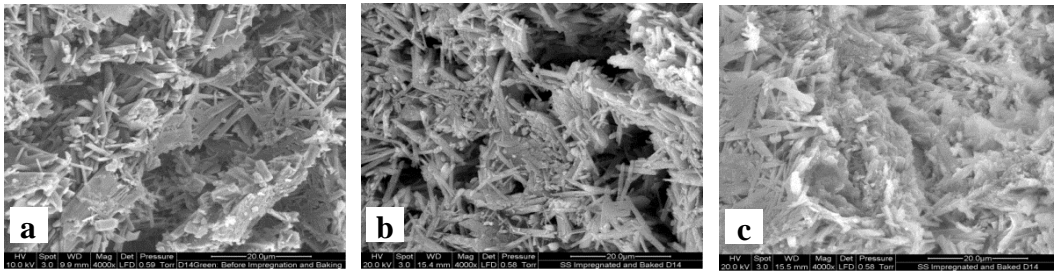


***$\alpha$ -Hemihydrate –50%, Terra Alba – 37.5% and Bentonite – 18.75%***

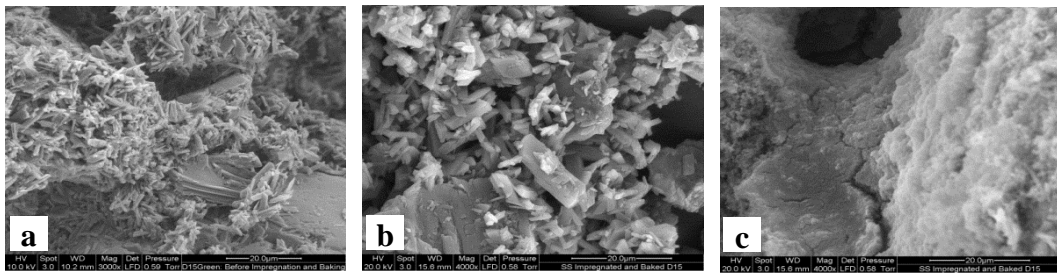
**Fig A2.17 Comparison of SEM photomicrographs of moulds at various stages, (a) Green, Impregnated and baked measured at centre (b) and at cavity (c) of samples from experimental trials 9 to 12 in Table A2.1 and measured at cavity**



*$\alpha$ -Hemihydrate –50%, Terra Alba – 25% and Bentonite – 12.5%*

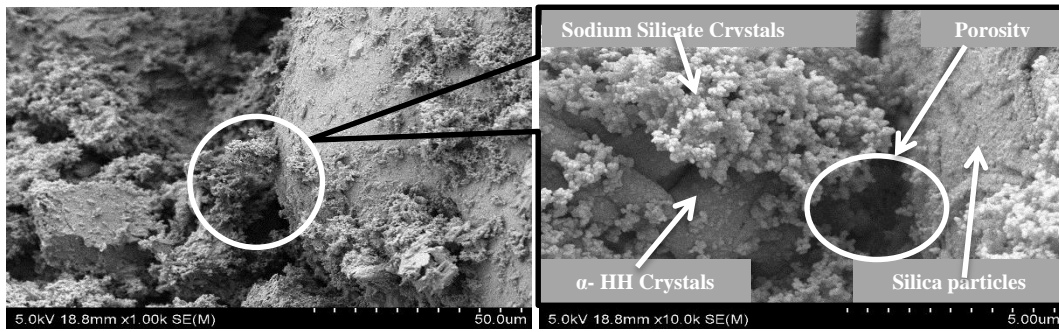


*$\alpha$ -Hemihydrate –50%, Terra Alba – 25% and Bentonite – 12.5%*

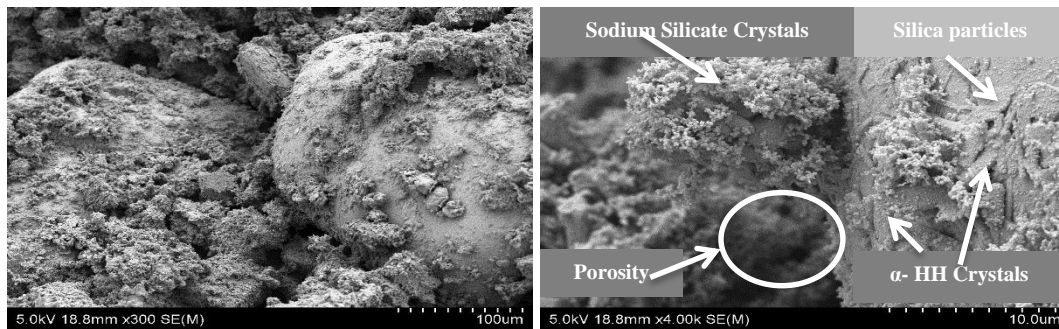


*$\alpha$ -Hemihydrate –50%, Terra Alba – 25% and Bentonite – 12.5%*

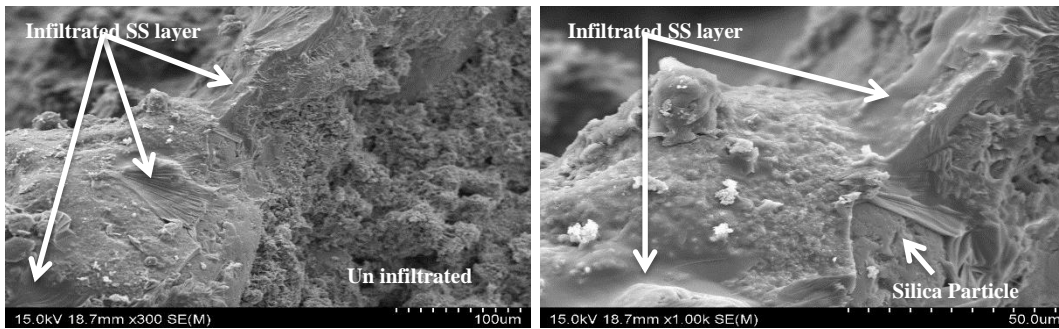
**Fig A2.18 Comparison of SEM photomicrographs of moulds at various stages, (a) Green, Impregnated and baked measured at centre (b) and at cavity (c) of samples from experimental trials 13 to 15 in Table A2.1 and measured at cavity**



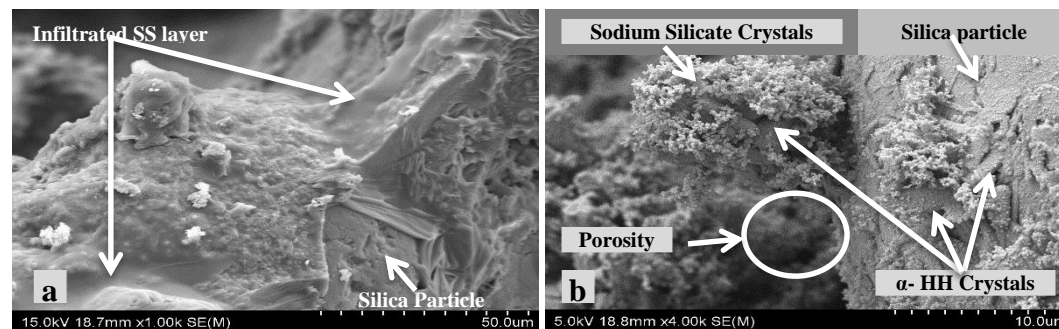
**Sodium silicate crystals,  $\alpha$ -HH crystals and porosity after baking the mould.**



**Sodium silicate crystals,  $\alpha$ -HH crystals and porosity after baking the mould.**



**Mould was soaked for 12hrs in diluted (1:5) sodium silicate with water and air dried (Green State).**



**a. Mould was soaked for 12hrs in diluted (1:5) sodium silicate with water and air dried, b. mould baked at 500°C for 24hrs.**

**Fig A2.19 Comparison of SEM photomicrographs of printed moulds with  $\alpha$ -Hemihydrate –50%, Terra Alba – 12.5% and Bentonite –6.25%, (Trial no 9)**



**Fig A2.20(a) Sodium silicate impregnated and un-impregnated zones of the baked mould wall, (b) Crystals of  $\alpha$ -HH and sodium silicate at impregnated zone,(c & d) Crystals of  $\alpha$ -HH at un-impregnated zone.**

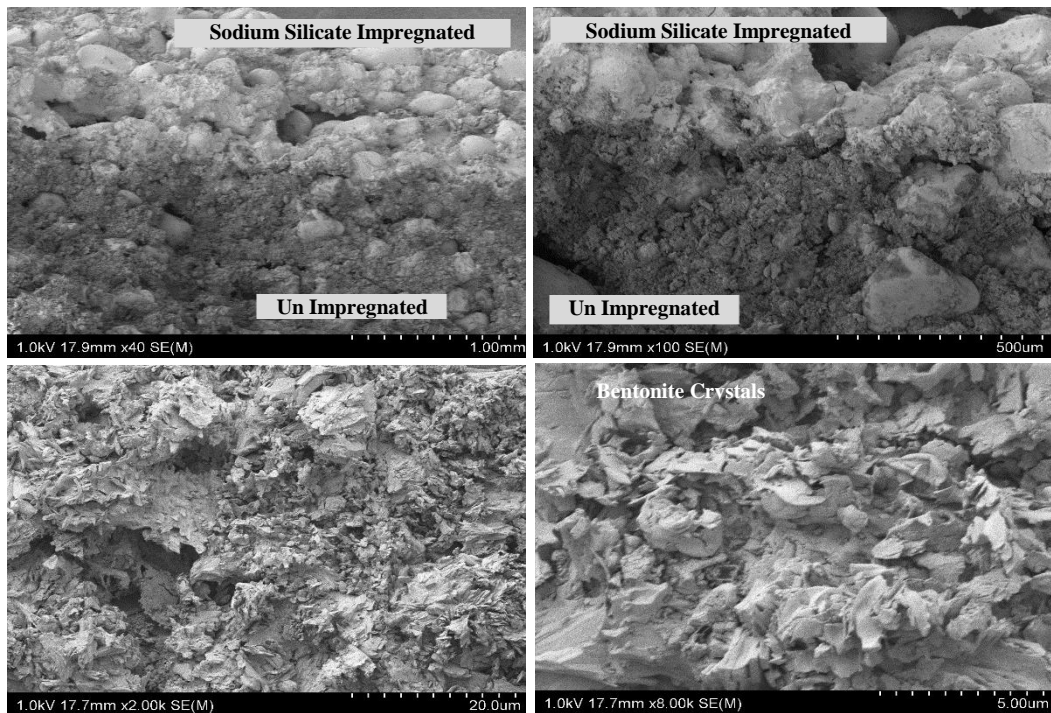


**Fig A2.21 Bentonite crystals of baked mould impregnated in diluted sodium silicate and dried**

### Appendix 3

## Resin coated sand material system: Additional experimental data and results

Table A3.1 L8 Modified two-level orthogonal array (one four level factor) with natural values

Trail No	Factor 1	Factor 2	X <sub>1</sub>	X <sub>2</sub>
1	1	1	6	5
2	1	2	6	10
3	2	1	8	5
4	2	2	8	10
5	3	1	10	5
6	3	2	10	10
7	4	1	12	5
8	4	2	12	10

Table A3.2 Percent volume contraction in green state (mould)

Run No	Trial 1	Trial 2	Trial 3	Trial 4	Trial 5	Trial 6	Average	St. Deviation	St. Error
1	1.19	-1.40	-1.00	-1.19	0.39	0.39	<b>-0.27</b>	1.06	0.43
2	-3.16	-3.38	-2.00	-0.42	-4.37	-0.80	<b>-2.35</b>	1.55	0.63
3	-3.17	-1.19	-2.38	-3.36	-2.97	-1.19	<b>-2.38</b>	0.97	0.39
4	-5.89	-5.69	-1.98	-4.53	-4.34	-3.56	<b>-4.33</b>	1.44	0.58
5	-1.98	-0.99	-3.37	-3.95	-2.78	-2.19	<b>-2.54</b>	1.05	0.43
6	4.00	-3.95	2.00	-3.77	-3.20	-2.01	<b>-1.15</b>	3.35	1.36
7	-1.21	-1.00	-2.21	-3.95	-3.57	-2.78	<b>-2.45</b>	1.21	0.49
8	-0.20	-2.99	-2.20	-1.65	-4.37	-2.41	<b>-2.30</b>	1.38	0.56

**Table A3.3 Percentage volume contraction in the baked state (mould)**

Run No	Trial 1	Trial 2	Trial 3	Trial 4	Trial 5	Trial 6	Average	St. Deviation	St. Error
1	1.19	-1.40	-1.00	-1.19	0.39	-0.20	<b>-0.37</b>	1.02	0.41
2	-3.16	-3.38	-2.00	-0.61	-4.75	-0.99	<b>-2.48</b>	1.57	0.64
3	-3.95	-1.98	-2.97	-5.11	-3.75	-2.18	<b>-3.32</b>	1.18	0.48
4	-6.08	-7.02	-1.98	-4.92	-4.53	-3.56	<b>-4.68</b>	1.79	0.73
5	-1.98	-1.59	-3.95	-3.95	-3.56	-3.17	<b>-3.04</b>	1.018	0.41
6	1.51	-3.95	-1.41	-4.36	-4.16	-2.60	<b>-2.49</b>	2.26	0.92
7	-2.19	-1.79	-2.99	-5.32	-5.12	-3.36	<b>-3.46</b>	1.47	0.60
8	-1.19	-3.38	-3.19	-2.42	-5.13	-2.79	<b>-3.02</b>	1.29	0.52

**Table A3.4 Flexural strength in the green state (mould)**

Run No	Trial 1 (MPa)	Trial 2 (MPa)	Trial 3 (MPa)	Average	St. Deviation	St. Error
1	0.60	0.54	0.73	<b>0.62</b>	0.09	0.05
2	0.67	0.66	0.54	<b>0.63</b>	0.07	0.04
3	0.29	0.27	0.46	<b>0.343</b>	0.10	0.06
4	0.57	0.26	0.36	<b>0.40</b>	0.16	0.09
5	0.20	0.19	0.21	<b>0.20</b>	0.01	0.006
6	0.55	0.47	0.29	<b>0.44</b>	0.13	0.08
7	0.49	0.63	0.54	<b>0.55</b>	0.07	0.04
8	0.27	0.18	0.32	<b>0.26</b>	0.07	0.04

**Table A3.5 Flexural strength in the baked State**

Run No	Trial 1 (MPa)	Trial 2 (MPa)	Trial 3 (MPa)	Average	St. Deviation	St. Error
1	3.42	4.46	2.76	<b>3.55</b>	0.86	0.49
2	4.21	5.71	4.69	<b>4.87</b>	0.77	0.44
3	3.24	1.97	2.44	<b>2.55</b>	0.64	0.37
4	5.14	3.10	3.12	<b>3.79</b>	1.17	0.68
5	4.00	3.67	3.21	<b>3.63</b>	0.40	0.23
6	1.41	1.86	1.94	<b>1.74</b>	0.28	0.16
7	3.29	2.56	2.21	<b>2.69</b>	0.55	0.32
8	2.71	4.01	2.93	<b>3.22</b>	0.70	0.40

**Table A3.6 Compressive strength in the green state (mould)**

Run No	Trial 1 (MPa)	Trial 2 (MPa)	Trial 3 (MPa)	Average	St. Deviation	St. Error
1	0.16	0.22	0.21	<b>0.20</b>	0.04	0.02
2	0.18	0.17	0.17	<b>0.17</b>	0.01	0.01
3	0.13	0.22	0.17	<b>0.17</b>	0.04	0.02
4	0.08	0.09	0.07	<b>0.08</b>	0.01	0.004
5	0.17	0.17	0.16	<b>0.17</b>	0.003	0.001
6	0.14	0.14	0.22	<b>0.17</b>	0.04	0.03
7	0.19	0.31	0.21	<b>0.24</b>	0.06	0.04
8	0.05	0.08	0.09	<b>0.07</b>	0.02	0.01

**Table A3.7 Compressive strength in the baked state (mould)**

Run No	Trial 1 (MPa)	Trial 2 (MPa)	Trial 3 (MPa)	Average	St. Deviation	St. Error
1	5.35	3.20	3.98	<b>4.17</b>	1.09	0.63
2	5.53	4.67	4.72	<b>4.97</b>	0.48	0.28
3	4.27	4.30	5.39	<b>4.66</b>	0.64	0.37
4	4.80	3.40	5.54	<b>4.58</b>	1.09	0.63
5	4.33	4.99	2.06	<b>3.79</b>	1.54	0.89
6	3.90	2.37	3.51	<b>3.26</b>	0.80	0.46
7	3.65	4.19	3.35	<b>3.73</b>	0.43	0.25
8	2.79	1.19	3.07	<b>2.35</b>	1.02	0.59

**Table A3.8 Percentage volume error of the stainless steel cast part**

Run No	Trial 1			Trail 2			Average (%)	St. Deviation	St. Error
	L1	L2	L3	L1	L2	L3			
1	-20.79	-26.04	-27.75	-27.75	-27.75	-31.11	-26.87	3.40	1.39
2	-3.96	-9.75	-6.88	-10.70	-5.91	-11.64	-8.14	3.01	1.23
3	-5.91	-5.91	-17.19	-7.84	-4.94	-4.94	-7.79	4.73	1.93
4	-9.75	-13.51	-11.64	-9.75	-9.75	-9.75	-10.69	1.57	0.64
5	-9.75	-9.75	-9.75	-9.75	-11.64	-6.88	-9.59	1.53	0.62
6	-10.70	-8.80	-13.51	-15.36	-9.75	-13.51	-11.94	2.56	1.05
7	-10.70	-13.51	-16.28	-12.58	-9.75	-6.88	-11.62	3.26	1.33
8	-16.28	-13.51	-19.00	-16.28	-17.19	-12.58	-15.81	2.38	0.97

**Table A3.9 Surface Roughness of the stainless steel cast part**

Run No	Trial 1		Trail 2		Average (Ra)	St. Deviation	St. Error
	Top	Bottom	Top	Bottom			
1	12.05	12.03	13.91	3.49	10.37	4.67	2.34
2	5.85	10.22	2.34	11.45	7.47	4.18	2.09
3	4.43	10.31	6.98	2.12	5.96	3.51	1.76
4	7.41	8.25	6.53	7.59	7.45	0.71	0.35
5	11.91	5.31	11.73	4.48	8.36	4.01	2.01
6	3.93	4.35	7.06	2.51	4.46	1.90	0.95
7	8.24	9.69	16.65	6.24	10.21	4.52	2.26
8	11.74	1.51	11.68	2.10	6.76	5.72	2.86

**Table A3.10 Ultimate Tensile Strength of the stainless steel cast part**

Run No	Trial 1	Trial 2	Average (MPa)	St. Deviation	St. Error
1	538.54	603.77	571.15	46.13	32.62
2	554.98	448.54	501.76	75.27	53.22
3	450.95	529.93	490.44	197.27	139.49
4	493.02	529.52	511.27	25.81	18.25
5	524.32	503.16	513.74	14.96	10.58
6	623.95	561.65	592.80	44.06	31.15
7	473.11	518.50	495.81	32.10	22.70
8	544.54	641.46	593.00	68.53	48.46

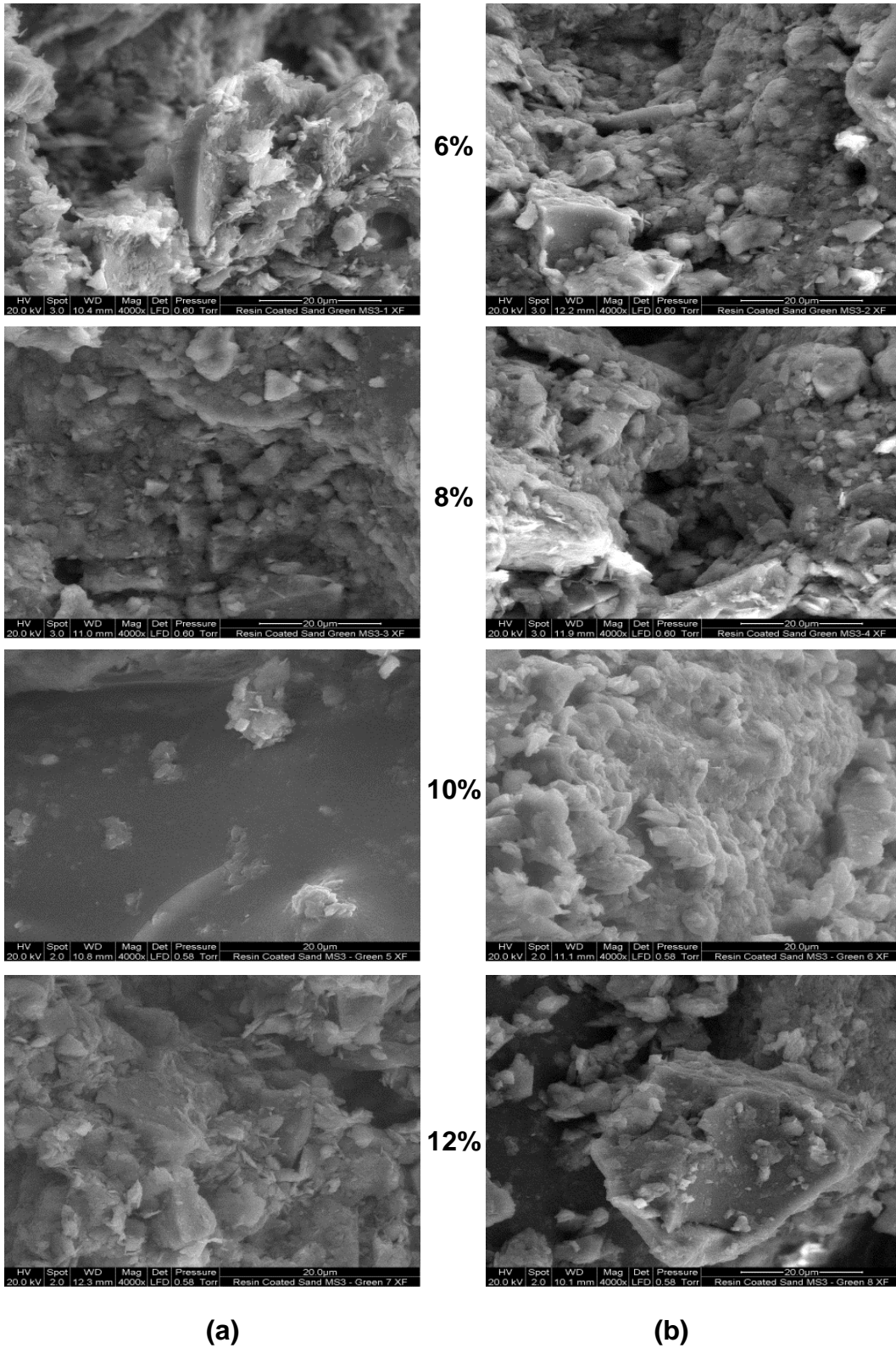


**Fig A3.1** Photomicrographs of fractured parts with silica flour (a) 5%, (b) 10% and clay varied from 6% to 12%.

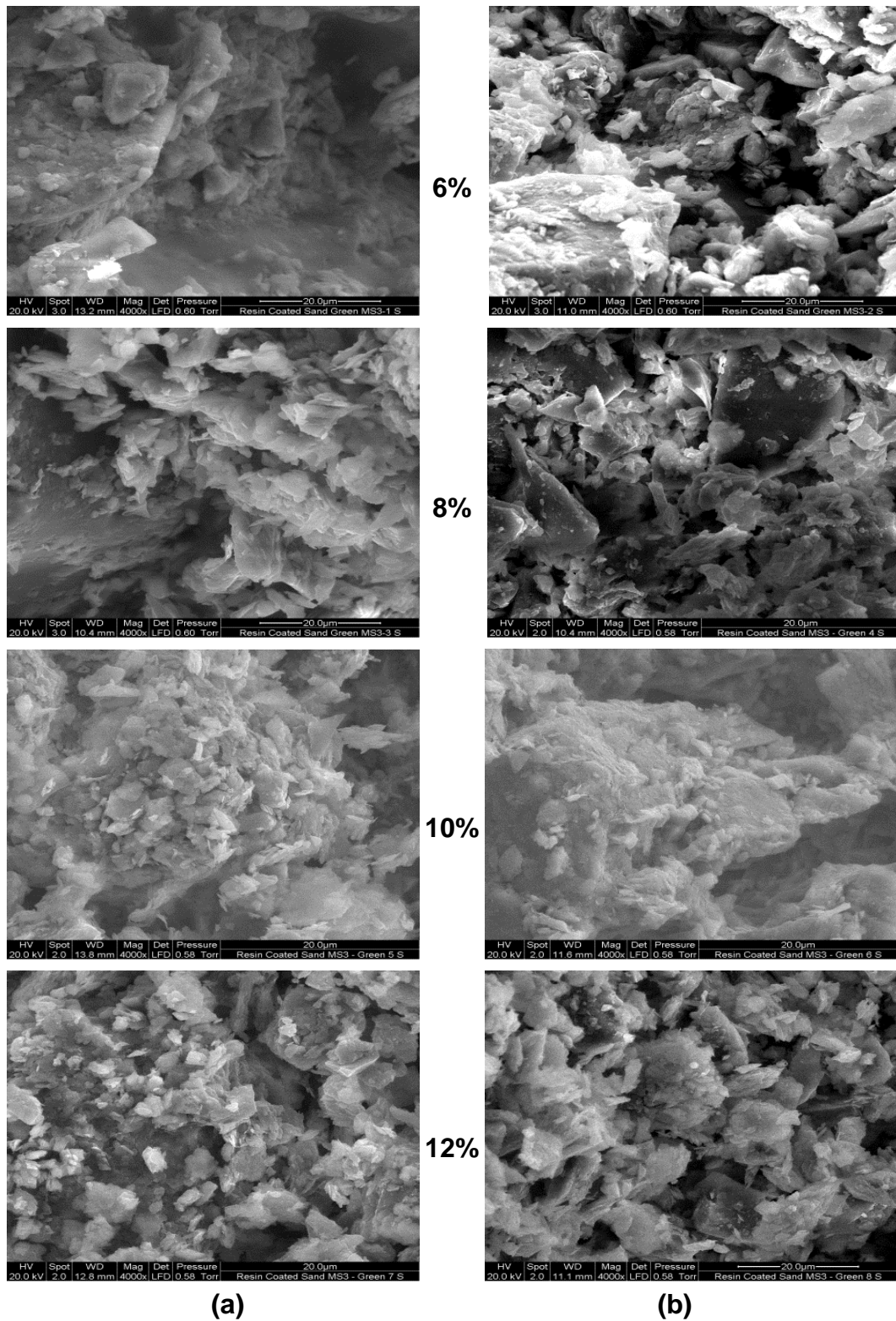


**Fig A3.2 Photomicrographs at the outer surfaces of printed green samples with silica flour at (a) 5%, (b) 10% and clay varied from 6% to 12%.**

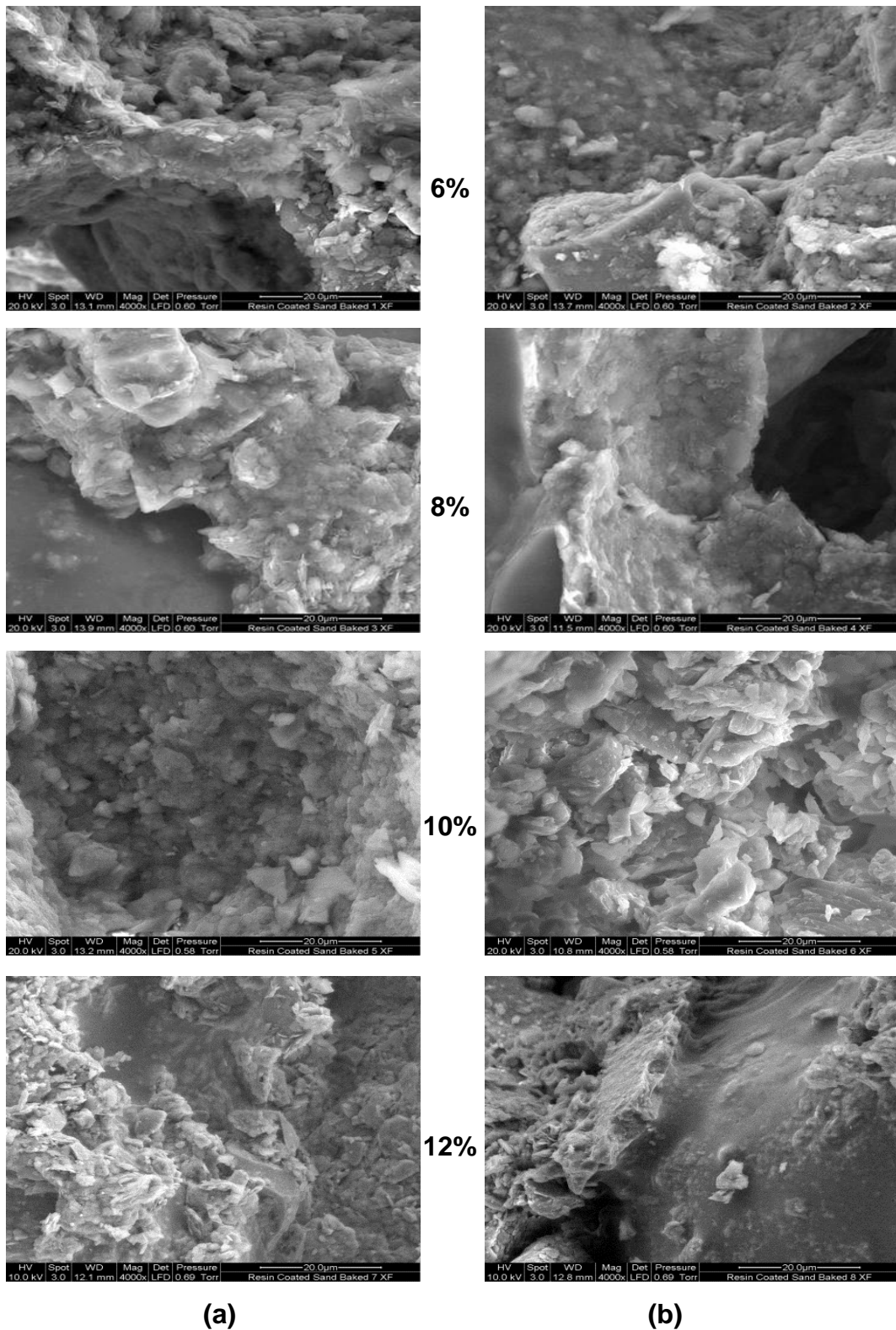


**Fig A3.3 Photomicrographs of fractured surfaces of baked parts with silica flour (a) 5%, (b) 10% and clay varied from 6% to 12%.**

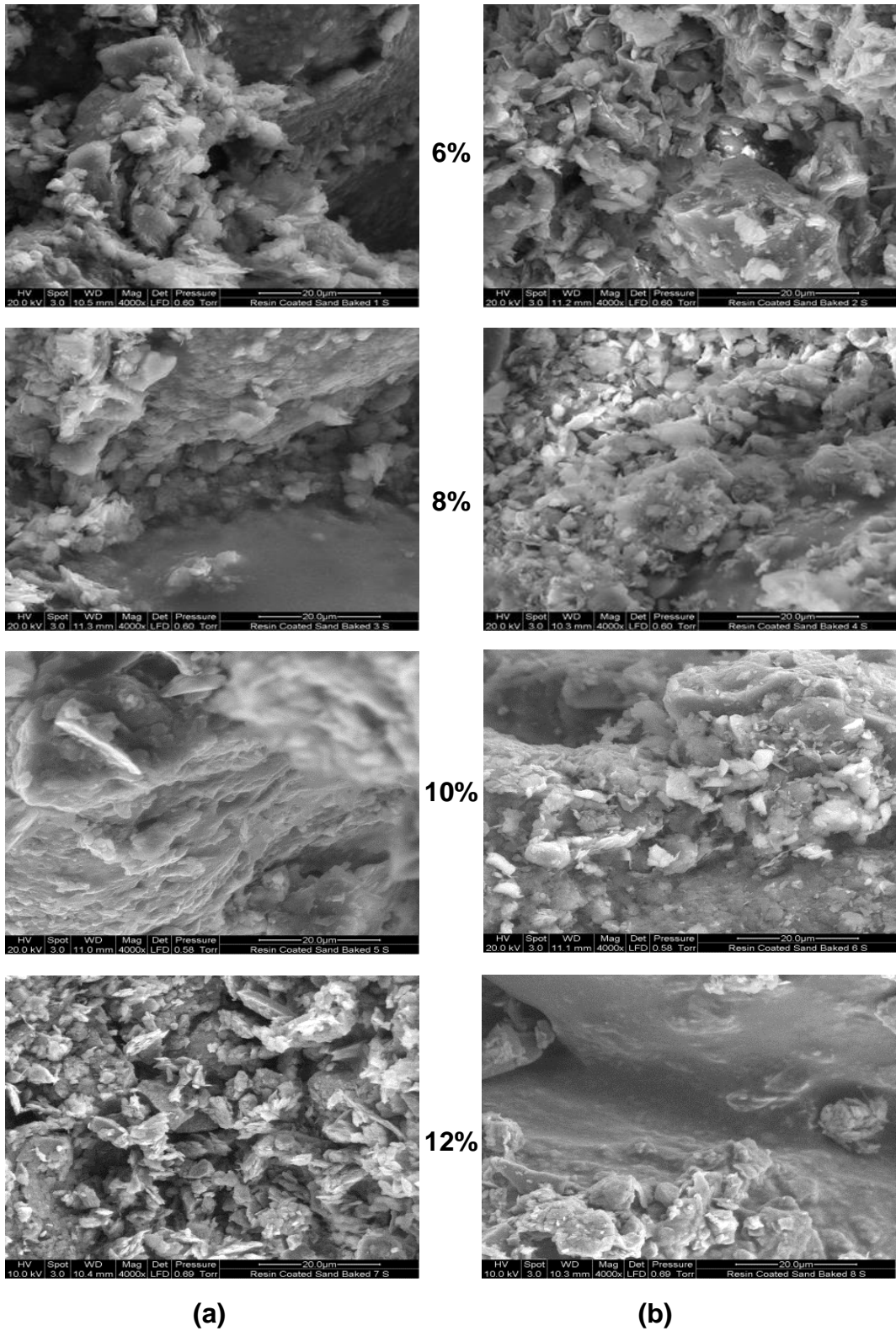


**Fig A3.4 Photomicrographs of baked parts at the outer surfaces with silica flour (a) 5%, (b) 10% and clay varied from 6% to 12%.**